

FINITE ELEMENT AND ELECTRICAL
CIRCUIT MODELLING OF FAULTY
INDUCTION MACHINES –
STUDY OF INTERNAL EFFECTS AND
FAULT DETECTION TECHNIQUES

A THESIS SUBMITTED TO THE UNIVERSITÉ LIBRE DE BRUXELLES (ULB)
FOR THE DEGREE OF DOCTEUR EN SCIENCES DE L'INGÉNIEUR

2007

By
Jonathan Sprooten

under the supervision of
Pr. Jean-Claude Maun and Pr. Johan Gyselinck
Department of Bio, Electro And Mechanical Systems (BEAMS)
Université Libre de Bruxelles

Contents

Abstract	9
Acknowledgements	11
1 Introduction	15
2 Failure modes of induction machines	17
2.1 Bearing faults and rotor eccentricity	18
2.1.1 Causes	18
2.1.1.1 Mechanical stress	19
2.1.1.2 Thermal stress	19
2.1.1.3 Magnetic stress	19
2.1.2 Consequences and evolution of the fault	19
2.2 Stator or armature faults	20
2.2.1 Causes	20
2.2.1.1 Thermal Stress	20
2.2.1.2 Electrical Stress	21
2.2.1.3 Mechanical Stress	21
2.2.1.4 Environmental Stress	22
2.2.2 Evolution of the fault	22
2.3 Broken rotor bars / end-ring faults	22
2.3.1 Causes	23
2.3.1.1 Thermal stress	23
2.3.1.2 Mechanical stress	23
2.3.2 Evolution of the fault	23

2.4	Conclusions	24
3	FE models and explanations of faulty machines	27
3.1	Introduction	27
3.2	Study of a healthy machine	28
3.2.1	A geometric description of the motor and materials	28
3.2.1.1	2D formulation	30
3.2.1.2	Domain limits	30
3.2.1.3	Equally filled stator slots	30
3.2.1.4	Neglected hysteresis	30
3.2.1.5	Discretisation of the geometry	31
3.2.1.6	Rolling layer	32
3.2.2	The electrical and mechanical connections	32
3.2.2.1	Computation of end-winding resistance R_{ew} and inductance L_{ew}	36
3.2.2.2	Computation of end-ring segment resistance R_{ers} and inductance L_{ers}	38
3.2.2.3	The mechanical coupling	40
3.2.3	Simulation Results	41
3.2.3.1	Magneto-dynamic simulations	41
3.2.3.2	Time-domain simulations	41
3.2.3.3	Comparison between time-domain and magneto-dynamic results .	45
3.3	Study of a machine with broken bars	45
3.3.1	Main influence of a broken bar on the machine behaviour	46
3.3.2	Broken bars in machine with parallel connected pole-pairs	47
3.3.3	Detailed influence of a broken bar on the machine behaviour	49
3.3.3.1	Healthy machine	53
3.3.3.2	Faulty machine: No modification of local saturation	53
3.3.3.3	Faulty machine: Modification of local saturation	59
3.3.3.4	Validation of the principle of superposition for broken bars	61
3.4	Study of a machine with stator short-circuits	63
3.4.1	Main influence of internal stator short-circuits on machine behaviour	64
3.4.2	Detailed influence of internal stator short-circuits on machine behaviour . .	66

3.5	Study of a machine with rotor eccentricities	70
3.5.1	Effect of eccentricity on the machine behaviour	73
3.6	Conclusions	76
4	Overview of condition monitoring	79
4.1	Mechanical techniques	79
4.1.1	Vibration monitoring	79
4.1.2	Speed fluctuation monitoring	80
4.2	Chemical techniques	82
4.3	Temperature monitoring	82
4.4	Partial Discharges monitoring	83
4.5	Electrical and magnetic techniques	83
4.5.1	Detection through axial flux	84
4.5.2	Detection through airgap flux	84
4.5.3	Monitoring of current spectral content (MCSA)	84
4.5.4	Monitoring of Voltage Spectral content (MVSA)	89
4.5.5	Monitoring of Power Spectral content (MPSA)	90
4.5.6	Study of airgap Torque Spectral content (TPSA)	91
4.5.7	Park Vector Approach (PVA)	92
4.5.8	Detection by computation of inverse impedance	93
4.5.9	Machine modelling	95
4.5.9.1	Parameter identification of symmetrical model	95
4.5.9.2	Parameter Identification of an asymmetrical model	96
4.5.9.3	Current difference from healthy model	96
4.5.9.4	Dynamic Model with Common and Differential mode approach	96
4.5.9.5	Transient model for stator short-circuits	97
4.5.9.6	Comparison of torque models (Vienna monitoring method)	97
4.6	Conclusions	98
5	Circuit Machine modelling	101
5.1	Introduction	101
5.2	Circuit model of healthy machine	107

5.2.1	Implementation	107
5.2.2	Numerical Implementation	110
5.3	Circuit model of a machine with broken bars	110
5.3.1	Model based on complete rotor cage description	110
5.3.1.1	Implementation 1	111
5.3.1.2	Numerical Implementation	113
5.3.1.3	Implementation 2	114
5.3.1.4	Initialisation	117
5.3.1.5	Numerical Implementation	118
5.3.2	Model based on Park transformation of the rotor	119
5.3.2.1	Implementation 1	119
5.3.2.2	Initialisation and identification of the rotor impedances	120
5.3.2.3	Implementation 2	123
5.3.2.4	Numerical Implementation	126
5.3.3	Model based on the superposition principle	128
5.3.3.1	Implementation 1	128
5.3.3.2	Numerical Implementation	130
5.3.3.3	Implementation 2	130
5.3.3.4	Numerical Implementation	132
5.3.4	Comparison of models for broken bars	133
5.4	Conclusion on circuit modelling	136

6 Parameter identification of circuit models 139

6.1	Introduction	139
6.2	Parameter estimation of healthy machine model (<i>ModelHealthy</i>)	140
6.2.1	Model structure	140
6.2.2	Identification procedure	141
6.2.2.1	Choice of measurements used	142
6.2.2.2	Choice of the cost function	142
6.2.2.3	Choice of working points	143
6.2.3	Data used to study the convergence of the formulation	144
6.2.4	Convergence of the identification	144

6.2.4.1	Does the identification presents problematic local minima?	145
6.2.4.2	Sensitivity of the identification to noise on the measurement of the currents, voltages or speed	149
6.2.5	Identification using data from FE simulation	149
6.2.5.1	Constant parameters for all working points	149
6.2.5.2	Sensitivity of the solution for each invariant	150
6.2.5.3	Parameters function of the working point	151
6.2.6	Simulation results	154
6.2.7	Conclusions	154
6.3	Estimation of the rotor cage parameters	155
6.3.1	Data of FE simulations	157
6.3.2	Parameter estimation	158
6.3.3	Results	160
6.3.4	Conclusions	161
6.4	Conclusions	161
7	Implementation of fault detection	163
7.1	Introduction	163
7.2	Detection and quantification using MCSA	163
7.3	Detection of broken bars using circuit models	166
7.3.1	Off-line implementation of the fault detection	167
7.3.1.1	Accuracy in the representation of the machine behaviour	167
7.3.1.2	Sensitivity of the parameters	173
7.3.2	On-line implementation of the fault detection	174
7.3.2.1	Algorithm based on <i>ModelSupBB</i>	175
7.3.2.2	Algorithm based on <i>ModelParkBB</i>	180
7.4	Conclusions	183
8	General conclusions and future work	185
	Bibliography	189
A	Demonstration of models	199
A.1	Torque expression	199

A.2	Space vector transformation of healthy machine model	200
A.2.1	Stator	200
A.2.1.1	Ψ_{ass} = Stator flux due to stator currents:	200
A.2.1.2	Ψ_{asr} = Stator flux due to rotor currents	201
A.2.1.3	Finally the stator flux is given by	202
A.2.2	Rotor	202
A.2.2.1	The rotor flux due to stator current is given by	202
A.2.2.2	Ψ_{rr} = Rotor flux due to rotor currents	203
A.2.2.3	Then the rotor flux is given by	205
A.2.2.4	Equivalent rotor resistance	205
A.2.3	Torque Expression	206
A.3	Complete circuit model of a machine	207
A.3.1	Stator	207
A.3.2	Rotor	208
B	Data of FE models	209
B.1	Geometrical Data of <i>IND1</i>	209
B.2	Electrical data of <i>IND1</i>	209
B.3	Electrical data of <i>IND1</i> with 10-turns stator short-circuit	210

Abstract

This work is dedicated to faulty induction motors. These motors are often used in industrial applications thanks to their usability and their robustness. However, nowadays optimisation of production becomes so critical that the conceptual reliability of the motor is not sufficient anymore. Motor condition monitoring is expanding to serve maintenance planning and uptime maximisation. Moreover, the use of drive control sensors (namely stator current and voltage) can avoid the installation and maintenance of dedicated sensors for condition monitoring.

Many authors are working in this field but few approach the diagnosis from a detailed and clear physical understanding of the localised phenomena linked to the faults. Broken bars are known to modulate stator currents but it is shown in this work that it also changes machine saturation level in the neighbourhood of the bar. Furthermore, depending on the voltage level, this change in local saturation affects the amplitude and the phase of the modulation. This is of major importance as most diagnosis techniques use this feature to detect and quantify broken bars. For stator short-circuits, a high current is flowing in the short-circuited coil due to mutual coupling with the other windings and current spikes are flowing in the rotor bars as they pass in front of the short-circuited conductors. In the case of rotor eccentricities, the number of pole-pairs and the connection of these pole-pairs greatly affect the airgap flux density distribution as well as the repartition of the line currents in the different pole-pairs.

These conclusions are obtained through the use of time-stepping finite element models of the faulty motors. Moreover, circuit models of faulty machines are built based on the conclusions of previously explained fault analysis and on classical Park models. A common mathematical description is used which allows objective comparison of the models for representation of the machine behaviour and computing time.

The identifiability of the parameters of the models as well as methods for their identification are studied. Focus is set on the representation of the machine behaviour using these parameters more than the precise identification of the parameters. It is shown that some classical parameters can not be uniquely identified using only stator measurements.

Fault detection and identification using computationally cheap models are compared to advanced detection through motor stator current spectral analysis. This last approach allows faster detection and identification of the fault but leads to incorrect conclusions in low load conditions, in transient situations or in perturbed environments (i.e. fluctuating load torque and

unideal supply). Efficient quantification of the fault can be obtained using detection techniques based on the comparison of the process to a model.

Finally, the work provides guidelines for motor supervision strategies depending on the context of motor utilisation.

Acknowledgements

This PhD-thesis is the result of a part-time research work from 2001 to 2007 at the Department of Bio-, Electro- And Mechanical Systems of the Université Libre de Bruxelles. The study was proposed by Professor Jean-Claude Maun. I gratefully acknowledge his assistance and the trust he placed in me throughout these years. I am also grateful to Professor Gyselinck for the valuable suggestions he proposed and for the extensive reviewing of this work.

I would like to express my gratitude to Professor Frédéric Robert and Professor Michel Kinnaert for their useful comments as well as for the inspiring image of a researcher they gave me, each in their own way.

Also, I would like to thank my colleagues for all the stimulating discussions, professional or not. Special thanks to Antonio del Castillo Zas, Ana Morales, Xavier Robe, Benjamin Genêt, Jacques Warichet and Pascal Provot.

Many thanks to my friends who supported me through the hard times of this work. Special thanks to François who helped me both technically and humanely when I needed it the most. I would also like to thank my parents, sister and grand mother for their unconditional support.

Thanks to Ana for Everything.

Finally, thanks to you, reader of this text, as it is the most rewarding to realise that this text is considered. I hope you'll keep reading other pages than this one the introduction and the conclusions.

Jonathan Sprooten Brussels, August 19th 2007

Nomenclature

Abbreviations

EMF	Electromotive force
FE	Finite Element
FFT	Fast Fourier Transform
MCSA	Motor current signature analysis
MMF	Magnetomotive force
PWM	Pulse width modulated supply
RMS	Root Mean Square value of the signal

Symbols

A	Magnetic vector potential
\underline{X}	The complex number X
\bar{X}	The vector X
f	Supply frequency
H	Magnetic field
J	Rotor moment of inertia
K	Current density
k	Any integer
k_{odd}	Any odd integer
l	Rotor axial length
μ_0	Permeability of the vacuum
n	Total number of bars of the squirrel cage

n_{BB}	Number of broken bars
\hat{n}_{BB}	Estimated number of broken bars
N_{sc}	Number of short-circuit coils
ω	Supply pulsation
Ω_r	The rotor mechanical speed
ω_r	Rotor electrical speed
P	Number of pole pairs
p	Laplace operator
ϕ	Flux
ρ	Resistivity of the material
ρ_{al}	Resistivity of the aluminium
rod	Rotor outer diameter
s	Motor slip
sid	Stator inner diameter
t	Time [s]
$\hat{\theta}_0$	Estimated initial rotor position
θ_0	Initial rotor angular position

Chapter 1

Introduction

Induction motors have been used for many years in industry. The main reasons are the simplicity of their use as well as the limitation of maintenance costs achieved thanks to the robustness of the machine. Fuses were protecting the motors and scheduled maintenance was a standard practice as labour force was inexpensive and equipment downtime of the installation was not critical. This was many years ago...

Nowadays, in order for the industries to continue being competitive, the motor conceptual reliability is not sufficient anymore. Furthermore, condition-based maintenance or reliability-based maintenance have, in most applications, supplanted the classical planned maintenance. These ensure cost-effective production by optimising maintenance costs and plant uptime. However, these maintenance strategies need information to perform their job. Machine condition monitoring devices were then introduced to monitor the health of the installation. Mechanical and thermal techniques are widely used. Furthermore, in some situations, the monitoring device can perform fault identification which helps to reduce maintenance time. Finally condition monitoring can be used to avoid situations which reduce component life.

In parallel with the elaboration of maintenance plans, developments have been made in machine control and protection. Motor protection relays are now numerical and based on current and voltage sensors. Motor speed or torque regulation is now common. It allows to enhance the performance of the drive by increasing its efficiency and the flexibility of its use.

The presence of these sensors is an opportunity to reduce investment costs and maintenance costs of the monitoring system by integrating its functions in the protection and/or the control of the drive. This opens the door to new developments in condition monitoring of electrical motors: electrical and magnetic techniques.

An important challenge of this new area is the understanding of the influence of the fault on the signals used for the diagnosis. This influence brings into play complex interactions between mechanical and magnetic phenomena inside the machine.

Another challenge lies in the "on-line" possibility to perform diagnoses. Indeed, some faults evolve quickly and one-off measurements can be ineffective. Moreover, the coupling of "on-line"

monitoring and protection can avoid costly repairs by stopping the fault evolution before it becomes catastrophic. However, on-line diagnosis is demanding in terms of computing power and the monitoring technique must always be reliable even when performed faster. False-alarms must be avoided. Improvements in computing power are allowing more sophisticated diagnosis to be implemented.

There is another field, strongly connected to condition monitoring in this work where the improvement of computing power allows powerful numerical tools to be used. This is Research...

In this work, the finite element method is used to understand the complex behaviour of **faulty induction motors**. This method requires extensive computing time but allows the modelling of the machine through local electromagnetic laws: the Maxwell's equations. The construction of **finite element models** of faulty machines as well as the analysis of local and global effects of the faults on the machine behaviour will be proposed in chapter 3. The information provided is of primary importance as a complete monitoring system relies on this understanding of the physical phenomena linked to the fault. In this work, FE models will also be used as a test bench for comparing and developing motor diagnosis methods. A useful review of **condition monitoring techniques** will be then proposed in chapter 4. The methods are tested on the same set of data which allows objective comparisons to be made.

The field of machine modelling is widely studied as the use of models covers many applications. Precise but computing-extensive models are mainly used for machine design and analysis of machine behaviour. This is for example the situation of finite element models or permeance network models. In the field of machine controls, circuit models are often used. Probably the most known is the model based on the Park equations. Nowadays, machine modelling is also used in condition monitoring as they can take into account more external conditions than classical techniques. This is useful to avoid false alarms and therefore optimise maintenance. Diagnosis based on models will be performed in chapter 7.

"On-line" diagnosis requires light models in terms of computing time. The reduction of this computing time compared to other models is achieved through mathematical developments and assumptions that need to be analysed. The realisation and comparison of different **electrical circuit models** will then be studied in chapter 5.

Finally, machine models are often useless without well-determined parameters. Indeed, models are used to represent devices from a certain aspect. The determination of the parameters of a model is therefore crucial in many applications. Furthermore, in the field of modelling for condition monitoring, faulty machines are (un-)fortunately rarely available and methods for **parameter identification** from the knowledge of healthy machines should be used. Some methods are proposed and discussed in chapter 6.

But this work would not have its *raison d'être* if induction motors were unbreakable. Then we will start at the beginning; "What types of faults affect induction motors?" and "How do they appear?" This will be the subject of chapter 2.

Chapter 2

Failure modes of induction machines

Failures in electrical rotating machines and especially in cage induction motors can be classified in 4 main groups:

- Bearing and rotor eccentricity faults;
- Stator winding faults;
- Rotor winding faults (i.e. rotor bars and end-rings in the case of squirrel cage motors);
- and faults in external devices which regroup the accessories of the drive system.

Several surveys [IEEECommittee 85, EPRI 82, Thorsen 95, Thorsen 99, Benbouzid 03] compare the occurrence rate of these faults in various applications. A comparison of the surveys is presented in figure 2.1. Even though the values presented in each survey depend for example on

- the number of samples;
- the environment in which the drive works;
- the maintenance strategies of the plant;
- and the construction of the machines;

One can clearly see that bearing faults are the most frequent failure mode in electrical machines. They are closely followed by stator winding faults, specially when inverters are used as supply. Rotor faults only account for a small part of the faults.

In order to understand the fault appearance and build a detection scheme, this chapter will focus on the solicitations and causes that lead to the apparition of the fault. Later we will detail fault evolution and their influence on the machine behaviour. This approach will be made for each group of faults.

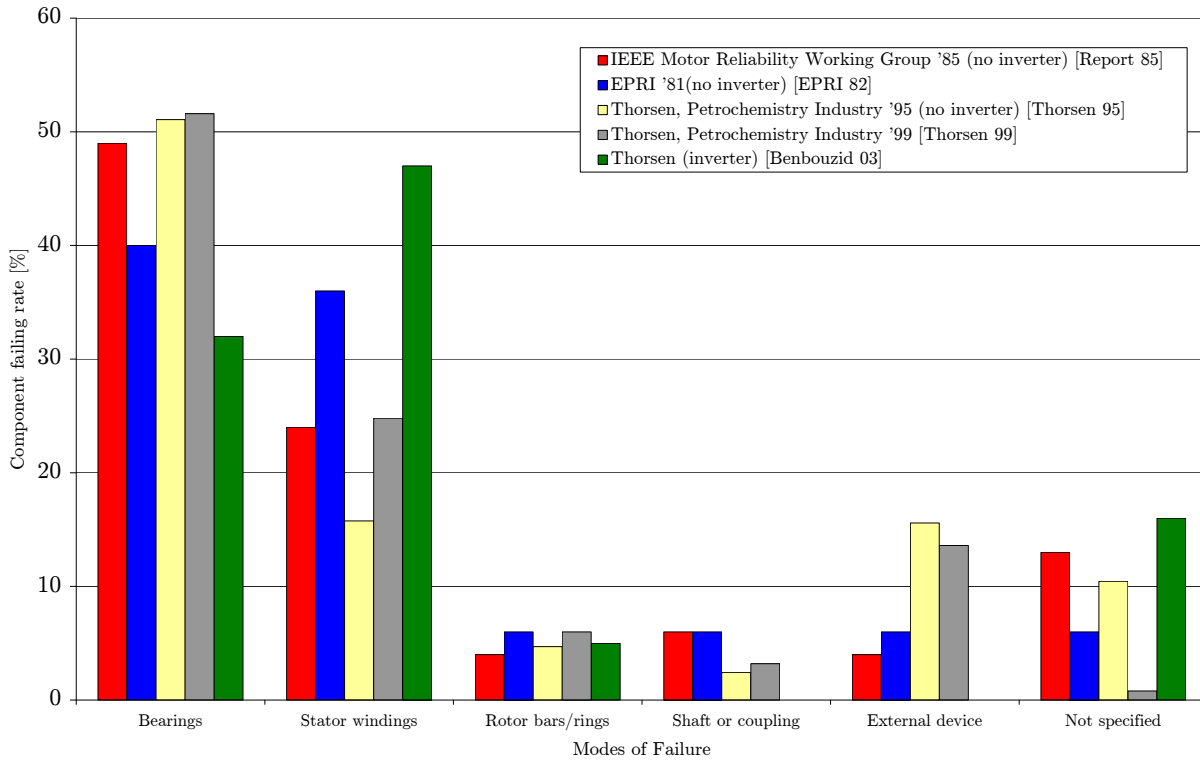


Figure 2.1: Induction motor component failing rate versus survey.

2.1 Bearing faults and rotor eccentricity

Bearing faults and rotor eccentricity are the most common faults in induction machines. In dedicated works, rotor eccentricities are often separated into:

- Static eccentricity when the position of minimum airgap is fixed in space. In this case, the rotor rotates around its centre which is different from the one of the stator.
- Dynamic eccentricity when the position of minimum airgap rotates with the rotor. This phenomenon arises when the centre of rotation of the rotor is different from its geometric centre.

On the other side, the destruction of a rolling element (ball, roller, ...) will produce a radial motion between rotor and stator. This displacement causes the airgap to vary and for this reason, bearing faults often manifest themselves the same way eccentricity does.

2.1.1 Causes

The main causes of bearing failures and eccentricities can be separated in three categories:

- mechanical stress

- thermal stress
- magnetic stress

2.1.1.1 Mechanical stress

Fatigue of the rotor bearings can create small fissures on the surface of the rolling elements. With time, these fissures can propagate and fragments could break loose. These abrasive fragments cause pitting and sanding of raceways and balls [Önel 05, Ong 00]. Of course, the situation gets worse when unbalanced weights, vibrations on load torque and misalignments are present. If uniform wear of the bearings appears, it manifests itself as static or dynamic eccentricity depending on the used raceway. Furthermore, the ellipticity of the stator from the assembly stage manifests also itself as static eccentricity.

2.1.1.2 Thermal stress

Because the shaft is made of steel, heat from the rotor core can easily be conducted to the bearing. However, overheating can originate from the bearing itself due to friction by mechanical degradations or improper lubrication. As the temperature rises, the lubrication becomes less efficient. This accelerates the failure and can at last lead to bearing seizure [Önel 05].

2.1.1.3 Magnetic stress

If rotor eccentricity is present due to bearing wear for example, the airgap length is not anymore constant along the rotor circumference. A greater force of attraction is applied on the rotor in the region of lower airgap reluctance (smaller airgap). This force called unbalanced magnetic pull (UMP) tends to increase this eccentricity and unevenly wears the bearing [Tenhunen 01, Dorrell 97].

Finally, asymmetrical flux pattern around the shaft due to eccentricities or cage asymmetries results in the presence of shaft voltages. If the voltage level becomes important, alternating current can flow through the bearings. This current causes overheating of the bearing oil as well as pitting on the balls [Ong 00].

2.1.2 Consequences and evolution of the fault

As it can be easily understood, a small level of rotor eccentricity often exists in rotating machines due to manufacturing or assembly methods. A danger arises when this eccentricity becomes larger due to the radial forces (UMP) that emphasise the phenomenon. The rotor can finish by rubbing the stator, resulting in the destruction of both elements.

The oscillating movements of the rotor create mechanical vibrations at particular frequencies depending on the rotational speed, ball characteristics and type of faults (outer bearing race defect, inner bearing race defect, ball defect or train defect or rotor eccentricity) [Schoen 95b].

Furthermore, the radial motion of the shaft causes oscillation of the airgap length, of mutual inductances and, as a result, frequency components are created in the currents. Moreover, it has been shown that at the point of minimum airgap, local saturation rises [Stavrou 94]. This has for effect to damp the fluctuation of the mutual inductance and therefore the amplitude of the harmonics of the currents.

Finally, eccentricity globally increases the airgap length and so reduces tooth pulsation and thus core losses [Bangura 00b]. This will be studied in more details in section 3.5.1.

2.2 Stator or armature faults

2.2.1 Causes

The main causes of stator winding failures can be separated in four categories:

- thermal stress
- electrical stress
- mechanical stress
- environmental stress

2.2.1.1 Thermal Stress

It is well known that the insulation is designed to have an extended lifetime at rated temperature (for example, insulations of class A have a lifetime of 20.000 hours at 105 °C). However, if temperature increases above this operating temperature, lifetime quickly shortens as it is shown in figure 2.2. This phenomenon is called Thermal Aging. This increase of temperature can be due to [Bonnett 92]:

- Voltage variation or unbalance. It is stated in [Bonnett 92] that "3.5% voltage unbalance per phase will lead to an increase of winding temperature of 25% in the phase with the highest current".
- Repeated starts within a short period of time;
- Overloading;
- Bad or defective ventilation;
- High ambient temperature.

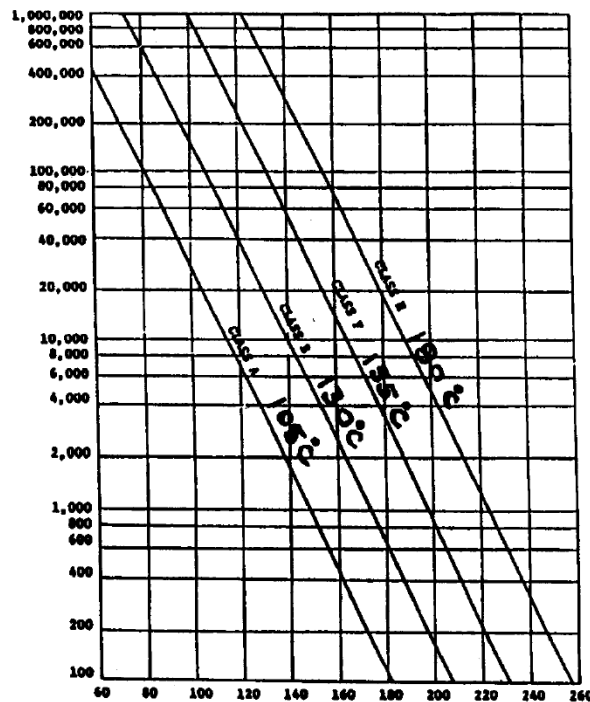


Figure 2.2: Total winding temperature [°C] versus life [hours] [Bonnett 92]

2.2.1.2 Electrical Stress

Higher voltage than nominal value or high dV/dt (capacitor switch, opening and closing of circuits, PWM drives, ...) will lead to the degradation of the dielectric. This is shown in figure 2.1 by comparing the last survey with the previous ones. The presence of an inverter clearly influences winding failures. Furthermore, as foreign material or moisture sneaks into the insulation, a small current could flow from phase to ground. This current can burn the material along its path, which will lead to a higher current flow [Bonnett 92].

For motors above 5kV, the presence of a strong electrical field will lead to internal discharge in cavities within the insulation. It results in carbonised spots in the insulation. These spots cause deformations of the electrical field (increase in the region of the burned spot). More discharges appear in these areas and a conductive path progress through the insulation (see figure 2.3). This phenomenon is called Arc or Insulation Tracking [Couneson 97, Bonnett 92].

2.2.1.3 Mechanical Stress

As shown before, repetitive starting has for consequence to rise winding temperature. Furthermore, this cyclic effect causes expansion and contraction of the insulation. This could lead to cracks in the insulation [Bonnett 92]. Furthermore, a force resulting from the interaction of the stator current and the magnetic field acts on the coil conductors. This force has an alternative component at twice the supply frequency [Bonnett 92, Jianzhong 98, Kogan 97]. The resulting



Figure 2.3: Arc tracking in a circuit breaker bushing [Paoletti 01].

vibrations cause erosion and abrasion of the insulation [Kogan 97]. More details on the calculation of these forces are available in [Jianzhong 98]. Finally, materials can strike the windings and damage the insulation.

2.2.1.4 Environmental Stress

The presence of moisture or chemicals can degrade the quality of the insulation and lead to winding failure.

2.2.2 Evolution of the fault

As the insulation is degrading, discharge currents in the insulation voids (see 2.2.1.2) influence voltage at the machine terminals. High frequency voltage spikes and dips occur. Another consequence of these so-called "partial discharges" is the creation of ozone and oxides of nitrogen. These components can combine with moisture to form nitric acid that destroys the insulation [Neacsu 02].

Once a complete carbonised path is created, the fault current can either flow to the stator core (phase to ground fault) or to another part of the winding (turn to turn fault) or to another winding placed in the same slot (phase to phase fault). The topology of the electrical circuit is influenced by these faults. Examples are shown in figure 2.4 for a three phases, two pole-pairs, Y connected machine.

2.3 Broken rotor bars / end-ring faults

As shown in figure 2.1, broken rotor bars only account for about 5% of the failures of induction machines. Nevertheless, it is quite the most studied type of fault.

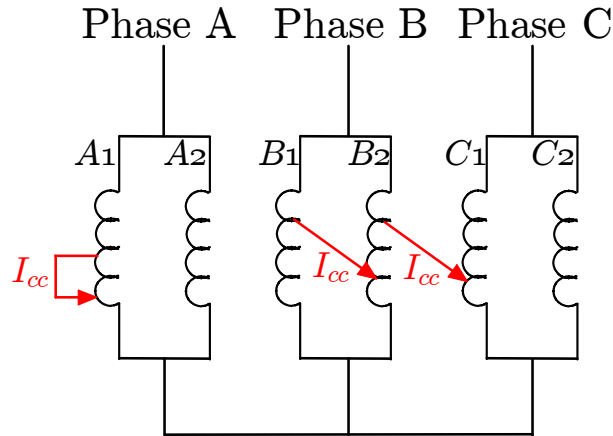


Figure 2.4: Types of stator short-circuits in 3 phases, 2 pole-pairs, Y connected machine [Xiangheng 00].

2.3.1 Causes

2.3.1.1 Thermal stress

The overheating of the rotor winding (bars and end-rings) could melt the brazing material or even the cage itself [Bonnett 92]. The source of heat can be located either in the bar (the bar is a heat source specially during repetitive starts, stalling or accelerations) or in the rotor core with heat transfer to the bars. This is for example the case of welded laminations.

Moreover, when supply voltages are unbalanced, high currents are induced in the rotor because of the low negative sequence impedance [Paoletti 89]. Furthermore, these negative sequence currents are unevenly distributed throughout the section of the bar due to enhanced skin effect present at their high frequency $((2 - s) f)$ [Souto 00].

Finally, at low speeds (high slip conditions), skin effect tends to increase thermal gradient through the bar which can lead to its degradation.

2.3.1.2 Mechanical stress

Similarly as in case of the stator windings, magnetic forces cause bars to vibrate. However, centrifugal forces due to the rotor rotation tend to hold the bar still in the slot. At low speed, rotor current frequency is around 50Hz and centrifugal forces are low. The bars are therefore vibrating which can lead to mechanical fatigue. The situation is much different at high speeds where centrifugal forces are much bigger than magnetic forces.

2.3.2 Evolution of the fault

When a bar is broken or partially broken, a part of the current initially flowing in the bar is redistributed in the adjacent bars. In these bars, the current is higher than normal and Joules

losses are increased. Furthermore, the flux distribution close to the broken bar changes. Flux density is increased on one side of the bar but decreased on the other side as it is illustrated using Finite Element (FE) computations in figure 2.5. The FE model and the explanation of this phenomenon will be given in chapter 3. This phenomenon results in an increase of the iron losses near the bar [Bangura 00b].

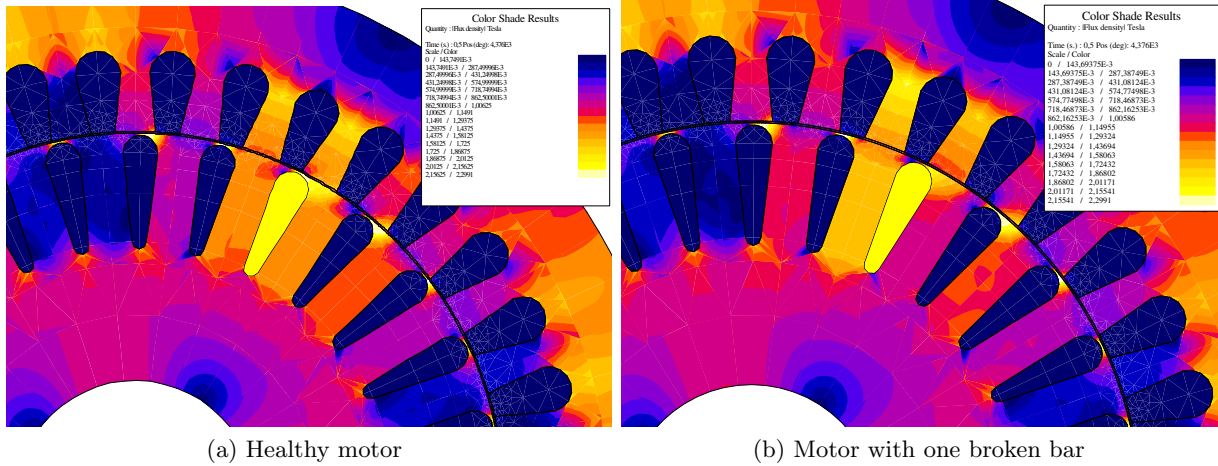


Figure 2.5: Flux density in the region of the broken bar (shown in yellow) for nominal conditions.

The two above mentioned losses lead to an increase of temperature of the bars adjacent to the broken one which could break in their turn.

In reality, the situation is a little less dangerous. Indeed, the current flowing in the broken bar is rarely zero; either the bar is only cracked and/or inter-bar currents exist [Walliser 94, Gyselinck 05].

The presence of inter-bar currents occurs when the rotor cage is not insulated from the core. The current enters the bar normally and along the length of the bar progressively reaches the adjacent bars. This is illustrated in figure 2.6. This flow of current through the iron core leads to the heating of the rotor core.

2.4 Conclusions

This chapter has presented an overview of the main stresses of an electric drive and the consequences on its health. Several surveys were analysed to identify the main causes of failure. Each survey leads to the same main faults listed by the probability of their apparition: bearing and rotor faults, stator winding faults, rotor cage faults and external devices faults. By comparing the surveys, the influence of power electronics on stator faults is clear.

Furthermore, the physical phenomena that lead to the apparition of the faults have been described and their possible evolutions have been given. This approach is rich in physical understanding of the stress to which a motor is placed and places the analysis of faulty machine in its

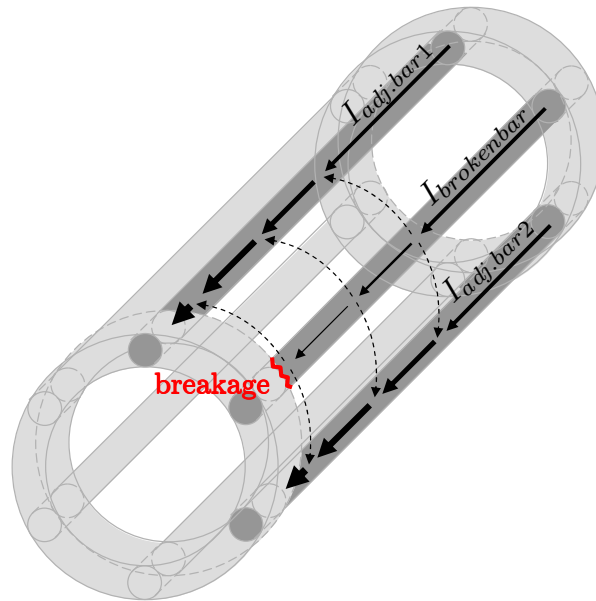


Figure 2.6: Representation of the flow of current in a broken bar and in the adjacent bars. Thickness of the lines qualitatively represents magnitude of the currents.

context. The following chapters will be devoted to the analysis of a faulty machine as well as diagnosis to detect the presence of the fault before catastrophic evolution is observed.

Chapter 3

Finite Element models and explanations of faulty induction machines

3.1 Introduction

The present section will be dedicated to the finite element modelling of healthy and faulty squirrel cage induction motor and will provide physical explanations of the internal modifications linked to the faults.

The FE approach is considered separately from the other models (presented in chapter 5) due to its status of reference machine representation. Indeed, a finite element modelling is very detailed and represents quite well a real machine [Lombard 92, Vassent 91].

FE simulations offer unique opportunities to understand faulty machine behaviour, elaborating monitoring and diagnosis strategies because simulation environment gives controls on all external conditions and machine construction. In the case of faulty machines, the fault severity is therefore well known.

However, some features of the machine will not be taken into consideration; these are for example all 3D effects (at machine axial extremities or between rotor bars) and temperature variation.

In this chapter, FE models will be used to explain in details fault internal effects and in the next chapter, about motor condition monitoring, several techniques will be illustrated using data obtained from the FE simulations. This justifies why FE models are not presented together with the other models.

The machine under study in this document is a 4-pole, 5.36 Hp, 4kW induction motor, further referred to as *IND1*. The pole-pairs are connected in parallel. It has been manufactured by

the Turk Elektrik Endustrisi (TEE) and has been used by several authors for the study of FE formulations [Pham 99], speed control [Mohammed 05] or broken rotor bars [Lopez-Fernandez 03]. The detailed characteristics are presented in table 3.1 and the schematics of the motor are presented in figure 3.1¹.

Nominal values	
Power	= 4.15[kW]
Voltage	= 190[V]
Frequency	= 50[Hz]
Rated speed	= 1459[rpm]
Geometry and windings	
Stator	<ul style="list-style-type: none"> • 36 slots each holding 44 turns from the same phase (1 layer²) • Phases are delta connected
Rotor	<ul style="list-style-type: none"> • Squirrel cage • 28 aluminium bars

Table 3.1: Motor characteristics

3.2 Study of a healthy machine

A commercial FE software package is used for modelling the machine. The choice of *Flux2D* results from a technical-economical comparison realised in 2002 and presented in [Sprooten 03].

The model of the motor is composed of several parts:

- A geometric description of the motor
- A description of the materials
- The electrical connections
- The mechanical characteristics and the load

3.2.1 A geometric description of the motor and materials

FE simulations of machines require several hypotheses in order to reduce model complexity and therefore computation time.

¹Note that this machine was primarily designed as a 380V machine with pole-pairs connected in series

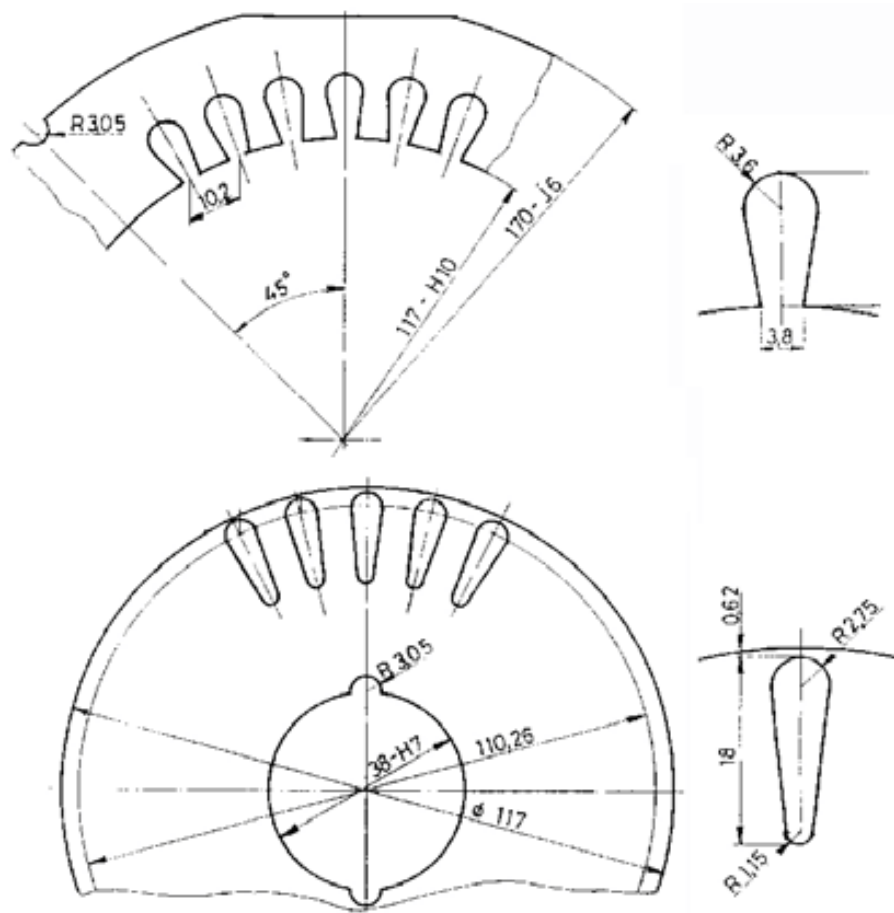


Figure 3.1: Motor schematics [Cedrat 99]

3.2.1.1 2D formulation

The first hypothesis that is going to be made is to consider the machine as a 2D entity. The reason for making this assumption is mainly the reduction of computing time. This hypothesis is acceptable because:

- The rotor and stator conductors are not skewed, and current paths are parallel to the shaft. The presence of interbar currents will not be modelled.
- The axial length of the machine ($l = 139.5mm$) is sufficient to consider that end-regions, in which flux lines are not perpendicular to the shaft, do not significantly contribute to the behaviour of the machine. However, as it will be shown in the next chapter, axial coupling can lead to the presence of specific harmonic components in the stator currents in case of stator faults. This will not be modelled.

Because a 2D formulation has been chosen, end-rings and end-windings which mainly contribute to leakage inductances and affect winding resistances have to be taken into consideration through lumped circuit elements placed in electrical circuit of the machine. The estimation of their values based on the end-portions geometries will be made later in this text.

3.2.1.2 Domain limits

The air surrounding the machine and the rotor shaft will not be modelled. Indeed, these regions have a high reluctance and no flux is crossing them. Therefore Dirichlet boundary conditions can be set on the mesh nodes of the stator outer radius and rotor inner radius. This condition forces flux lines to be tangential to the surface.

In order to compare healthy and faulty motors, no pole symmetries will be assumed. Indeed, even though in the case of a healthy induction machine symmetries can reduce the number of equations, this is not anymore the case for faulty machines.

3.2.1.3 Equally filled stator slots

This next hypothesis concerns the distribution of the conductors inside a stator slot. A coil will be modelled by considering its conductors to be equally distributed in the slot (stranded conductor). The required parameters to define the winding are therefore the number of turns and the resistance of the stranded conductors.

3.2.1.4 Neglected hysteresis

Due to presence of isolated iron sheets for building rotor and stator cores, magnetic hysteresis effect is relatively small³. However flux saturation has to be taken into consideration because it

³These sheets are isolated to limit the flow of eddy currents.

influences the spectrum of line currents. For good numerical conditioning and representation of the saturation curve defined by the data of table 3.2, a cubic spline function is used [Vassent 89]. Figure 3.2 illustrates the saturation characteristic and the input points.

$H(A/m)$	$B(T)$
0	0.00
129	0.50
243	1.10
1850	1.60
3700	1.70
9900	1.85
22100	2.00
43000	2.10

Table 3.2: B-H data [Cedrat 99]

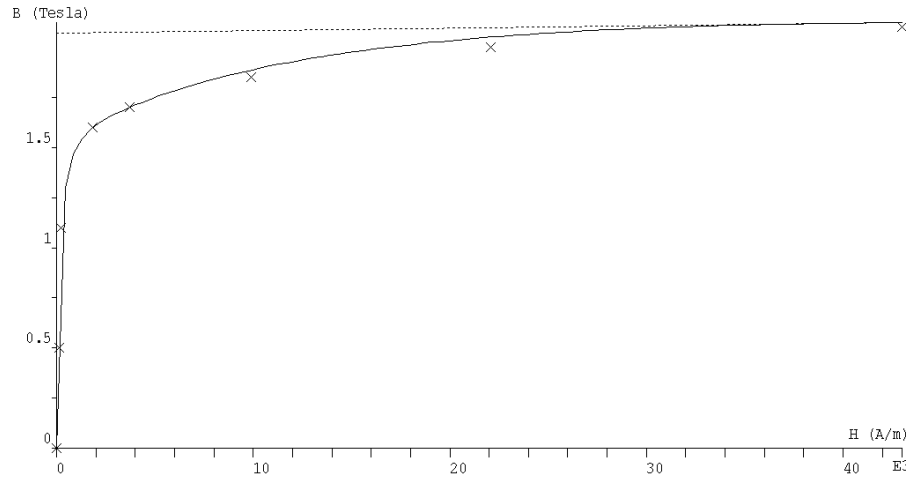


Figure 3.2: Cubic spline created from input points to characterise iron permeability [Cedrat 99]

The other materials, namely copper and aluminium, are defined by their resistivity.

3.2.1.5 Discretisation of the geometry

In order to perform FE calculations, a discretisation of this geometry into elements has to be realised. The first step of this process is taken care of by *Flux2D* mesher. After defining mesh size at particular points in the geometry, the automatic mesher proposes a solution and computes the quality of each element which quantifies the similitude between the element and an equilateral triangular element. If elements of bad quality are present, a second proposal of mesh size at particular locations is to be made. After that, a non-linear magneto-dynamic solution for a healthy motor is computed and observed for coherence. This solver uses a complex formulation

of the magnetic vector potential (A) valid if it is assumed that both A and the source current density (K) are sinusoidal functions of the time. This formulation is much quicker than time-domain formulation but neglects the presence of time and spatial harmonics. The details of this algorithm are presented in [Vassent 89, Vassent 91]. In figure 3.3, the flux density at the bottom of a rotor bar is inspected for continuity between two elements of same magnetic properties. If a good quality solution is not reached, the mesh has to be refined in these regions. It has to be kept in mind that an increase of the number of mesh elements will result in an increase of mesh quality but also in an increase of computing time. The final mesh is shown in figure 3.4.

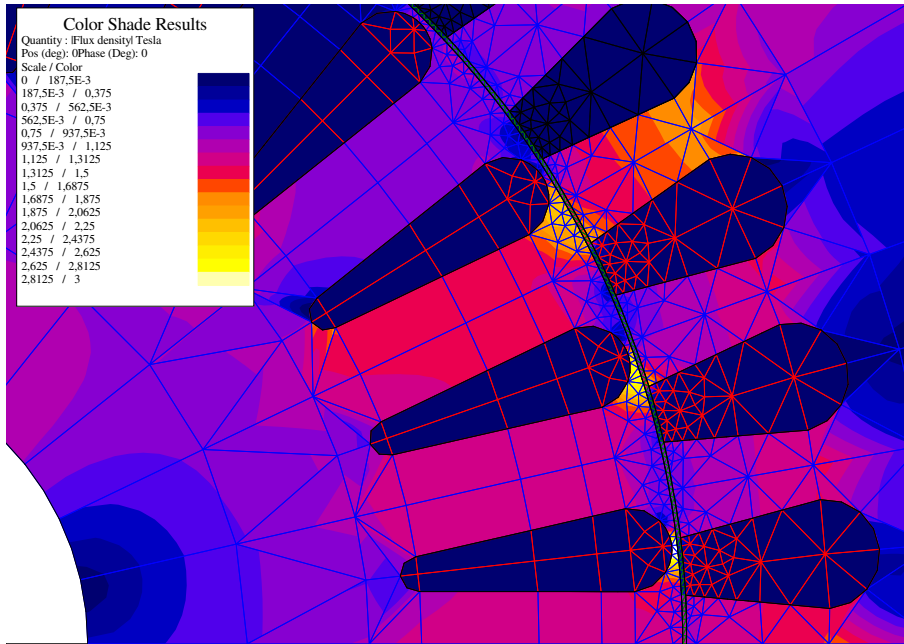


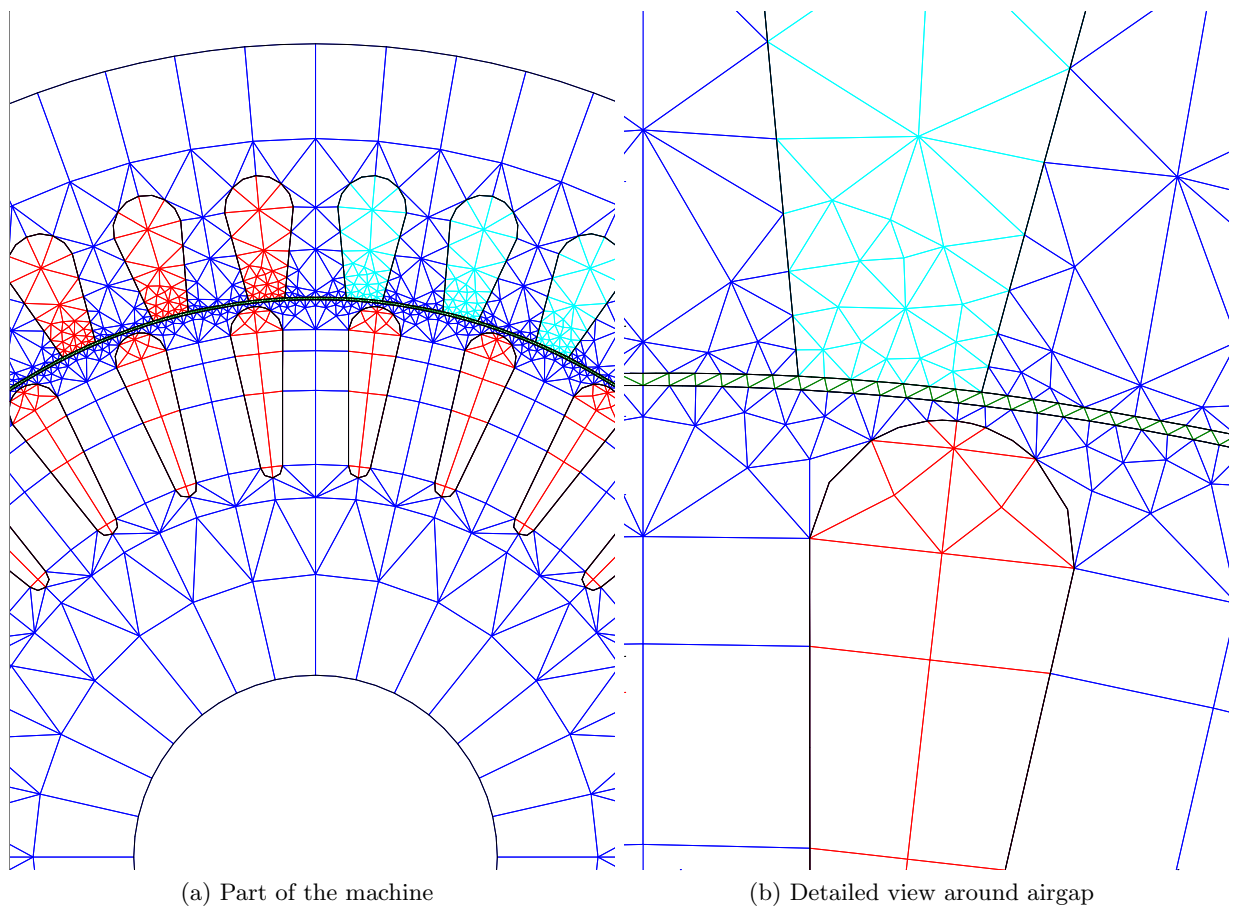
Figure 3.3: Map of flux density around the motor slots at nominal load using magneto-dynamic computations.

3.2.1.6 Rolling layer

The realisation of the rotation is performed using a "rolling layer". This rolling layer consists of a ring-shaped region situated in the airgap. At each instant of the simulated time, the rotor is moved by a certain angle. The only part of the geometry which has to be remeshed is the rolling layer that connects the displaced rotor mesh elements to the stator mesh elements. In our case, the rolling layer consists of the entire airgap region.

3.2.2 The electrical and mechanical connections

The next step in the definition of the finite element model is the description of the windings and the connection of the bars. The electrical circuits of *IND1* is defined as shown in figure 3.5 and the conductors are placed in the slots as shown in figure 3.6.

Figure 3.4: FE mesh of machine *IND1*

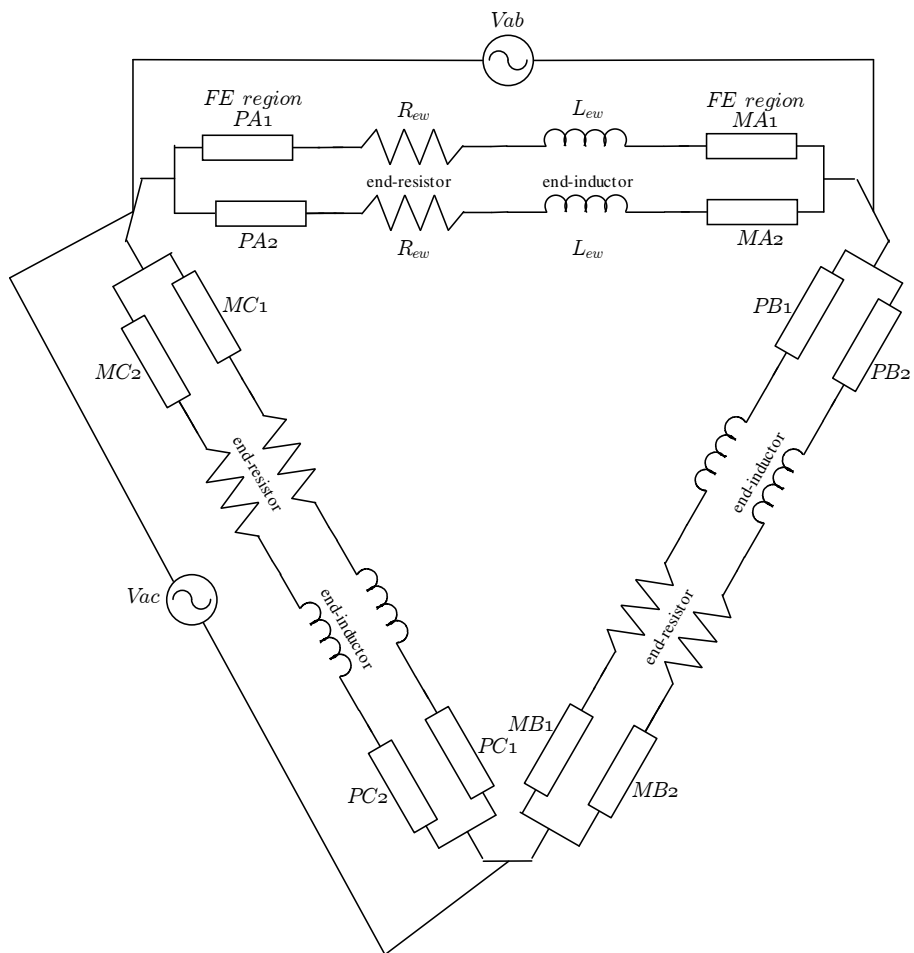


Figure 3.5: Electrical connexion of windings of machine *IND1*.

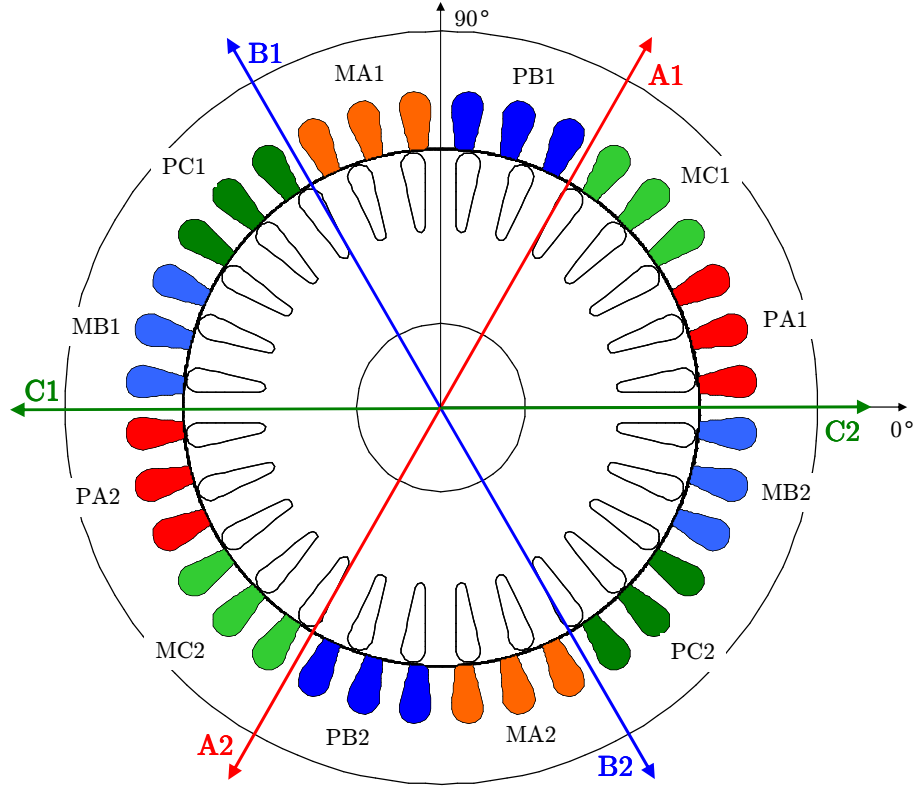


Figure 3.6: Repartition of the stator windings in the slots.

For each stator phase one can see:

- 2 poles,
- A voltage source,

and for each pole,

- 2 stranded conductors groups represent the conductors going into (+) and out of (-) the plane of the FE model (ex: PA1⁴ and MA1). The resistance of each of these groups can be computed using formula

$$R_{group} = \frac{\rho_{cu} l N_{tsp} N_{spp} 4}{\pi d_w^2} \quad (3.1)$$

where d_w is the wire diameter, N_{tsp} and N_{spp} are the number of turns per slot per phase and the number of slots per pole per phase respectively.

This leads to the resistance for the group of stranded conductors (R_{group}) of 0.46557Ω

Numerical Details:

The value of R_{group} presented above is obtained using $N_{tsp} = 44$, $N_{spp} = 3$, $d_w = 0.932mm$, $\rho_{cu} = 1.724 \cdot 10^{-8}\Omega m$ and $l = 139.5mm$.

⁴Plus conductors of phase **A** pole-pair **1** representing conductors entering the plane.

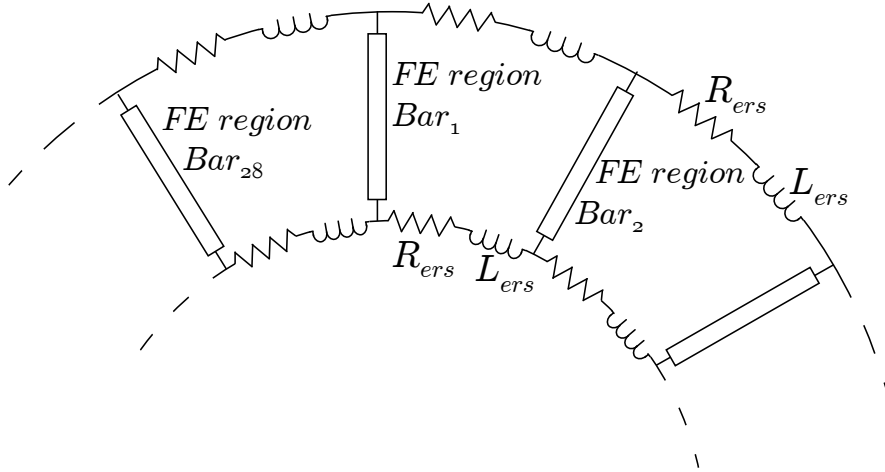


Figure 3.7: Electrical connexion of rotor cage of machine *IND1*.

- A leakage inductance representing the end-windings flux (L_{ew}).
- A resistance representing Joules losses in the end-windings (R_{ew}).

Finally, the rotor cage is composed of

- the massive conductors modelled by the FE approach. These represent the rotor bars.
- the lumped elements for the resistances and inductances of the end-ring portions between two adjacent bars (R_{ers} and L_{ers}).

These elements are connected to form the cage as shown in figure 3.7.

3.2.2.1 Computation of end-winding resistance R_{ew} and inductance L_{ew}

Much work has been made in the determination of end-windings impedance. The approaches are either analytical, empirical, numerical or a combination of these.

If it is assumed that the end-windings follow an arc of angle $\frac{\pi}{P}$ and of diameter $sid + h_{ss}$ (where P is the number of pole-pairs, sid is the stator inner diameter and h_{ss} is the stator slot height) and that this arc is situated at an axial distance of l_{zew} out of the machine, the resistance can be computed through equation 3.2.

$$R_{ew} = \frac{8 \rho_{cu} l_{gew} N_{tsp} N_{spp}}{\pi d_w^2} \quad (3.2)$$

where l_{gew} is the end-winding length which is computed by

$$l_{gew} = \tau_p + 2l_{zew}$$

where $\tau_p = \frac{\pi}{2P}(sid + h_{ss})$ and l_{zew} is the axial length of the end-winding as shown in figure 3.8.

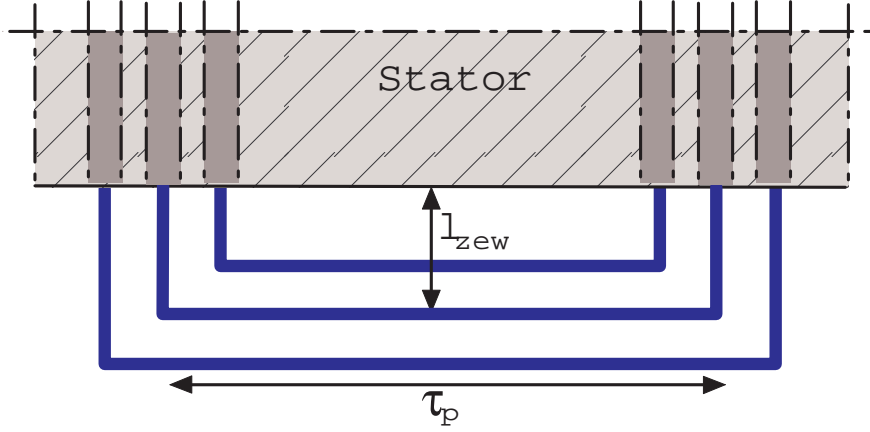


Figure 3.8: View of the stator end section

Using data of the machine presented in appendix B, we find an end-winding resistance (R_{ew}) of 1.115Ω .

Numerical Details:

With $sid = 117\text{mm}$ and $h_{ss} = 13\text{mm}$, we find $\tau_p = 102.1\text{mm}$. Then, with $l_{zew} = 32.5\text{mm}$, we have $l_{gew} = 167.1\text{mm}$ and the value of R_{ew} presented above.

For information, the resistance of a stator phase of the machine with pole-pairs connected in parallel can be computed by

$$R_s = \frac{R_{ew} + 2 * R_{group}}{P}$$

which gives a value of 1.023Ω .

For end-winding inductance calculation, simplifications proposed by Liwschitz in [Liwschitz 67, p. 83-88] will be used.

$L_{ew} = 4 \mu_0 (N_{spp} N_{tsp})^2 \mathcal{P}$ where the permeance \mathcal{P} is computed by

$$\mathcal{P} = \begin{cases} 0.67 l_{gew} - 0.43 \tau_p & \text{for end-windings per pole-pair per phase regrouped in one bundle} \\ 0.47 l_{gew} - 0.3 \tau_p & \text{for end-windings regrouped in several bundles} \end{cases}$$

As this machine corresponds to the first situation, an end-winding inductance (L_{ew}) of 0.0042H is found.

Numerical Details:

With previously computed values of τ_p and l_{gew} , we find $\mathcal{P} = 4.79 \cdot 10^{-2}\text{H}$ which leads to the value of L_{ew} presented above.

3.2.2.2 Computation of end-ring segment resistance R_{ers} and inductance L_{ers}

Trickey has proposed to use 3.3 to compute the end-ring resistance [Trickey 36]

$$R_{er} = \frac{\rho_{Al} \pi P (D_r - D_i)}{e h} \frac{D_r^2 P + D_i^2 P}{D_r^2 P - D_i^2 P} \quad (3.3)$$

As shown in figure 3.9, D_r and D_i are respectively the diameter at the bar centre and at the ring bottom, e and h are the ring thickness and height.

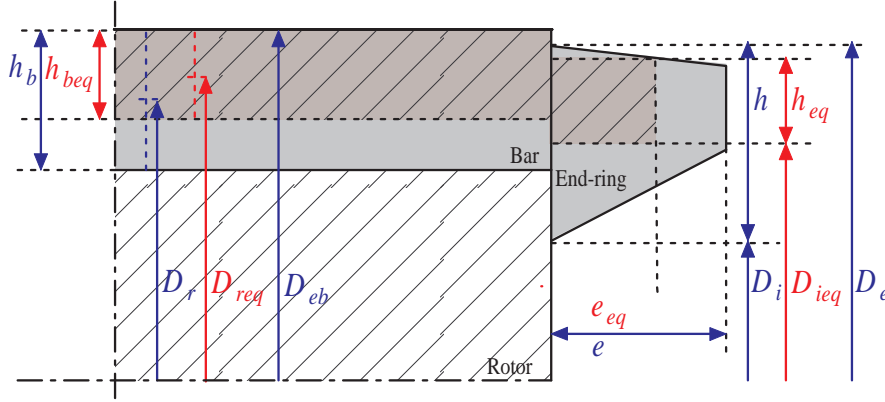


Figure 3.9: View of the rotor end section

Further, as shown in [Cedrat 05], this formula can be modified take into account the skin effect.

An equivalent height of the ring can be recomputed as $h_{eq} = \frac{\rho_{Al} \pi D_e}{R_{er} e + \pi \rho}$, where D_e is the external ring diameter.

The useful height of the bar can be computed using the method proposed in [Liwschitz-Garik 55];

$$\begin{aligned} \xi &= h_b \sqrt{\frac{\pi \mu_0 f s}{\rho_{Al}}} \\ \epsilon &= \xi \frac{\sinh(2\xi) + \sin(2\xi)}{\cosh(2\xi) - \cos(2\xi)} \\ h_{beq} &= \frac{h_b}{\epsilon} \end{aligned}$$

where h_b is the bar height. The equivalent thickness of the ring is then computed by $e_{eq} = \frac{e k}{\epsilon}$ where the coefficient k depends on the contact surface between the bar and end-ring. It is computed using

$$k = \begin{cases} 0.01 X^2 - 0.08 X + 1.07 & \text{if } X < 2.36 \\ -0.017 X + 0.977 & \text{otherwise} \end{cases}$$

with $X = \frac{h_{eq}}{h_x}$ and $h_x = h_{beq} - \frac{D_{eb} - D_e}{2}$.

Therefore, the end-ring resistance can be recomputed using

$$R_{er} = \frac{1}{n} \frac{\rho_{Al} \pi P (D_{req} - D_{ieq})}{e_{eq} h_{eq}} \frac{D_{req}^{2P} + D_{ieq}^{2P}}{D_{req}^{2P} - D_{ieq}^{2P}}$$

where $D_{req} = D_{eb} - h_{beq}$ and $D_{ieq} = D_e - h_{eq}$

Numerical computations are performed for nominal speed. This gives an end-ring segment resistance ($R_{ers} = \frac{R_{er}}{n}$) of $2.5 \cdot 10^{-6} \Omega$.

Numerical Details:

With $D_{eb} = 115.76\text{mm}$ and $h_b = 18\text{mm}$, we find $D_r = D_{eb} - h_b = 97.76\text{mm}$.

Then, using formula 3.3 with $e = 5.7\text{mm}$, $h = 27.3\text{mm}$ and $D_i = 61.1\text{mm}$, we find a first estimate, $R_{er} = 5.59 \cdot 10^{-5} \Omega$.

The equivalent height of the ring is then computed using $D_e = D_i + h = 115.76\text{mm}$; $h_{eq} = 24.89\text{mm}$. A slip value of $s = 0.5$ is taken as the end-ring impedance have much influence during starting. Then, we find $\xi = 1.073$, $\epsilon = 1.11$ and $h_{beq} = 16.18\text{mm}$.

The part of the equivalent bar which is in contact with the ring is given by $h_x = 16.18\text{mm}$. This lead to $X = 1.54$, $k = 0.97$ and an equivalent ring thickness of $e_{eq} = 4.97\text{mm}$.

Finally, the end-ring segment resistance presented above is obtained with $D_{req} = 95.58\text{mm}$ and $D_{ieq} = 65.97\text{mm}$.

For the computation of the end-ring inductance, the formula proposed in [Cedrat 05, p. 12] will be used:

$$L_{er} = \pi \mu_0 (D_e - h_{eq}) \lambda_a \quad (3.4)$$

where $\lambda_a = 0.365 \log_{10} \left(3 \pi \frac{D_{aext} - h_{eq}}{4(h_{eq} + e_{eq})} \right)$.

This gives an end-ring segment inductance ($L_{ers} = \frac{L_{er}}{n}$) of $4 \cdot 10^{-9} H$. The order of magnitude of this end-ring segment inductance can be cross-checked using the comprehensive formula of [Gyselinck 00, p. 9-63]

$$L_{er} = \mu_0 \frac{D_g}{2} \left(\frac{1}{4} + \frac{1}{2} \ln \left(\frac{\Delta^2}{r_{sew} r_{rew}} \right) \right) \quad (3.5)$$

where $r_{sew} = \sqrt{\frac{S_{sew}}{\pi}}$ and $r_{rew} = \sqrt{\frac{e_{eq} h_{eq}}{\pi}}$ are respectively the radius of the equivalent circular section of the stator end-winding bundle and of the rotor end-ring, S_{sew} is the section of the end-winding bundle, D_g is the diameter at airgap middle and Δ is the distance between the centre of these section. Δ is given by $\Delta = \sqrt{(l_{zew} - \frac{E_{eq}}{2})^2 + ((sid + h_{ss}) - (D_{ieq} + h_{eq}))^2}$. These quantities are graphically represented in figure 3.10.

This lead to an end-ring segment inductance of $4.9 \cdot 10^{-9} H$, which validates the use of formula 3.4.

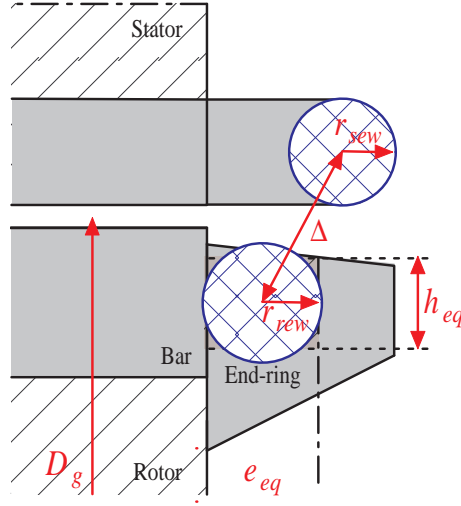


Figure 3.10: Machine end-section

Numerical Details:

Using previously computed values, we find $\lambda_a = 0.312H$. Then, using formula 3.4, we obtain an end-ring segment inductance of $410^{-9}H$.

The formula issued from [Gyselinck 00] is evaluated using $S_{ew} = 191mm^2$, $r_{sew} = 7.8mm$, $r_{rew} = 6.3mm$ and $\Delta = 35.8mm$.

3.2.2.3 The mechanical coupling

Two types of mechanical coupling are considered in this work:

- A load with infinite inertia. In this case the speed is imposed and no mechanical equation is used by the solver.
- The load torque is imposed as well as a friction coefficient. The equation 3.6 shows the integration of the FE results and the mechanical coupling.

$$J \frac{d\Omega_r}{dt} = T_{em} - F\Omega_r - T_l \quad \text{where} \quad \left\{ \begin{array}{l} J = \text{Moment of inertia} \\ \Omega_r = \text{Rotor Speed} \\ T_{em} = \text{Electromechanical torque computed by FE} \\ F = \text{Friction Coefficient} \\ T_l = \text{Load torque} \end{array} \right. \quad (3.6)$$

The inertia of the machine and its load is $J = 0.07kg \text{ m}^2$ and the friction coefficient is $F = 0.001N \text{ m s}$.

This model will now be used to perform several simulations.

3.2.3 Simulation Results

3.2.3.1 Magneto-dynamic simulations

In our work, the magneto-dynamic solver has mainly 2 applications:

The first application is the initialisation of time-domain simulations as its average computing time is very short compared to time-domain simulations. The order of magnitude is 40s^5 [Salon 90].

It is to be noted that magneto-dynamic simulations suppose that the relative position between the rotor and the stator remains constant. This is the case even though virtual displacement of rotor conductors with regard to the stator is considered. The steady-state values of current I_{as} given by the magneto-dynamic simulation at nominal speed for different rotor position is given in figure 3.11 by the curve labelled "without symmetry". An important dependence with the rotor position can be observed due to the presence of the stator and rotor slots. However, because in healthy conditions, the machine is symmetrical, the a , b and c currents can be forced to have equal magnitude and phase shifted by 120° . This is realised by the following equations:

$$\underline{I}_s = \underline{I}_{as} + \underline{I}_{bs} e^{j\frac{2\pi}{3}} + \underline{I}_{cs} e^{-j\frac{2\pi}{3}}$$

and

$$\underline{I}_{as} = \frac{|\underline{I}_s|}{3} e^{j \text{angle}(\underline{I}_s)}; \underline{I}_{bs} = \frac{|\underline{I}_s|}{3} e^{j (\text{angle}(\underline{I}_s) - \frac{2\pi}{3})}; \underline{I}_{cs} = \frac{|\underline{I}_s|}{3} e^{j (\text{angle}(\underline{I}_s) + \frac{2\pi}{3})};$$

This leads to the curve "with symmetry" of the same figure. Later in this work, for healthy machines, we will always apply this transformation for magneto-dynamic results.

The second application is the simulation of steady-state characteristics. As example and because these curves will be used in chapter 6, magneto-dynamic simulations are used to draw the torque-speed characteristic, the circle diagram and the no-load characteristics. This is illustrated in figure 3.12.

3.2.3.2 Time-domain simulations

The time step used to perform time-domain simulations has been chosen to best suit different constraints:

- **Rolling layer :** The results are most accurate if, between each computing instant (Δt), the rotation angle creates a rotor displacement along the airgap smaller than the size of

⁵Computing times are given using version 9.3.3 of *Flux2D* which features an incredible evolution of computing time comparing to previous versions used for this work; a reduction of the computing time by a factor of 10 was commonly observed.

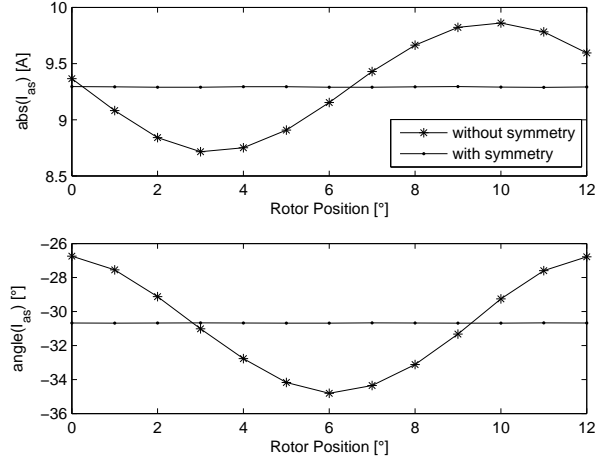


Figure 3.11: Current I_{as} from magneto-dynamic simulations of *IND1* at nominal speed with and without phase symmetry.

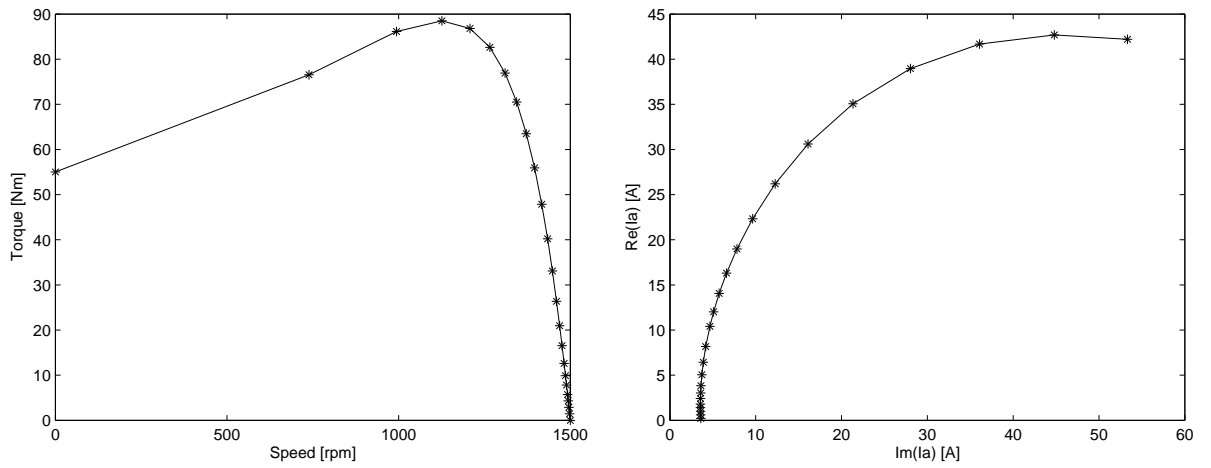
one element of the rolling layer. Figure 3.13 illustrates this description. Of course, this depends on the rotating speed of the rotor. The smaller are the airgap elements, the more difficult it is to achieve this condition. As airgap elements are chosen to be $1.54 \cdot 10^{-4}m$ wide (L_{mesh}) and nominal rotating speed is 1459rpm, the Δt should satisfy the condition $\frac{r_{od}}{2} \tan(\Omega_r \Delta t) \leq L_{mesh}$ which leads to $\Delta t < 1.7 \cdot 10^{-5}s$. It can now be easily understood why mesh discretisation of the airgap was not refined even more.

- **Slotting effect:** The presence of slots creates high frequency variations of the airgap width and therefore of the stator currents. These phenomena must be correctly modelled.
- **Computing time:** FE calculations require a lot of computing time. However, the smaller are the time steps, the smaller is the computing time required per step but more computations are then required to represent the same simulated duration. As indication, simulation of *IND1* requires about 1 min to compute 10 time steps.
- **Rounded sampling frequency:** For easy manipulation of the signal, a time step which corresponds to a round sampling frequency will be chosen.

Based on these criteria, several choices can be made.

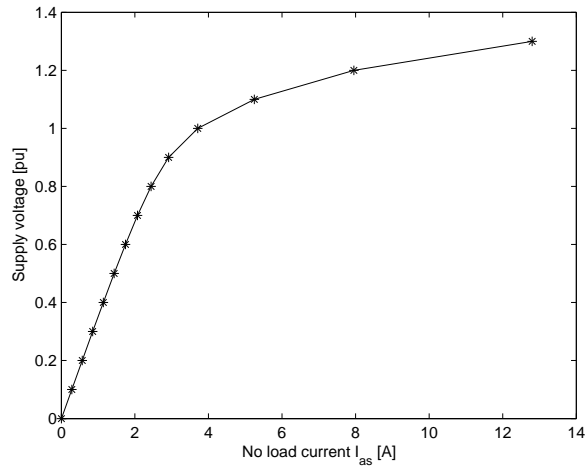
- Either the satisfaction of all criteria which leads to $\Delta t = 10^{-5}s$ and requires 13 days 21 hours of computing time to obtain 2s of simulated time.
- Or a time step of $\Delta t = 5 \cdot 10^{-5}s$ which requires "only" 2 days 18 hours of computing time to obtain 2 s of simulated time.

Numerical comparison between the 2 solutions is given by figures 3.14a and 3.14b. As it can be observed, after a transient phenomenon of 0.03s of simulated time, results are quite close.



(a) Torque versus speed

(b) Circle diagram



(c) No load characteristic

Figure 3.12: Results of magneto-dynamic simulations of *IND1*.

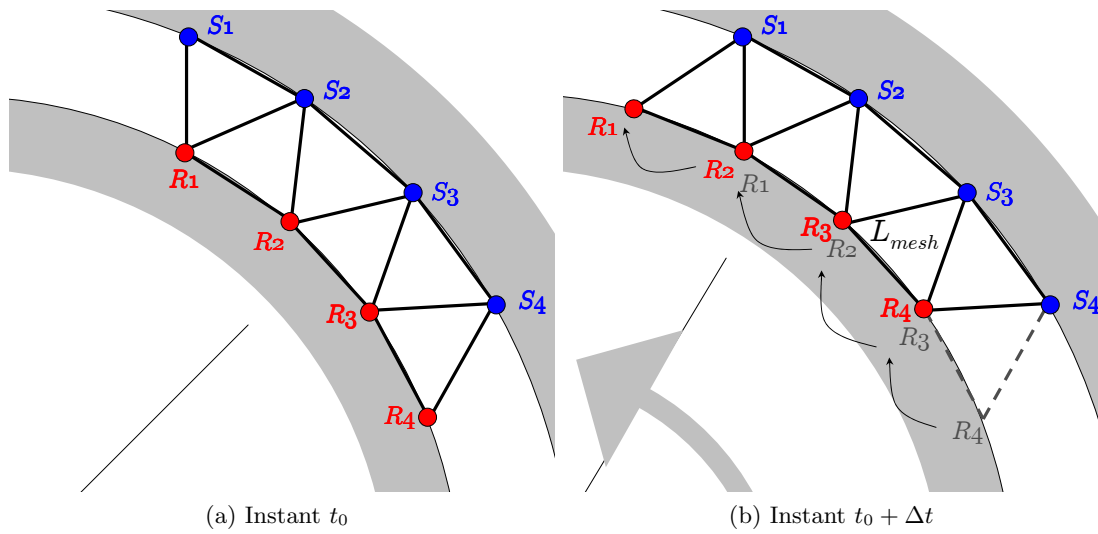
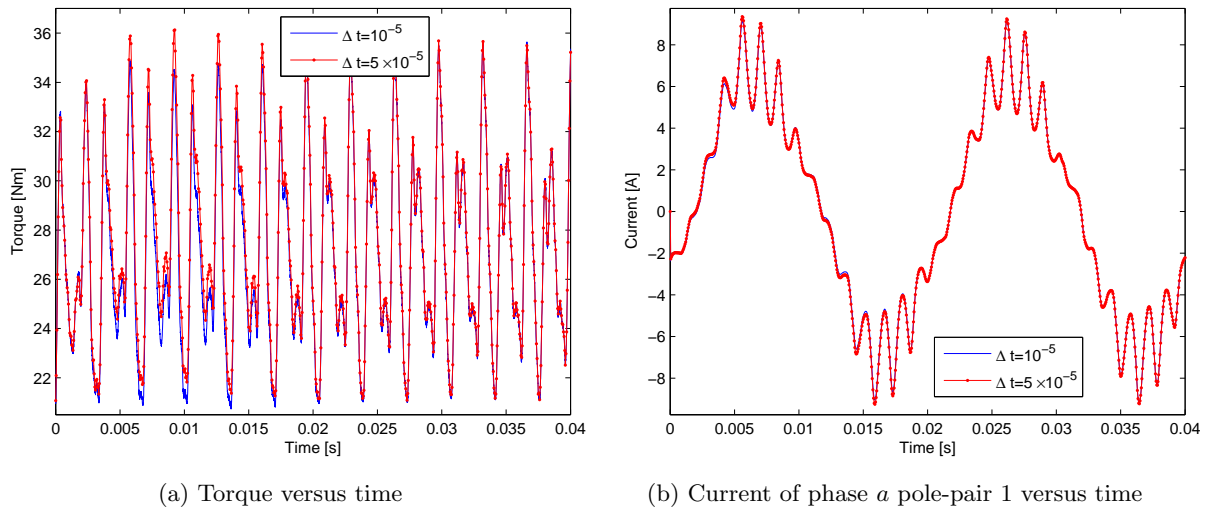


Figure 3.13: Illustration of airgap re-meshing

This transient appears due to the less accurate results given by the magneto-dynamic simulation and used as initialisation. However, this transient is smaller when a smaller time step is used.

As long as we are interested in results obtained after the instant $t = 0.03\text{s}$, a time step of $\Delta t = 5 \cdot 10^{-5}\text{s}$ gives good results with lower computing time. This time step value will therefore be used for the rest of the work.

Figure 3.14: Results of time-domain simulations of *IND1* with different time steps

3.2.3.3 Comparison between time-domain and magneto-dynamic results

A comparison between time-domain and magneto-dynamic results is shown in figure 3.16a for low-slip conditions and in figure 3.16b for high-slip conditions. In order to be able to compare the results, currents computed by the time-domain simulations are filtered to remove the influence of saturation and slots on the harmonic content of the currents.

The filter used is a Butterworth filter of fifth-order. The cutoff frequency is chosen to be 120Hz which allows to remove most of the influence of saturation (150Hz). The Bode plot is shown in figure 3.15 where it can be seen that the attenuation of the 50Hz is insignificant. Furthermore, the filter is applied on the signal and on its inverse time-sequence to remove phase shifts. This is realised by the Matlab function *filtfilt*. This filter will be used in whole text.

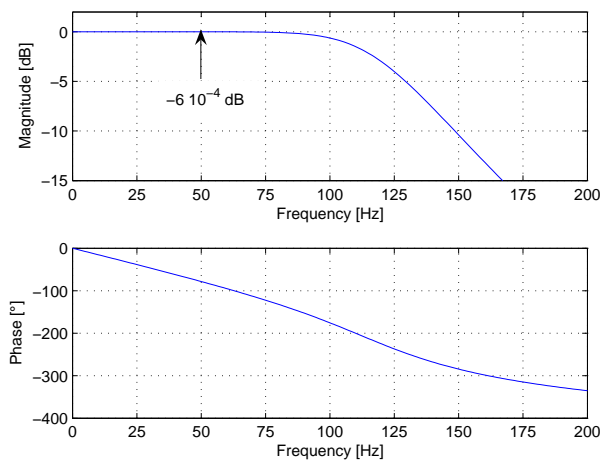


Figure 3.15: Bode plot of a fifth-order Butterworth filter with cutoff frequency of 120Hz

In high slip conditions, the slot harmonics are present at low frequencies. For this reason, the signal does not only contain one component at 50Hz and magneto-dynamic simulations fail to correctly represent the steady-state behaviour. Similar conclusions are reached in [Pham 99] for the computation of the torque.

At lower slip, slot harmonics appear as high frequencies. Correspondence between magneto-dynamic and time-domain is therefore of better quality even though some phase shift remains. As an example, at nominal speed, the error in amplitude is 0.04% and the error in phase is 1.18° ($6.556 \cdot 10^{-5}$ s).

3.3 Study of a machine with broken bars

In order to represent a machine with a partially broken bar or one or more completely broken bars, the only change which is required is to assign a different material to the region representing the broken bar. The resistivity of this new material is then defined as:

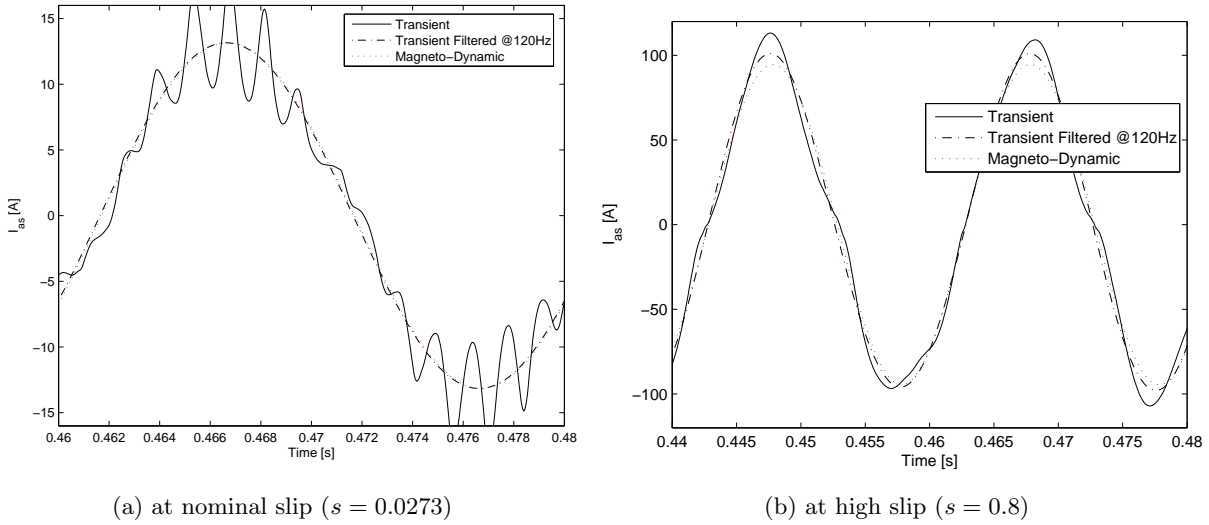


Figure 3.16: Comparison between time-domain and magneto-dynamic results of *IND1*

- For a partially broken bar, resistivity of this region is increased. As an example, FE simulations are performed for a resistivity multiplied by 2 (i.e. $\rho = 5.56 \cdot 10^{-8} \Omega \text{ m}$).
- For one or several completely broken bars, the resistivity of these regions will be changed to a very high value (i.e. $\rho = 1 \cdot 10^4 \Omega \text{ m}$).

In [Bangura 00b], 2D FE models are used to compare losses in healthy and faulty machines and to show the influence of PWM feeding on the same losses. Similar models are also used to show that skewed rotor bars tend to attenuate sidebands components [Watson 99]. This can be understood because the skewing of a bar is introduced to reduce the overall flux linkage and then to reduce the influence of the rotor bar.

Speed ripple was finally taken into account by the same authors using sinusoidally modulated time steps. Through this mechanism, speed ripple is shown to produce upper sideband in stator current and attenuate lower sideband.

We will now focus on the understanding of the influence of the broken bar on the machine behaviour for different saturation level (voltage levels).

3.3.1 Main influence of a broken bar on the machine behaviour

The main influence of a broken bar on the induction machine behaviour can be understood using an approach based on rotating fields. Under positive-sequence supply voltage, the stator windings create a forward rotating field in the air-gap at electrical speed ω . The rotor, rotating at electrical speed $(1 - s)\omega$, is therefore seeing the rotating field at speed $s\omega$. Induced currents at frequency sf are flowing in the rotor bars. The induced currents in these meshes create a rotating field at $s\omega$ in the forward direction with respect to the rotor. This field rotates at ω with respect to the

stator. As the total magnetic field in the air-gap is only a function of the supply voltage, currents of frequency f circulate in the stator windings. This explains the well known behaviour of a healthy machine. The electromechanical torque depends on the angular difference between rotor and stator fields and its derivative is proportional to the variation of the difference of rotating speed of both fields. In the case of the healthy machine, both fields rotate at ω and the torque is, for this reason, constant.

A broken bar can then be represented as the superposition of a healthy bar and a current source injecting, at all times, a current in the bar of opposite value as the current flowing in the healthy bar [Kliman 88, Deleroi 82]. The resulting current in the bar is therefore null. This superimposed current (current source) creates a pulsating field of pulsation $s\omega$ with regard to the rotor. This pulsating field can be split in two rotating fields of opposite directions. The forward rotating field, rotating at $s\omega$ with regard to the rotor and therefore at ω with regard to the stator windings, affects the value of the fundamental stator currents. The backward rotating field induces currents at frequency $(1 - 2s)f$ in the stator windings. This is the main signature of a broken rotor bar. In this case, the torque has a constant component and a component fluctuating at $2sf$. This last torque component creates speed ripple at the same frequency.

When the rotor speed is smaller i.e. $\omega_{r0} - \Delta\omega$, EMF appear in the bars at an increased frequency $2s_0f + 2\Delta f$. For this reason the forward rotating field rotates at ω with regard to the stator. The stator sees no changes with comparison to case of constant rotor speed. However, the backward rotating field created by the broken bar rotates at $(1 - 2s_0)\omega - 2\Delta\omega$ with regard to the stator.

When the rotor speed is higher, the backward rotating field rotates at $(1 - 2s_0)\omega + 2\Delta\omega$ with regard to the stator. Therefore, the rotor speed fluctuation creates an angular fluctuation of the rotor and stator fields at frequency $2s\omega$, this angular fluctuation modulates in amplitude torque and stator currents at frequency $2sf$. A modulation at $2sf$ of a signal at f is given by:

$$A(t) = (1 + M_{mod} \cos(2s\omega t)) A_0 \cos(\omega t) = A_0 \cos(\omega t) + A_0 \frac{M_{mod}}{2} \cos((\omega \pm 2s\omega)t)$$

This phenomenon modifies the component of current at $(1 - 2s)f$ and adds another component at $(1 + 2s)f$. If this approach is continued, stator current components at frequencies $(1 \pm 2ks)f$ where $k = 1, 2, 3, \dots$ can be found [Bellini 00]. Some illustrations of these effects will be shown in chapter 4 in section on Motor Current Signature Analysis (section 4.5.3) and on Speed Fluctuation Monitoring (section 4.1.2).

3.3.2 Broken bars in machine with parallel connected pole-pairs

The machine under study will be considered to be either in perfect condition or with bar number 1 broken. The slip is maintained at 2.73% which corresponds to nominal conditions. Two 2D time-domain FE simulations are conducted at nominal voltage

The two FE simulations are:

- *SimHealthy*: This simulation represents a healthy machine (see section 3.2.3 for more details).
- *SimFaulty*: The second simulation represents a machine with one broken bar (see section 3.3 for more details).

These FE simulations are used to illustrate the influence of a broken bar explained in section 3.3.1. The current in rotor bar 1 is shown in figure 3.17. Note that the high frequencies of the rotor current are due to the presence of the stator slots. It will not be of much influence in the development of this section. One can see that, as an example, at time $t = 0.35\text{s}$, the effect of the increase of the resistance of the bar is very small as the current normally flowing in this bar is null. On the contrary, the effect of a bar breakage is very high at $t = 0.2\text{s}$ when the current normally flowing in the bar is high. This pulsating effect (alternance of effect or no effect of the breakage) can be observed in figure 3.18 on the stator current I_{as} .

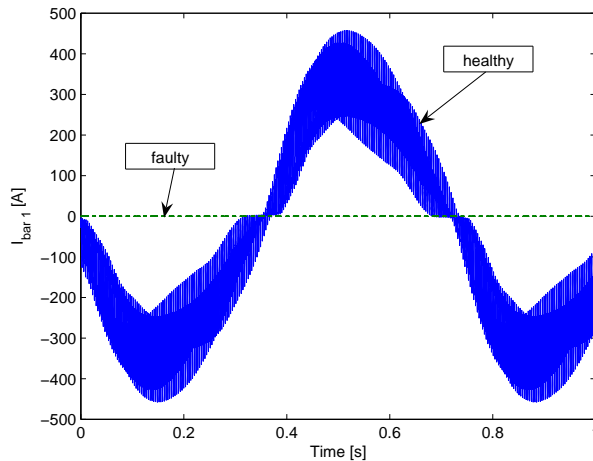
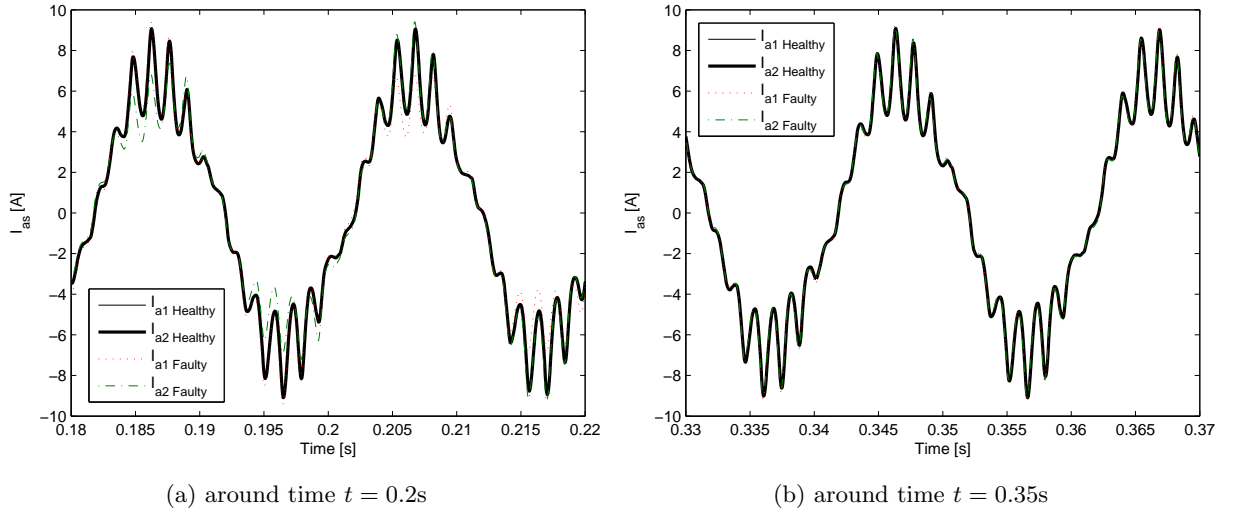


Figure 3.17: Current in rotor bar 1 in healthy and faulty situations

This stator current is the sum of the stator currents of phase a of the two pole-pairs as they are connected in parallel. First of all, no change can be observed between the healthy stator current of phase a and pole-pair 1 ($I_{a1\text{ healthy}}$) and the same current for pole-pair 2 ($I_{a2\text{ healthy}}$). This is expected as the machine is perfectly symmetrical. Around $t = 0.35\text{s}$, healthy and faulty situations are almost identical. However, this is not anymore the case at time $t = 0.2\text{s}$. This illustrates the pulsating effect of the broken bar mentioned in the previous section.

Furthermore, figure 3.18a shows that the broken bar mainly influences the stator currents of the pole-pair under which it is located. In the first part of this figure ($0.18 - 0.2\text{s}$) the broken bar is situated under the second pole-pair while it is under the first pole-pair in the second part of the figure. This observation will be used in the following section.

Figure 3.18: Stator currents of phase a of the 2 pole-pairs

3.3.3 Detailed influence of a broken bar on the machine behaviour

It is important to notice that the theory presented in section 3.3.1 does not take into account any change in local saturation due to the broken bar. In this section, a detailed field analysis by means of drawings based on Faraday's and Ampère's laws is performed. Each case will be validated using FE simulations. For this, a third 2D time-domain FE simulation will be conducted and two voltage levels will be considered; Nominal voltage and half voltage which will illustrate a lower saturation level of the machine. These two working points will be studied in parallel in the rest of this section in order to enhance similarities and differences. Furthermore, the analysis will be made at the time instant of 0.2s where the effect of the broken bar is the most visible but it remains valid at all times.

The third FE simulation is:

- *SimFaultyFrozen*: As one will realise, the presence of a broken bar will lead to modification of the permeability of the iron in its neighbourhood. In order to study this influence, a model where the permeability of each iron element is frozen at a certain value is built. The main application of this model will be to freeze the iron permeability of a model with broken bars at the value computed by the healthy FE model for the same working point. This way, we will be able to neglect changes in saturation around the broken bar.

In order to perform this action, the flux density of each mesh element of iron and for each time instant of the healthy FE model is stored in files. A Fortran subroutine is called at each time step of the simulation process and loads the appropriate forementioned file. Knowing the value of the flux of each element and the B-H curve of the iron used in the healthy model⁶, the subroutine computes the permeability of each iron element. The iron

⁶A squared region placed outside of the machine is added to the model. This square is made of original iron and is used to know the value of the B-H curve. The presence of this square does not influence the geometry of

permeability of the healthy model which is identical to the one of a model with one broken bar and "frozen iron" is shown in figure 3.19 for nominal voltage.

This implementation is validated by comparing the stator currents computed by *SimHealthy* to this model of healthy machine with permeability frozen at the value computed by *SimHealthy*. The difference between the stator currents is numerically null.

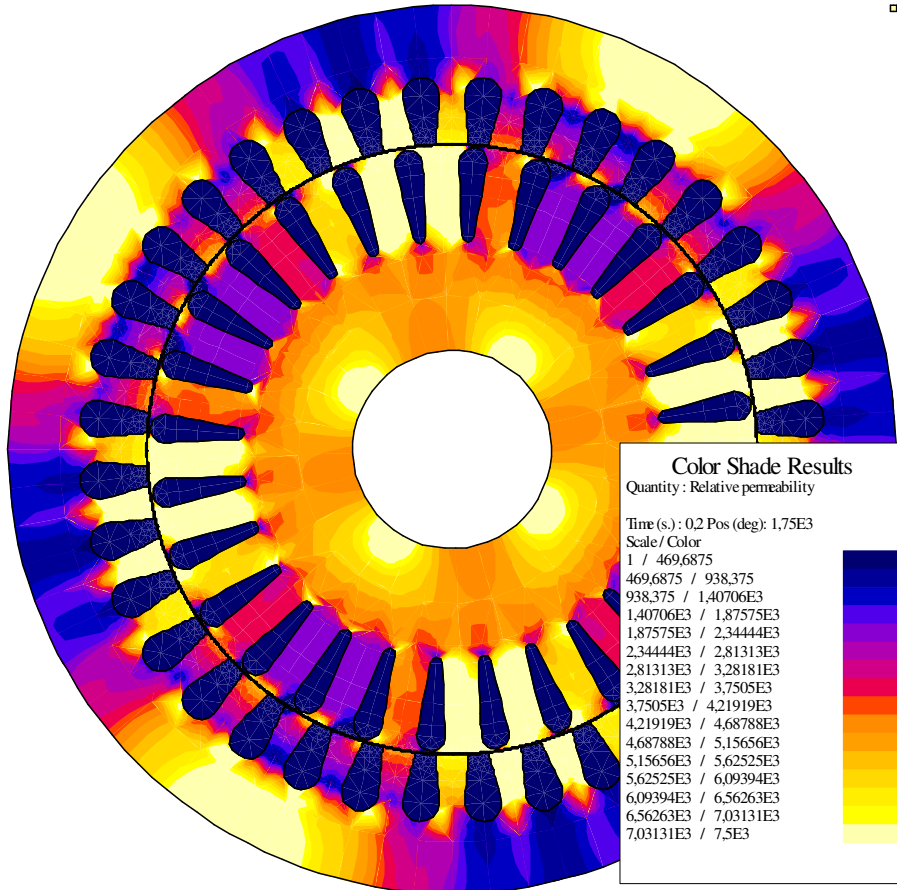


Figure 3.19: Relative permeability of time-domain simulation of *IND1* at $t=0.2s$

The simulation *SimFaultyFrozen* represents a faulty machine in which, at each simulation time step, the permeability of the iron remains equal to the healthy situation *SimHealthy*.

The following approach will be based on two fundamental hypotheses:

- The current in each rotor bar is in phase opposition with the induced voltage in the same bar. This is justified by the fact that the voltage drop across the bar is very small as a result of the low impedance of the end-rings. This is validated using FE simulation of the healthy machine at nominal speed (*SimHealthy*). Voltage, current and flux seen by a bar are computed by the FE calculation.

the machine as Dirichlet boundary conditions are specified on the external perimeter of the stator. The square is shown on the top right corner of figure 3.19

Note that, as the integral of the vector potential on a closed path is equal to the flux linking that path [Salon 90], the flux seen by a bar is equal to the vector potential of this bar time the axial length of the machine (because the vector potential on the rotor inner boundary was set to zero).

The resistance of the bar is calculated from the resistivity of the bar. The induced EMF is obtained by performing a time derivation of the flux. Figure 3.20 is then obtained by extracting fundamental values and using equation 3.7.

$$\underline{\epsilon} = \underline{V} - (R\underline{I} + \underline{E}) \quad (3.7)$$

where \underline{V} is the voltage drop in the bar, R is the resistance of the bar \underline{I} is the current flowing in the bar, $\underline{E}(t) = -\frac{d\phi}{dt}$ is the induced EMF in the bar and $\underline{\epsilon}$ is the closing error of the equation. If we neglect skin effect which is the case at rotor frequency of $sf = 1.3667\text{Hz}$, the bar resistance is equal to $R = 5.849 \cdot 10^{-5}\Omega$.

Numerical Details:

At a frequency of 1.3667Hz , the skin depth is given by $\delta = \frac{1}{\sqrt{\frac{\pi f \mu_0}{\rho_{al}}}} = 7.18\text{cm}$ which is much greater than the bar height of 18mm . The resistance is equal to $R = \frac{\rho_{al} l}{S} = 5.849 \cdot 10^{-5}\Omega$ where $\rho_{al} = 2.78 \cdot 10^{-8}\Omega\text{m}$ is the resistivity of the aluminium, l is the length of the bar and S is the section of the bar.

Figure 3.20 shows that, under nominal voltage and at full load, the phase shift between bar current and the phase opposition of the induced EMF in the bar is equal to 1.01° (0.24° for half voltage condition). At the nominal speed considered, during this time delay between the induced voltage in the bar and the apparition of the resulting current, the bar has moved with regard to the fundamental magnetic field by 0.49° (0.12° for half voltage) which is negligible compared to the position difference of 2 consecutive bars (12.86°).

Numerical Details:

For the nominal voltage situation, the time shift corresponding to a phase shift of 1.01° is $\Delta t = \frac{1}{f} \frac{1.01^\circ}{360^\circ} = 0.0020\text{s}$. The rotor is rotating at $(\frac{1500-1459}{60} 360^\circ) = 246^\circ/\text{s}$ with regard to the rotating field. This corresponds to a relative shift with regard to the fundamental field of $246 \Delta t = 0.49^\circ$.

- The fundamental flux density field in the airgap is independent of the machine condition (healthy or faulty). This hypothesis implies low leakage inductance and resistance of the stator windings. This validated by FE simulation as shown in figure 3.21. Moreover, the flux density seen by each bar is not affected much by the relative position of the stator and rotor teeth. Therefore, in the following approach, the flux density seen by each bar is assumed to be the value of the fundamental flux density in the airgap at the position of the bar.

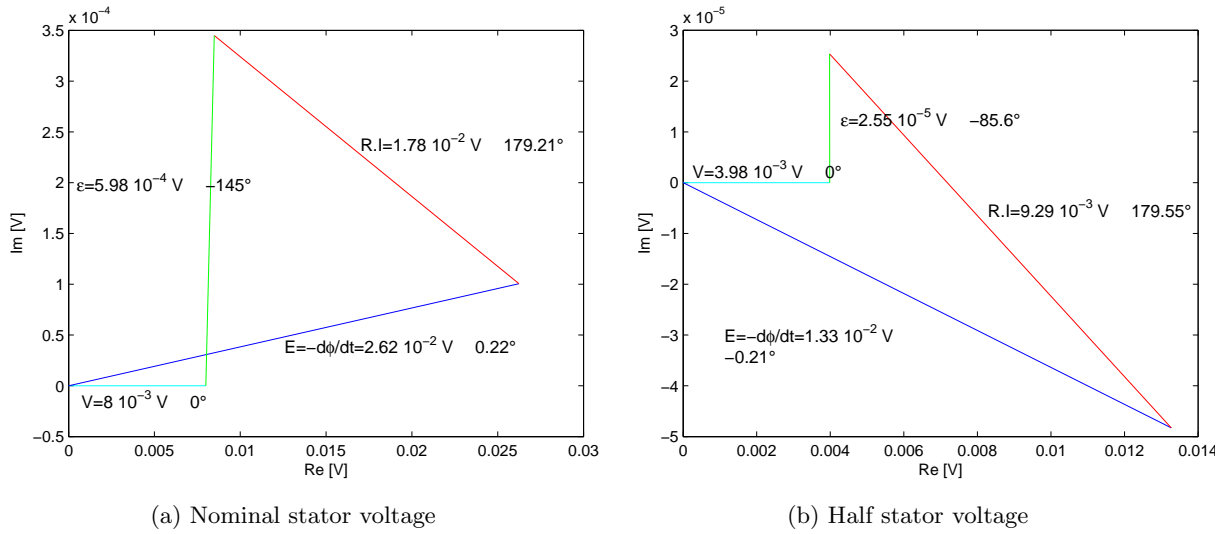


Figure 3.20: Phasor diagram of voltage drops in a bar at nominal conditions. It should be noted that the scales of x and y axes are very different.

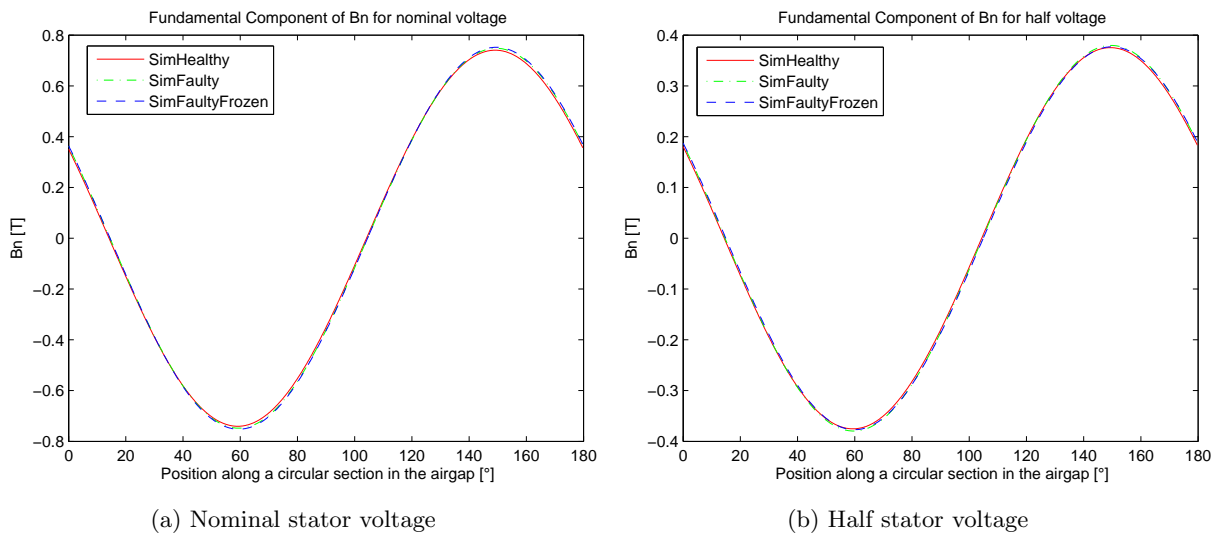


Figure 3.21: Fundamental component of the radial part of the induction on a circle at the middle of the airgap.

3.3.3.1 Healthy machine

At the instant of time considered, the fundamental magnetic field is aligned with bar 2. If we don't consider the rotor bar currents and if we represent the flux paths by arrows of thickness proportional to the flux density, we obtain figure 3.22.

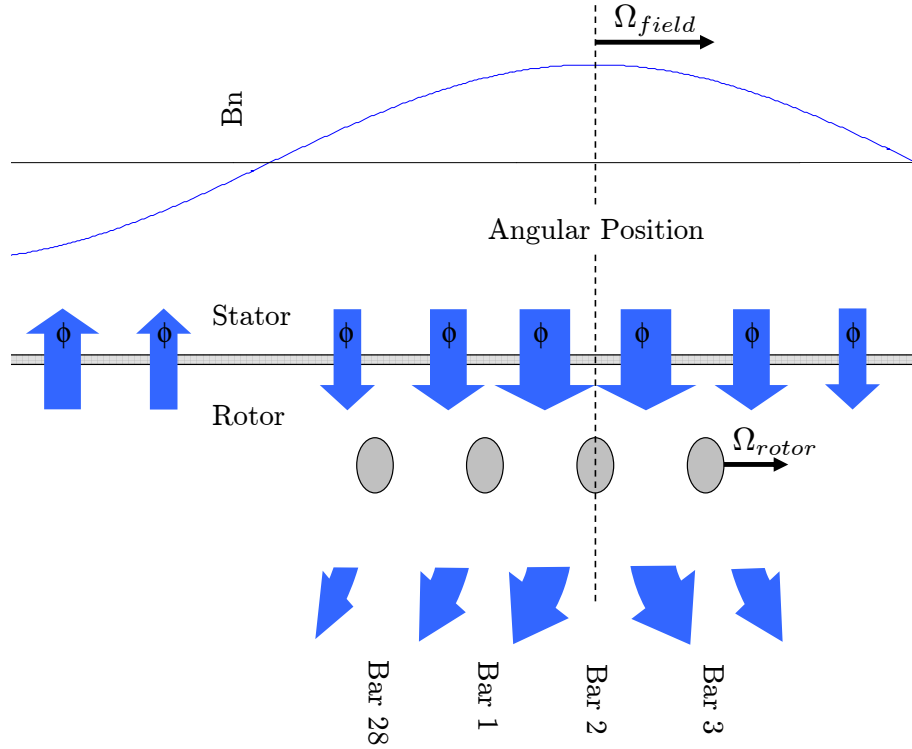


Figure 3.22: Flux density and flux paths neglecting the presence of the rotor circuit.

If, for each rotor bar, the relation $E = \int_{bar} \bar{v} \times \bar{B} \cdot d\bar{l}$ and Ampère's law are used, we obtain, for the case of a healthy machine, the flux lines distribution of figure 3.23. E is the induced emf \bar{v} is the velocity of the bar, \bar{B} is the induction seen by the bar and $d\bar{l}$ is the length element of the bar. This can be validated using FE simulation *SimHealthy* in figure 3.24. On this figure, one can realise that the iron in the region on top of the bars is saturated. This can be confirmed by looking at the permeability of the iron plotted for each element of the core in figure 3.25.

3.3.3.2 Faulty machine: No modification of local saturation

In the case of a faulty machine, the flux lines encircling each bar and created by the current in the bars (Ampère's law) are not present around the broken bar. If we assume that neither the current in the adjacent bars nor the local saturation are affected by the broken bar, the flux repartition becomes as given in figure 3.26a. The next step is to consider that the bars are connected in cage through end-rings. Therefore the currents in the other bars will increase because the sum of the bar currents must be equal to zero [Kliman 88]. Furthermore, the current not flowing

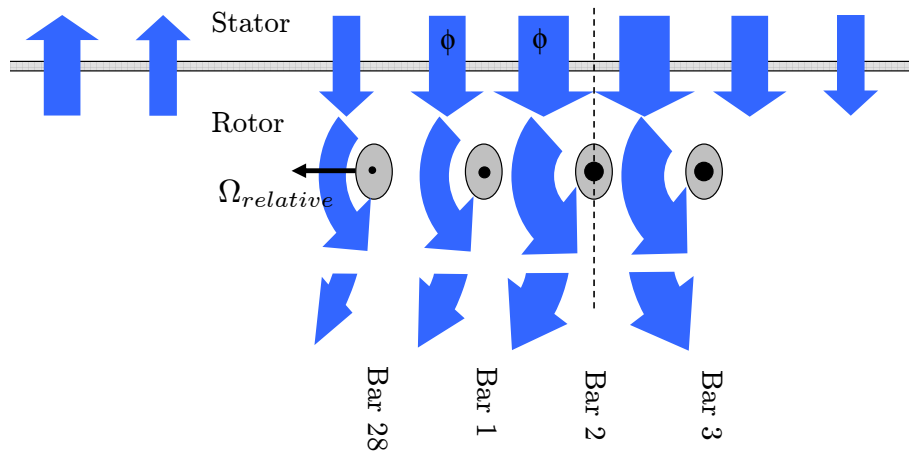


Figure 3.23: Flux density and flux paths in the case of a healthy machine.

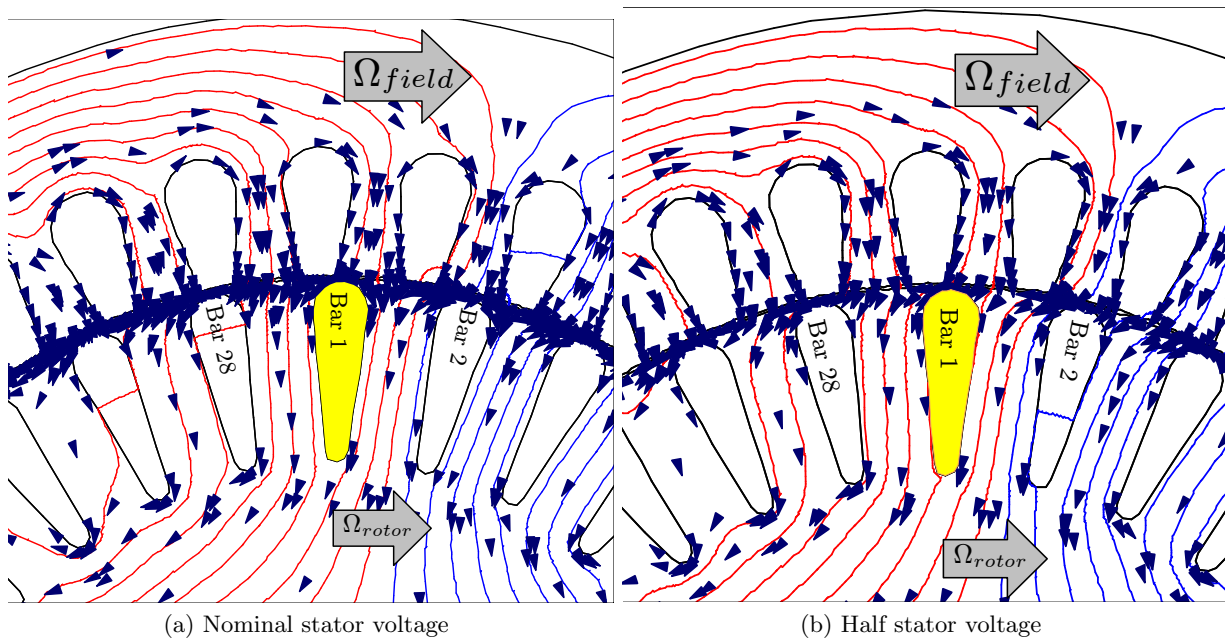


Figure 3.24: Flux lines in the case of a healthy machine at nominal load.

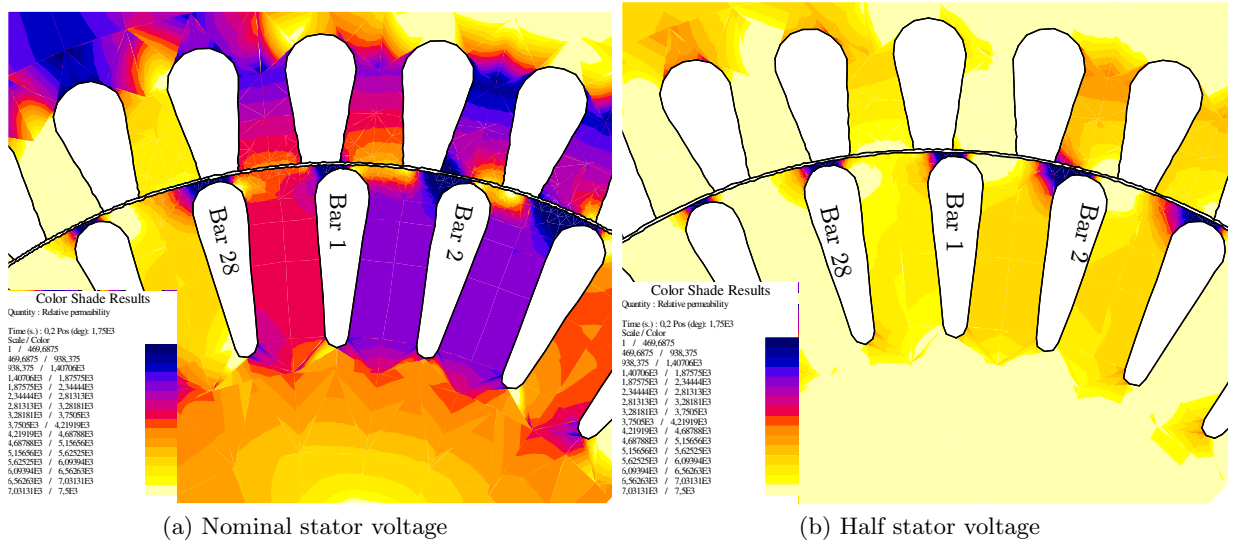


Figure 3.25: Relative permeability of the iron in the case of a healthy machine. The iron on top of the bars is saturated (*SimHealthy*).

through the broken bar will be mainly redistributed on the adjacent bars. This has been shown in [Deleroi 82] and will be confirmed in section 6.3. Then the flux lines distribution becomes as given in figure 3.26b.

This drawing can be validated through the results of FE simulation *SimFaultyFrozen* in figure 3.27. Furthermore, figure 3.28 shows the radial induction in the rotor teeth. This is computed on a circle crossing the bars at mid-height by FE simulation *SimFaultyFrozen*. In figure 3.29 where the difference between the radial induction in the rotor teeth is shown, one can observe that the redistribution of the current is not only limited to the 2 adjacent bars and that the flux density distribution of the whole machine is affected. This effect is however of lower magnitude.

At the time instant considered ($t = 0.2s$), the broken bar is in front of the slots holding part of the conductors of the phase c of pole-pair 2. The disturbance of the flux density distribution created by the broken bar will therefore affect derivative of the flux seen by this coil. As the field is going in the right direction on the figures and as a bigger flux density is located on the right side of bar 1, the coil will see earlier than in the healthy case a variation of the flux but will see a smaller flux variation as the left side of bar 1 passes in front of the slots. Therefore the stator currents of this phase and this pole-pair is modified as shown in figure 3.30. Note that the total flux seen by the other stator coils is not much modified even if the flux distribution in the region embraced by the coil is modified. The conclusions are identical for nominal voltage or reduced voltage.

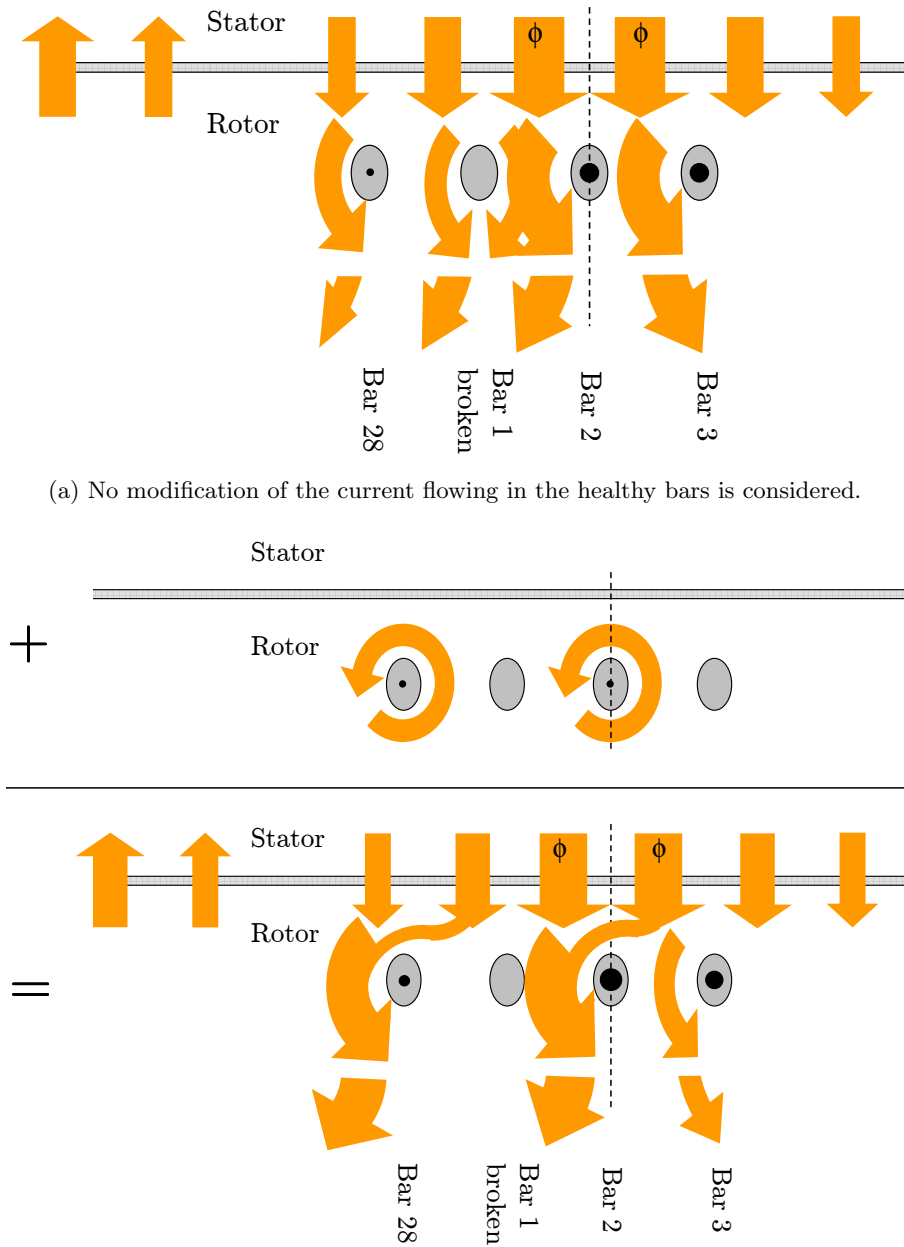


Figure 3.26: Flux density and flux paths in the case of a machine with bar 1 broken. No modification of local saturation is considered.

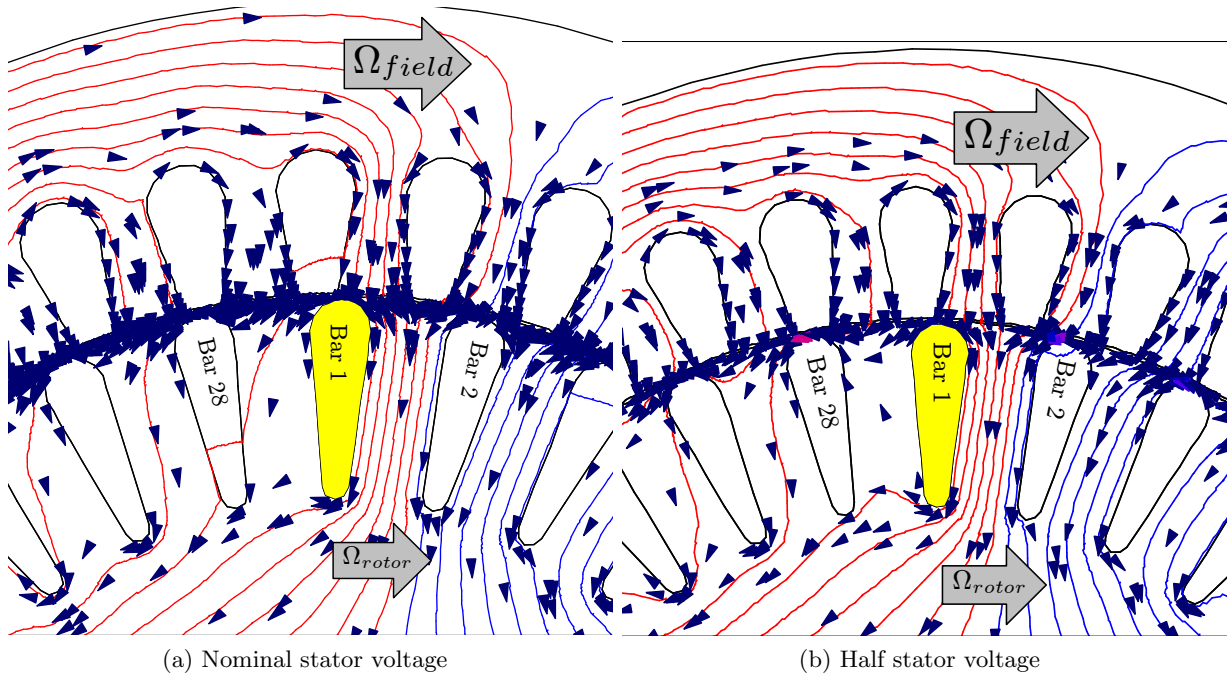


Figure 3.27: Flux lines and magnetic field in the case of a broken bar without modification of local saturation. (*SimFaultyFrozen*)

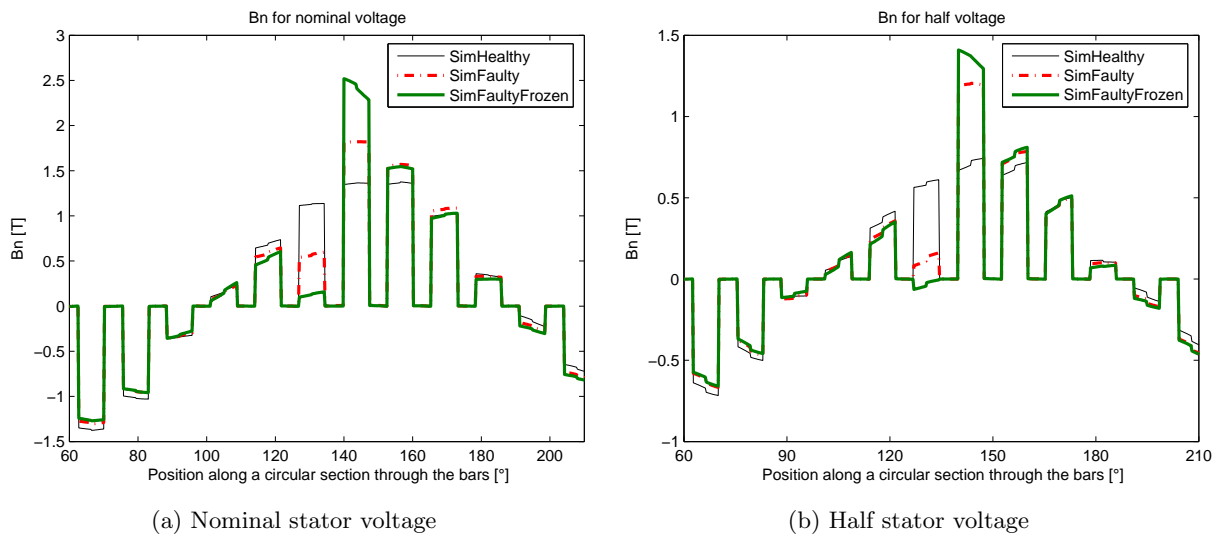


Figure 3.28: Radial part of the induction on a circle crossing the bars at mid-height.

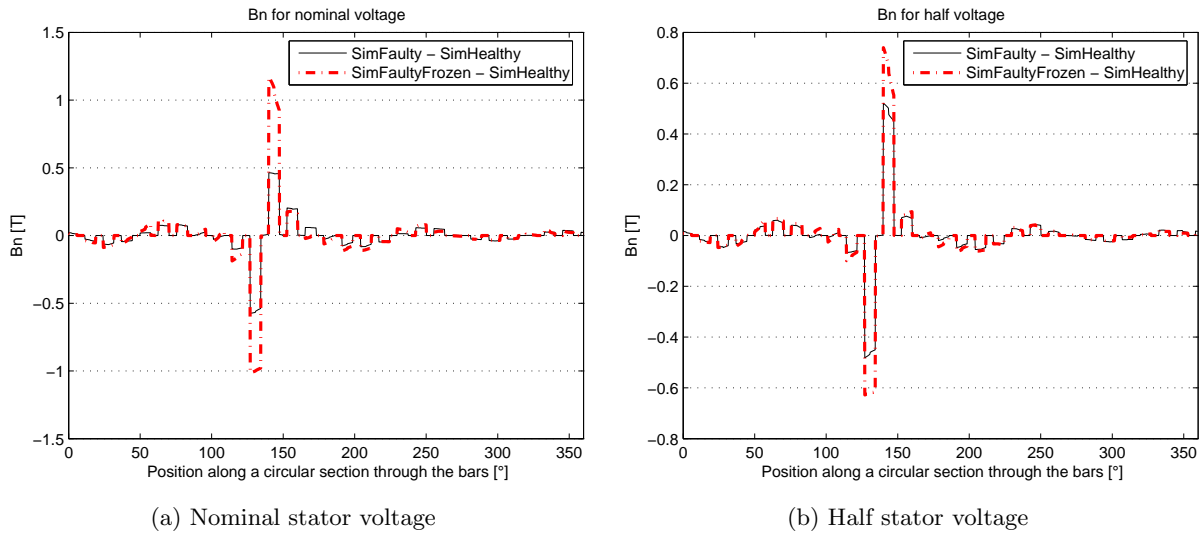


Figure 3.29: Difference in radial part of the induction on a circle crossing the bars at mid-height between healthy and faulty simulations.

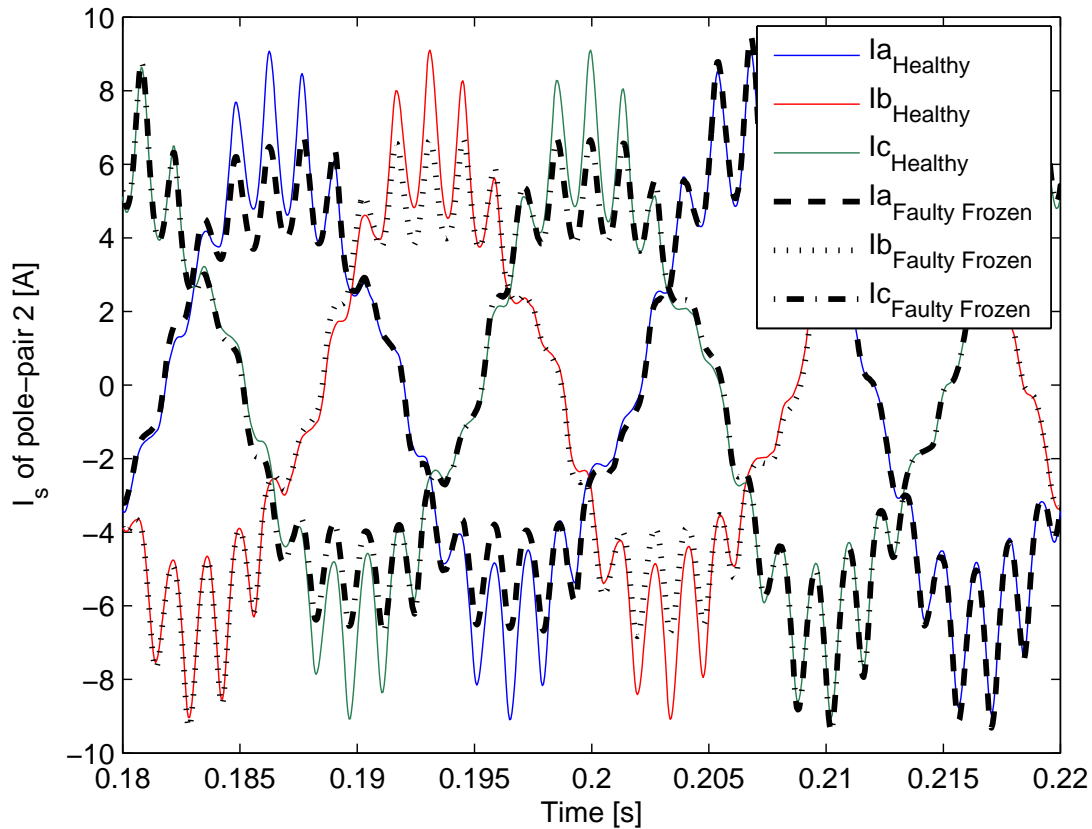


Figure 3.30: Stator currents of pole-pair 2 from *SimHealthy* and *SimFaultyFrozen* for nominal stator voltage.

3.3.3.3 Faulty machine: Modification of local saturation

From previous results (figures 3.26b and 3.27) we can see that the flux density in some regions around the broken bar (specially on its right side) is much higher than in the case of the healthy machine. Therefore, if the permeability of the iron is not frozen at its value obtained by the healthy simulation, these regions will saturate and some flux lines will be redistributed as illustrated in figure 3.31. Less flux lines will flow between bar 1 and bar 2 and more flux will flow in the adjacent teeth, mainly between bar 28 and bar 1.

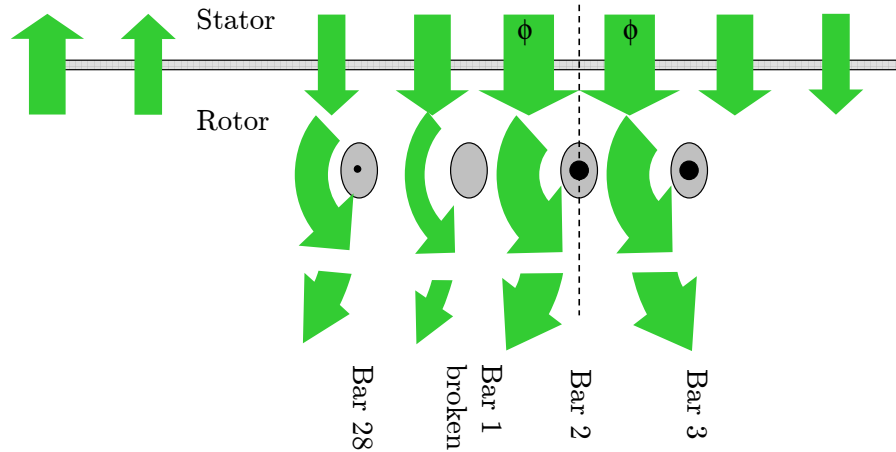


Figure 3.31: Flux density and flux paths in the case of a machine with bar 1 broken.

This drawing can be validated through the results of FE simulation *SimFaulty* in figure 3.32.

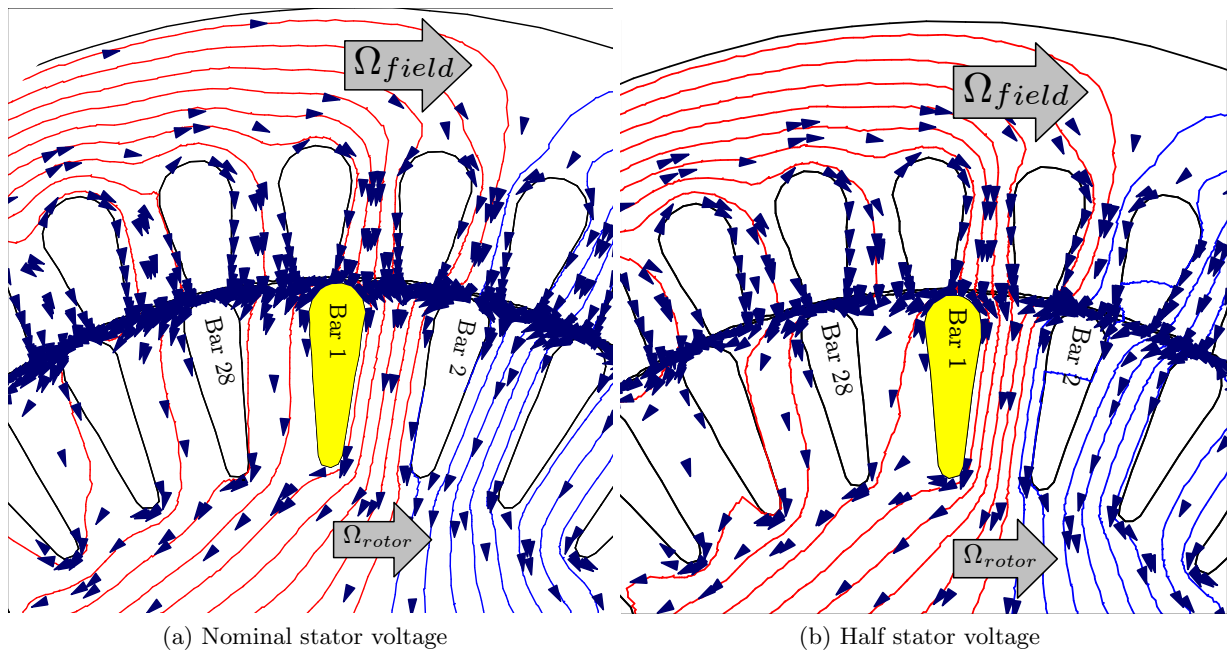


Figure 3.32: Flux lines and magnetic field in the case of a broken bar with modification of local saturation. (*SimFaulty*)

The comparison of figures 3.31 and 3.23 shows that the difference in the flux distribution between the healthy and faulty machine is much smaller (*SimHealthy* vs. *SimFaulty*) than their difference when no modification of saturation due to the broken bar is assumed (*SimHealthy* vs. *SimFaultyFrozen*). The redistribution of the flux lines to the tooth situated on the left side of bar 1 has also for effect to phase shift the flux density perturbation due to the broken bar compared to the case where no modification of saturation was taken into account (*SimFaulty* vs. *SimFaultyFrozen*). Therefore, the modification of the currents due to a broken bar is visible earlier in the period of the currents. The running RMS value of the current is an indicator of the effect of the broken bar as the position of the flux density perturbation with regard to the fundamental flux is moving at slip speed. The comparison of current from *SimFaulty* and *SimFaultyFrozen* is shown in figure 3.33.

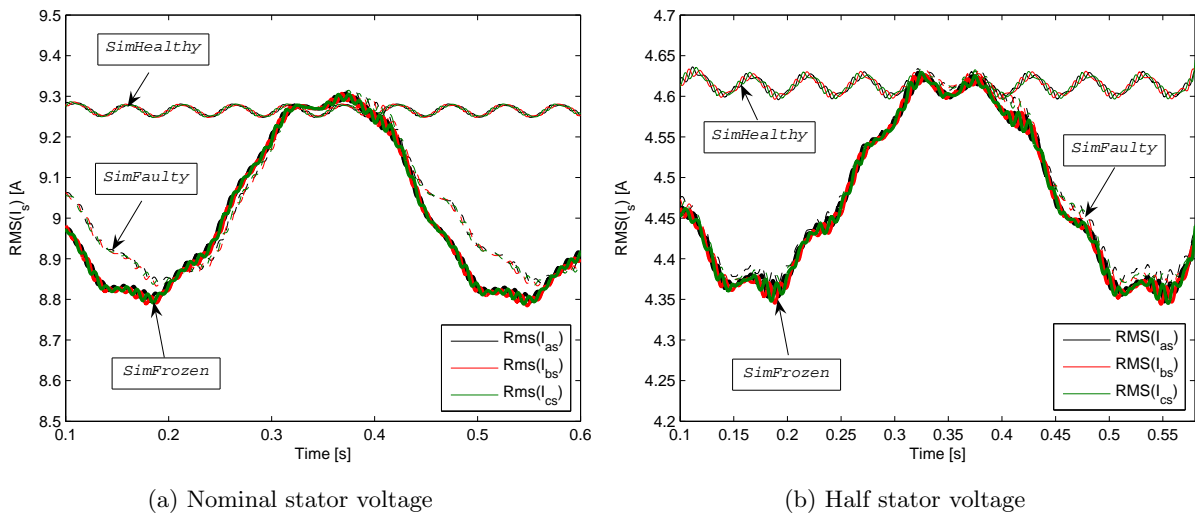


Figure 3.33: 50Hz running RMS value of the three stator currents obtained from the three FE simulations.

Therefore, the presence or not of modification of local saturation slightly influence the position of the field perturbation due to broken bar as well as the amplitude of the perturbation. This influences significantly the phase and the amplitude of the oscillation of the RMS value of the stator currents. This is specially the case when the machine is saturated. Localisation as well as quantification of broken bars is therefore affected by the voltage level of the supply.

Furthermore, as it is shown in figure 3.34, local saturation greatly varies in the region of the broken bar. The increase of saturation in some regions leads to an important rise of local iron losses [Bangura 00b]. Local temperatures will mainly increase in the region situated on the side of the broken bar given by the sense of rotation (right side on the example). Along with the redistribution of the current normally flowing in the broken bar, this phenomenon influences the progression of the fault to the bar, adjacent to the broken one and situated in this region.

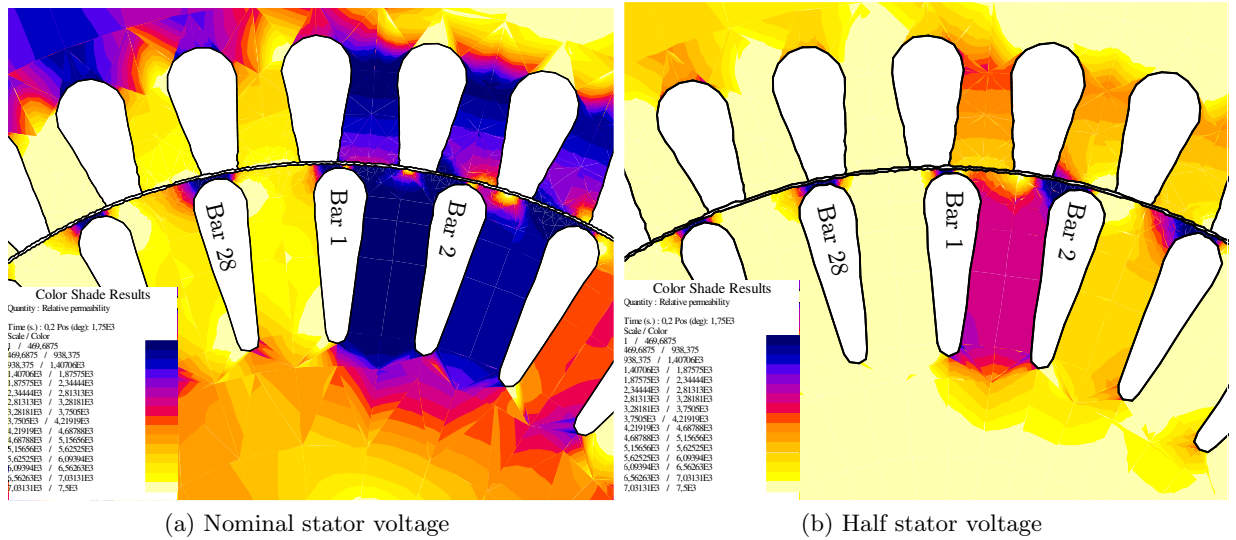


Figure 3.34: Relative permeability of the iron in the case of a machine with bar 1 broken. (*SimFaulty*)

3.3.3.4 Validation of the principle of superposition for broken bars

In the previous section, the local effect of broken bars and saturation has been analysed. The principle of superposition was used in section 3.3.1 to explain the general influence of a broken bar on the behaviour of an induction motor. In this section, we will see if a machine with broken bars and constant speed can be modelled with a reasonable accuracy using the principle of superposition.

In the case of a linear machine (i.e. iron has constant permeability) (*INDICP*) and in the case of a machine with local saturation (*IND1*), the three previously described FE simulations *SimHealthy*, *SimFaulty* and *SimFaultyFrozen* as well as fourth simulation *SimSuperimposed* are conducted to verify the superimposed approach. This last simulation can be described as:

- *SimSuperimposed*: The superimposed phenomenon of the broken bar is represented. In the electrical circuit of the cage, a current source is placed in series with bar 1 which is intended to be broken. The stator voltage sources are short-circuited (superposition theorem). The value of the source current is the opposite value of the current of bar 1 computed by the healthy FE simulation (*SimHealthy*). The permeability of the iron is computed in the same way as in *SimFaultyFrozen*.

Note that, in the case of the linear iron, the geometry of the machine has to be edited. Indeed, if the region on top of the bars is not saturated, the leakage inductances rise and the machine is not any longer realistic. Therefore, the regions on top of the bars have to be filled by a low magnetic material (as is the case of open rotor slots). The rotor and stator relative permeability is assumed to be equal to 4000 and the region on top of the bars has a relative permeability of 200. These values are chosen to have a working point similar to the one of *IND1*

under nominal voltage. The permeabilities of the machine computed by time-domain simulations of *IND1* and *IND1CP* are compared in figure 3.35. The stator currents computed by the magneto-dynamic simulations in the same conditions are given in table 3.3. The correspondence is not precise but the working points are comparable.

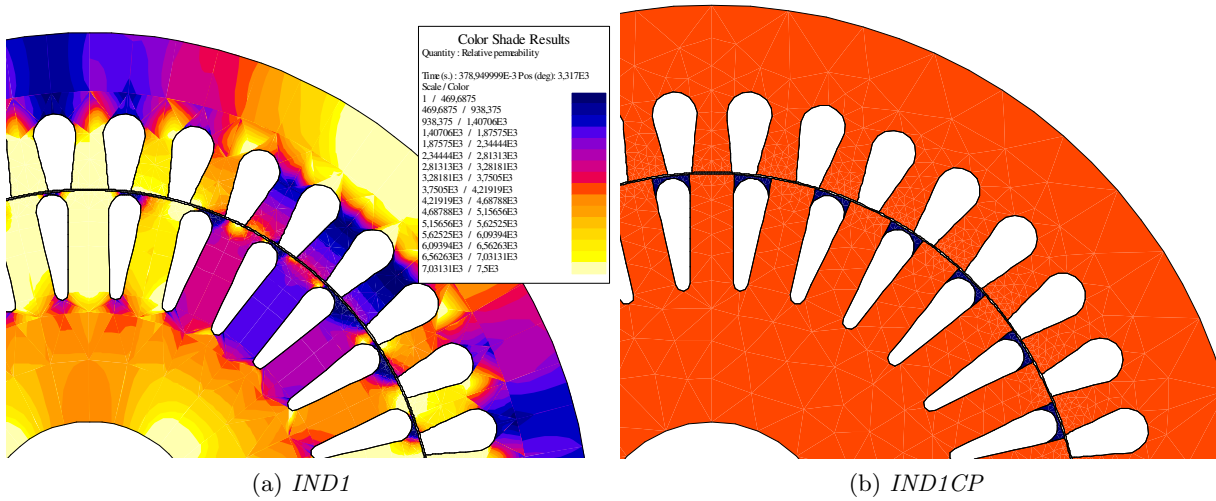


Figure 3.35: Iron relative permeability for nominal condition in the case of the machines.

Stator Currents [A]	<i>IND1</i>	<i>IND1CP</i>
I_{as}	$9.29 \angle -30.68^\circ$	$9.06 \angle -29.25^\circ$
I_{bs}	$9.29 \angle -150.68^\circ$	$9.06 \angle -149.25^\circ$
I_{cs}	$9.29 \angle 89.32^\circ$	$9.06 \angle 90.75^\circ$

Table 3.3: Comparison of stator currents computed by magneto-dynamic simulations of *IND1* and *IND1CP* at nominal load.

The stator current of phase *a* from the healthy FE simulation ($I_{a_{Healthy}}$) and from the superimposed FE simulation ($I_{a_{Sup}}$) are added and compared to the stator current of phase *a* from the faulty machine FE simulation ($I_{a_{Faulty}}$). A residual error $\epsilon(t)$ is defined as

$$\epsilon(t) = \frac{|(I_{a_{Healthy}}(t) + I_{a_{Sup}}(t)) - I_{a_{Faulty}}(t)|}{RMS(I_{a_{Healthy}})}$$

In the case of the linear machine the error $\epsilon(t)$ stays for each time step lower than 0.02%. This result validates the representation used for the superimposed model.

In the case of the saturable machine the error $\epsilon(t)$ stays lower than 8.5%, with a mean value of error lower than 1.1%. The difference between healthy and faulty currents around the time instant 0.2s is shown in figure 3.36. As an indication, the comparison with the linearised problem *SimFaultyFrozen* is also shown.

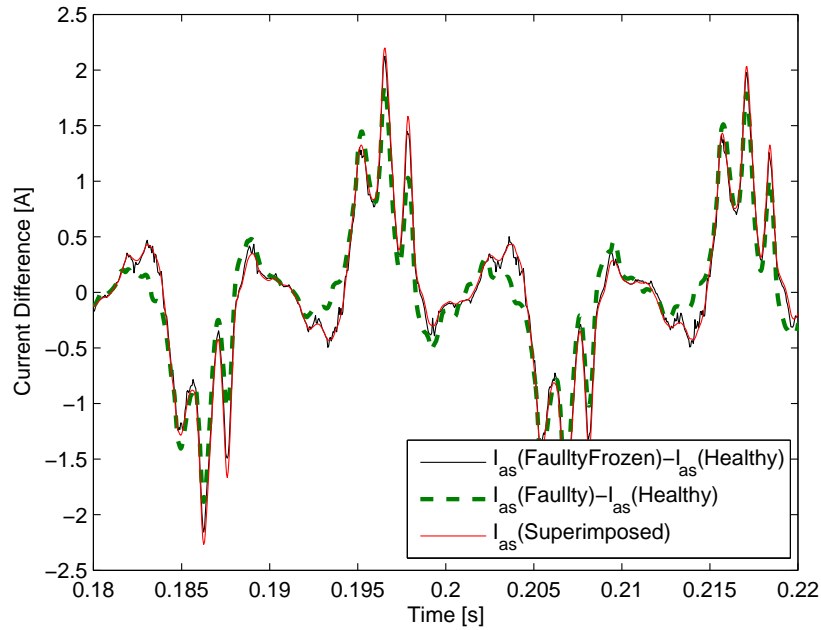


Figure 3.36: Difference between the currents of the FE simulations.

Therefore, even though the broken bar affects local saturation in its neighbourhood, the broken bar effect can then be considered with good approximation as a superimposed phenomenon. This observation will be used later in this work to model a machine with broken bars.

3.4 Study of a machine with stator short-circuits

For the representation of stator short-circuits, two stator slots of phase a of the pole-pair 1 are split in two parts, one part for healthy conductors of the slot and another for the faulty conductors (see figure 3.37). As the conductors of this phase are distributed in several slots, the FE model of this phase is composed of 6 stranded conductors connected in series. Two stranded conductors represent the conductors of the slots not holding the short-circuit and going into and out of the plane. Two other ones represent the healthy conductors of the split slots and two last ones, the faulty conductors of these slots. In parallel with the coil representing the shorted turns is placed a resistance and a switch representing the short-circuit. This is illustrated in figure 3.38.

This approach implicitly implies that the position of the shorted turns in the slot as well as the surface of the slot occupied by these turns does not have much influence on the machine behaviour.

Different simulations are performed depending on the number of shorted turns and on the resistance of the short-circuit. In particular, the following cases will be illustrated:

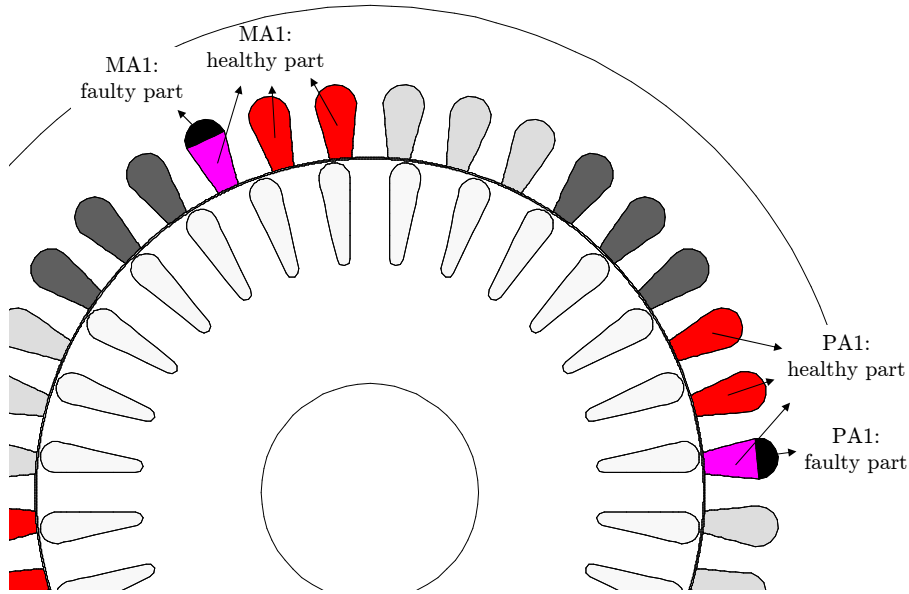


Figure 3.37: Geometrical description of a machine with short-circuits

- 1 turn out of the 44 of the first slot of phase a and pole-pair 1 is short-circuited through a resistance of 0.01Ω which is of the same order of magnitude as the resistance of one turn. This corresponds to 0.76% of the winding (1 out of 132 turns).
- 10 turns of the first slot of phase a and pole-pair 1 are short-circuited with correspond to 7.6% of the winding. The resistance of the short-circuit is assumed to be 0.01Ω .
- 1 turn of the first slot of phase a and pole-pair 1 is removed from the winding. This corresponds to a winding reduction of 0.76%.

The electrical details of the windings are given in table B.3 of appendix B.

3.4.1 Main influence of internal stator short-circuits on machine behaviour

At the early stage of a turn-to-turn fault, little change can be noticed in the motor performance. However, as it will be explained in section 3.4.2, the current flowing in the short circuit can reach several times the nominal current. The stator currents from a time-domain FE simulation, representing induction motor *IND1* at full load and with 1 turn in short-circuit are shown in figure 3.39a. The short-circuit current is important while the stator line currents are not much affected. From the outputs of the machine, this situation is very similar to a 1-turn reduction of phase a . The difference between these two situations is shown in figure 3.39b. The line currents are very similar while the first situation is much more dangerous due to the presence of the short-circuit current which leads to a rise of the coil temperature and to the extension of the fault.

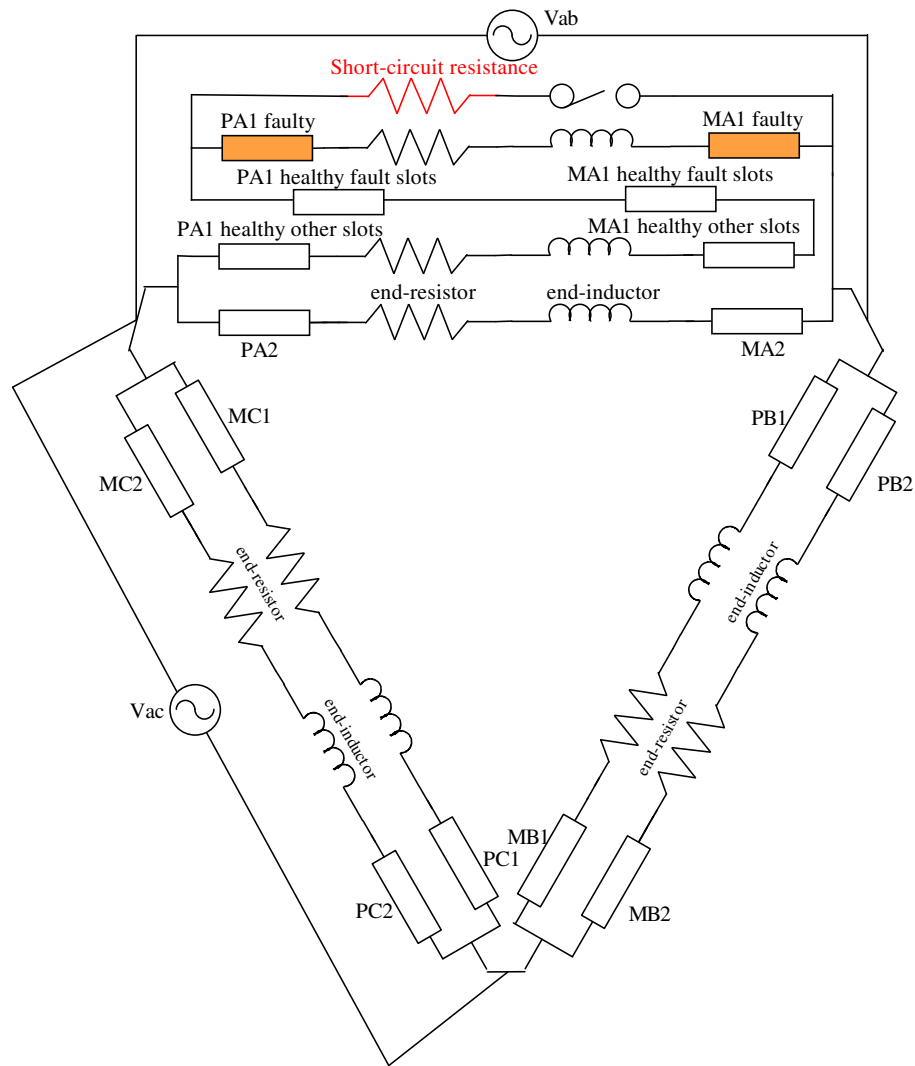


Figure 3.38: Electrical connexion of FE model of machines *IND1* with short-circuit

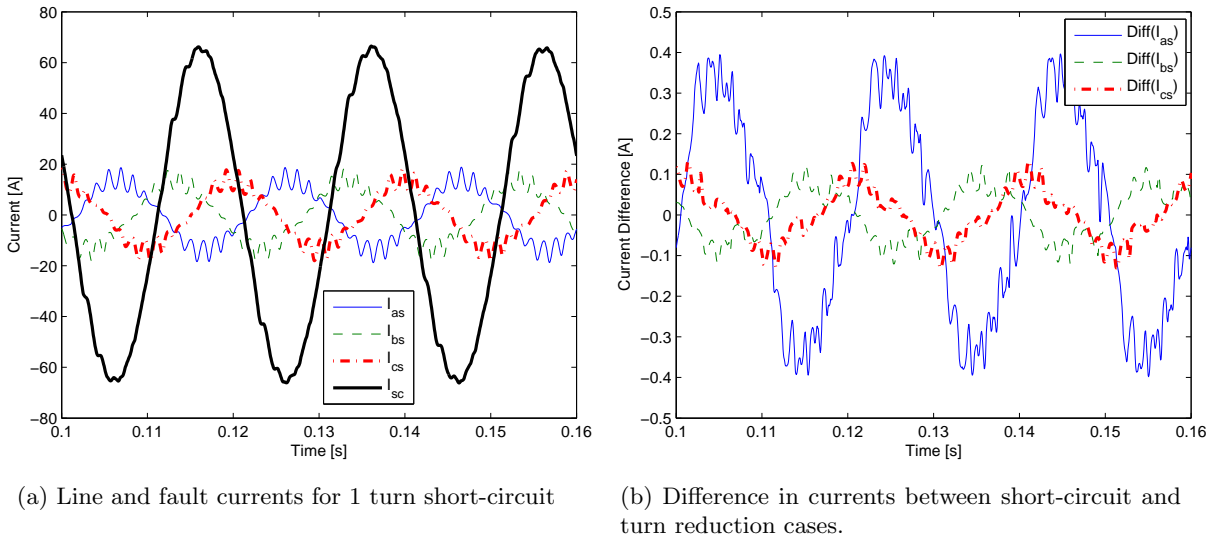


Figure 3.39: Comparison between 1-turn short-circuit and 1-turn phase reduction of phase a at nominal load.

Furthermore, the presence of the short-circuit coil will affect the flux distribution in the airgap. The flux density at time instant $t = 0.12715\text{s}$ from the healthy FE simulation and the FE simulation with 10% of phase a in short-circuit is shown in figure 3.40. The chosen instant corresponds to instant of the maximum influence of the short-circuit on the machine behaviour. The detailed analysis of this flux density distribution will be given in the next section. The deformation of the airgap field will also affect the rotor currents as it will also be studied in the next section.

3.4.2 Detailed influence of internal stator short-circuits on machine behaviour

This approach will analyse a particular situation and FE simulations will be used to go deeper into the understanding of the effect of the short-circuit on the machine behaviour.

Let us first consider that the flux density in the airgap and created by stator windings is sinusoidal and is rotating at constant speed. Figure 3.41 illustrates this situation. The quantity represented on the horizontal axis is the angular position along a circular section place in the middle of the airgap. The flux density is considered positive if flux lines are crossing the airgap from stator to rotor. A short-circuited coil is made of 10 conductors placed in the regions *MA1 Faulty* and *PA1 Faulty*. At a certain instant of time, the flux seen by this coil is shown by the filled area of figure 3.41. The flux distribution is supposed to be sinusoidal and at that time instant, the derivative of this flux is positive.

Therefore, the induced voltage in this coil, given by $e = -N_{sc} \frac{d\phi}{dt}$, is negative. N_{sc} is the number of short-circuited turns. The current flowing in the coil will be in such a direction that it creates a flux that minimises the flux variation. The flux density created by this coil can be qualitatively given by figure 3.42a. The currents and flux lines are given in figure 3.42b. This

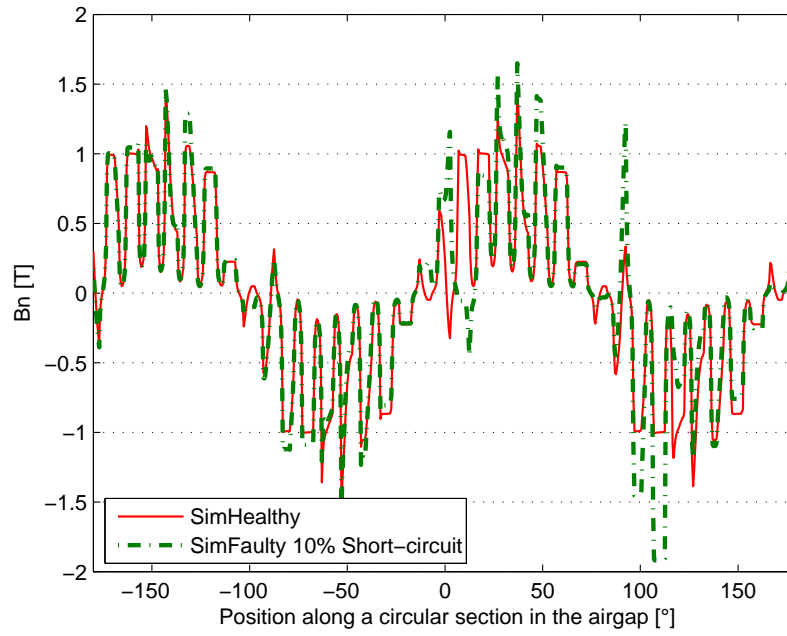


Figure 3.40: Radial part of the induction on a circle situated in the middle of the airgap.

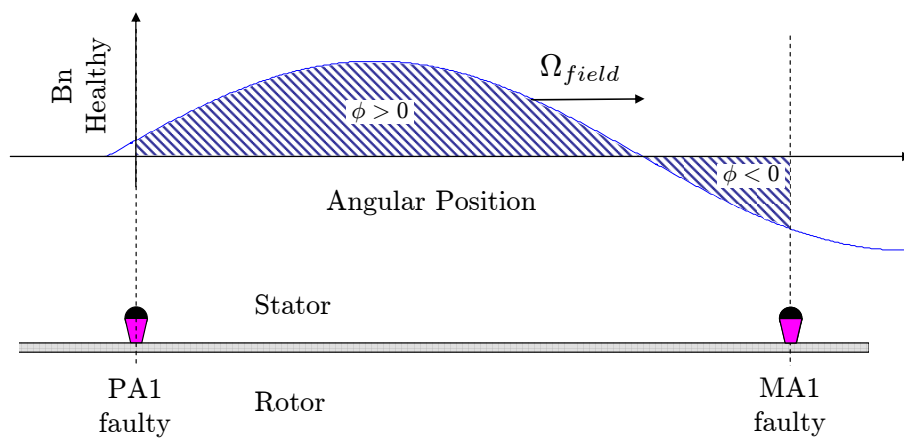


Figure 3.41: Normal flux density along the airgap. The arrow represents the moving direction of the field.

situation is similar to the one of the FE simulation with 10% short-circuit in phase *a* of pole-pair one at time instant $t = 0.12715$ s. As the current of the FE simulation is considered positive when flowing out of the plane, the current of the short-circuit coil is positive.

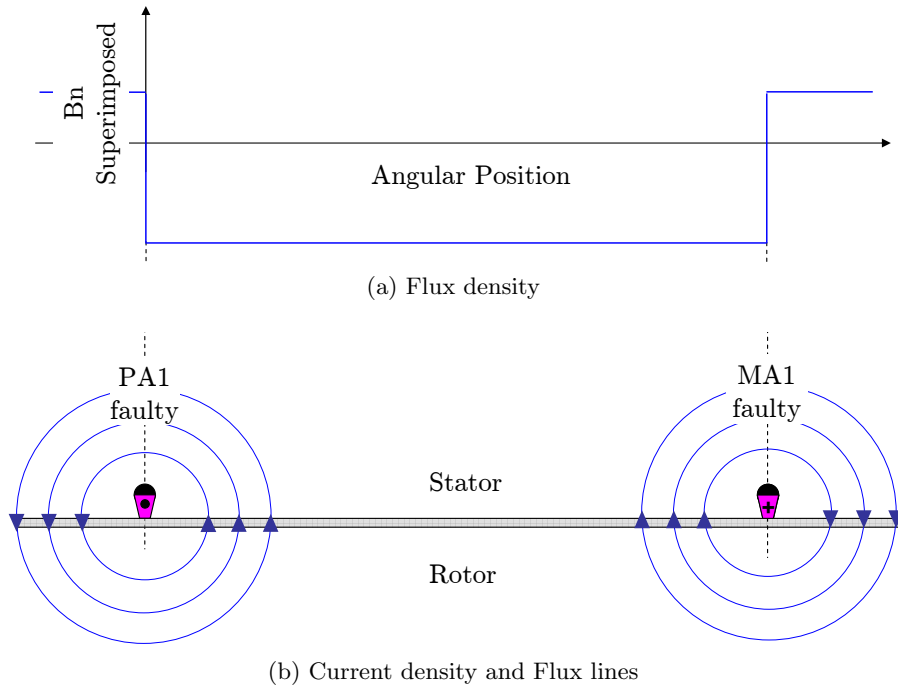


Figure 3.42: Fields created by induced currents in the short-circuited coil. The + represents a current flowing into the plane and • represents a current flowing out of the plane.

However, in the machine, the situation is not so simple as couplings between this short-circuited coil, the other stator windings and rotor bars should be considered. These couplings will be computed through time-domain FE simulations.

The first scenario considered is the case of a machine *IND1CP*, made of iron of constant permeability, running at nominal speed, fed by nominal sinusoidal voltages but *without* conductive rotor bars. The rotor slots are present and the region on top of the rotor bars is filled with low magnetic material as detailed in section 3.3.3.4. Two simulations are performed to represent the healthy and faulty situations.

The difference of normal induction in the airgap computed by FE simulation with and without short-circuit is proposed in the bold curve (green) of figure 3.43. Only the presence of the stator windings is considered. Instead of having a square distribution of the flux density as proposed in figure 3.42b, currents are induced in the other stator windings, primarily of the same pole-pair, in such ways as to minimise the flux density perturbation due to the fault. However, due to the fact that stator coils are distributed through 6 slots and short-circuited coil is distributed in only 2 slots, the healthy stator windings can not create an opposite MMF in the 2 teeth situated just next to the slot holding the short-circuited coil. This is clear in figure 3.43.

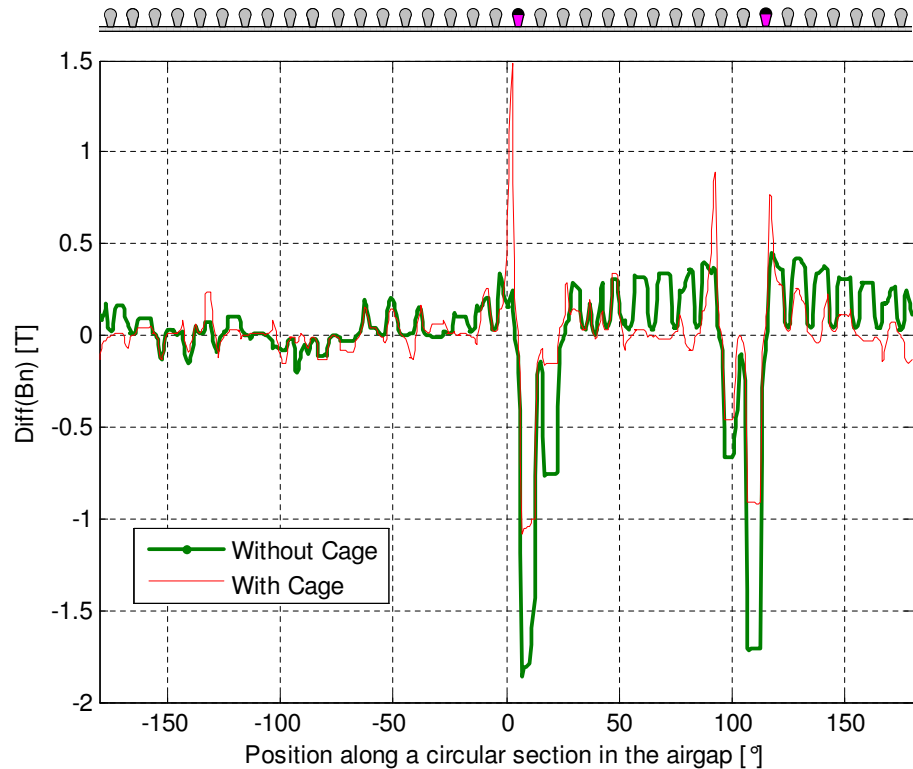


Figure 3.43: Difference between healthy and faulty radial induction on a circle situated in the middle of the airgap.

If the presence of the rotor cage is taken into account, between healthy and faulty cases additional voltages are induced in the bars as they go through a region of additional induction. Through previous analysis mainly 2 regions have been identified. They consist in the teeth situated next to the slots holding the short-circuit. When a bar passes through these regions, current will be induced such as to lower the additional induction that has created it. This can be understood by looking at the difference between the thin (red) and thick (green) curves, respectively with and without rotor cage, of figure 3.43.

However, as the sum of the currents in the bars is equal to zero, the additional current of the bars passing in front of the short-circuit slots should be redistributed on the adjacent bars. This results in an increase of the flux density on the other side of the short-circuit slot.

The situation of machine *IND1* is totally identical and, at time instant $t = 0.12715s$, the bars 27 and 6 are situated respectively in the regions of the slots *PA1 faulty* and *MA1 faulty*. The currents of these bars as well as the current of bar 7 (that passed *MA1 faulty* earlier) are shown in figure 3.44.

One can see on the figure, the passage of bar 6 in front of *PA1 faulty* around $t = 0.117s$ and in front of *MA1 faulty* around $t = 0.12715s$. The additional current flowing in bar 6 at this last instant is mainly redistributed in bar 7 which is on the other side of the short-circuit slot. It is important to understand that the modification of the currents of the rotor bar is local and

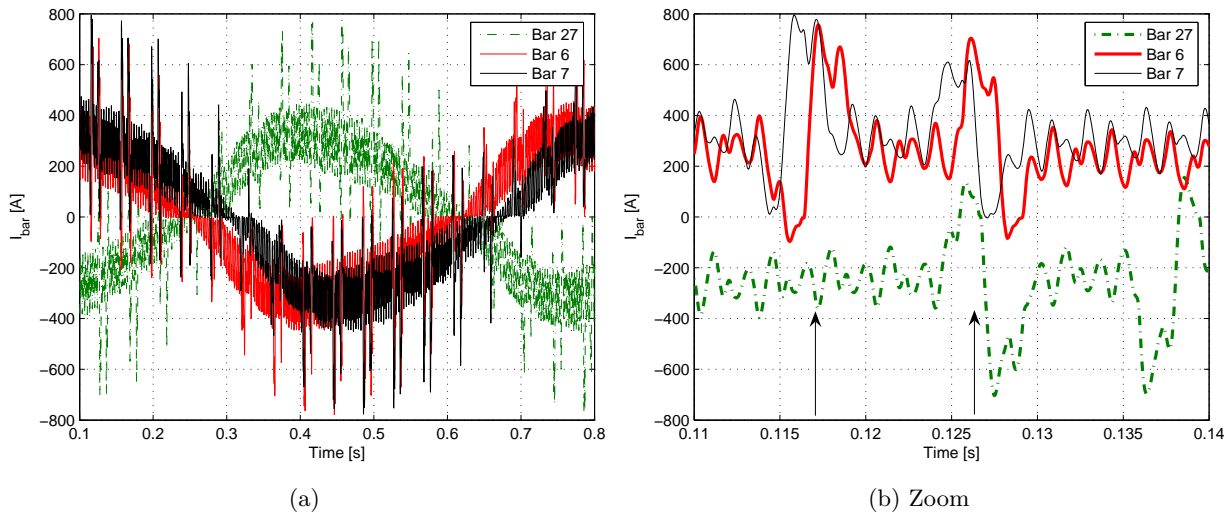


Figure 3.44: Current in rotor bar 27 and 6. The spikes represent the passage of the bars alternatively in front of *PA1 faulty* and *MA1 faulty*

happens twice per rotation. However, it is only happening under one pole-pair for this machine with parallel connected pole-pairs.

The harmonics present in the rotor bars and linked to the fault will therefore have components at $\frac{\Omega_r}{60}$ Hz, $P \frac{\Omega_r}{60}$ Hz and $2P \frac{\Omega_r}{60}$ Hz which respectively corresponds to once per turn, and once per pole-pair and twice per pole-pair. However these depend on the winding configuration. This can be confirmed through the FFT of the current of bar 27 in figure 3.45.

Numerical Details:

In the case of a rotor speed of 1459rpm and a machine with 2 pole-pairs, the main frequency of the rotor currents at $s f = 1.37$ Hz and the above-mentioned stator short-circuit related components are 24.32Hz, 48.62Hz and 97.27Hz.

The previous approach has been made for time instants where EMF is induced in the short-circuit coil. However, when the derivative of the flux seen by the short-circuit coil is null no current will be flowing in this coil and no MMF difference will be observed between healthy and faulty cases. Considering the different positions of the stator field with regard to the short-circuited coil, it can be confirmed that the current in the short-circuit is sinusoidal and that the MMF difference between healthy and faulty cases is a phenomenon fixed in space and with a pulsating amplitude.

3.5 Study of a machine with rotor eccentricities

In order to model a machine with rotor eccentricities, the geometry of the FE model has to be modified. Two types of rotor eccentricities will be considered:

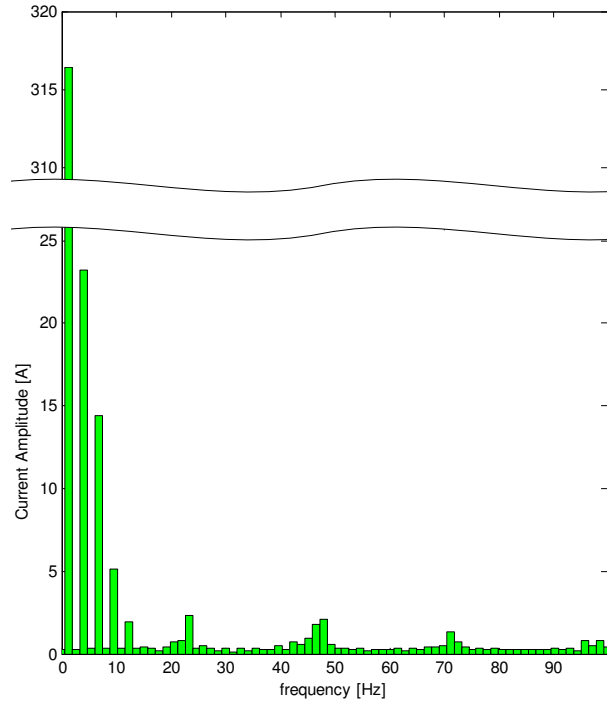


Figure 3.45: Amplitude of the FFT of the current of bar 27 in the case of stator short-circuit.

- Dynamic eccentricities where the centre of the rotor describes a circle of radius $R_{DynEcc}\%$ of the airgap width (g) and rotates at rotor speed.
- Static eccentricities where the centre of the rotor is offset by $R_{StatEcc}\%$ of the airgap width from the centre of the stator.

In order to implement these eccentricities, the rolling layer of the FE model is still centred around (0,0) while the centre of the rotor is moved by $\frac{R_{DynEcc}g}{100}$ and the centre of the stator is moved by $\frac{R_{StatEcc}g}{100}$, with of course $|R_{DynEcc}| + |R_{StatEcc}| < 100$ to avoid collision between rotor and stator.

The rolling layer is then constructed by dividing the minimum distance between the exterior boundary of the rotor and the interior boundary of the stator in three zones:

- the most inner one is the "rotor airgap" which is a part of air rotating with the rotor;
- the centre one which is the rolling layer delimited by two concentric circle of centre (0,0) and radii given by equation 3.8 where sid is the stator inner diameter and rod is the rotor outer diameter.
- the most outer one is the "stator airgap" which is the fixed part of air.

$$R_{rolling} = \frac{\frac{sid}{2} + \frac{(|R_{DynEcc}| - |R_{StatEcc}|)g}{100} + \frac{rod}{2}}{2} \pm \frac{100 - |R_{StatEcc}| - |R_{DynEcc}|}{100} \frac{g}{6} \quad (3.8)$$

These geometries are illustrated in figure 3.46 for $rod = 4$ and $g = 2$. On these figures, the rotor is represented at four different instants of time.

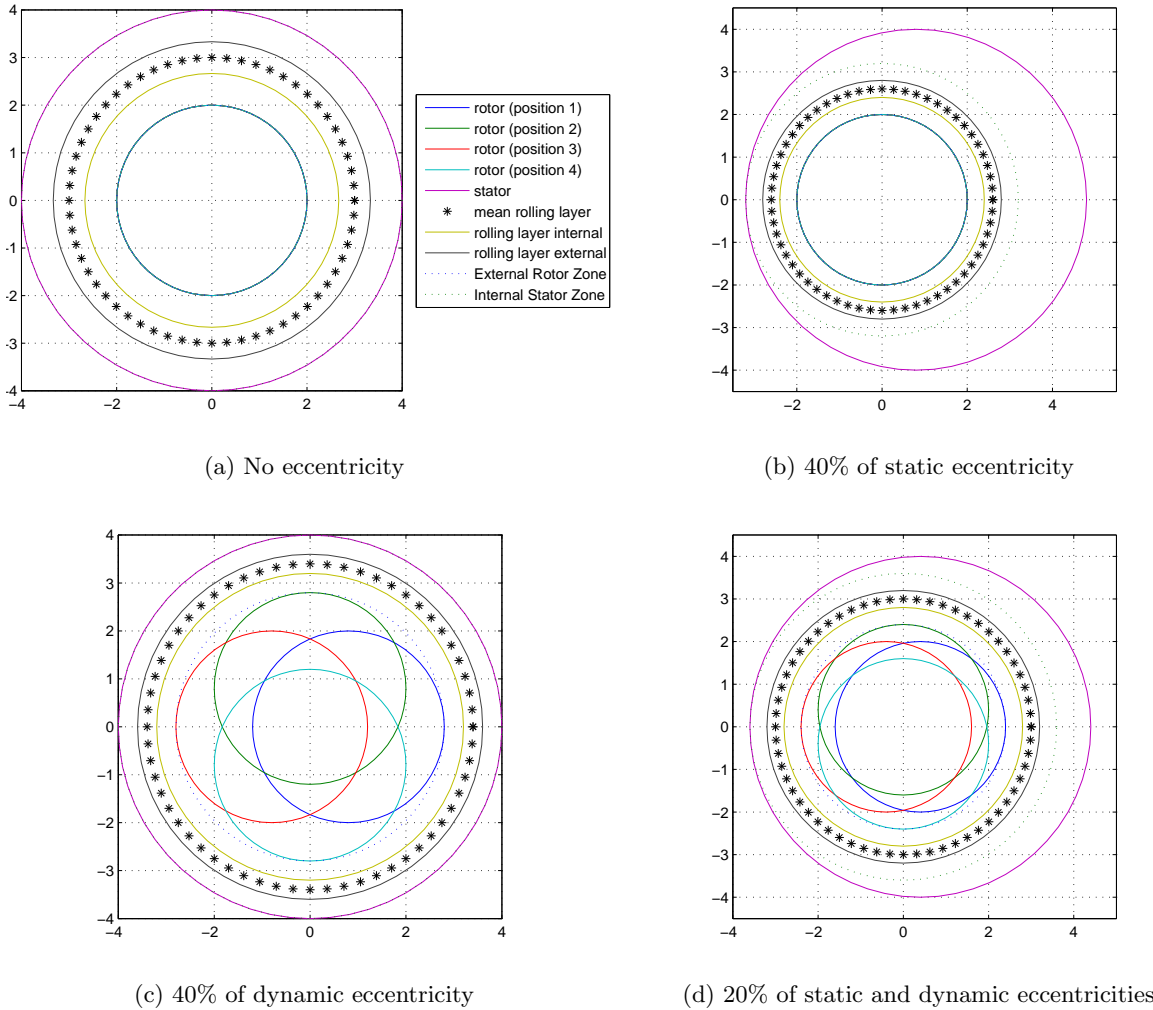


Figure 3.46: Geometry and rolling layer for different eccentricities

Using this method, the rolling layer is much thinner than in the other models and the mesh has to be refined in this region to assure good quality elements. The main drawback of this increase of the number of elements is the increase of the computing time. These models will be used to understand the influence of rotor eccentricities on the machine behaviour.

3.5.1 Effect of eccentricity on the machine behaviour

In the present section, the influence of eccentricities on a two pole-pair parallel connected machine (*IND1*) will be studied.

In the case of static eccentricities, the position of minimum airgap is fixed with regard to the stator. It will be chosen to be 180° which corresponds to the separation between the pole-pairs as shown in figure 3.6. If the airgap is described counterclockwise (which is the sense of rotation of the magnetic field); pole-pair 1 covers half of the machine circumference from the angular position of maximum airgap (0°) to the angular position of minimum airgap (180°). The second pole-pair starts from the region of minimum airgap to the region of maximum airgap.

As the voltage is imposed on parallel stator windings, the stator flux is divided in the 2 pole-pairs. In the case of a healthy machine, the normal flux density along a circle placed in the middle of the airgap is equally distributed on the 2 pole-pairs. This can be seen in figure 3.47. The chosen time instant, $t = 1.034\text{s}$, corresponds an orientation of the rotating field with 0° .

In the case of static eccentricity, the normal flux density is given with the plain line (red) on the same figure. If stator leakage inductances and resistances are neglected, the stator flux of each pole-pair is identical. In the case of pole-pair 1 whose flux crosses the airgap around 0° and 90° , as the airgap is bigger than in the healthy case, the total reluctance of the flux path is also bigger. Therefore, the MMF in the stator windings will be higher and so will be the stator currents of this pole-pair. In the case of pole-pair 2, the total reluctance of the flux path is smaller than in the healthy case. Therefore the stator currents will be smaller.

If the presence of leakage inductances and resistances are considered, the voltage drop on these elements influences the repartition of the flux between the 2 pole-pairs. The flux of pole-pair 1 (higher reluctance) will be smaller than the flux of pole-pair 2. Therefore the asymmetries in the stator currents will lower [Stavrou 94, Tenhunen 01] and so will the asymmetries in flux distribution. Furthermore if the flux of pole-pair 2 (smaller reluctance) is bigger so will be saturation of this flux path. The effective airgap will therefore be increased with tends to lower the influence of eccentricity [Stavrou 94].

Therefore, in the case of a machine with two pole-pairs which are parallel-connected, the total flux will be distributed almost equally under the 2 pole-pairs. However stator currents of the different phases will be much different as one will understand further down this section. The situation is much different in the case of pole-pairs connected in series. Indeed, same currents will be flowing on the stator windings of both pole-pairs and flux density will not be distributed equally between the pole-pairs.

On figure 3.47, some other differences can be observed between flux density around 0° and 180° . The stator slot influence is bigger in low airgap length regions (180°) and smaller in higher airgap length. Indeed the slot influence is bigger when the ratio between airgap length and stator slot opening is smaller. This is clearly shown in figure 3.47. Finally, the mean airgap length

is increased compared to the healthy case [Bangura 00a]. Indeed, as shown on figure 3.46, the airgap is reduced in a small part of the circumference and increased in a bigger part.

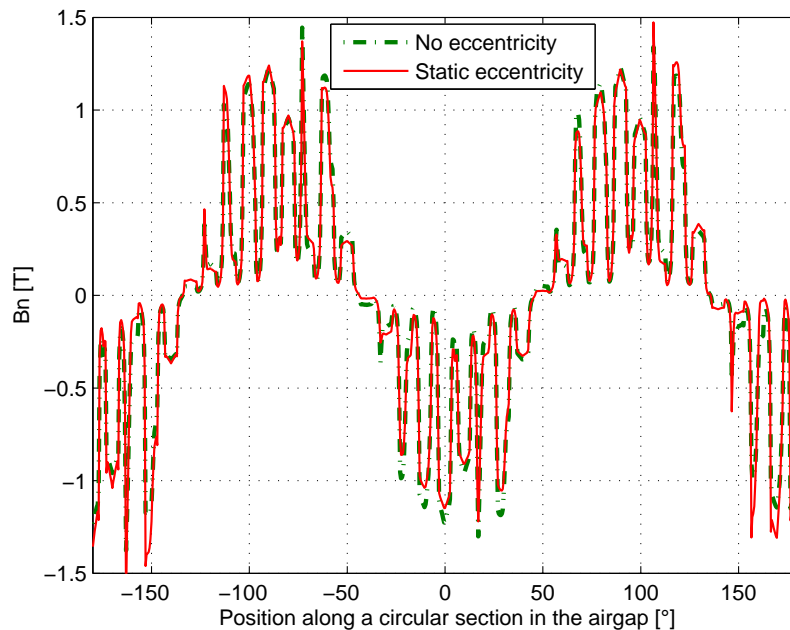


Figure 3.47: Radial part of the induction on a circle situated in the middle of the airgap at $t = 1.034s$.

If one studies in more details the stator currents, depending on the asymmetry orientation, each stator winding will have a different magnetising inductance and the 50Hz RMS value of its current will be different. This can be observed in figure 3.48. On that figure, the small oscillation of RMS value even present in healthy case is due to the presence of remaining harmonic components in the filtered stator currents. It has no influence on the conclusion of this section.

As the stator windings of phase c are oriented perpendicularly to the eccentricity, the modification of the reluctance of the flux path when the stator current c is maximum is small. The flux path at this time instant $t = 1.04s$ is shown in figure 3.49. Therefore, the RMS value of the current is not much affected. However, situation of pole-pair 1 and 2 is anti-symmetrical. If one of the currents of phase c is smaller than in the healthy case, the other one will be bigger. The position of phase $a1$ and $b2$ with regard to the eccentricity are similar as both windings are situated in a region of higher airgap length. The phase currents will therefore be more important than in the healthy case. Finally, phase currents $b1$ and $a2$ will hold a smaller current.

Therefore, through the measurement of the RMS value of the phase currents and the knowledge of the winding configuration, it is possible to determine the orientation of the eccentricity. It is oriented with the coil holding the smallest current and perpendicular with the coil showing no variation of its current.

In the case of dynamic eccentricity, the situation is different as the position of minimum airgap is rotating at Ω_r with regard to the stator windings. In order to understand its effect, we will suppose that the rotor is rotating at synchronous speed. This way, every half period of the

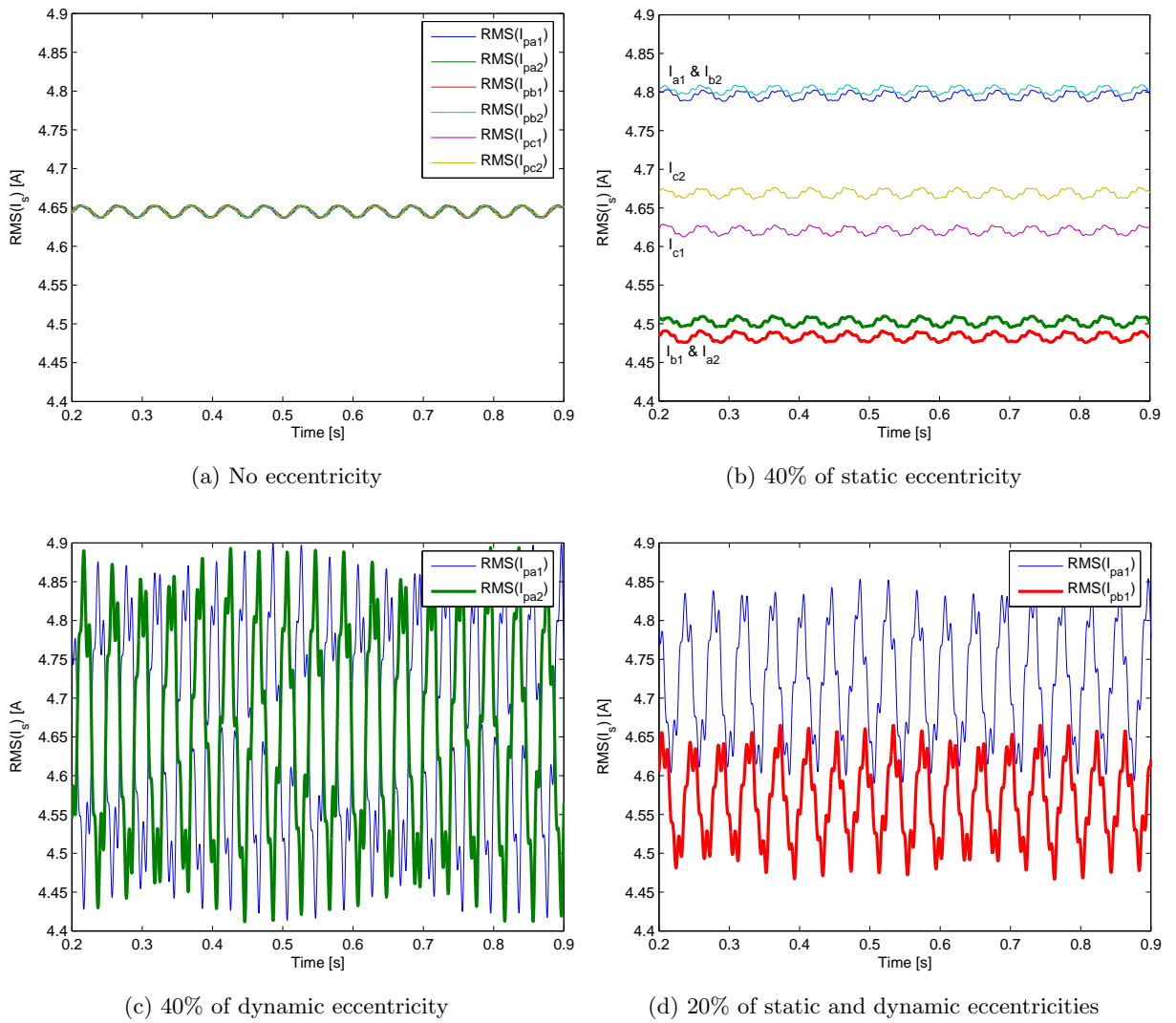


Figure 3.48: Running 50Hz RMS value of the stator currents

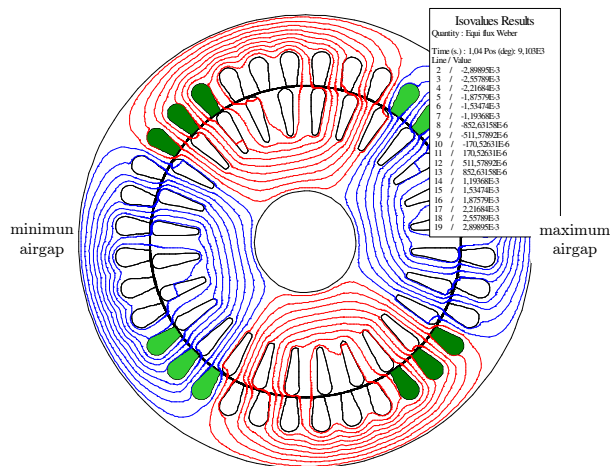


Figure 3.49: Flux path at time instant $t = 1.04s$ wich correspond to a maximum in current of phase c

fundamental, the position of minimum airgap switches between pole-pair 1 and 2. Therefore, the 50Hz RMS value of the stator current oscillates between values similar to the extremum values of the case of static eccentricity for pole-pair 1 and 2. This is illustrated in figure 3.48. The RMS value of the current of each stator coil will depend on the average position of the eccentricity with regard to the position of the rotating field. If the slip is not null, this average position varies at slip speed and so will the RMS value of the currents.

Finally, the case of mixed eccentricity is a combination of the effects of previous eccentricities. The RMS values of the currents oscillate at sf and $2f$ and have a constant offset.

3.6 Conclusions

In this chapter 2D finite element models of healthy and faulty induction motors have been implemented and the external behaviour of these motors has correctly been represented using time-domain simulations. The use of a magneto-dynamic simulation is an efficient method for initializing the time-domain simulation but the accuracy of this method to represent the machine clearly depends on the working points and on the quantity observed; rotor currents are not correctly represented and both stator currents and torque lack precision in low speed conditions.

The time-domain FE method is a powerful tool to analyse machine behaviour and to serve as test-bench with precisely known and controlled environment. The main drawback of this method is the extensive time required for machine modelling, simulation and data manipulation.

Furthermore, FE models have been used to analyse the behaviour of faulty machines. The main effect of a broken bar has been explained and illustrated using these models. It mainly consists in the creation of a pulsating field rotating with the rotor. This field modulates stator currents. Furthermore, the airgap flux distribution has been physically explained using Faraday and Ampère's laws. The effect of variation of local saturation due to the presence of a broken bar has also been studied. It has for consequence to phase-shift the airgap flux density perturbation due to the broken bar from the position of the fundamental flux. The magnitude and the phase of the stator current oscillation are then affected.

The FE method has also been used to explain the major differences between the short-circuit of several turns of the stator winding and a winding turn reduction. The presence of the short-circuit does not much influence the line currents but greatly influences Joules losses in the machine. Furthermore, it induces currents in the rotor bars as they pass in front of the stator slots holding the short-circuit.

Finally, on the analysis of rotor eccentricity, it has been shown that a configuration of parallel-connected pole-pairs in the case of a 2 pole-pairs machine tends to minimise the perturbation of the airgap flux distribution. However, the fundamental stator currents are greatly affected. The influence of the eccentricity on the stator currents also clearly depends on the position of the eccentricity with regard to the stator windings. This information can be used to localise the eccentricity. Furthermore, this study suggests that the number of pole-pairs as well

as the connection of these pole-pairs greatly influence the effect of the eccentricity on the machine behaviour.

From the analysis of these three faults, one can conclude that the winding and pole-pair configuration have much influence on the consequences of the fault on the machine behaviour. Furthermore, currents from the stator windings are more affected than line currents and they should be used for monitoring when available.

Finally, thanks to the use of FE models, a deep physical understanding of the faulty machine has been obtained.

Chapter 4

Overview of condition monitoring and fault diagnostic of induction motors

Condition monitoring of electrical machines is a field profusely studied for several decades. Each proposed method has been introduced to perform the diagnosis using fewer data, in broader conditions, faster or with more details than the previous ones. In this chapter, several existing methods used to monitor and diagnose induction motors are presented and new valuable information is proposed by testing these methods in the same conditions. These conditions are created using FE simulations of healthy and faulty motors. As data are identical, objective comparisons are therefore possible. Of course, as some effects of the faults are not modelled by the FE approach used (see chapter 3), the methods that rely on the monitoring of these effects are presented but not tested. One may think of vibrations, temperature, partial discharges or axial flux effects which are neglected in the FE models.

In this chapter, particular attention will be devoted to electrical and magnetic approaches as they are closely related to the approach presented in this work.

In the following presentation, a classification of the methods will be made on the physical quantities monitored to perform the diagnostic.

4.1 Mechanical techniques

4.1.1 Vibration monitoring

It has been explained in chapter 2 that each fault in induction machines will produce mechanical vibrations. The frequency spectrum of these vibrations can be used to identify the type of fault. In the case of bearing faults, several authors have linked the frequencies of vibration shown in equation 4.1 to the type of fault and to the geometry of the bearings [Önel 05, Lee 05, Schoen 95b].

$$\begin{aligned}
f_{outer} &= N_b \frac{f_r}{2} \left(1 - \frac{D_b}{D_c} \cos \beta\right) \\
f_{inner} &= N_b \frac{f_r}{2} \left(1 + \frac{D_b}{D_c} \cos \beta\right) \\
f_b &= \frac{f_r}{2} \frac{D_c}{D_b} \left(1 - \frac{D_b^2}{D_c^2} \cos^2 \beta\right)
\end{aligned} \tag{4.1}$$

f_{outer} , f_{inner} and f_b are respectively the frequencies of vibration for an outer race defect, an inner race defect or a ball defect. N_b is the number of balls; f_r is the rotor speed in revolution per seconds; D_b and D_c are respectively the ball and cage diameter, and β is the contact angle of bearing¹. Note that, as an example, for bearings between 6 and 12 rolling elements, f_{outer} and f_{inner} can be approximated using formulas [Önel 05, Schoen 95b]:

$$\begin{aligned}
f_{outer} &= 0.4 N_b f_r \\
f_{inner} &= 0.6 N_b f_r
\end{aligned}$$

Similarly, stator faults create vibrations at multiples of the line frequency [Lee 05] and broken-bar faults produce vibrations at $k_{odd} f_r \pm 2k f_s$ where k_{odd} is any odd integer [Jang 03]. Static eccentricities generate frequencies at $2f_r$ while dynamic eccentricities produce frequency components at $k_{odd} f_r$ which are similar to broken bar signatures [Jang 03].

Illustrations of these statements are provided in figure 4.1. The results are obtained from the FE models presented in chapter 3. The x-component of the force (F_x) applied on the rotor is computed using the integration of the surface forces on the rotor (Maxwell's tensor method). F_x is always null for the healthy case as it can be seen in the figures.

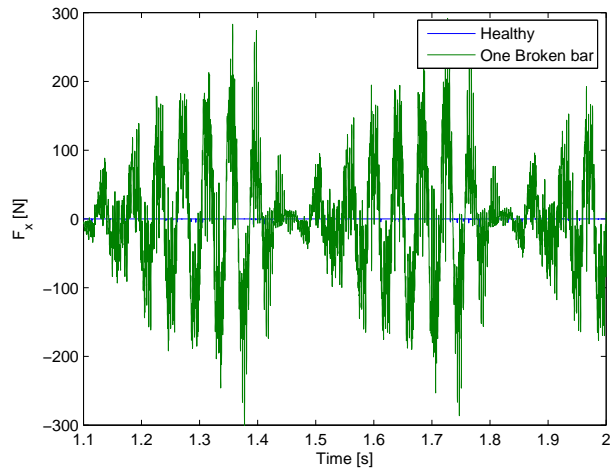
In practice, vibration signals can be acquired using for example piezo-electric accelerometers mounted on the outer casing of the motor or on the bearings [Önel 05].

The main drawback of this technique is that it requires specific sensors. However, the sensitivity of this method is fairly high [Jang 03, Dorrell 97].

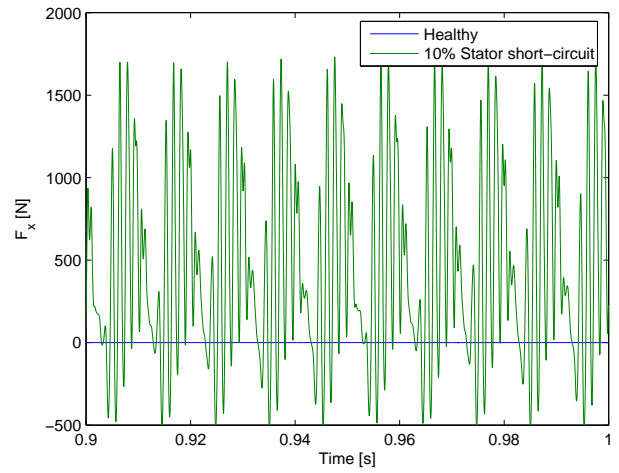
4.1.2 Speed fluctuation monitoring

When rotor currents, fluxes and stator currents contain other frequency components than the fundamental, motor torque can fluctuate (see section 3.3.1). Consequently the motor speed oscillates under constant load torque conditions [Hirvonen 94]. The main drawback of this approach is its sensitivity to load variations that also create speed oscillations [Thorsen 95]. FE simulations are used to illustrate the speed oscillation of a healthy induction motor with constant and oscillating resistant torque as well as of an induction motor with one broken bar (Figure 4.2). The torque oscillation is chosen to be a 10% torque ripple at $2sf$ which of course correspond to the worst situation. This kind of torque profile can be found in applications where the motor is driving

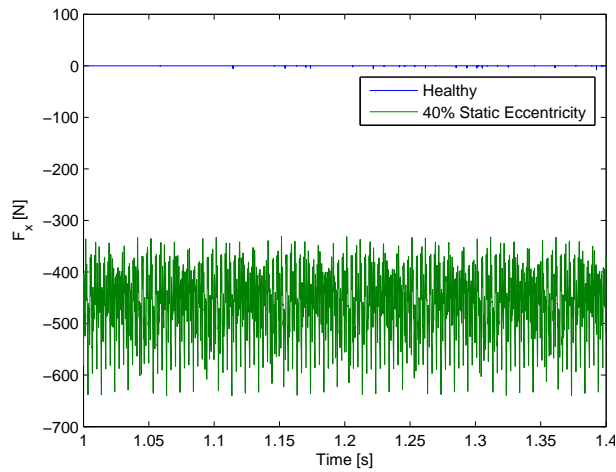
¹The contact angle of a ball bearing is the angle between the contact point of the ball on the outer race and the contact point on the inner race.



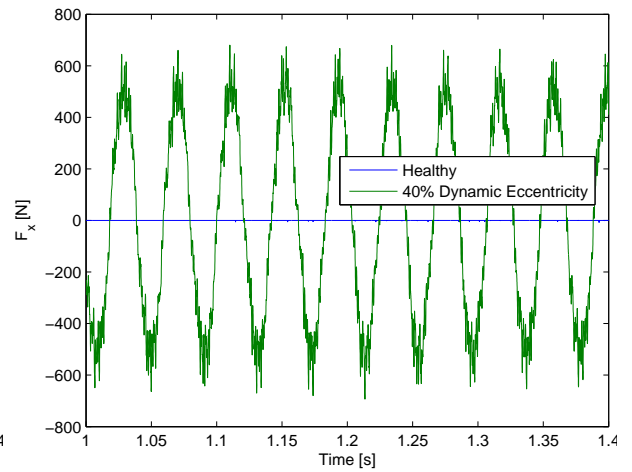
(a) One Broken bar



(b) 10% Stator short-circuit



(c) 40% Static Eccentricity



(d) 40% Dynamic Eccentricity

Figure 4.1: x-component of the force acting on the rotor versus time.

reduction gears, large fans, pumps, etc [Bossio 05]. Using this technique, a false alarm is difficult to avoid in such conditions.

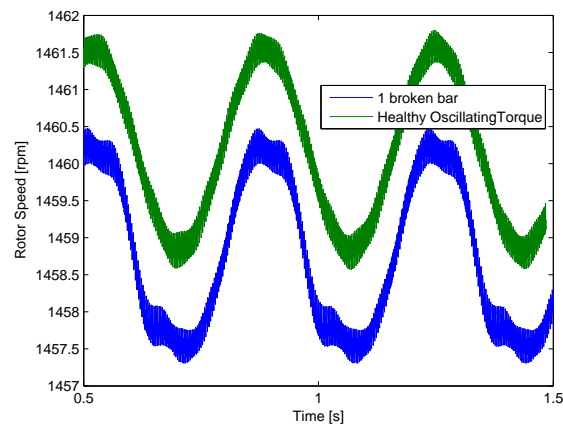


Figure 4.2: Speed oscillations of an induction motor in nominal conditions.

4.2 Chemical techniques

In case of large motors with circulatory lubricant system, oil can be analysed for presence of particles of metal (bearing wear), fibre (winding wear), etc. [Thorsen 95]

The cooling air can also be analysed for carbon monoxide resulting from the degradation of the winding insulation [Thorsen 95].

4.3 Temperature monitoring

Thermocouples placed on the bearing or on the motor casting or infrared cameras can be used to indicate friction in a faulty bearing, excessive Joules losses due to short-circuit as well as excessive saturation of the iron core in case of broken bars. As example, figure 4.3 shows infrared measurement used to diagnose bearing failure².

The main disadvantages of this method are that thermocouples perform localised measurement and are sensitive to the quality of the contact between sensor and surface. This contact can deteriorate due to vibration. Infrared measurements are one-off measurements but have the main advantage to not require any fixed installation.

Fiber-optic sensors located in windings can be used to diagnose stator faults. It is possible to find single-point measurements or along-the-fiber-length measurements [Boiarski 95]. The information obtained from these sensors is precise but the sensors have to be integrated while manufacturing the machine.

²figure obtained from the website http://www.monition.com/condition_monitoring_thermography.htm.

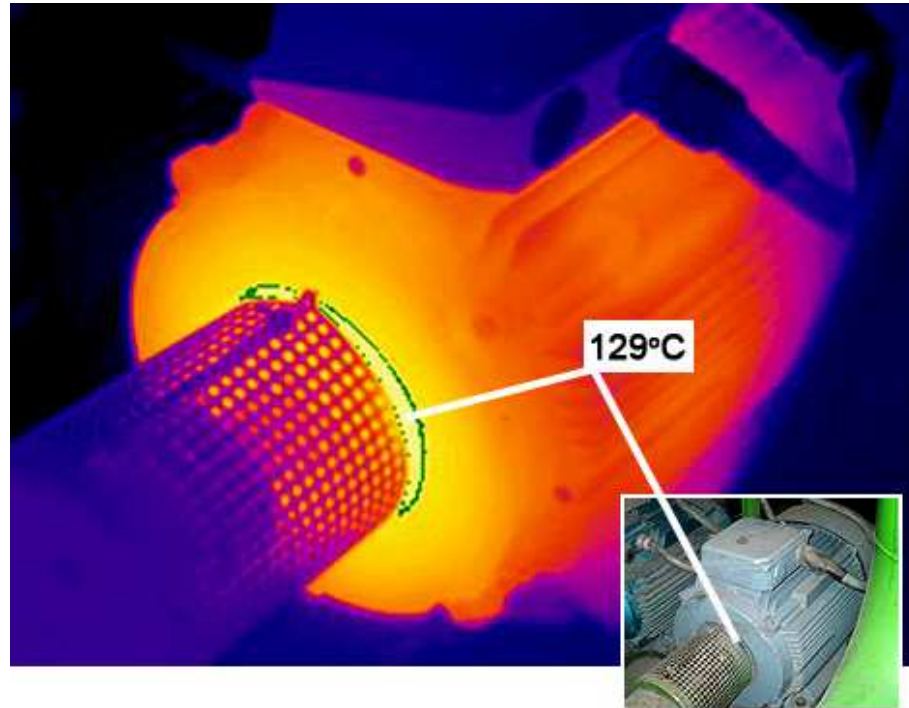


Figure 4.3: Infrared measurement for bearings monitoring. Light colors represent highest temperatures

The main advantage of this method is to directly monitor the action of the fault on the motor health.

4.4 Partial Discharges monitoring

The electrical pulses at machine terminals created by the partial discharges through the winding insulation can also be monitored. Statistical evolution of the magnitude and the phase angle of these pulses versus occurrence rate is used as indicator to quantify insulation degradation [Contin 00, Ramirez-Niño 98].

However, these measurements are difficult to perform due to the high level of magnetic noise present in the motor.

4.5 Electrical and magnetic techniques

Many methods rely on electromagnetic effects created by the faults inside the motors. Their main advantage is to use electrical measurements which are often already available for the protection or the control of the machine. In the presentation of this section, the different techniques will be roughly ordered by the quantity of measurements needed as well as by the complexity of the analysis.

4.5.1 Detection through axial flux

In healthy machines, stator and rotor currents flowing in end-windings are balanced and no axial leakage flux is produced (This is not exactly the case for machines with skewed rotor cages and/or interbar currents [Hirvonen 94, Meshgin-Kelk 02]). However, in the case of asymmetries in windings, airgap or materials, axial flux rises. Its harmonic content is directly related to the harmonic content of currents and therefore related to the spatial harmonic content of the airgap flux [Fink 94, Penman 86].

In order to detect this leakage flux, search coils can be mounted outside of the motor housing and concentrically with the shaft [Fink 94, Hirvonen 94]. In order to localise stator faults, several search coils can be placed axisymmetrically to the shaft in the end plane of the machine. Information given by each coil concerns only the windings in front of it and therefore the faulty windings can be identified.

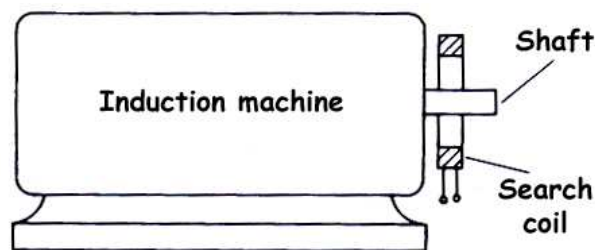


Figure 4.4: Axial Flux search coil [Penman 86].

A variation of this technique is proposed by [Elkasabgy 92] and consists in placing the search coil on the motor frame.

4.5.2 Detection through airgap flux

Some authors propose to place a coil around one of the stator tooth and to monitor the induced voltage in the coil [Cabanas 05]. This method gives good results for rotor faults. It is quite similar to the one of the next section but is much more invasive. Moreover, the induced voltage can be integrated and the fluctuation of the zero crossing of this flux can be monitored [Cabanas 05]. This fluctuation is linked to the pole-length fluctuation explained in section 3.3.3.

The main advantage of this method is its insensitivity to load fluctuations which will not be the case of the following method.

4.5.3 Monitoring of current spectral content (MCSA)

MCSA (Motor Current Signature Analysis) is one of the most studied techniques in recent years and it is seen as a good replacement for the widely-spread vibration monitoring. The principle is to use the stator winding itself as a sensor placed inside the machine.

In the section 3.3.1 it has been explained that frequency components appear at $(1 - 2s)f$ and $(1 + 2s)f$ in the spectrum of the stator current in case of broken bars. The latter component is only present if the fault causes speed variations. The current spectra given in figure 4.5 show the side-bands in the case of a FE simulation at full load of machine *IND1* with one broken bar. It can also be observed that the fault also affect the fundamental component as explained in section 3.3.1.

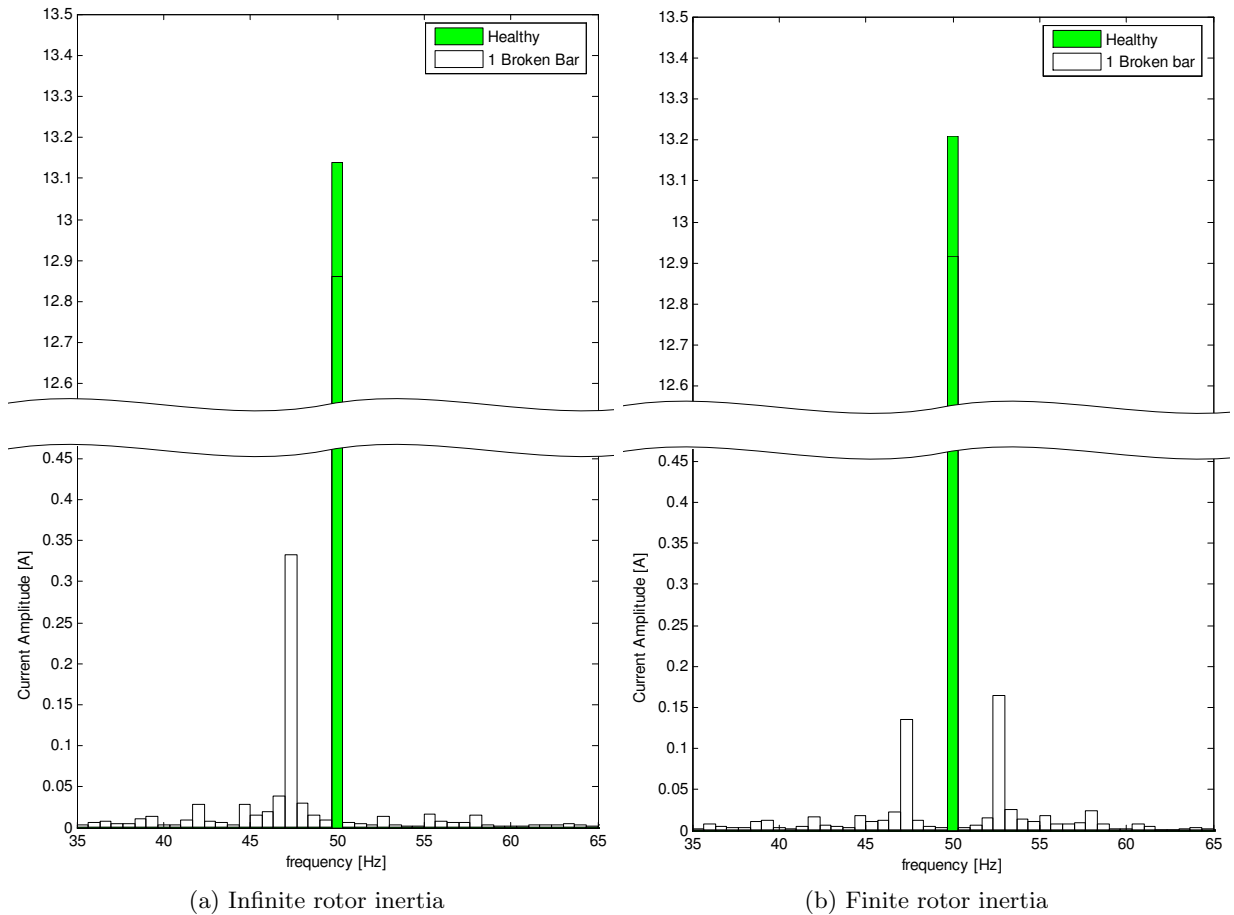


Figure 4.5: Spectrum of the stator current for healthy rotor and rotor with 1 broken bar out of 28.

The fault detection method consists in monitoring particular frequency component like the ones mentioned earlier for broken bars. The main advantage of this method is its noninvasive character as current sensors are often needed to control the process. Furthermore, as no additional sensors are added to the process, its availability is not affected by the instrumentation system.

Even though this method is very promising, limitations are numerous. First of all, to perform precisely the FFT, the machine must be in steady-state during a least a period of the modulation, which can be long in case of low-slip conditions. More details on the application of FFT for fault detection will be given in chapter 7. Moreover, as the slip lessens, side-bands $(1 \pm 2s)f$ are becoming very close to the main peak (f) and if the FFT resolution is not very high, it is difficult to separate these peaks. This is even more complicate since low slip conditions

correspond to low-load with low current magnitude. As example, in the case of motor *IND1* which has a nominal slip of 0.0273, the maximum separation between the f component and its sidebands is 2.73Hz. At 10% load the FFT of figure 4.5a is shown in figure 4.6. The distinction between faulty and healthy frequency component becomes very difficult. The situation is even worse for bigger motors which work with smaller slip.

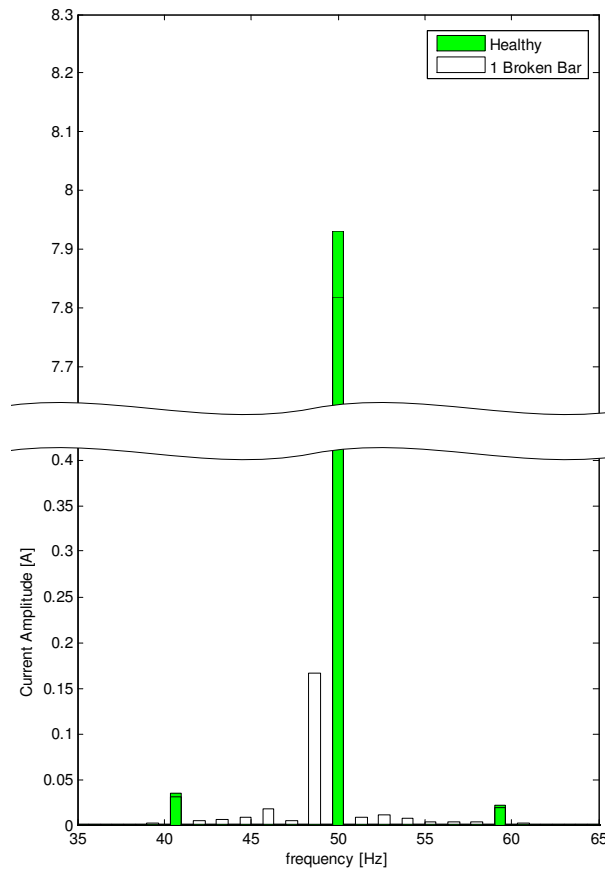


Figure 4.6: Spectrum of the stator current for healthy rotor and rotor with 1 broken bar out of 28 in low-load conditions.

Finally, it is easy to understand that harmonics in voltage supply or in mechanical load create perturbed current spectra in which the detection becomes very complicated [Schoen 95a]. As an example, figure 4.7 illustrates the spectrum of the stator current when an oscillating torque at $2sf$ is present. The monitoring of the $(1 \pm 2s)f$ component would lead to the same false diagnostic as for the monitoring of speed oscillation.

Further complications have been illustrated in [Bellini 00]; in the case of star-connected machines, the flux saturation produces a rotor frequency component at $3sf$ [Liao 94]. The field linked to this component will be seen by the stator at $(1 + 2s)\omega$ and will therefore create a stator current component at $(1 + 2s)f$ which can delude diagnosis.

From the quantification point of view, some authors have concluded that the amplitude of the $(1 - 2s)f$ component is linked to the number of adjacent broken bars by [Filippetti 92]

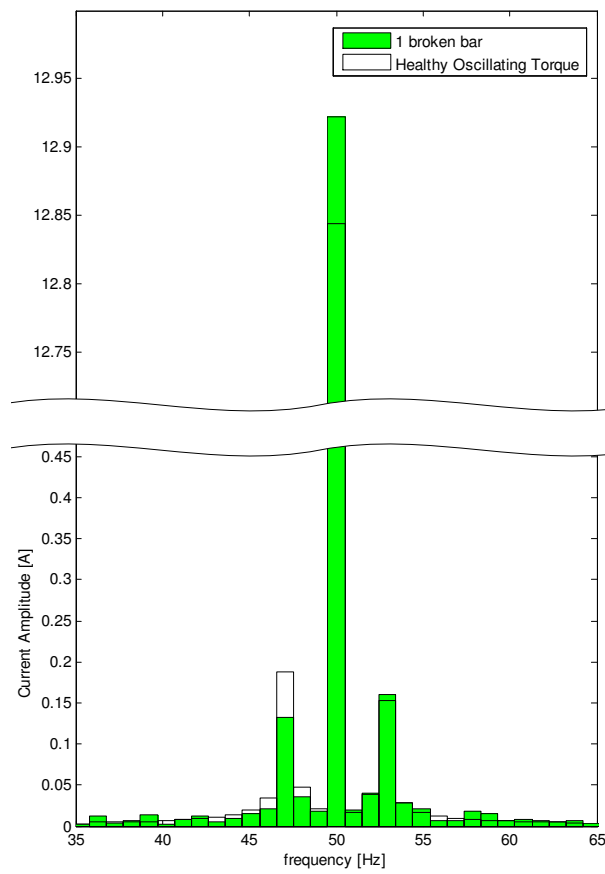


Figure 4.7: Spectrum of the stator current for healthy rotor with 10% torque oscillation around nominal conditions and faulty rotor with constant load torque.

$$\frac{I_{(1-2s)f}}{I_f} = \frac{n_{BB}}{n}$$

where n_{BB} is the number of broken bars, n is the total number of bars of the squirrel cage, and I_x is the amplitude of the x Hz component of the stator current. However, some doubts on the precision of this technique could rise by comparing the amplitudes of the $(1-2s)f$ sidebands of the two sub-figures of figure 4.5 obtained for the same number of broken bars but different inertia. Indeed, an approximate demonstration of the dependence of the lower sideband with inertia has been given in [Bellini 00]. The sum of the two sidebands is independent of the inertia and is therefore a better indicator of the magnitude of the fault. According to [Bellini 00], the lower and upper sidebands can be detailed as

$$\begin{aligned} I_{(1-2s)f} &= \left(1 - \frac{m}{J}\right) \cdot I_{(1-2s)f|J=\infty} \\ I_{(1+2s)f} &= -\frac{m}{J} \cdot I_{(1-2s)f|J=\infty} \end{aligned}$$

where $I_{(1-2s)f|J=\infty}$ is the amplitude of the $(1-2s)f$ component when the inertia of the machine (J) is infinite and m is a coefficient depending on the slip, the stator flux and the impedance of the stator winding.

Furthermore, this approach does not take into account the presence of inter-bar currents which are known to lessen the influence of the broken bar on the machine behaviour. The current flowing in a completely broken bar versus the length of the rotor (l_x) can be estimated by [Hirvonen 94]

$$\frac{I_{BB}}{I_{healthy}} \cong 1 - \frac{1}{\cosh \lambda l_x}$$

where $\lambda = \sqrt{3\left|\frac{Z_b}{R_c}\right|}$, Z_b is the bar impedance and R_c is the contact resistance between the bar and the rotor core.

For motors in which the flux density distribution is modified due to the presence of eccentricity (see section 3.5.1), slot harmonics can be monitored to indicate the presence of faults. MCSA can then be also applied in these conditions.

In the case of stator-related faults, detection using MCSA becomes very complicated. Indeed, stator faults induce frequency components in the rotor currents but these rotor current harmonics only influence the stator currents through flux coupling between stator and rotor end-windings or through interaction with small asymmetries [Stavrou 01]. Furthermore, depending on the winding configuration, some of the time harmonic present in the airgap flux and linked to the fault will not induce frequency components in the stator current [Stavrou 01].

In order to enlarge the conditions in which MCSA can be used, some authors have considered to use short time discrete Fourier transform (STDFT) [Burnett 96], wavelet transform [Burnett 94, Roger-Folch 04] or smooth Wigner Ville distribution [Burnett 96]. These approaches

allow the machine to be diagnosed during starting, i.e. when both the current magnitude and slip are big. Finally, by monitoring the machine in transient situations, the displacement of the $(1 - 2s)f$ component with speed gives an additional information to locate this component when the slip is not precisely known. In figure 4.8, a no-load start of a motor with three broken bars is shown. The path of the $(1 - 2s)f$ component is outlined using dash lines. As the slip varies from 0 to 0.5, the component moves from 50Hz to 0Hz and then as the slip continues to lessen, the sideband moves from 0Hz to almost 50Hz [Burnett 94].

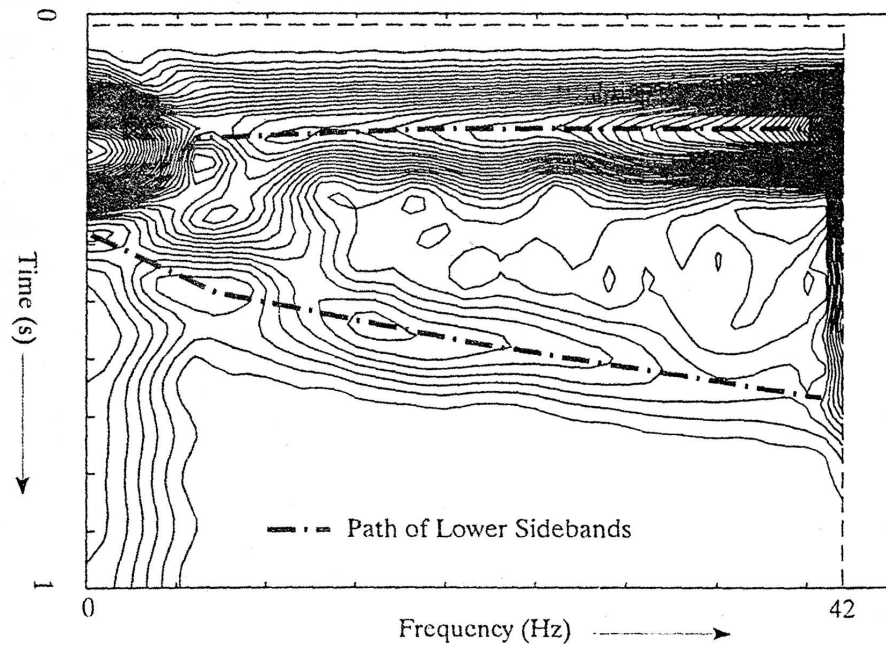


Figure 4.8: Spectrogram obtained by wavelets [Burnett 94]

Other authors propose to sample the signal at multiples of the stator frequency to avoid leakage of the fundamental frequency and to be able to perform a FFT in some of the transient conditions created by a variable speed drive [Innes 94, Raison 00]. Note that, in order to detect the presence of rotor faults, the slip should remain constant during these transient conditions.

The fault detection techniques proposed in the next two sections illustrate solutions of spectral analysis of electrical signals not affected by harmonics present in the power supply.

4.5.4 Monitoring of Voltage Spectral content (MVSA)

In order to detect frequency components in the voltage, the machine can be temporarily disconnected from its supply [Nandi 00]. Immediately after switch-off, voltages are induced in the stator windings due to the presence of the rotor currents. The currents flowing in the shorted stator turns create additional MMF and induce voltages in the opened stator windings.

One of the main advantages of this method is its independence of supply unbalance and harmonics. However, the motor can not be used for its application while the test is performed.

This is limiting for the fast expanding faults that are stator short-circuits. For this type of faults, an evaluation of the machine health should be frequently done.

4.5.5 Monitoring of Power Spectral content (MPSA)

Motor Power Signature Analysis (MPSA) is another variant of MCSA. This method proposed in [Legowski 96] is based on the fact that, in the power spectrum, frequency components representing the fault are not present anymore as sidebands of the fundamental frequency. Indeed, a modulated stator current can be written as:

$$i(t) = i_0 [1 + M \cos(\omega_1 t)]$$

with $i_0 = i_{m0} \cos(\omega t + \varphi)$ being the healthy current and ω_1 the modulating frequency. Therefore we obtain:

$$\begin{aligned} i(t) &= i_0 + M I_{m0} \cos(\omega_1 t) \cos(\omega t + \varphi) \\ &= \underbrace{i_0}_{\text{healthy part}} + \underbrace{\frac{M I_{m0}}{2} [\cos((\omega + \omega_1)t + \varphi) + \cos((\omega - \omega_1)t + \varphi)]}_{\text{faulty part}} \end{aligned}$$

The "healthy part" of the instantaneous power of one phase can be computed as

$$\begin{aligned} p_0(t) &= v(t) i_0(t) = V_m \cos(\omega t) I_{m0} \cos(\omega t + \varphi) \\ &= \frac{V_m I_m}{2} \left(\underbrace{\cos(\varphi)}_{\text{dc component}} + \underbrace{\cos(2\omega t - \varphi)}_{2f \text{ component}} \right) \end{aligned}$$

and the faulty part of this power is expressed as

$$\begin{aligned} p_0(t) &= v(t) \frac{M I_{m0}}{2} [\cos((\omega + \omega_1)t + \varphi) + \cos((\omega - \omega_1)t + \varphi)] \\ &= \frac{V_m M I_{m0}}{2} (\cos(\omega t) \cos((\omega + \omega_1)t + \varphi) + \cos(\omega t) \cos((\omega - \omega_1)t + \varphi)) \\ &= \frac{V_m M I_{m0}}{2} \left[\underbrace{\cos((2\omega + \omega_1)t + \varphi)}_{\text{upper sideband around } 2f} + \cos(\omega_1 t + \varphi) + \underbrace{\cos((2\omega - \omega_1)t + \varphi)}_{\text{lower sideband around } 2f} + \cos(-\omega_1 t + \varphi) \right] \end{aligned}$$

It can be seen from these equations that sidebands appear not only around the $2f$ component but also around the DC component.

Filtering is therefore more effective because it consists in removing a DC offset and applying a low-pass filter to eliminate $2f$ and higher components. This method has been applied in the same condition

as the one of figure 4.5. The DC offset has been removed in the time domain. The results obtained from FE simulations are shown in figure 4.9.

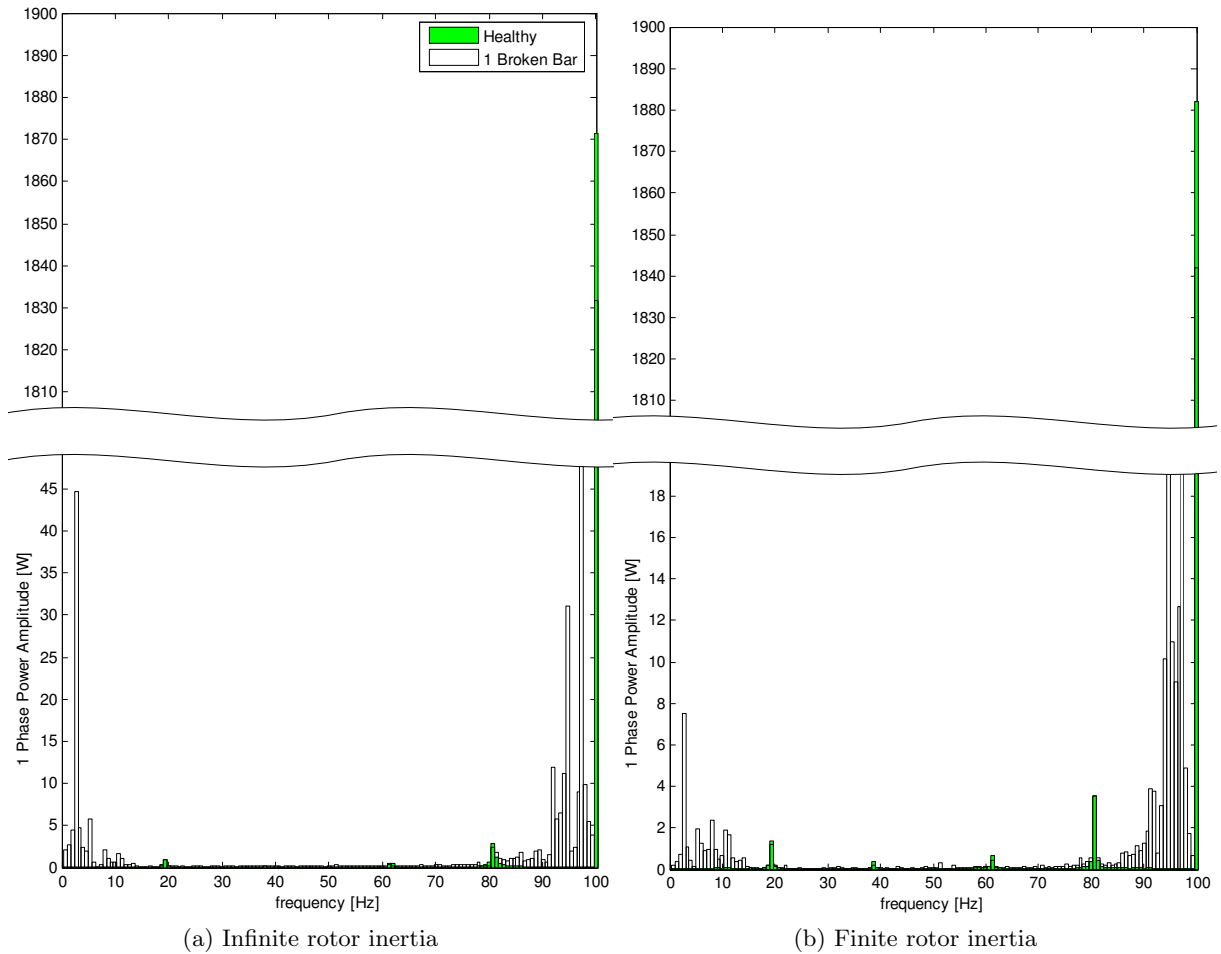


Figure 4.9: Spectrum of the power of phase a for healthy rotor and rotor with 1 broken bar out of 28.

The identification of the low frequency harmonic representing the fault is easier than in the case of MCSA. However, quantification and identification are perturbed when inertia is not infinite due to the interaction of the 2 sidebands of the currents. This can be seen by comparing the amplitude of the sf component for the different inertia of figure 4.9.

4.5.6 Study of airgap Torque Spectral content (TPSA)

Torque Profile Signature Analysis (TPSA) can also be used as sensor to detect faults in induction machines. In [Thomas 03, Hsu 95, Yahoui 96], measured voltages and currents are used for the reconstruction of the airgap torque. The advantage of this method is quite similar to the previous ones. However, the diagnosis is still sensitive to speed oscillations as the model of the machine used to compute the torque does not take into account speed or resistant torque.

4.5.7 Park Vector Approach (PVA)

The graphical representation of the Park current vector ($I_{ds}(t), I_{qs}(t)$) in a fixed reference frame of a healthy machine is well known to be a circle in the space vector plane ($q = f(d)$). If asymmetries arise this circular locus is deformed. However, this technique brings new information by considering the three phases of the machine; the localisation of the fault can be achieved. A fixed reference frame can be used to diagnose stator faults [Cardoso 99]. The locus then becomes elliptic with the major axis of the ellipse oriented with the faulty phase. This is illustrated in figure 4.10. For other types of faults, a pattern recognition technique is proposed in [Houdouin 03]. Patterns are shown in figure 4.10. In the figure illustrating broken bar faults, the perturbation is clearly not fixed with regard to the stator as indicated by the oscillation of the radius. Static and dynamic eccentricities does not much affect the stator line currents as it was explained in section 3.5.1.

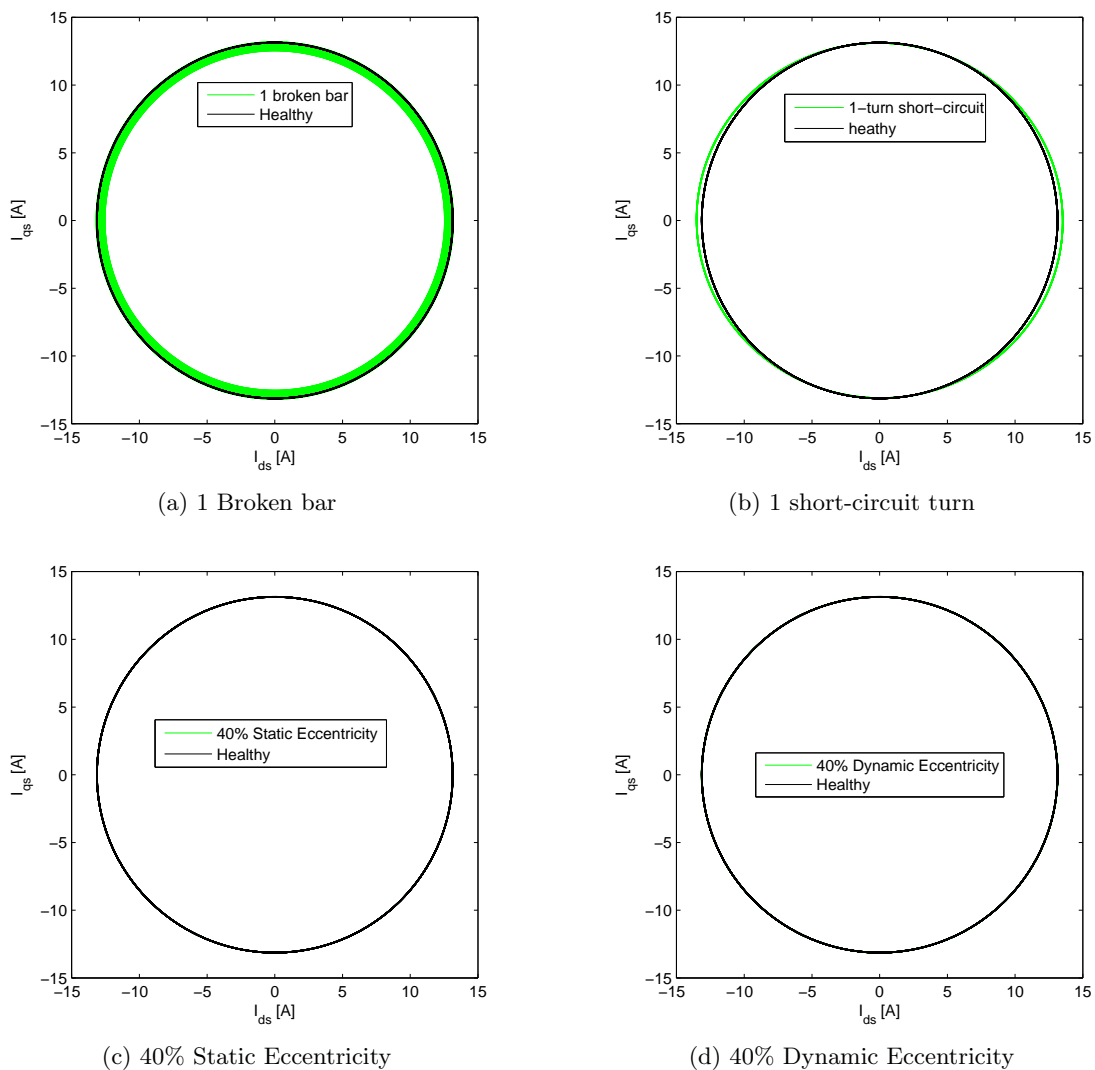


Figure 4.10: Park current vector locus in fixed reference frame for different faults.

Using a similar approach, we propose to use a $d - q$ transformation in a reference frame rotating with the rotor. This allows the detection of rotor related faults as broken bars. The locus is shown in figure 4.11. The deformation is fixed with regard to the rotor.

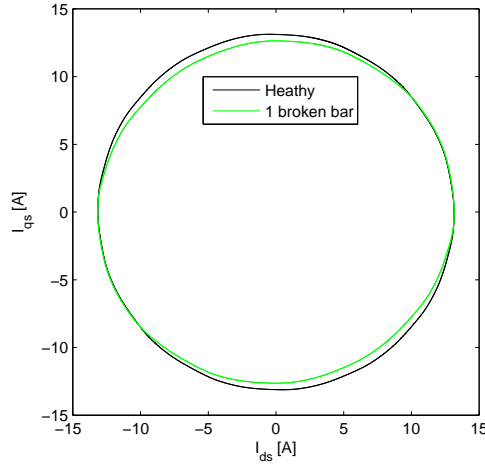


Figure 4.11: Park current vector locus for broken bars in a reference frame rotating with the rotor.

In [Cruz 00], the pattern recognition technique is the FFT of the Park vector modulus. This method is known as extended Park vector approach (EPVA). In a similar way as the torque or power spectral analysis, the healthy value corresponds to a DC offset that can easily be removed. Other authors have preferred to monitor the angular fluctuations of the Park vector (Space Vector Angular Fluctuation: SVAF) instead of its amplitude [Kostic-Perovic 00]. Indeed, if we add to the healthy current a component at a different frequency, we obtain a locus that is being drawn at fluctuating speed. These fluctuations are measured by comparing the monitored signal to a signal at fundamental frequency; the supply voltage is often used. A frequency spectrum of this SVAF is performed and the conclusions are identical as the ones of the EPVA as it is shown in figure 4.12. These methods present the same information as the Park current vector but give a tool for interpreting this information. SVAF is more complicate to implement and provides the same information as the EPVA which is simply the Park vector modulus.

The main drawback of these technique is it sensibility to voltage perturbation, the following methods proposes a solution to lower this sensibility.

4.5.8 Detection by computation of inverse impedance

The presence of asymmetries in faulty machines can also be used as fault indicator. Indeed, in case of fault, negative-sequence currents arise. The main problem is that the negative-sequence component is not only related to the presence of the fault but also to unbalance of the voltage supply.

For this reason, the inverse impedance $Z_i = \frac{V_i}{I_i}$ can be monitored [Sottile 93]. This quantity is only weakly dependent on the operating speed for low slip conditions as this can be understood using the negative-sequence equivalent circuit proposed in [Sottile 93] (figure 4.13). Indeed, figure shows that the impedance $-\left(\frac{1-s}{2-s}\right)R_r$ does not vary much if slip varies while remaining small.

However results have shown that changes in Z_i due to the presence of faults are unpredictable because the formulation does not take into account the interaction between direct and inverse circuits.

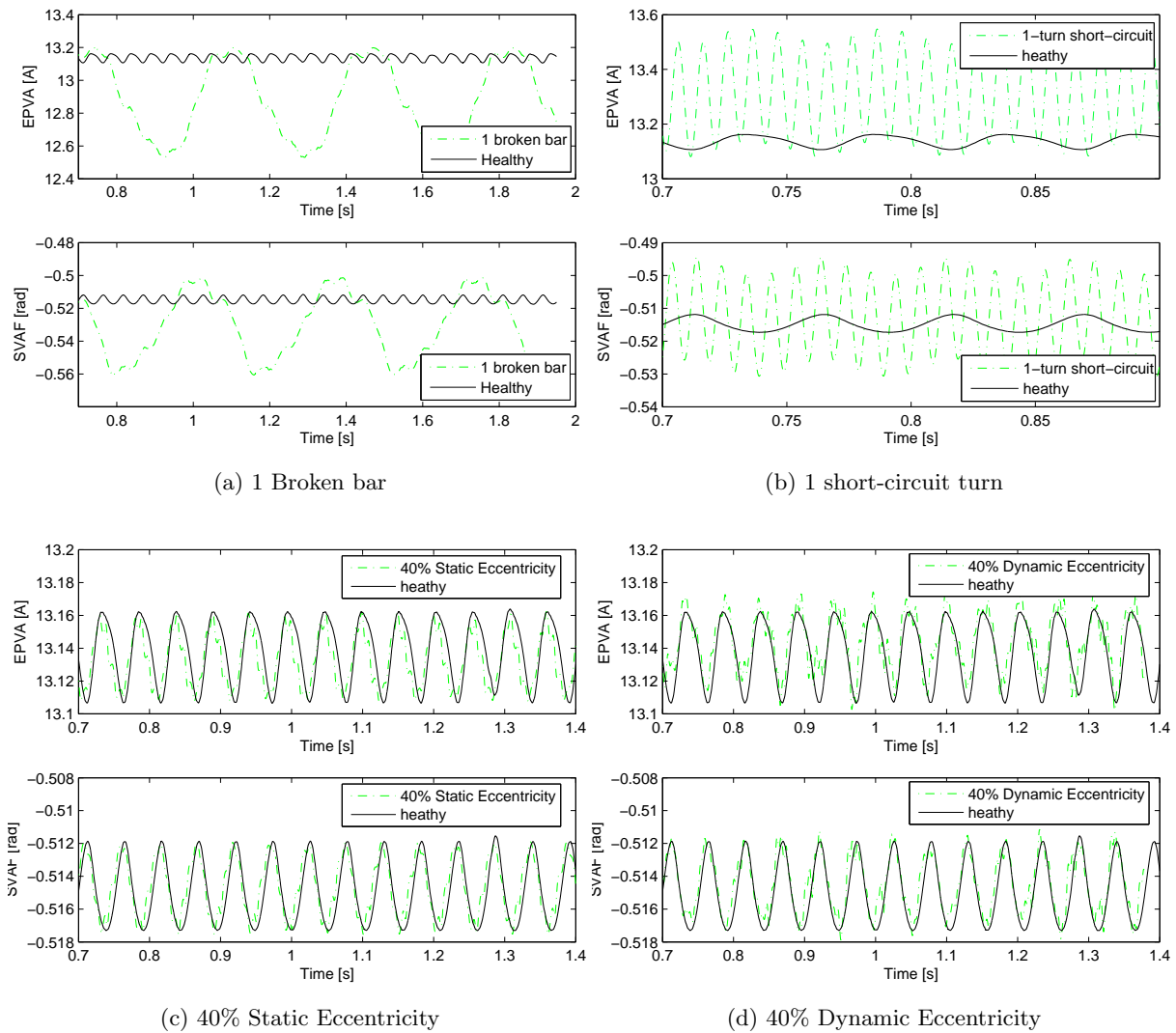


Figure 4.12: SVAF and EPVA for different faults

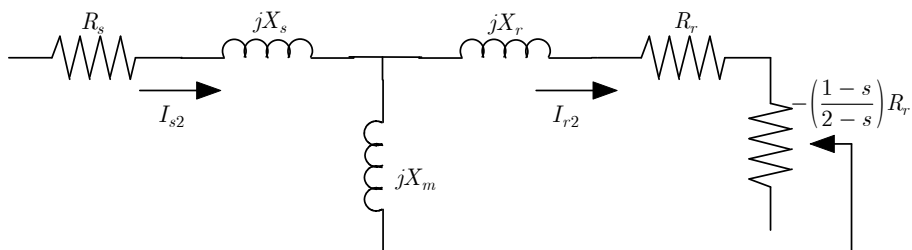


Figure 4.13: Negative sequence equivalent circuit [Sottile 93].

Moreover, this method requires the use of three currents sensors and three voltage sensors which must be precisely calibrated to avoid false alarms. Later on, the same authors have considered representing the previously mentioned interaction [Sottile 00]. The quantity Δ defined by equation 4.2 is then monitored. It is assumed that no homopolar current exists. However this approach requires the creation of a library of Z_{xy} for different operating speeds.

$$\Delta = \begin{pmatrix} V_{d,measured} \\ V_{i,measured} \end{pmatrix} - \begin{pmatrix} Z_{dd} & Z_{di} \\ Z_{id} & Z_{ii} \end{pmatrix} \cdot \begin{pmatrix} I_{d,measured} \\ I_{i,measured} \end{pmatrix} \quad (4.2)$$

This method offers an introduction to the following ones by illustrating how more complex methods could be used to avoid false alarms.

4.5.9 Machine modelling

In the field of machine modelling for condition monitoring, the constant challenge is to find a good compromise between accuracy and computing time.

From a more global point of view, the uses of MCSA or inverse impedance are primitive models of the motor that require few computing resources. This advantage allows their use for on-line monitoring of machine health.

On the opposite side of machine modelling, we find 3D FE simulations which, for example, take into account the presence of saturation, slots and end-winding geometry. However this approach requires a lot of computing time, especially in the case of faulty machines where symmetries used to simplify the models of healthy machines are no more present.

Unfortunately, a clear correlation between the amount of data and computing time required by a model and its precision can be observed.

In the following sections, several models for condition monitoring will be presented. For each of them, the benefits and drawbacks will be outlined. However, much more work has been done on the modelling of faulty machines but the computing time required by these models prohibits (at the present time) their use in fault diagnosis even though some off-line motor health checks could be performed. The part of these models using FE approach was detailed in chapter 3 and the models not suitable for condition monitoring and using circuit modelling will be detailed in chapter 5. One category of models has been set aside in this document. It consists of permeance network models (or magnetic equivalent circuit models). These models allow more precise results than electrical circuit models while requiring less computing time than FE ones. In this work, no place is kept to this approach as its application is replaced by the FE approach. More information can be found in [Hénao 01, Gyselinck 06].

4.5.9.1 Parameter identification of symmetrical model

Many authors propose to perform the diagnostic of the machine by considering the fundamental change in the machine behaviour [Cho 92, Schaeffer 98, Said 00, Raison 00]. They consider that the presence of a broken bar modifies the rotor equivalent resistance and that a short-circuit influences all the machine parameters. The main difficulty is that these changes are small for incipient faults and the variation of temperature should be taken into consideration to avoid false detection [Cho 92, Said 00].

The machine rotating speed is either measured or estimated as it is detailed in [Said 00]. The parameter identification is performed either using a least-square error index [Cho 92, Schaeffer 98] or using extended Kalman filters [Said 00, Raison 00].

4.5.9.2 Parameter Identification of an asymmetrical model

A $d - q$ model of the machine is used in [Tnani 02, Razik 03]. The $d-q$ rotor resistances matrix is then obtained by applying a Park transformation to the rotor matrix of the rotor cage. These resistances are therefore linked to the resistances of the rotor bars. A parametric identification of the $d - q$ resistance ([Razik 03]) or of the bar resistance ([Tnani 02]) is then realised. A detailed study of these models is presented in chapter 5.

For the detection of stator short-circuits, a term representing the influence of the fault can be added to the currents computed by a model of an healthy machine [Schaeffer 99]. This term has the same phase as the supply voltage and an amplitude proportional to the stator frequency. By this the authors increase by one the number of state-variables to allow better match between measurements and model outputs.

4.5.9.3 Current difference from healthy model

The method proposed in [Schoen 97] consists in performing an FFT on the current difference between the measured current and the current computed by a $d - q$ healthy-machine model. As an FFT is performed, this method is only valid in steady-state but has the main advantage to be insensitive to oscillating load torque as this phenomenon is taken into consideration by the healthy model.

Furthermore, the measurement of the rotor speed is not required as the compared current is the d -axis current of a synchronous reference frame aligned with the rotor flux (i.e. $\phi_{qr} = 0$). However the position of this reference frame has to be estimated iteratively which is time-consuming. This estimation is then done for one time instant and the reference frame is considered to rotate at a constant speed ω . Therefore, any fluctuation of the supply frequency could perturb the system.

4.5.9.4 Dynamic Model with Common and Differential mode approach

The model proposed in [Bachir 01] is composed of a classical dynamic model of a healthy machine by means of Park transformation and a differential mode representing the fault.

The broken bar creates a stationary magnetic field with regard to the rotor. This field is identified by an angle θ_0 which allows the localisation of the faulty bar and by η_0 , the percentage of faulty turns in the rotor phase.

The differential mode is then obtained by adding to the three rotor windings a fourth one representing the fault. The model therefore contains three complex equations and three complex current variables: \underline{I}_{dqs} , \underline{I}_{dqr} , \underline{I}_{dqr0} , where \underline{I}_{dqr0} represents the current in the faulty winding. A parametric identification process is realised by minimising the error between the measured currents and the computed ones.

4.5.9.5 Transient model for stator short-circuits

This model, presented in [Tallam 00], considers the influence of a stator short-circuit by adding a fourth winding on the stator of the machine as illustrated in figure 4.14. The rotor is modelled using three windings. The importance of modelling of this current was illustrated in section 3.4.2.

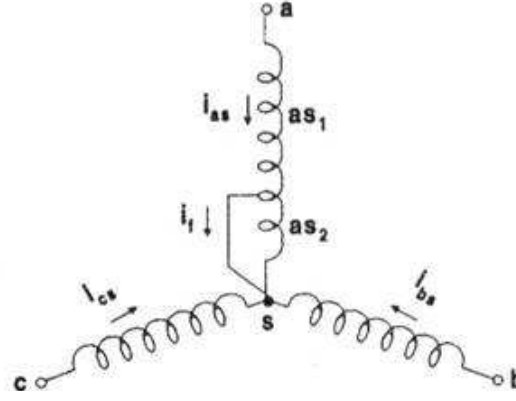


Figure 4.14: Model for stator short circuits [Tallam 00].

The stator current variables are given by

$$I_s = [I_{as}, I_{as} - I_f, I_{bs}, I_{cs}]$$

and the rotor currents are more classically

$$I_r = [I_{ar}, I_{br}, I_{cr}]$$

It is assumed that the leakage reactance of the shorted turns is μL_{ls} where μ is the proportion of shorted turns. However this assumption is not correct due to the fact that the leakage reactance depends on physical location of the fault.

A Park transformation in a stationary reference frame is then applied to the equations of the model. The q axis is aligned with the faulty stator coil so that only one equation needs to be written to represent its behaviour. The mutual inductance matrix is then independent of the rotor position which allows fast computing time.

The model is then used to reconstruct the positive, negative and zero sequence currents which are monitored to detect and quantify the fault.

4.5.9.6 Comparison of torque models (Vienna monitoring method)

This method issued from [Kral 00a] proposes to compare torque obtained from two symmetrical induction machine models: a "voltage model" and a "current model". The computations of the torque t_v using the "voltage model" and of the torque t_c using the "current model" are detailed in figure 4.15. The superscript S shows that the space phasor quantities are evaluated in a reference frame fixed with the stator and the superscript R shows that the space phasor quantities are evaluated in a reference frame fixed with the rotor.

The equation that links the two quantities requires the knowledge of the rotor position γ_m . The quantities r_s , x_r and τ_r are respectively the stator resistance, the rotor reactance and the rotor time constant.

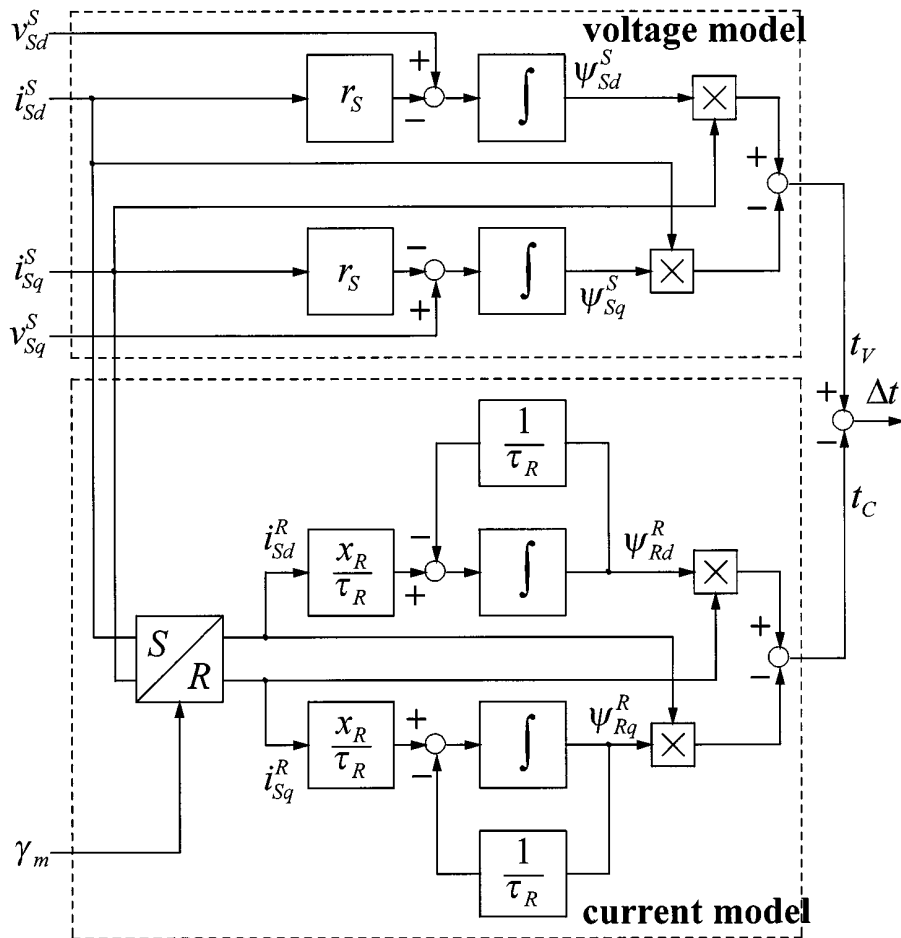


Figure 4.15: Voltage and Current models for the calculation of the rotor fault indicator [Kral 00b]

In the case of a healthy machine, the difference in the torque values t_v and t_c is null. However, in the case of an asymmetrical rotor, the two computed torque values become different. The main advantages of this method are thus its independence of load torque and supply voltage and its small computing time.

4.6 Conclusions

This review offers a clear view of the state of the art in induction machine condition monitoring. It shows current trends and offers a chance to draw a path for further research.

Classical monitoring techniques which are mainly based on non-electric or non-magnetic signals are widely-spread but have the main disadvantage to require specific sensors. Nowadays, the use of adjusted-speed drives or numerical protection devices is expanding and therefore so is the availability of current, voltage and sometimes speed sensors. New monitoring techniques use the signals given by these sensors to perform the diagnosis.

In this field, it can be said that FFT of measured signals can be effectively used to realise the fault detection of a sinusoidally-fed induction machine with constant torque. Nevertheless, oscillation of the main supply frequency is critical and either the sampling frequency should be adapted or demodulation techniques based on the measurement of the stator voltages and on space vector or power monitoring should be used. In all other conditions such as transient situations, presence of oscillating torque or presence of harmonics in supply voltages, the discrepancy between measurement and faulty models give good results even when the model of the healthy machine is basic.

More advanced models can be used to quantify the fault as this information is of major concern. Indeed, imperfections are always present in healthy machines and an objective threshold is difficult to set. It often requires performing tests on faulty machines but this greatly limits the practical use of such methods in industry.

The main drawbacks of models are their computing time, the number of measurement they require as well as the amount information on the machine they need. Indeed some models are built on parameters that need to be determining through extensive testing which complicates the commissioning.

Furthermore, few models offer a complete machine health monitoring as they focus on particular faults.

In this work, we will focus on fault detection and quantification by comparison of the outputs of a model with measurements. Several models will then be presented and studied in the next chapter and fault detection methods will be proposed in chapter 7.

Chapter 5

Machine modelling using magnetically coupled electrical circuits

5.1 Introduction

In the field of electrical drives, diverse applications require different models of the machine that need to be well selected. As example one can think of

- Models for control drives (Vector or Direct Torque Control algorithms),
- Off-line models for research or gauging of applications,
- And finally models for drive condition monitoring.

Furthermore, in order to obtain an adequate model, several issues are important;

- The model structure; this matter will be discussed in the present section;
- The parameter identification; this point will covered in chapter 6.

In this chapter, several circuit models of healthy and faulty machines are presented¹. In order to compare the different models they will be derived from the same machine description but the system of equations to solve will be obtained using different additional hypotheses. As it will be demonstrated in the following, the additional hypotheses only affect the faulty machine behaviour.

The introduction will detail the common mathematical description of the machine then each model will be presented and compared to others in terms of phenomena representation and computing time under Matlab using ODE solver. The practical identification of the parameters of the models will be discussed in chapter 6.

A quite common magnetically coupled electrical circuits approach can be written using the following assumptions [Toliyat 95, Krause 02, Fiser 97, Casimir 03]:

¹It is to be recalled that FE models were presented in chapter 3 and some existing models for condition monitoring were presented in chapter 4.

- Sinusoidally distributed stator windings;
- Permeability of the stator and rotor core considered infinite when compared to the permeability of the airgap;
- Neglected saturation;
- Uniform airgap;
- Negligible interbar currents;
- Evenly distributed rotor bars;
- Stator windings of the different pole pairs connected in series;
- Negligible flux coupling between the different windings without airgap crossing.

Using the hypothesis on the sinusoidal distribution of stator windings, the *turn functions*² of these windings can be written as:

$$\begin{aligned} N_a(\theta) &= \frac{N_s}{2P} \cos(P\theta) \\ N_b(\theta) &= \frac{N_s}{2P} \cos\left(P\theta - \frac{2\pi}{3}\right) \\ N_c(\theta) &= \frac{N_s}{2P} \cos\left(P\theta + \frac{2\pi}{3}\right) \end{aligned}$$

where $N_a(\theta)$ is the turn function of phase a . N_s is linked to the total number of turns per phase and per pole-pair number of the sinusoidally distributed winding having the same fundamental component as the actual winding distribution by

$$N_s = \frac{4}{\pi} N K_d K_p K_s \quad (5.1)$$

where $N = P N_{tsp} N_{spp}$ is the total number of turns for the windings of phase a , K_d is the distribution factor, K_p is the pitch factor and K_s is the skew factor [Poncelet 99, Schmitz 65]. N_{tsp} is the number of turns per slot per phase and N_{spp} is the number of slot per pole per phase. These parameters are expressed as

$$\begin{aligned} K_d &= \frac{\sin\left(\frac{i N_{spp} P \epsilon_m}{2}\right)}{N_{spp} \sin\left(\frac{i P \epsilon_m}{2}\right)} \\ K_p &= \cos\left(i P \delta_m\right) \\ K_s &= \frac{\sin\left(\frac{i P \rho_m}{2}\right)}{\frac{i P \rho_m}{2}} \end{aligned}$$

where i is the considered spatial harmonic number, N_{spp} is the number of slots holding the winding of one pole, ϵ_m is the mechanical angle between adjacent slots, δ_m is the mechanical angular difference between the beginning and the end of the slot (in the axial direction), this is related to the skewing of the slot and ρ_m is the mechanical angle reduction between the actual turns and a diametral turn.

Numerical Details:

If we recall the details of motor IND1 presented in chapter 3, the number of stator slots was $N_{ss} = 36$,

²The turn function of a winding is the number of turns of this windings enclosed by a path determined by a segment crossing the airgap at angular position 0, another crossing the airgap at position θ and two circular segments concentric with the airgap and situated respectively in the stator core and in the rotor core such as to enclose stator and rotor windings.

the number of turns per slot and per phase was $N_{t_{sp}} = 44$ and the number of slots per pole per phase was $N_{spp} = 3$.

With this information the turn function of the stator phase a can be drawn. It is shown with the square markers in figure 5.1a. As it is shown in figure 5.1b, the order to the main harmonic is 2 because the machine has 2 pole pairs. Other frequency components can be seen.

As the windings are made of diagonal turns and slots are parallel to the axis, K_p and K_s are equal to 1. If we consider the fundamental component of this 2 pole-pairs machine ($i = 1$ in equation 5.1) the distribution factor is equal to $K_s = 0.9598$ ($\epsilon_m = \frac{2\pi}{N_{ss}}$).

Therefore, $N_s = 322.62$ and the equivalent sinusoidal distribution of stator windings is shown in figure 5.1a.

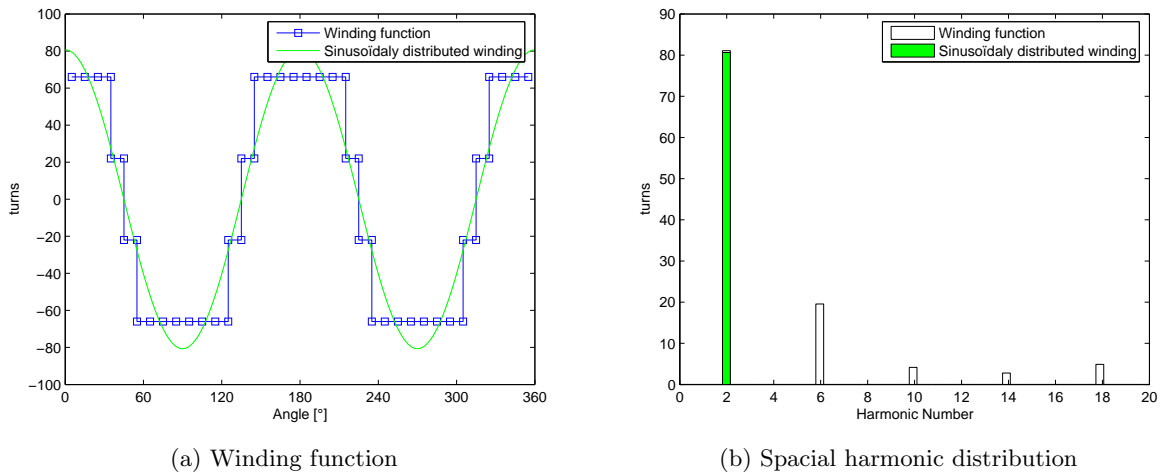


Figure 5.1: Windings function of phase a for motor *IND1*

Using the winding function approach [Al-Nuaim 98], one can define the mutual coupling between the stator circuits of phases a and b by

$$\begin{aligned}
 L_{ab} &= \int_0^{2\pi} N_a(\theta) N_b(\theta) \frac{\mu_0 l r}{g} d\theta \\
 &= -\frac{1}{2} \left(\frac{N_s}{2P} \right)^2 \pi \frac{\mu_0 l r}{g} \\
 &= -\frac{L_{ms}}{2}
 \end{aligned} \tag{5.2}$$

Likewise, the self coupling of phase a of which flux lines cross the airgap is given by

$$\begin{aligned}
 L_{aa} &= \int_0^{2\pi} N_a^2(\theta) \frac{\mu_0 l r}{g} d\theta \\
 &= \left(\frac{N_s}{2P} \right)^2 \pi \frac{\mu_0 l r}{g}
 \end{aligned} \tag{5.3}$$

Similarly, for the other couplings between the stator windings, we have

$$\begin{bmatrix} \Psi_{ass} \\ \Psi_{bss} \\ \Psi_{css} \end{bmatrix} = \begin{bmatrix} L_{ls} + L_{ms} & -\frac{L_{ms}}{2} & -\frac{L_{ms}}{2} \\ -\frac{L_{ms}}{2} & L_{ls} + L_{ms} & -\frac{L_{ms}}{2} \\ -\frac{L_{ms}}{2} & -\frac{L_{ms}}{2} & L_{ls} + L_{ms} \end{bmatrix} \begin{bmatrix} I_{as} \\ I_{bs} \\ I_{cs} \end{bmatrix} \quad (5.4)$$

where L_{ls} is the leakage inductance of the stator winding, Ψ_{iss} is the flux created by the three stator currents and linked by the winding i and $L_{ms} = \left(\frac{N_s}{2P}\right)^2 \pi \frac{\mu_0 l r}{g}$.

The rotor currents of the squirrel cage are defined as $(I_{r1}, I_{r2}, \dots, I_{rn})$ and I_e is the current of loop created by one of the end-ring as shown in figure 5.2. The rotor circuit is represented in figure 5.3. The turn function for each rotor loop i is given by

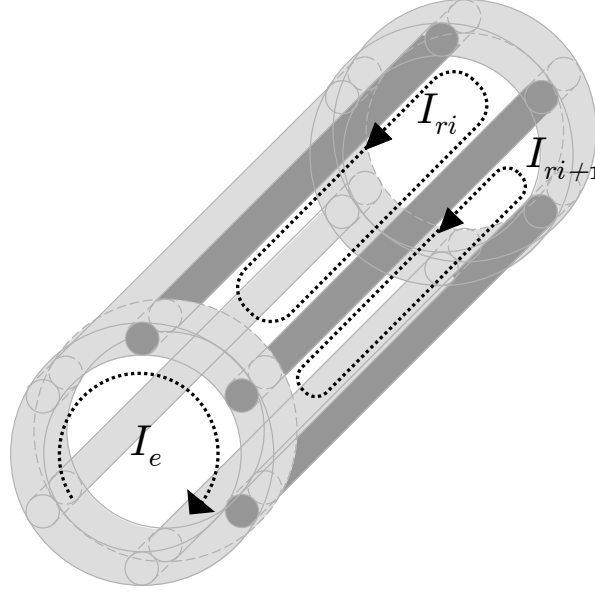


Figure 5.2: Rotor cage and rotor loop currents.

$$N_i(\theta) = \begin{cases} -\frac{\alpha_r}{2\pi} & 0 < \theta < \theta_i \\ 1 - \frac{\alpha_r}{2\pi} & \theta_i < \theta < \theta_{i+1} \\ -\frac{\alpha_r}{2\pi} & \theta_{i+1} < \theta < 2\pi \end{cases} \quad (5.5)$$

where $\alpha_r = \frac{2\pi}{n}$, $\theta_i = \theta_r + (i-1)\alpha_r$ is the position of bar i and θ_r is the rotor position with regard to the stator as defined by

$$\theta_r(t) = \theta_0 + \omega_r(t - t_0) \quad (5.6)$$

where θ_0 is the position of the first rotor bar with reference to the position of the fundamental MMF of phase a of the first pole pair at instant $t = t_0$.

Using the turn functions of stator and rotor circuits, the mutual inductances between stator winding a and rotor loop i becomes

$$L_{ai} = \frac{\mu_0 l r}{g} \int_0^{2\pi} N_a(\theta) N_i(\theta) d\theta$$

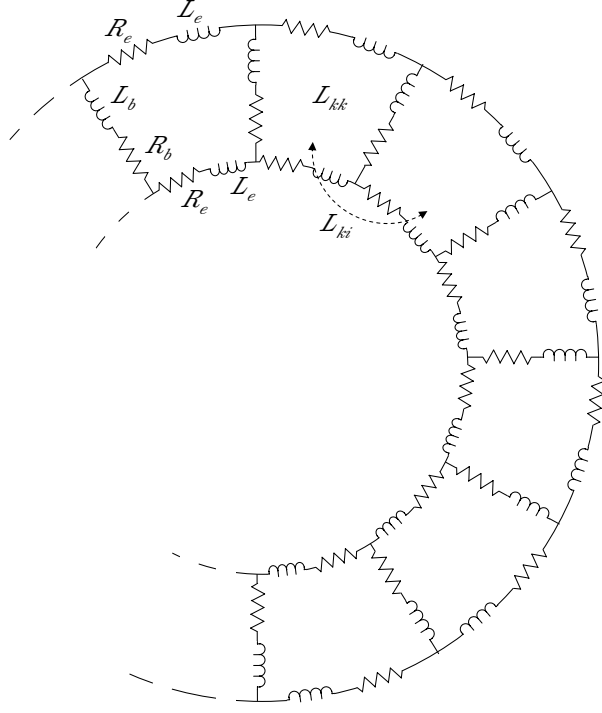


Figure 5.3: Rotor Circuit.

$$\begin{aligned}
L_{ai} &= \frac{\mu_0 l r}{g} \frac{N_s}{2P} \left(\int_0^{\theta_i} -\frac{\alpha_r}{2\pi} \cos(P\theta) d\theta + \int_{\theta_i}^{\theta_{i+1}} \left(1 - \frac{\alpha_r}{2\pi}\right) \cos(P\theta) d\theta + \int_{\theta_{i+1}}^{2\pi} -\frac{\alpha_r}{2\pi} \cos(P\theta) d\theta \right) \\
&= \frac{\mu_0 l r}{g} \frac{N_s}{2P} \frac{1}{P} (\sin(P\theta_i) \cos(P\alpha_r) + \sin(P\alpha_r) \cos(P\theta_i) - \sin(P\theta_i)) \\
&= \frac{\mu_0 l r}{g} \frac{N_s}{2P} \frac{1}{P} (\sin(P\alpha_r) \cos(P\theta_i) - (1 - \cos(P\alpha_r)) \sin(P\theta_i)) \\
&= \frac{\mu_0 l r}{g} \frac{N_s}{2P} \frac{1}{P} \left(\underbrace{\sin(P\alpha_r) \cos(P\theta_r + (i-1)P\alpha_r) + \cos(P\alpha_r) \sin(P\theta_r + (i-1)P\alpha_r)}_{\sin(P\theta_r + (i-1)P\alpha_r + P\alpha_r)} - \sin(P\theta_r + (i-1)P\alpha_r) \right) \\
&= \frac{4}{\pi N_s} L_{ms} \frac{1}{2} \left(\sin \left(\underbrace{P\theta_r + (i-1)P\alpha_r + \frac{P\alpha_r}{2}}_A + \underbrace{\frac{P\alpha_r}{2}}_B \right) - \sin \left(\underbrace{P\theta_r + (i-1)P\alpha_r + \frac{P\alpha_r}{2}}_A - \underbrace{\frac{P\alpha_r}{2}}_B \right) \right)
\end{aligned}$$

Using Simpson's formula $\frac{1}{2} (\sin(A+B) - \sin(A-B)) = \cos(A) \sin(B)$ we find

$$\begin{aligned}
L_{ai} &= \frac{4}{\pi N_s} L_{ms} \cos(P(\theta_r + (i-1)\alpha_r + \delta)) \sin(P\delta) \\
&= L_m \cos(P(\theta_r + (i-1)\alpha_r + \delta))
\end{aligned} \tag{5.7}$$

where $\delta = \frac{\alpha_r}{2}$ and $L_m = \frac{4 \sin(P\delta)}{\pi N_s} L_{ms}$. Analogously, for the other stator phases we have

$$\begin{aligned}
L_{bi} &= L_m \cos \left(P(\theta_r + (i-1)\alpha_r + \delta) - \frac{2\pi}{3} \right) \\
L_{ci} &= L_m \cos \left(P(\theta_r + (i-1)\alpha_r + \delta) + \frac{2\pi}{3} \right)
\end{aligned} \tag{5.8}$$

Finally, the mutual inductances between the rotor windings can be computed by

$$\begin{aligned}
L_{kk} &= \frac{\mu_0 l r}{g} \int_0^{2\pi} N_k^2(\theta) d\theta \\
&= \frac{\mu_0 l r}{g} \left(\int_0^{\theta_k} \left(\frac{\alpha_r}{2\pi}\right)^2 d\theta + \int_{\theta_k}^{\theta_{k+1}} \left(1 - \frac{\alpha_r}{2\pi}\right)^2 d\theta + \int_{\theta_{k+1}}^{2\pi} \left(\frac{\alpha_r}{2\pi}\right)^2 d\theta \right) \\
&= \frac{\mu_0 l r}{g} \left(\int_0^{2p\pi} \left(\frac{\alpha_r}{2\pi}\right)^2 d\theta + \int_{\theta_k}^{\theta_k+\alpha_r} d\theta - \int_{\theta_k}^{\theta_k+\alpha_r} 2\frac{\alpha_r}{2\pi} d\theta \right) \\
&= \frac{\mu_0 l r}{g} \left(2\pi \left(\frac{\alpha_r}{2\pi}\right)^2 + \alpha_r - 2\alpha_r \frac{\alpha_r}{2\pi} \right) \\
&= \frac{\mu_0 l r}{g} \alpha_r \left(1 - \frac{\alpha_r}{2\pi} \right)
\end{aligned}$$

and if $k \neq i$,

$$\begin{aligned}
L_{ki} &= \frac{\mu_0 l r}{g} \int_0^{2\pi} N_k(\theta) N_i(\theta) d\theta \\
&= \frac{\mu_0 l r}{g} \left(\int_0^{\theta_k} \left(\frac{\alpha_r}{2\pi}\right)^2 d\theta + \int_{\theta_k}^{\theta_k+\alpha_r} \left(1 - \frac{\alpha_r}{2\pi}\right) \left(-\frac{\alpha_r}{2\pi}\right) d\theta \right. \\
&\quad \left. + \int_{\theta_k+\alpha_r}^{\theta_i} \left(\frac{\alpha_r}{2\pi}\right)^2 d\theta + \int_{\theta_i}^{\theta_i+\alpha_r} \left(1 - \frac{\alpha_r}{2\pi}\right) \left(-\frac{\alpha_r}{2\pi}\right) d\theta + \int_{\theta_i+\alpha_r}^{2\pi} \left(\frac{\alpha_r}{2\pi}\right)^2 d\theta \right) \\
&= \frac{\mu_0 l r}{g} \left(-\frac{\alpha_r^2}{2\pi} \right)
\end{aligned}$$

The stator circuit equations can be written straightforwardly and for each rotor loop k , one can write

$$0 = 2 (R_b + R_e) I_{rk} - R_b I_{r(k-1)} - R_b I_{r(k+1)} - R_e I_e + p\psi_{rk}$$

Note that if there is no axial flux, and if the end-rings of the rotor cage are composed of n identical segments, this current is equal to 0.

The system of equations that describes the machine can be written as

$$\begin{cases} \bar{V}_s = R_{ss} \bar{I}_s + \frac{d\Psi_s}{dt} \\ = R_{ss} \bar{I}_s + L_{ss} \frac{d\bar{I}_s}{dt} + P \Omega_r \frac{dL_{sr}}{d\theta_r} \bar{I}_r + L_{sr} \frac{d\bar{I}_r}{dt} \\ \bar{0} = R_{rr} \bar{I}_r + \frac{d\psi_r}{dt} \\ = R_{rr} \bar{I}_r + L_{rr} \frac{d\bar{I}_r}{dt} + P \Omega_r \frac{dL_{sr}^t}{d\theta_r} \bar{I}_s + L_{sr}^t \frac{d\bar{I}_s}{dt} \end{cases} \quad (5.9)$$

$$\text{with } \bar{V}_s = \begin{bmatrix} V_{as} \\ V_{bs} \\ V_{cs} \end{bmatrix}, \bar{I}_s = \begin{bmatrix} I_{as} \\ I_{bs} \\ I_{cs} \end{bmatrix} \text{ and } \bar{I}_r = \begin{bmatrix} I_{r1} \\ \vdots \\ I_{rn} \\ I_e \end{bmatrix}$$

and with

$$L_{ss} = \begin{bmatrix} L_{ls} + L_{ms} & -\frac{L_{ms}}{2} & -\frac{L_{ms}}{2} \\ -\frac{L_{ms}}{2} & L_{ls} + L_{ms} & -\frac{L_{ms}}{2} \\ -\frac{L_{ms}}{2} & -\frac{L_{ms}}{2} & L_{ls} + L_{ms} \end{bmatrix}$$

$$R_{ss} = \begin{bmatrix} R_s & 0 & 0 \\ 0 & R_s & 0 \\ 0 & 0 & R_s \end{bmatrix}$$

$$L_{sr} = \begin{bmatrix} L_{a1} & \cdots & L_{an} & L_{ae} \\ L_{b1} & \cdots & L_{bn} & L_{be} \\ L_{c1} & \cdots & L_{cn} & L_{ce} \end{bmatrix}$$

$$R_{rr} = \begin{bmatrix} R_0 & -R_b & 0 & \cdots & -R_b & -R_e \\ \vdots & \vdots & \vdots & \vdots & \vdots & \vdots \\ -R_b & 0 & \cdots & \cdots & R_0 & -R_e \\ -R_e & -L_e & \cdots & \cdots & -R_e & n R_e \end{bmatrix}$$

$$L_{rr} = \begin{bmatrix} L_{kk} + L_0 & L_{ki} - L_b & L_{ki} & \cdots & L_{ki} - L_b & -L_e \\ \vdots & \vdots & \vdots & \vdots & \vdots & \vdots \\ L_{ki} - L_b & L_{ki} & \cdots & \cdots & L_{kk} + L_0 & -L_e \\ -L_e & -L_e & \cdots & \cdots & -L_e & n L_e \end{bmatrix}$$

where $R_0 = 2(R_b + R_e)$ and $L_0 = 2(L_b + L_e)$.

For the applications we are considering in this work, i.e. machine monitoring, the mechanical coupling does not need to be modelled. This implies that the inputs of the models consist of the stator voltages and the rotor speed versus time instead of the load torque. The outputs of the models are identical to its state variables representing the stator and rotor currents.

For completeness of the presentation of the proposed approach, the torque expression is given in appendix A.1.

5.2 Circuit model of healthy machine

A circuit model of a healthy machine has been proposed in [White 59, Muñoz 99]. This is a variation of a classical Park model that allows the computation of every rotor bar current and not only the currents of a three-phase equivalent rotor circuit. The reasons for using this model are mainly the clear link between the geometrical dimensions and material characteristics of the machine and the parameters of the model as well as its capacity to reconstruct the rotor bar currents. This last point will be of interest for the creation of the superimposed model for broken bars presented in section 5.3.3.

5.2.1 Implementation

A space vector transformation of the stator voltage is classically given by equation 5.10.

$$\underline{V}_s = \frac{2}{3} (V_{as} + \underline{\alpha} V_{bs} + \underline{\alpha}^2 V_{cs}) \quad \text{where } \underline{\alpha} = e^{j\frac{2\pi}{3}} \quad (5.10)$$

The space vector transformation of the rotor cage currents $[I_{r1}, I_{r2}, \dots, I_{rn}]$ is given by equation 5.11

$$\underline{I}_r = \frac{2}{n} \begin{bmatrix} 1 & \underline{\beta} & \cdots & \underline{\beta}^{n-1} \end{bmatrix} \begin{bmatrix} I_{r1} \\ \vdots \\ I_{rn} \end{bmatrix} \quad \text{where } \underline{\beta} = e^{j\frac{2\pi}{n}} \quad (5.11)$$

By applying these transformations to the equations of the machine presented in section 5.1, we obtain the system of complex equations 5.12. The details of this development are proposed in appendix A.2.

$$\begin{cases} \underline{V}_s &= R_s \underline{I}_s + L_s p \underline{I}_s + \frac{n}{2} L_m e^{jP\theta_r + \delta} (p + jP\Omega_r) \underline{I}_r \\ \underline{0} &= R_r \underline{I}_r + L_r p \underline{I}_r + \frac{3}{2} L_m e^{jP\theta_r + \delta} (p - jP\Omega_r) \underline{I}_s \end{cases} \quad (5.12)$$

$$\text{where } \begin{cases} R_s &= \text{stator resistance} \\ L_s &= \text{total stator inductance} \\ &= L_{ls} + \frac{3}{2} L_{ms} \\ L_m &= \text{mutual inductance} \\ R_r &= \text{rotor resistance} \\ &= 2R_e + 2R_b (1 - \cos(P\alpha_r)) \\ L_r &= \text{total rotor inductance} \\ &= 2L_e + 2L_b (1 - \cos(P\alpha_r)) + \frac{\mu_0 l_r}{g} \alpha_r \end{cases}$$

The above equations (5.12) can then be projected on a reference frame that we can choose, for example³, to be rotating at supply pulsation (ω). The projection is given by equations

$$\begin{aligned} \underline{V}_{dqs} &= e^{-j\omega t} \underline{V}_s \\ \underline{V}_{dqr} &= \sqrt{\frac{3}{n}} e^{-j(P(\theta_r + \delta) - \omega t)} \underline{V}_r \quad \text{where } \underline{V}_{dq} = V_d + jV_q \end{aligned} \quad (5.13)$$

If we apply the projection to equations 5.12 we obtain for the stator equation

$$\begin{aligned} \underline{V}_s &= R_s \underline{I}_s + L_s p \underline{I}_s + \frac{n}{2} L_m e^{jP(\theta_r + \delta)} (p + jP\Omega_r) \underline{I}_r \\ &= R_s \frac{3}{2} e^{j(\theta)} \underline{I}_{dqs} + L_s p \frac{3}{2} e^{j(\theta)} \underline{I}_{dqs} + \frac{n}{2} L_m e^{jP(\theta_r + \delta)} (p + jP\Omega_r) \frac{3}{2} \sqrt{\frac{3}{n}} e^{j(\theta - (\theta_r + \delta)P)} \underline{I}_{dqr} \\ &= \frac{3}{2} e^{j(\theta)} R_s \underline{I}_{dqs} + \frac{3}{2} e^{j(\theta)} L_s p (\underline{I}_{dqs}) + \frac{3}{2} e^{j(\theta)} \underbrace{j\omega}_{p(e^{j(\theta)})} L_s \underline{I}_{dqs} \\ &\quad + \frac{3}{2} e^{j(\theta)} \frac{n}{2} \sqrt{\frac{3}{n}} L_m jP\Omega_r \underline{I}_{dqr} + \frac{3}{2} e^{j(\theta)} \frac{n}{2} \sqrt{\frac{3}{n}} L_m p (\underline{I}_{dqr}) + \frac{3}{2} e^{j(\theta)} \frac{n}{2} \sqrt{\frac{3}{n}} L_m \underbrace{j(\omega - P\Omega_r)}_{p(e^{j(\theta - (\theta_r + \delta)P)})} \underline{I}_{dqr} \\ &= \frac{3}{2} e^{j(\theta)} \left(R_s \underline{I}_{dqs} + L_s p (\underline{I}_{dqs}) + j\omega L_s \underline{I}_{dqs} + \frac{n}{2} \sqrt{\frac{3}{n}} L_m p (\underline{I}_{dqr}) + j\omega \frac{n}{2} \sqrt{\frac{3}{n}} L_m \underline{I}_{dqr} \right) \end{aligned}$$

Then we have

$$\underline{V}_{dqs} = R_s \underline{I}_{dqs} + L_s p (\underline{I}_{dqs}) + \frac{3}{2} \sqrt{\frac{n}{3}} L_m p (\underline{I}_{dqr}) + j\omega \left(L_s \underline{I}_{dqs} + \frac{3}{2} \sqrt{\frac{n}{3}} L_m \underline{I}_{dqr} \right)$$

In a similar way, the rotor equation becomes

$$\begin{aligned} 0 &= R_r \underline{I}_r + L_r p \underline{I}_r + \frac{3}{2} L_m e^{-jP(\theta_r + \delta)} (p - jP\Omega_r) \underline{I}_s \\ &= \frac{3}{2} \sqrt{\frac{3}{n}} e^{j(\theta - P(\theta_r + \delta))} \\ &\quad \cdot (R_r \underline{I}_{dqr} + L_r p (\underline{I}_{dqr}) + \frac{3}{2} \sqrt{\frac{n}{3}} L_m p (\underline{I}_{dqs}) + j(\omega - P\Omega_r) (L_r \underline{I}_{dqr} + \frac{3}{2} \sqrt{\frac{n}{3}} L_m \underline{I}_{dqs})) \end{aligned}$$

Then we have

³The speed of the reference frame is chosen to obtain DC d and q components in steady-state.

$$0 = R_r \underline{I}_{dqr} + L_r p(\underline{I}_{dqr}) + \frac{3}{2} \sqrt{\frac{n}{3}} L_m p(\underline{I}_{dqs}) + j(\omega - P\Omega_r) \left(L_r \underline{I}_{dqr} + \frac{3}{2} \sqrt{\frac{n}{3}} L_m \underline{I}_{dqs} \right)$$

For the torque we have

$$\begin{aligned} Tem &= -\frac{n}{2} \frac{3}{2} P L_m Im \left(\underline{I}_{dqs}^* e^{-j(\theta)} \sqrt{\frac{3}{n}} \underline{I}_{dqr} e^{j(\theta - P(\theta_r + \delta))} e^{jP(\theta_r + \delta)} \right) \\ &= -\frac{\sqrt{3n}}{2} \frac{3}{2} P L_m Im \left(\underline{I}_{dqs}^* \underline{I}_{dqr} \right) \end{aligned}$$

By distinguishing real from the imaginary parts, the previous equations lead to

$$\frac{d}{dt} \begin{bmatrix} I_{ds} \\ I_{qs} \\ I_{dr} \\ I_{qr} \end{bmatrix} = \frac{1}{L} \left(\begin{bmatrix} V_{ds} \\ V_{qs} \\ 0 \\ 0 \end{bmatrix} - (R + L_\omega) \begin{bmatrix} I_{ds} \\ I_{qs} \\ I_{dr} \\ I_{qr} \end{bmatrix} \right) \quad (5.14)$$

with

$$L = \begin{bmatrix} L_s & 0 & \frac{\sqrt{3n}}{2} L_m & 0 \\ 0 & L_s & 0 & \frac{\sqrt{3n}}{2} L_m \\ \frac{\sqrt{3n}}{2} L_m & 0 & L_r & 0 \\ 0 & \frac{\sqrt{3n}}{2} L_m & 0 & L_r \end{bmatrix}$$

$$R = \begin{bmatrix} R_s & 0 & 0 & 0 \\ 0 & R_s & 0 & 0 \\ 0 & 0 & R_r & 0 \\ 0 & 0 & 0 & R_r \end{bmatrix}$$

$$L_\omega = \begin{bmatrix} 0 & -\omega L_s & 0 & -\omega \frac{\sqrt{3n}}{2} L_m \\ \omega L_s & 0 & \omega \frac{\sqrt{3n}}{2} L_m & 0 \\ 0 & (P\Omega_r - \omega) \frac{\sqrt{3n}}{2} L_m & 0 & (P\Omega_r - \omega) L_r \\ (\omega - P\Omega_r) \frac{\sqrt{3n}}{2} L_m & 0 & (\omega - P\Omega_r) L_r & 0 \end{bmatrix}$$

After solving this system, an inverse transformation is applied to stator and rotor d and q currents to reconstruct the stator phase currents and rotor loop currents.

$$\begin{cases} \underline{I}_s = \underline{I}_{dqs} e^{j\omega t} \\ I_{is} = \text{real}(\underline{\alpha}^{-(i-1)} \underline{I}_s) \end{cases} \quad \text{where } i = a, b, c \quad (5.15)$$

and

$$\begin{cases} \underline{I}_r = \underline{I}_{dqr} e^{j(\omega - P\Omega_r)t} \\ I_{ir} = \text{real}(\underline{\beta}^{-(i-1)} \underline{I}_r) \end{cases} \quad \text{where } i = 1, 2, \dots, n \quad (5.16)$$

5.2.2 Numerical Implementation

Note that, for clarity of explanations, this model will be referred to as "*ModelHealthy*" in the rest of this document.

In steady-state situations, the state variables I_{ds} , I_{qs} , I_{dr} and I_{qr} are constant functions of the time. This is an important advantage for numerical integration of the system of equations. The time step can be taken large which lowers the computing time. This is quite important when using the model for on-line monitoring.

Many numerical implementations can be realised but we will detail here the application in which the model will be used for practical fault detection later in this work:

- The inputs of the model (i.e. Stator voltages and rotor speed) are supposed to be sampled at a frequency of 2kHz which corresponds to a tenth of the frequency of computation used for the time-domain FE simulations and which is bigger than twice the highest harmonic present in the FE stator currents.
- The evaluation of these inputs at a determined time will be done by searching for the value corresponding to the nearest time sample available. Another solution which consists in an interpolation between the available inputs to obtain the value at the correct instant does not improve accuracy and is time consuming.
- The Matlab solver for ordinary differential equations *ODE113* seems to give the best compromise between accuracy and computing time. It consists in a variable order Adams-Bashforth-Moulton multistep solver with variable time step. The step is adapted to ensure a relative error of 10^{-3} on the solution set.
- For the simulation of steady-state behaviour, initial values of the state variables can be computed using equation 5.14, considering that the derivative of the currents is null.

The computing time⁴ is about 1s to represent 2s of steady-state operation with constant parameters. It is important to realise that the given computing time is only here to have an order of magnitude as it is increasing with the variability of the currents and with the length of the time vectors for stator voltages and speed (This length is function of the simulated time).

This information will be used later in this chapter to compare the performances of this model with the following ones.

5.3 Circuit model of a machine with broken bars

5.3.1 Model based on complete rotor cage description

This model is the implementation of the equations proposed in section 5.1. The advantage of this approach is the easy and precise incorporation of rotor bar faults. The main drawback is that rotor-stator mutual inductances and their derivatives are functions of the rotor position and have to be computed at each instant of time.

⁴On a Pentium 4 - 2GHz

This method can easily be generalised to any number of broken bars. However, the presence of resistances of very high values (i.e. $R_{bb} = \infty$) complicates the numerical resolution. For this reason, a complete broken bar will be modelled by $R_{bb} = 10^4 \Omega$.

Incorporation of broken bars: method 2 The other solution is to merge the two loops adjacent to the broken branch. The matrix structure is modified and the inductances of this new loop have to be recomputed. This implementation is presented in [Cunha 05, Toliyat 95].

The resistance and leakage inductance of this extended loop are given by

$$\begin{aligned} R_{0mod} &= 2(R_b + 2R_e) = 2R_0 - 2R_b \\ L_{0mod} &= 2(L_b + 2L_e) \end{aligned}$$

The self and mutual inductances with the other rotor loops are given by

$$\begin{aligned} L_{kkmod} &= \frac{\mu_0 l r}{g} \int_0^{2\pi} N_k^2(\theta) d\theta \\ &= \frac{\mu_0 l r}{g} \left(\int_0^{\theta_k} \left(\frac{2\alpha_r}{2\pi}\right)^2 d\theta + \int_{\theta_k}^{\theta_k + \alpha_r} \left(1 - \frac{2\alpha_r}{2\pi}\right)^2 d\theta + \int_{\theta_k + 2\alpha_r}^{2\pi} \left(\frac{2\alpha_r}{2\pi}\right)^2 d\theta \right) \\ &= \frac{\mu_0 l r}{g} 2\alpha_r \left(1 - \frac{2\alpha_r}{2\pi}\right) \\ L_{kimod} &= \frac{\mu_0 l r}{g} \int_0^{2\pi} N_k(\theta) N_i(\theta) d\theta \\ &= \frac{\mu_0 l r}{g} \left(\int_0^{\theta_k} 2 \left(\frac{\alpha_r}{2\pi}\right)^2 d\theta + \int_{\theta_k}^{\theta_k + \alpha_r} -\frac{2\alpha_r}{2\pi} \left(1 - \frac{\alpha_r}{2\pi}\right) d\theta + \int_{\theta_k + \alpha_r}^{\theta_i} 2 \left(\frac{\alpha_r}{2\pi}\right)^2 d\theta \right. \\ &\quad \left. + \int_{\theta_i}^{\theta_i + 2\alpha_r} -\frac{\alpha_r}{2\pi} \left(1 - \frac{2\alpha_r}{2\pi}\right) d\theta + \int_{\theta_i + 2\alpha_r}^{2\pi} 2 \left(\frac{\alpha_r}{2\pi}\right)^2 d\theta \right) \\ &= \frac{\mu_0 l r}{g} \left(-\frac{4\alpha_r^2}{2\pi}\right) \end{aligned}$$

And the mutual inductance between stator winding a and the rotor loop i becomes

$$\begin{aligned} L_{aimod} &= \frac{\mu_0 l r}{g} \int_0^{2\pi} N_a(\theta) N_i(\theta) d\theta \\ &= \frac{\mu_0 l r}{g} \frac{N_s}{2} \left(\int_0^{\theta_i} -\frac{2\alpha_r}{2\pi} \cos(P\theta) d\theta + \int_{\theta_i}^{\theta_i + 1} 1 - \frac{2\alpha_r}{2\pi} \cos(P\theta) d\theta + \int_{\theta_i + 1}^{2\pi} -\frac{2\alpha_r}{2\pi} \cos(P\theta) d\theta \right) \\ &= \frac{\mu_0 l r}{g} \frac{N_s}{2} \frac{1}{P} (\sin(P(\theta_i + 2\alpha_r)) - \sin(P\theta_i)) \\ &= L_m \cos(P\delta) \cos(P(\theta_r + i\alpha_r)) \end{aligned}$$

and analogously

$$\begin{aligned} L_{bimod} &= L_m \cos(P\delta) \cos\left(P(\theta_r + i\alpha_r) - \frac{2\pi}{3}\right) \\ L_{cimod} &= L_m \cos(P\delta) \cos\left(P(\theta_r + i\alpha_r) + \frac{2\pi}{3}\right) \end{aligned}$$

The advantage of this method is the reduction of the number of equations to solve and its drawback is the reconstruction of the matrix for each rotor fault. Furthermore, partially broken bars cannot be implemented using this method; a mix of the two methods should therefore be implemented. For simplicity, only *method 1* will be used in this work.

5.3.1.2 Numerical Implementation

Note that, for the sake of clarity, this model will be referred as "*ModelFullBB*" in the rest of this document.

The main difficulty in the numerical solving of this model stands in the variation of the inductances with the rotor position. In order to obtain acceptable numerical integration of the system of equations, the variable time step size is kept low by the solver. This has as a consequence to greatly increase the computing time. Unlike the implementation of *ModelHealthy*, faster and more accurate computing is obtained by performing an interpolation of the time-sampled inputs V_{as} , V_{bs} , V_{cs} , Ω_r and θ_r to obtain their value at the current instant of time.

- Healthy machine

In the case of a healthy machine, steady-state initialisation is performed using equation 5.14, considering that the derivative of the currents is null as done for the Park model of the healthy machine. The comparison of *ModelFullBB* and *ModelHealthy* shows quasi-equal stator and rotor currents: the difference between the stator currents stays smaller than 1%.

This validates the fact that the two models are equivalent in healthy working conditions and is in agreement with the fact that no information is lost by applying a Park transformation to a symmetrical machine. However, the computing time of *ModelFullBB* is much longer and reaches a value of 91s to represent 2s of simulated steady-state operation.

- Faulty machine

The initialisation of the simulation of faulty machine behaviour will be detailed in the next section. If one looks at the results of a computation for nominal load and one broken bar, the amplitude of the stator currents are modulated at $(1 - 2s)f$ as shown in figure 5.5a. The difference in stator currents between healthy and faulty situations is plotted. A modulation can clearly be observed. The stator currents around 0.9s are shown in figure 5.5b. This second figure is useful to illustrate the amplitude of the perturbation caused by the broken bar compared to the amplitude of the healthy current.

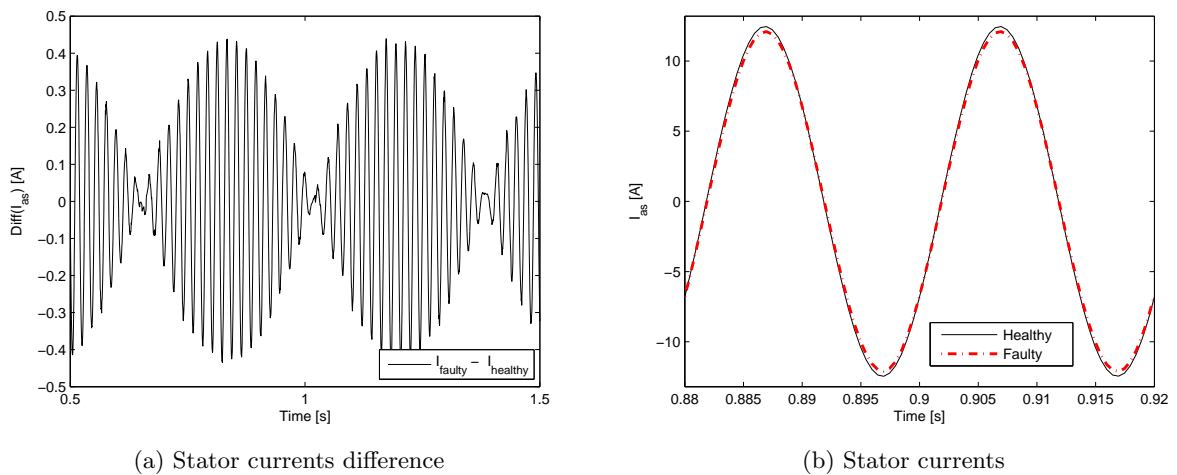


Figure 5.5: Comparison between healthy and faulty (1 broken bar) conditions at full load.

Note that the effect of the broken bar can easily be seen on the 50Hz running RMS value of the stator current. This quantity is computed by

Number of broken bars	CPU Time
0	91s
1	405s
2	467s
3	505s
4	524s
5	530s

Table 5.1: Computing time of *ModelFullBB* for a simulated time of 2s versus the number of broken bars.

$$\text{RMS}(I_{as}) = \sqrt{\frac{1}{N} \sum_{i=1}^N I_{as}^2 \left(t + \frac{i-1}{f_e} \right)}$$

where RMS is the root mean square value of the signal, f_e is the sampling frequency, multiple of 50Hz and N is the number of points in one period of the 50Hz signal. This quantity is plotted in figure 5.6 for the same conditions as in figure 5.5. A reduction of the amplitude of the f component can also be seen clearly. This representation will often be used in this text as it is quite convenient for representing the effect of broken bars.

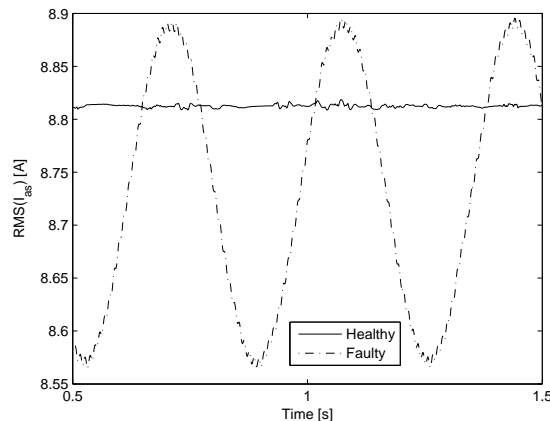


Figure 5.6: Comparison between healthy and faulty conditions at full load with one broken bar.

The main disadvantage of *method 1* is that, as the number of broken bars is increasing, the circuit becomes more difficult to solve and the computing time is increasing as it is shown in table 5.1.

5.3.1.3 Implementation 2

In the previously proposed approach, both computing time and accuracy are affected by the numerical computation of the mutual coupling and of its derivative at each time step. Therefore, as long as the stator is healthy, a Park transformation with a reference frame rotating with the rotor can be applied to the stator equations of this model. By doing this, mutual inductances between the d and q stator windings and original rotor windings will be independent of the rotor position [Vas 94, Razik 03]. The Park transformation can be given by

$$\begin{aligned}\underline{I}_{dq_s} &= \underline{I}_s e^{-jP(\theta_r + \delta + \theta_d)} \\ \underline{I}_s &= \frac{2}{3}(I_{as} + \underline{\alpha} I_{bs} + \underline{\alpha}^2 I_{cs})\end{aligned}\quad (5.17)$$

where θ_d allows us to change the position of the d axis with regard to the position of bar 1 (obtained for $\theta_d = 0$). The reason for introducing this quantity will be explained while introducing the next model. In this section θ_d will be kept at 0 as it has no influence on the stator phase currents.

The space vector transformation of the stator quantities in the stator equation of *ModelFullBB* can be written as (see appendix A.2 for a detailed demonstration of *ModelFullBB*)

$$\underline{V}_s = R_s \underline{I}_s + p(\underline{\Psi}_{ss} + \underline{\Psi}_{sr}) \quad (5.18)$$

with $\underline{\Psi}_{sr} = L_s \underline{I}_s$ and

$$\underline{\Psi}_{sr} = L_m e^{jP(\theta_r + \delta)} \begin{bmatrix} 1 & \underline{\beta} & \dots & \underline{\beta}^{n-1} \end{bmatrix} \begin{bmatrix} I_{r1} \\ \dots \\ I_{rn} \end{bmatrix}$$

If we apply the Park transformation defined here above, we obtain

$$\begin{aligned}\underline{V}_{dq_s} &= R_s \underline{I}_{dq_s} + L_s p(\underline{I}_{dq_s}) + jP\Omega_r L_s \underline{I}_{dq_s} \\ &+ \frac{2}{3} L_m e^{-jP\theta_d} \begin{bmatrix} 1 & \underline{\beta} & \dots & \underline{\beta}^{n-1} \end{bmatrix} p \begin{bmatrix} I_{r1} \\ \dots \\ I_{rn} \end{bmatrix} \\ &+ jP\Omega_r \frac{2}{3} L_m e^{-jP\theta_d} \begin{bmatrix} 1 & \underline{\beta} & \dots & \underline{\beta}^{n-1} \end{bmatrix} \begin{bmatrix} I_{r1} \\ \dots \\ I_{rn} \end{bmatrix}\end{aligned}\quad (5.19)$$

which leads to

$$\begin{bmatrix} V_{ds} \\ V_{qs} \end{bmatrix} = \left(\begin{bmatrix} R_{ss} & R_{sr} \end{bmatrix} + \begin{bmatrix} L_{ss\omega} & L_{sr\omega} \end{bmatrix} \right) \begin{bmatrix} I_{ds} \\ I_{qs} \\ I_{r1} \\ \vdots \\ I_{ri} \\ \vdots \\ I_{rn} \end{bmatrix} + \begin{bmatrix} L_{ss} & L_{sr} \end{bmatrix} \frac{d}{dt} \begin{bmatrix} I_{ds} \\ I_{qs} \\ I_{r1} \\ \vdots \\ I_{ri} \\ \vdots \\ I_{rn} \end{bmatrix} \quad (5.20)$$

with

$$\begin{bmatrix} R_{ss} & R_{sr} \end{bmatrix} = \begin{bmatrix} R_s & 0 & 0 & \dots & 0 \\ 0 & R_s & 0 & \dots & 0 \end{bmatrix}$$

$$\begin{bmatrix} L_{ss} & L_{sr} \end{bmatrix} = \begin{bmatrix} L_s & 0 & \dots & \frac{2}{3} L_m (\cos P\theta_d \cos(P\alpha_r(i-1)) + \sin P\theta_d \sin(P\alpha_r(i-1))) & \dots \\ 0 & L_s & \dots & \frac{2}{3} L_m (\cos P\theta_d \sin(P\alpha_r(i-1)) - \sin P\theta_d \cos(P\alpha_r(i-1))) & \dots \end{bmatrix}$$

$$[L_{ss\omega} \quad L_{sr\omega}] = P \Omega_r \begin{bmatrix} 0 & -L_s & \dots & \frac{2}{3} L_m (\sin P \theta_d \cos (P \alpha_r (i-1)) - \cos P \theta_d \sin (P \alpha_r (i-1))) & \dots \\ L_s & 0 & \dots & \frac{2}{3} L_m (\cos P \theta_d \cos (P \alpha_r (i-1)) + \sin P \theta_d \sin (P \alpha_r (i-1))) & \dots \end{bmatrix}$$

where i is the i th rotor loop.

On the rotor side, the rotor fluxes due to the stator currents are given by

$$\begin{aligned} \begin{bmatrix} \Psi_{r1s} \\ \Psi_{r2s} \\ \dots \\ \Psi_{rns} \end{bmatrix} &= \begin{bmatrix} L_{a1} & L_{b1} & L_{c1} \\ \vdots & \vdots & \vdots \\ L_{an} & L_{bn} & L_{cn} \end{bmatrix} \begin{bmatrix} i_{as} \\ i_{bs} \\ i_{cs} \end{bmatrix} \\ &= \frac{L_m}{2} \left(\begin{array}{c} e^{jP(\theta_r+\delta)} \begin{bmatrix} 1 \\ \underline{\beta} \\ \vdots \\ \underline{\beta}^{(n-1)} \end{bmatrix} \begin{bmatrix} 1 & \underline{\alpha}^2 & \underline{\alpha} \end{bmatrix} \\ +e^{-jP(\theta_r+\delta)} \begin{bmatrix} 1 \\ \underline{\beta}^{-1} \\ \vdots \\ \underline{\beta}^{(1-n)} \end{bmatrix} \begin{bmatrix} 1 & \underline{\alpha} & \underline{\alpha}^2 \end{bmatrix} \end{array} \right) \begin{bmatrix} i_{as} \\ i_{bs} \\ i_{cs} \end{bmatrix} \end{aligned} \quad (5.21)$$

In a similar way as for the stator equation, we obtain

$$\begin{bmatrix} \Psi_{r1s} \\ \Psi_{r2s} \\ \dots \\ \Psi_{rns} \end{bmatrix} = \frac{L_m}{2} \left(\begin{array}{c} e^{jP(\theta_r+\delta)} \begin{bmatrix} 1 \\ \underline{\beta} \\ \vdots \\ \underline{\beta}^{(n-1)} \end{bmatrix} \frac{3}{2} \underline{I}_s^* \\ +e^{-jP(\theta_r+\delta)} \begin{bmatrix} 1 \\ \underline{\beta}^{-1} \\ \vdots \\ \underline{\beta}^{(1-n)} \end{bmatrix} \frac{3}{2} \underline{I}_s \end{array} \right) \quad (5.22)$$

and if we apply the Park transformation to the above equation, the derivative of the flux becomes

$$\frac{d}{dt} \begin{bmatrix} \Psi_{r1s} \\ \Psi_{r2s} \\ \dots \\ \Psi_{rns} \end{bmatrix} = \frac{9}{4} \frac{L_m}{2} \left(\begin{array}{c} e^{-jP\theta_d} \begin{bmatrix} 1 \\ \underline{\beta} \\ \vdots \\ \underline{\beta}^{(n-1)} \end{bmatrix} \underline{I}_{dq_s}^* \\ +e^{jP\theta_d} \begin{bmatrix} 1 \\ \underline{\beta}^{-1} \\ \vdots \\ \underline{\beta}^{(1-n)} \end{bmatrix} \underline{I}_{dq_s} \end{array} \right) \quad (5.23)$$

where each line can be written as

$$\begin{aligned} \frac{d}{dt} \Psi_{ris} &= \frac{9}{4} L_m \left[\underbrace{\cos P \theta_d \cos (P \alpha_r (i-1)) + \sin P \theta_d \sin (P \alpha_r (i-1)) \quad \cos P \theta_d \sin (P \alpha_r (i-1)) - \sin P \theta_d \cos (P \alpha_r (i-1))}_{L_{rs}(i,:)} \right] \\ &\quad \frac{d}{dt} \begin{bmatrix} I_{ds} \\ I_{qs} \end{bmatrix} \end{aligned}$$

where $M(i, :)$ means row i of the matrix M .

The rest of the rotor equations remains identical to *implementation 1*. Finally the system of equations becomes

$$\begin{bmatrix} V_{ds} \\ V_{qs} \\ 0 \\ \vdots \\ 0 \end{bmatrix} = \left(\underbrace{\begin{bmatrix} R_{ss} & R_{sr} \\ R_{rs} & R_{rr} \end{bmatrix}}_R + \underbrace{\begin{bmatrix} L_{ss} \omega & L_{rs} \omega \\ L_{sr} \omega & 0 \end{bmatrix}}_{L_\omega} \right) \begin{bmatrix} I_{ds} \\ I_{qs} \\ I_{r1} \\ \vdots \\ I_{ri} \\ \vdots \\ I_{rn} \end{bmatrix} + \underbrace{\begin{bmatrix} L_{ss} & L_{sr} \\ L_{rs} & L_{rr} \end{bmatrix}}_L \frac{d}{dt} \begin{bmatrix} I_{ds} \\ I_{qs} \\ I_{r1} \\ \vdots \\ I_{ri} \\ \vdots \\ I_{rn} \end{bmatrix} \quad (5.24)$$

5.3.1.4 Initialisation

In case of broken bars and in steady-state at constant speed, the stator currents can be described using four parameters linked to the amplitude and the phase of the 2 frequencies f and $(1-2s)f$. This will lead to stator currents I_{ds} and I_{qs} and rotor currents I_{ri} of frequency sf .

$$\begin{aligned} I_{ds} &= I_{dsc} \cos s\omega t + I_{dss} \sin s\omega t \\ I_{qs} &= I_{qsc} \cos s\omega t + I_{qss} \sin s\omega t \\ I_{ri} &= I_{ric} \cos s\omega t + I_{ris} \sin s\omega t \end{aligned} \quad (5.25)$$

with $i = 1, \dots, n$ and their derivative can easily be written as

$$\begin{aligned} \frac{dI_{ds}}{dt} &= -s\omega I_{dsc} \sin s\omega t + s\omega I_{dss} \cos s\omega t \\ \frac{dI_{qs}}{dt} &= -s\omega I_{qsc} \sin s\omega t + s\omega I_{qss} \cos s\omega t \\ \frac{dI_{ri}}{dt} &= -s\omega I_{ric} \sin s\omega t + s\omega I_{ris} \cos s\omega t \end{aligned} \quad (5.26)$$

The stator voltages can be written as

$$\underline{V}_s = \sqrt{2} V_{as} (\cos(\omega t + \phi_a) + j \sin(\omega t + \phi_a))$$

where ϕ_a is the phase of the voltage source of phase a .

Using the transformation defined in equation 5.17, we find

$$\begin{aligned}
V_{ds} &= \sqrt{2} V_{as} (\cos(P\Omega_r(t-t_0) + P(\theta_0 + \delta + \theta_d)) \cos(\omega t + \phi_a) + \sin(P\Omega_r(t-t_0) + P(\theta_0 + \delta + \theta_d)) \sin(\omega t + \phi_a)) \\
&= \sqrt{2} V_{as} (\cos(s\omega t) \cos(P(\theta_0 + \delta + \theta_d) - (1-s)\omega t_0 - \phi_a) + \sin(s\omega t) \sin(P(\theta_0 + \delta + \theta_d) - (1-s)\omega t_0 - \phi_a)) \\
&= V_{dsc} \cos s\omega t + V_{dss} \sin s\omega t
\end{aligned}$$

and

$$\begin{aligned}
V_{qs} &= \sqrt{2} V_{as} (\cos(P\Omega_r(t-t_0) + P(\theta_0 + \delta + \theta_d)) \sin(\omega t + \phi_a) - \sin(P\Omega_r(t-t_0) + P(\theta_0 + \delta + \theta_d)) \cos(\omega t + \phi_a)) \\
&= \sqrt{2} V_{as} (\sin(s\omega t) \cos(P(\theta_0 + \delta + \theta_d) - (1-s)\omega t_0 - \phi_a) - \cos(s\omega t) \sin(P(\theta_0 + \delta + \theta_d) - (1-s)\omega t_0 - \phi_a)) \\
&= V_{qsc} \cos s\omega t + V_{qss} \sin s\omega t
\end{aligned}$$

As the stator voltages are also composed of terms in $\cos s\omega t$ and in $\sin s\omega t$ we can write the system of equations of this model (5.24) as

$$\begin{bmatrix} V_{dsc} \\ V_{qsc} \\ 0 \\ \vdots \\ 0 \\ V_{dss} \\ V_{qss} \\ 0 \\ \vdots \\ 0 \end{bmatrix} = \begin{bmatrix} R + L\omega & s\omega L \\ -s\omega L & R + L\omega \end{bmatrix} \begin{bmatrix} I_{dsc} \\ I_{qsc} \\ I_{r1c} \\ \vdots \\ I_{rnc} \\ I_{dss} \\ I_{qss} \\ I_{r1s} \\ \vdots \\ I_{rns} \end{bmatrix} \quad (5.27)$$

The initial values are then obtained by solving the system above and injecting its results in equation 5.25 evaluated for t by t_0 .

5.3.1.5 Numerical Implementation

As expected, the numerical resolution of this version of the model is quicker as it takes about 31s to represent 2s of simulated time in healthy conditions. As for the case of *Implementation 1*, when the number of broken bars increases, so is the computing time. For 5 broken bars, it is around 85s which is still much smaller than *Implementation 1*.

In the rest of this document, "*ModelFullBB*" will always refer to this second implementation. The accuracy is also greatly improved as the difference in healthy conditions between *ModelHealthy* and *ModelFullBB* is much smaller than the 1% error observed for *Implementation 1*.

5.3.2 Model based on Park transformation of the rotor

5.3.2.1 Implementation 1

The model implementation is equivalent to the one of *ModelHealthy* with the difference of the Park reference frame which is taken fixed with regard to the rotor as shown in equation 5.28.

$$\begin{aligned}\underline{I}_{dqs} &= \underline{I}_s e^{-jP(\theta_r + \delta + \theta_d)} \\ \underline{I}_{dqr} &= \sqrt{\frac{n}{3}} \underline{I}_r e^{-jP(\theta_d)}\end{aligned}\quad (5.28)$$

where $\underline{I}_{dqs} = I_{ds} + jI_{qs}$.

The main interest of this reference frame is to easily represent rotor faults. This transformation allows us to represent rotor circuit faults as asymmetries in the d and q axis rotor resistances R_{rd} and R_{rq} and inductances L_{rd} and L_{rq} . The d axis will be chosen to be oriented with the fault direction which is the average position of the adjacent broken bars thanks to the variable θ_d defined by

$$\theta_d = \begin{cases} (i_{bbar} - 1) \alpha_r & \text{if } n_{BB} < 1 \\ (i_{bbar} - 1) \alpha_r + (n_{BB} - 1) \delta & \text{otherwise} \end{cases}$$

where i_{bbar} is the number of the first broken bar. Note that the stator transformation is identical to the one of *ModelFullBB*.

The system can be written as

$$\begin{bmatrix} V_{ds}(t) \\ V_{qs} \\ 0 \\ 0 \end{bmatrix} = (R + L\omega) \begin{bmatrix} I_{ds}(t) \\ I_{qs} \\ I_{dr} \\ I_{qr} \end{bmatrix} + L \frac{d}{dt} \begin{bmatrix} I_{ds}(t) \\ I_{qs} \\ I_{dr} \\ I_{qr} \end{bmatrix}\quad (5.29)$$

with

$$L = \begin{bmatrix} L_s & 0 & L_m & 0 \\ 0 & L_s & 0 & L_m \\ L_m & 0 & L_{rd} & 0 \\ 0 & L_m & 0 & L_{rq} \end{bmatrix}$$

$$L\omega = \begin{bmatrix} 0 & -P\Omega_r L_s & 0 & -P\Omega_r L_m \\ P\Omega_r L_s & 0 & P\Omega_r L_m & 0 \\ 0 & 0 & 0 & 0 \\ 0 & 0 & 0 & 0 \end{bmatrix}$$

$$R = \begin{bmatrix} R_s & 0 & 0 & 0 \\ 0 & R_s & 0 & 0 \\ 0 & 0 & R_{rd} & 0 \\ 0 & 0 & 0 & R_{rq} \end{bmatrix}$$

5.3.2.2 Initialisation and identification of the rotor impedances

This model will be referred as "*ModelParkBB*" in the rest of this document.

The initialisation process is quite similar to the one of *ModelFullBB* except that only two rotor currents are needed. The expressions for V_{dsc} , V_{dss} , V_{qsc} and V_{qss} are identical. The identification of the parameters R_{rd} , R_{rq} , L_{rd} , L_{rq} consists in equalising the expression of the $\sin(s\omega t)$ and $\cos(s\omega t)$ coefficients of the stator currents using the equations of the steady-state solutions of *ModelFullBB* and *ModelParkBB*. This system offers one solution as long as the two stator current frequencies sf and $(1 - 2s)f$ are distinct, which is no more the case when $s = 0$ or $s = 0.5$. In the first situation, no currents are flowing in the rotor windings and any given value for the four rotor parameters will solve the problem. In the second situation ($s = 0.5$), we have only two equations and an infinite number of solutions can be found. Two additional constraints can therefore be taken. For example, the system is then satisfied if we choose $R_{rd} = R_{rq}$ and $L_{rd} = L_{rq}$ which corresponds to a healthy machine with a modified rotor.

The solution for different speeds and fault magnitude is shown in figure 5.7. As it can be observed, at 750 rpm ($s = 0.5$), discontinuities appear as the solution around this working point does not converge with the $d - q$ symmetry supposed for $s = 0.5$. Note that other constraints could have been chosen to assure continuity of the parameter with speed but the objective of the figure is to illustrate the previous statement. At all working points, the system of equations is perfectly satisfied.

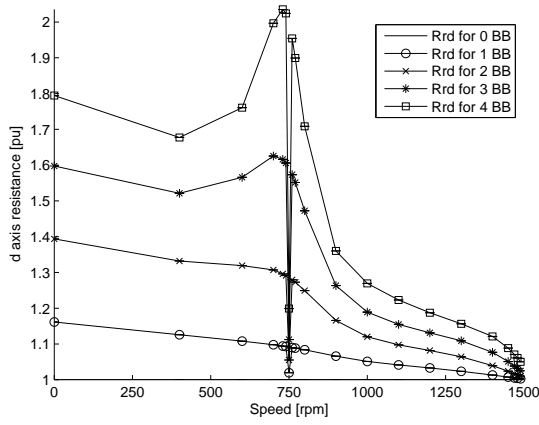
The main disadvantage of this model is that its parameters are not only function of the slip but also of the fault magnitude.

Numerical Implementation As an illustration, a comparison of *ModelParkBB* and *ModelHealthy* at nominal load and one broken bar is performed. The stator currents are identically represented by both model but great difference can be observed in the rotor currents as shown in figure 5.8. It can be observed that the fault is considered to be sinusoidally distributed along the rotor circumference and having the same number of pole pair as the stator windings.

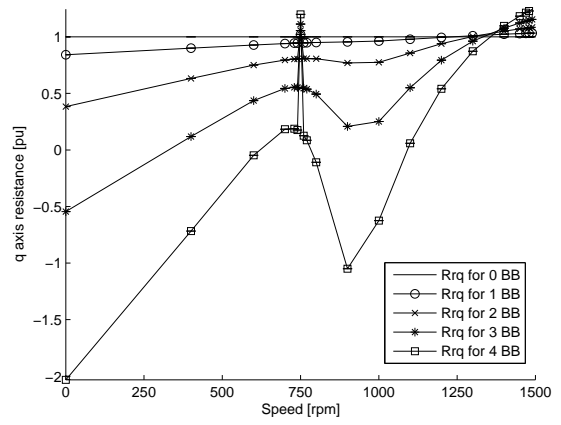
However, as the parameters of *ModelParkBB* vary with the slip for a given fault magnitude, the correspondence is not perfect if one considers a transient behaviour with constant parameters. This is illustrated in the case of a transient condition consisting in a constant acceleration between 1000 rpm and 1500 rpm. For each model, the difference between healthy and faulty (1 broken bar) stator currents is plotted in figure 5.9.

Another drawback is that, for certain speed conditions and fault magnitudes, the q rotor resistance becomes negative which greatly complicates the numerical integration of the differential equations (see figure 5.7). This model is therefore not usable in these situations. Furthermore, it is important to precise that the values taken for the parameters do not have physical interpretations. Therefore, this model can not be used to understand the effects of the fault eventhough it correctly represents the machine behaviour from the stator point of view.

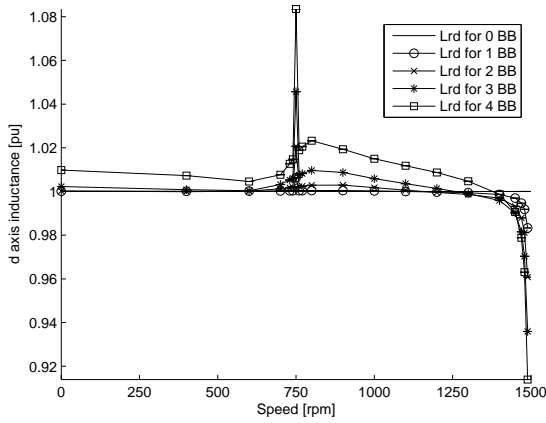
An approximate solution valid for the whole range can be found and gives a closing error lower than 6% for less than 3 broken bars. The variation of the parameters with the number of broken bars is shown in figure 5.11. However, when the number of broken bars is increased to 4, the closing error quickly rises as shown in figure 5.10. This is also the case for the variation of the parameters; for 4 broken bars the



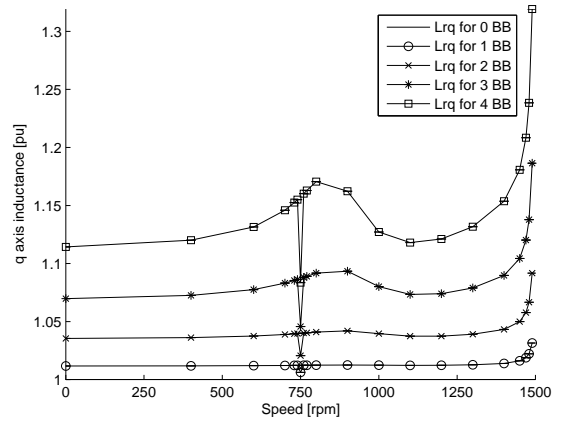
(a) *d* rotor resistance



(b) *q* rotor resistance



(c) *d* rotor inductance



(d) *q* rotor inductance

Figure 5.7: Rotor impedances normalised by healthy values versus speed for different number of adjacent broken bars.

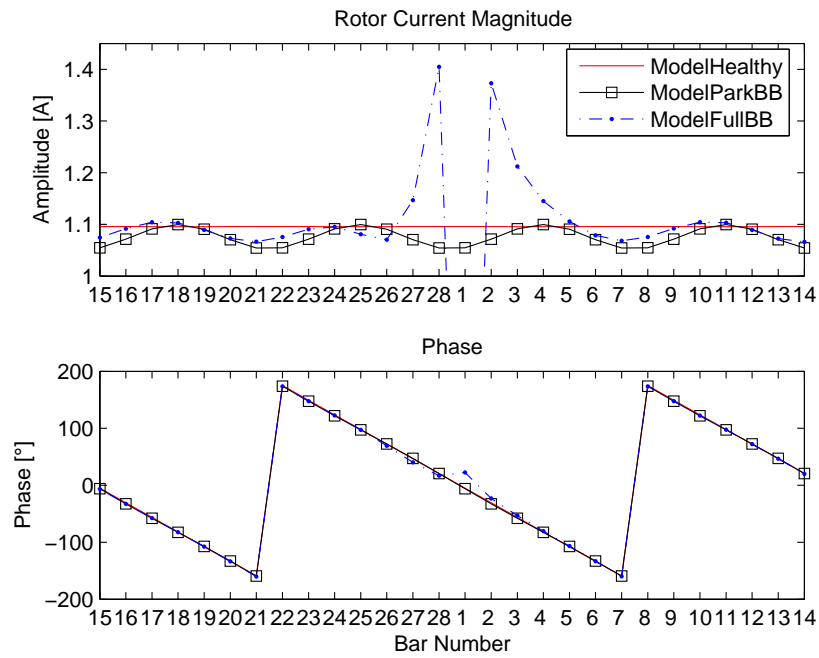


Figure 5.8: Rotor phasors for the two models at nominal load with one broken bar.

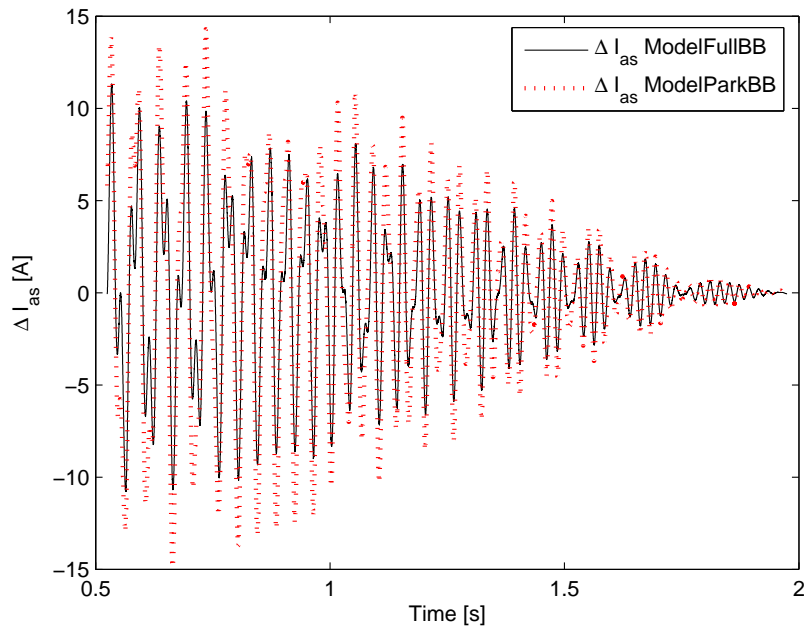


Figure 5.9: Difference between faulty and healthy stator current for the two models with one broken bars and constant rotor acceleration between 1000 rpm and 1500 rpm.

parameters are $R_{rd} = 3.3\text{pu}$, $R_{rq} = -15.6\text{pu}$, $L_{rd} = 1.03\text{pu}$ and $L_{rq} = 1.13\text{pu}$ which are much different than the values of the figure. This is in contradiction with the conclusion that broken bars only slightly affect the machine.

Therefore, if one working point is considered at a time, this model represents perfectly the stator currents of *ModelFullBB*. However, an acceptable match for the whole speed range is not possible. Improvement of this model will be proposed in *Implementation 2*.

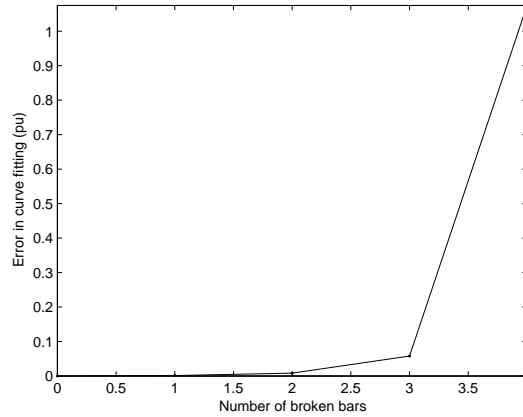


Figure 5.10: Closing error of approximate solution versus number of adjacent broken bars.

The approximate solution was found using a nonlinear optimisation algorithm based on the simplex search method. This function is called several times (500) with different initial conditions taken within the neighbourhood (between -1 and 3 times the value of the parameters representing the healthy situation) of the solution for a healthy machine to ensure a convergence to the global minimum. The function to minimise is the closing error of the equations comparing the stator currents. It is defined as

$$\epsilon = \frac{1}{N_{Speeds}} \sum_{i=1}^{N_{Speeds}} \sqrt{\left(\frac{I_{dsc\ Park}(i) - I_{dsc\ Full}(i)}{I_{dsc\ ParkNoFault}(i)}\right)^2 + \left(\frac{I_{qsc\ Park}(i) - I_{qsc\ Full}(i)}{I_{qsc\ ParkNoFault}(i)}\right)^2 + \left(\frac{I_{dss\ Park}(i) - I_{dss\ Full}(i)}{I_{dss\ ParkNoFault}(i)}\right)^2 + \left(\frac{I_{qss\ Park}(i) - I_{qss\ Full}(i)}{I_{qss\ ParkNoFault}(i)}\right)^2}$$

where N_{Speeds} is the number of speeds considered.

The reason for trying several initialisations is that even for an initial estimation very close from the optimal solution, the systems can converge to a local minimum. An illustration is shown in figure 5.12 for 3 broken bars where the closing error is plotted versus R_{rq} and L_{rd} in the neighbourhood of the optimal solution. R_{rd} and L_{rq} are fixed at their optimal value. It can be observed that if the optimisation algorithm is moving in this plane, the global minimum can only be found if the initial value of R_{rq} is bigger than the optimal value.

More detail on the use of such algorithms will be given in chapter 6.

5.3.2.3 Implementation 2

In [Razik 03] a similar approach is performed to represent rotor faults. The authors propose to use a rotor matrix with identical L_{rd} and L_{rq} and additional d and q cross coupling using $R_{rdq} = R_{rqd} \neq 0$ and a

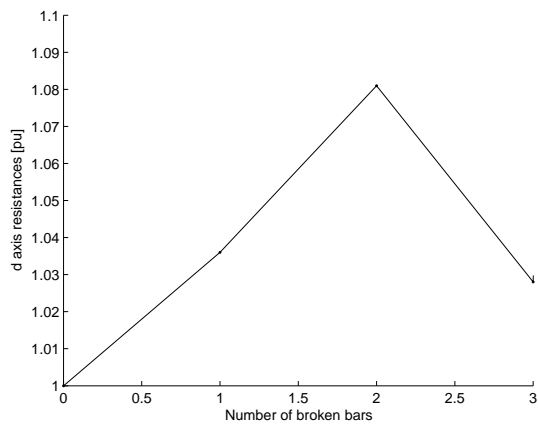
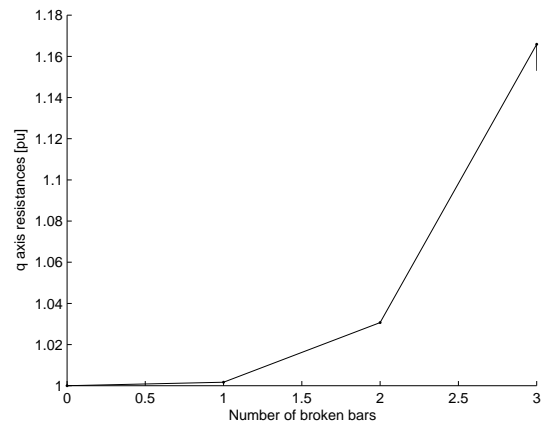
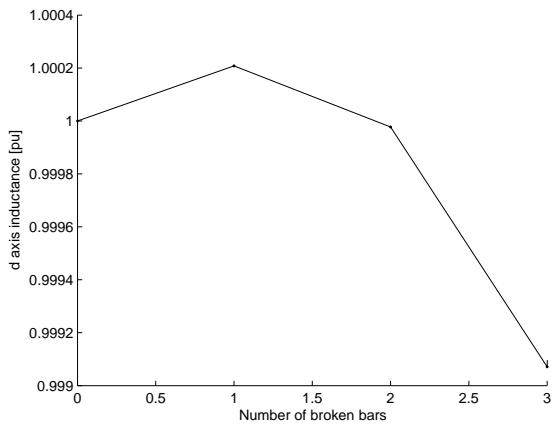
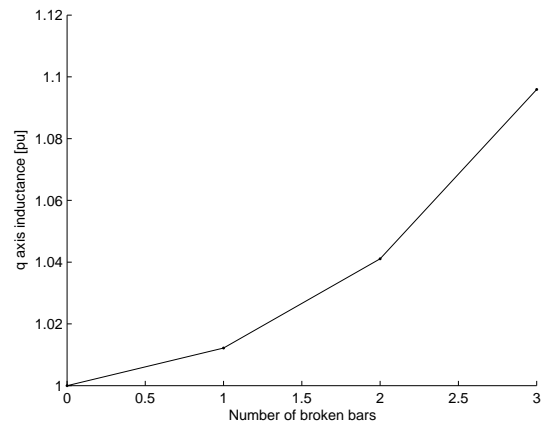
(a) d rotor resistance(b) q rotor resistance(c) d rotor inductance(d) q rotor inductance

Figure 5.11: Rotor impedances normalised by healthy values versus number of adjacent broken bars.

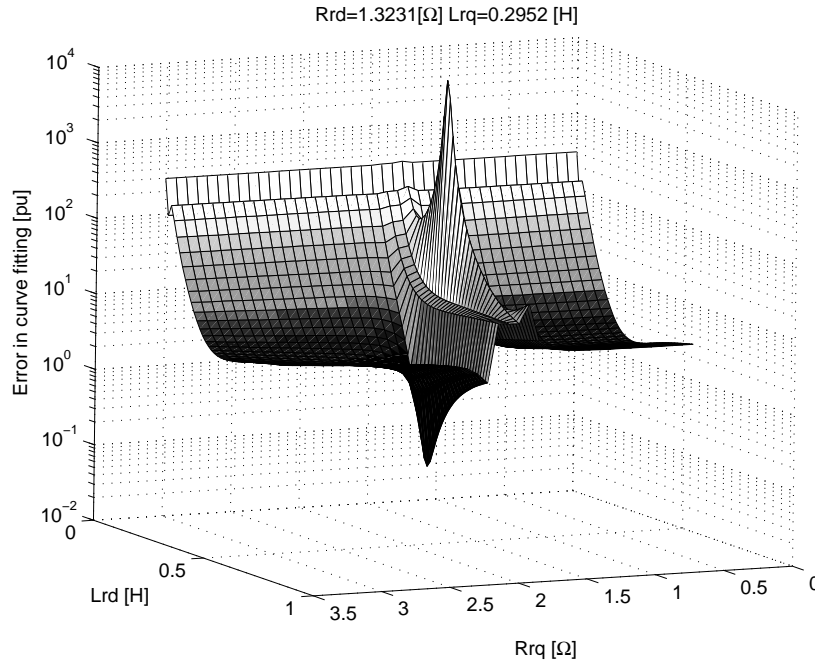


Figure 5.12: Closing error in neighbourhood of the optimal solution for three adjacent broken bars.

reference frame not depending on the position of the faults. His choice is based on the hypothesis that the fault consists in an increase of the resistance of some bars and that it will only affect the resistance matrix.

The choice of the reference frame presents the difficulty that it leads to different values of the parameters for a same fault magnitude for each fault position. A diagnostic based on such model is then difficult to perform. The idea of using a reference frame oriented towards the fault allows us to decouple fault position and magnitude.

The implementation of the model proposed by [Razik 03] leads to similar conclusions as the approach based on different d and q rotor impedance and no cross-coupling resistances (*Implementation 1*). The main difference is that the position of the reference frame θ_d varies not only with the number of broken bars but also with speed. This method is then of less good quality as the one proposed in *Implementation 1*.

In [Penman 96], Penman proposes to use a complete matrix with cross coupling inductances ($L_{rdq} \neq 0$ and $L_{rqd} \neq 0$) as well as different d and q mutual coupling inductances between stator and rotor windings and cross coupling mutual inductances. This possibility was not tested in this work.

However, if one considers the following rotor matrices

$$\begin{bmatrix} R_{rd} & R_{rdq} \\ R_{rdq} & R_{rq} \end{bmatrix} \quad \text{and} \quad \begin{bmatrix} L_{rd} & L_{rdq} \\ L_{rdq} & L_{rq} \end{bmatrix}$$

which corresponds to six coefficients instead of two for a healthy machine, we can find an approximate solution for the whole speed range with closing error lower than 1% up to five adjacent broken bars as shown in figure 5.13. Furthermore, the variation of the parameters with the number of broken bars is shown in figure 5.14. The variation is monotonically increasing for every parameters and q axis parameters are the most affected but the change remains lower than 1 pu.

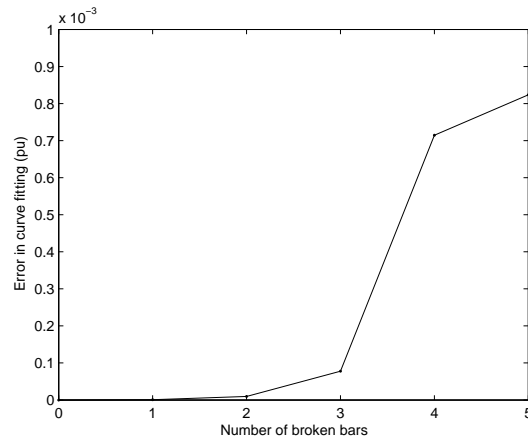


Figure 5.13: Closing error of the approximate solution versus number of adjacent broken bars.

Parameters	A	B	C	sse
R_{rd}	$6.905 \cdot 10^{-4}$	3.458	R_r	$3.85 \cdot 10^{-5}$
R_{rq}	$3.438 \cdot 10^{-2}$	1.737	R_r	$3.66 \cdot 10^{-4}$
R_{rdq}	$1.077 \cdot 10^{-2}$	1.346	0	$2.77 \cdot 10^{-7}$
L_{rd}	$6.673 \cdot 10^{-5}$	3.116	L_r	$3.23 \cdot 10^{-8}$
L_{rq}	$2.532 \cdot 10^{-3}$	2.029	L_r	$7.88 \cdot 10^{-7}$
L_{rdq}	$2.047 \cdot 10^{-4}$	2.671	0	$2.23 \cdot 10^{-6}$

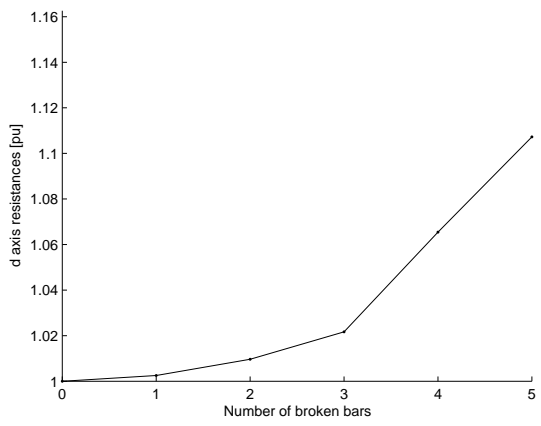
Table 5.2: Coefficients of dependence of the parameters with broken bars.

5.3.2.4 Numerical Implementation

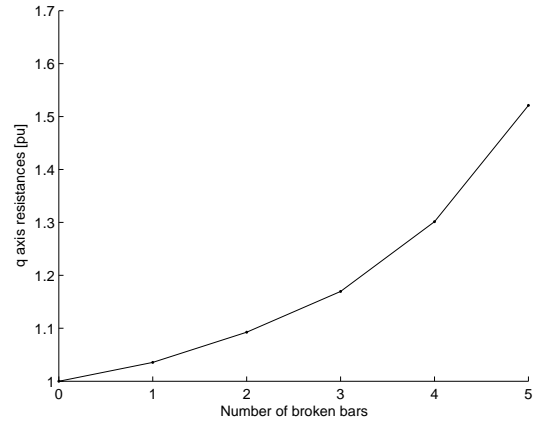
Henceforward, only the second implementation of this model (*ModelParkBB*) will be used as it is more convenient to use since its parameters are constant for all speeds. Furthermore, the dependence of the rotor parameters with the number of broken bars can be approximated using functions of the type $A (n_{BB})^B + C$ where C is equal to the healthy value of the parameters. The identification is based on the value of the parameters for the first four broken bars. The coefficients and the sum of the squared errors (sse) of the identification are given in table 5.2.

As an illustration, the running RMS value of the stator currents for nominal load and with three broken bars is illustrated in figure 5.15. On this figure the error made using the 6 constant rotor parameters for all speeds is shown by comparing curves "*ModelFullBB*" and "*ModelParkBB* - Original parameters". This error is very small as the curves are almost identical. The error due to the approximation with the function $A (n_{BB})^B + C$ to represent the dependence of the parameters with the fault magnitude can be seen by comparing the curve "*ModelParkBB* - Function for parameters" to the curve "*ModelParkBB* - Original parameters". This error affects both the phase and the amplitude of the modulation of the RMS value of the stator currents.

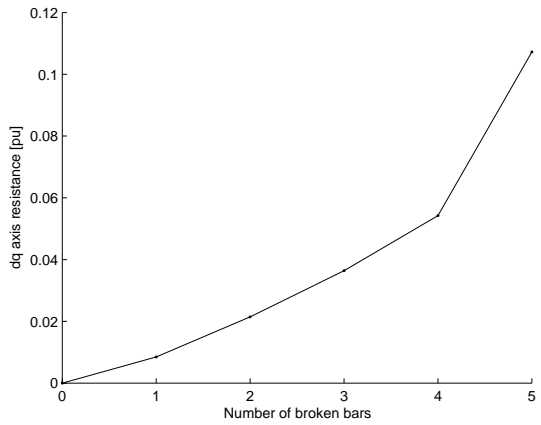
The computing time is about 2.1s to represent 2s of simulated time which corresponds to an impressive reduction compared to *ModelFullBB*.



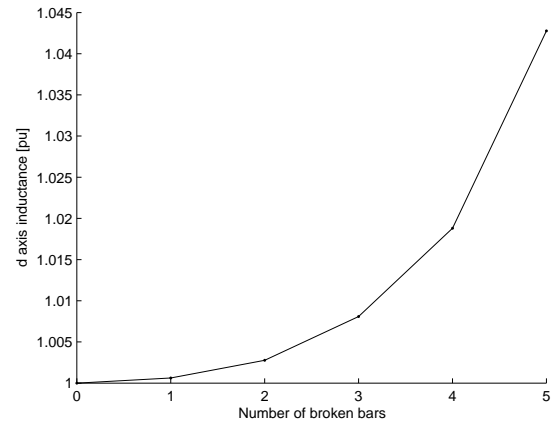
(a) *d* rotor resistance



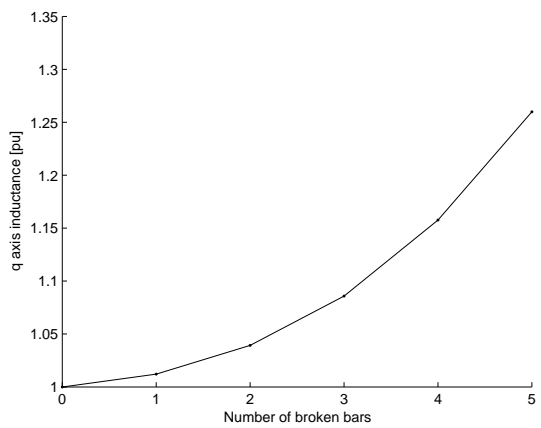
(b) *q* rotor resistance



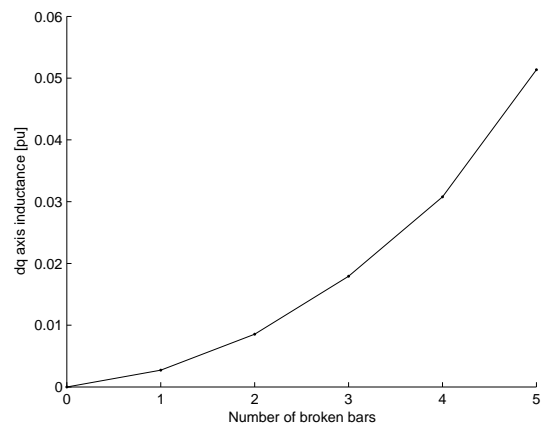
(c) *dq* rotor resistance



(d) *d* rotor inductance



(e) *q* rotor inductance



(f) *dq* rotor inductance

Figure 5.14: Rotor impedances normalised by healthy values versus number of adjacent broken bars.

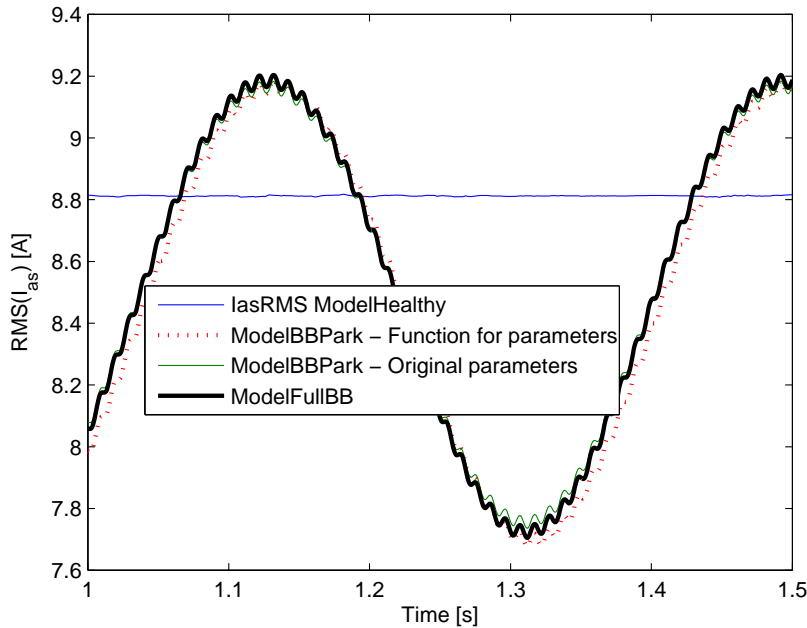


Figure 5.15: Comparison between *ModelHealthy* and *ModelParkBB* at full load with three broken bars.

5.3.3 Model based on the superposition principle

The principle of superposition was used to explain the general influence of a broken bar on the behaviour of an induction motor in section 3.3.1 and it was validated for early stage faults in section 3.3.3.4. A broken bar can then be represented as the superposition of a healthy bar and a current source injecting, at all times, a current in the bar of opposite value as the current flowing in the healthy bar. The resulting current in the bar is therefore null. This principle will be used to represent a faulty machine with broken bars.

5.3.3.1 Implementation 1

The model is separated in a healthy machine model and a superimposed model. The latter is only excited when the machine is faulty. The main objective of this decomposition is to reduce computational time by putting forward symmetries that exist in faulty induction machines.

The healthy part consists in *ModelHealthy*. The rotor circuit of the superimposed model is given in figure 5.16. The d and q stator windings are short-circuited. The speed $\Omega_r(t)$ is considered as an input of the superimposed model and therefore no speed ripple due to the fault will be considered. This is valid for small fault magnitudes and/or high inertial load. The stator and rotor currents computed by the two parts of the model are then added together to represent the faulty induction motor. This is illustrated in figure 5.17. n_{BB} is defined as the ratio between the current flowing in the bar in the healthy machine and the "fault current" (I_f), input of the superimposed model. A partially broken bar is represented using $n_{BB} < 1$ and a totally broken bar by $n_{BB} = 1$.

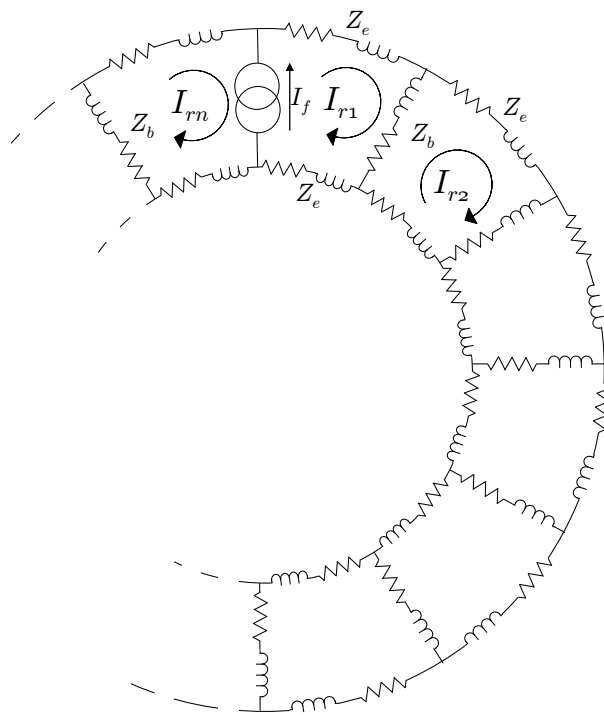


Figure 5.16: Circuit of the rotor cage.

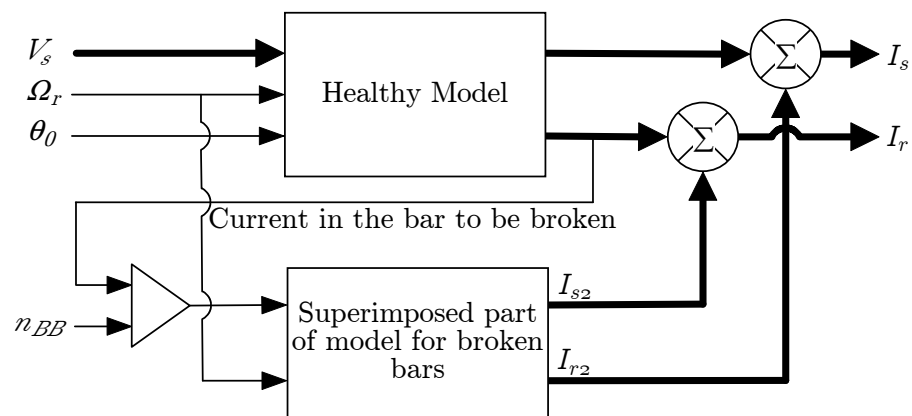


Figure 5.17: Circuit model of a faulty machine using the principle of superposition.

5.3.3.2 Numerical Implementation

The initialisation is obtained by subtracting to the initial condition of *ModelFullBB*, the initial condition of *ModelHealthy*. The resolution of the superimposed part is similar to the one of *ModelFullBB* but the presence of a current source in a branch without parallel impedances implies some changes in the electrical circuit. Indeed, no loop equation can be written for the loops of $I_{r\ bbar}$ and $I_{r\ bbar-1}$ where $bbar$ is the number of the bar which is broken. Furthermore, one of the loop current can be eliminated. The loop current $I_{r\ bbar-1}$ is replaced by a loop current $I_{r\ bbar-1\ bbar}$ and therefore, the loop current $I_{r\ bbar}$ is equal to I_f and can be eliminated from vector of unknowns (currents) and its product with the impedance in which it is flowing can be added to the loop voltages. The loop is shown in figure 5.18 and its equation can be written as

$$\begin{aligned}
& 0 - (2L_e + L_{ki} + L_b + L_{kk}) \frac{dI_f}{dt} - (2R_e + R_b) I_f \\
& = \\
& (2L_{kk} + 2L_{ki} + 4L_e + 2L_b) \frac{dI_{r\ bbar-1\ bbar}}{dt} + (2L_{ki} - L_b) \left(\frac{dI_{r\ bbar-1}}{dt} + \frac{dI_{r\ bbar+1}}{dt} \right) \\
& + \sum (2L_{ki}) \frac{dI_{ri}}{dt} + (M_{ds\ bbar-1} + M_{ds\ bbar}) \frac{dI_{ds}}{dt} + (M_{qsn} + M_{qs1}) \frac{dI_{qs}}{dt} \\
& + (4R_r + 2R_b) I_{r\ bbar-1\ bbar} + (2L_{ki} - L_b) (I_{r\ bbar-1} + I_{r\ bbar+1}) \\
& + (M_{ds\ bbar-1} + M_{ds\ bbar}) I_{ds} + (M_{qs\ bbar-1} + M_{qs\ bbar}) I_{qs}
\end{aligned}$$

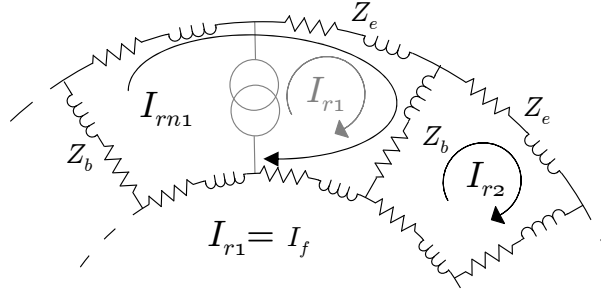


Figure 5.18: Loop $I_{r\ bbar-1\ bbar} (= I_{n1})$ in the rotor circuit.

The other loop- and stator-equations are written following the same method.

As no resistance of high value is used to represent the broken bar, the convergence of the differential equations of the superimposed part is much quicker than in the case of *ModelFullBB* with a computing time of about 7s for 2s of simulated time. The computing time of *ModelHealthy* has to be added to this time to represent the faulty machine.

The error in stator current between this model and *ModelFullBB* is smaller than 1% of the superimposed stator currents (i.e. difference between healthy and faulty (1 broken bar) stator currents) in case of a transient condition consisting in a constant acceleration between 1000 rpm and 1500 rpm. In steady-state, the stator and rotor currents are perfectly modelled using this approach. This again validates the implementation of the superposition principle.

5.3.3.3 Implementation 2

In order to lower the computing time even more, this second implementation presents two approximations and for each, the superimposed part is computed in two steps:

- The first step consists in the computation of the rotor currents neglecting the influence of the stator. The two approximations will propose two different methods to realise this operation.
- In the second step, the induced stator currents created by these rotor currents are computed. This part will be identical for the two approximations.

Computation of the superimposed rotor currents: *method 1* The broken bar is represented by a current source I_f . The electrical circuit to be solved is presented in figure 5.16. Symmetries and Thevenin-Norton transformation can be used to reduce the system as shown in figures 5.19a and 5.19b for an even number of bars. In case of an odd number of bars, by symmetry of the problem, the loop current $[\frac{n}{2}]$ is null and the equation of this loop can be removed from the problem.

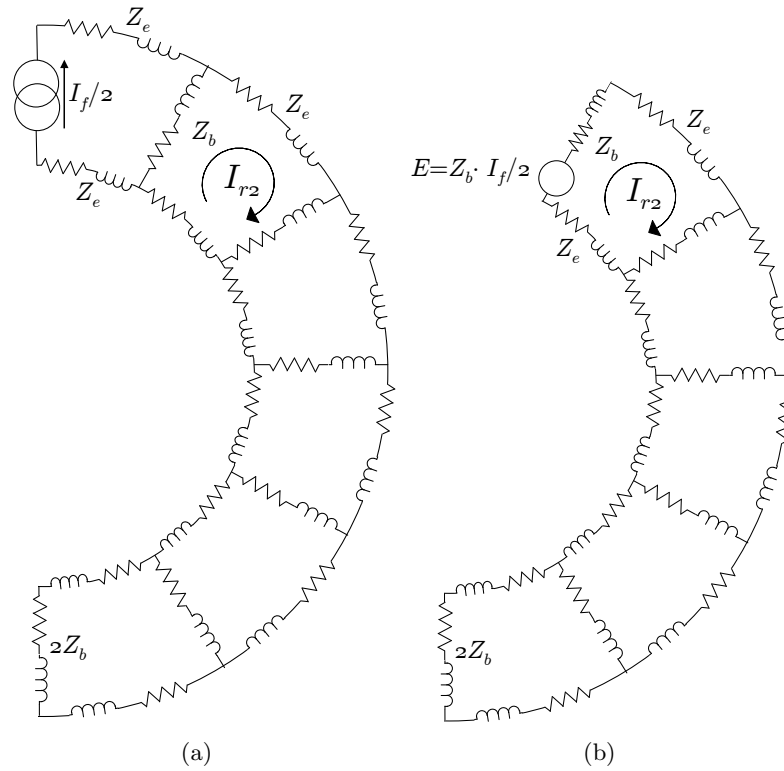


Figure 5.19: Simplification of the rotor circuit

Finally, the system of equations to be solved can be written as $E = R I + L \frac{d}{dt} I$

$$\text{where } E = \begin{bmatrix} (R_b + L_b \frac{d}{dt}) \frac{I_f}{2} \\ 0 \\ \vdots \\ 0 \end{bmatrix}, R = \begin{bmatrix} R_o & -R_b & 0 & 0 \\ -R_b & \ddots & \ddots & 0 \\ 0 & \ddots & R_o & -R_b \\ 0 & 0 & -R_b & R_o - 2R_b \end{bmatrix},$$

$$L = \begin{bmatrix} L_o + L_{kk} - L_{ki} & -L_b & 0 & 0 \\ -L_b & \ddots & \ddots & 0 \\ 0 & \ddots & L_o + L_{kk} - L_{ki} & -L_b \\ 0 & 0 & -L_b & L_o + L_{kk} - L_{ki} - 2L_b \end{bmatrix}$$

Computation of the superimposed rotor currents: *method 2* As in the case of *method 1*, the broken bar is represented by a current source but we will make the hypothesis that, as Z_b is smaller than Z_e , the current from the current source will only flow through the two bars adjacent to the broken one. The only benefits for choosing this hypothesis is to reduce the computing time required to represent the behaviour of a machine with broken bars.

Computation of the superimposed stator currents The n superimposed rotor currents computed by one of the two presented methods are then converted to d and q superimposed rotor currents using the Park transformation in a reference frame rotating with the rotor. Then, equation 5.30 realises the operation of computing the stator currents induced by the superimposed rotor currents computed earlier.

$$\begin{aligned} \begin{bmatrix} L_s & 0 \\ 0 & L_s \end{bmatrix} \frac{d}{dt} \begin{bmatrix} I_{ds} \\ I_{qs} \end{bmatrix} + \begin{bmatrix} R_s & -\omega L_s \\ \omega L_s & R_s \end{bmatrix} \begin{bmatrix} I_{ds} \\ I_{qs} \end{bmatrix} = \\ -\sqrt{\frac{3n}{2}} L_m \begin{bmatrix} dI_{dr}/dt - \omega I_{qr} \\ \omega I_{dr} + dI_{qr}/dt \end{bmatrix} \end{aligned} \quad (5.30)$$

Combination of the healthy machine model and the superimposed model The superimposed stator and rotor currents are then added to the solution provided by the healthy model to represent the faulty machine as it is summarised in figure 5.17. The variable n_{BB} is now defined as

- $n_{BB} = 1$, if the bar is totally broken, no inter-bar currents are present.
- $n_{BB} \leq 1$, if the bar is partially broken or inter-bar currents are present.
- $n_{BB} \geq 1$, if more than one bar is broken. Note that this model has limits when n_{BB} is big because it assumes that the "fault current" is supported by only one bar which is not correct when several bars are broken.

5.3.3.4 Numerical Implementation

For the sake of clarity, this model will be referred as "*ModelSupBB*" in the rest of this document.

- Analysis of the computation of the superimposed rotor currents

The two proposed methods are compared in steady-state with the superimposed rotor currents obtained the model of *Implementation 1* (or by difference between healthy and faulty (1 broken bar) simulation of model *ModelFullBB* detailed in section 5.3.1 which is equivalent).

The superimposed rotor phasors are shown in figure 5.20. The comparison of the results obtained with *Implementation 1* and *method 1* illustrates the influence of the stator windings which will be detailed in section 6.3. The main part of the error can be observed on the phase of the currents of the bars adjacent to the broken one. *Method 2* is less precise but requires less computing time (almost 0s versus a computing time of 0.9s for 2s of simulated time with *method 1*). The consequence of this error is shown in figure 5.21 by comparing stator current from the superimposed model with superimposed rotor current obtain from *Implementation 1* and superimposed current obtained from *method 1* ("SupBBarre" on the figure).

- Study of the computation of the superimposed stator currents

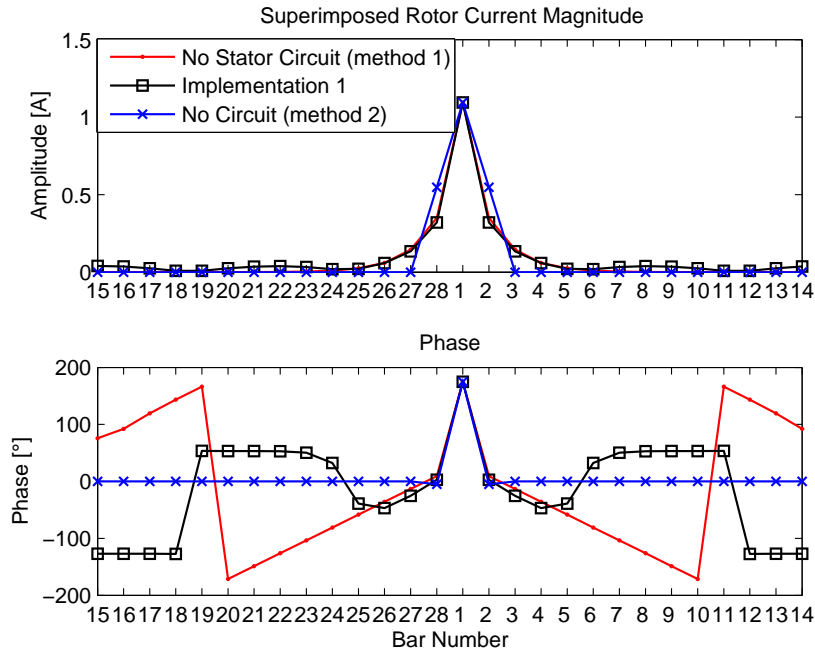


Figure 5.20: Comparison of the superimposed rotor currents computed by the different methods.

In order to validate the computation of the superimposed stator currents, the model detailed earlier is compared to the superimposed stator circuit computed using the stator equations of *ModelFullBB* with null stator voltages and imposed rotor currents.

No difference can be observed in the stator currents shown in figure 5.21⁵ but in terms of computing time the proposed method is much faster (1.46s for 2s of simulated time). This indicates again that the $d - q$ transformation of three sinusoidally distributed stator windings does not affect the representation of the phase currents.

The comparison of *ModelSupBB* using *methods 1* and *2* of *Implementation 2* and *ModelFullBB* is shown in figure 5.22. It can be seen that an error in the representation of the phase and the amplitude of the modulation is present. The fault modelled by *ModelSupBB* that would minimise this error is 2.1 broken bars with the first broken bar being the number 28 (out of 28). This is illustrated in figure 5.23.

As the effect of the stator on the rotor currents is neglected, the accuracy of this model decreases when the slip rises. As an example, the comparison of the running RMS value of the stator currents is shown in figure 5.24 for a speed of 1000rpm ($s=0.33$). *ModelSupBB* only represents correctly the behaviour of a faulty machine in low slip conditions.

5.3.4 Comparison of models for broken bars

In the previous sections, many comparisons have been made between the different implemented models representing a machine with broken bar. A summary is now proposed.

First of all, it is important to stress that the models *ModelHealthy*, *ModelSupBB*, *ModelParkBB* and *ModelFullBB* are equivalent in healthy conditions.

⁵The instant considered correspond to the maximum effect of one broken bar on the stator current I_{as}

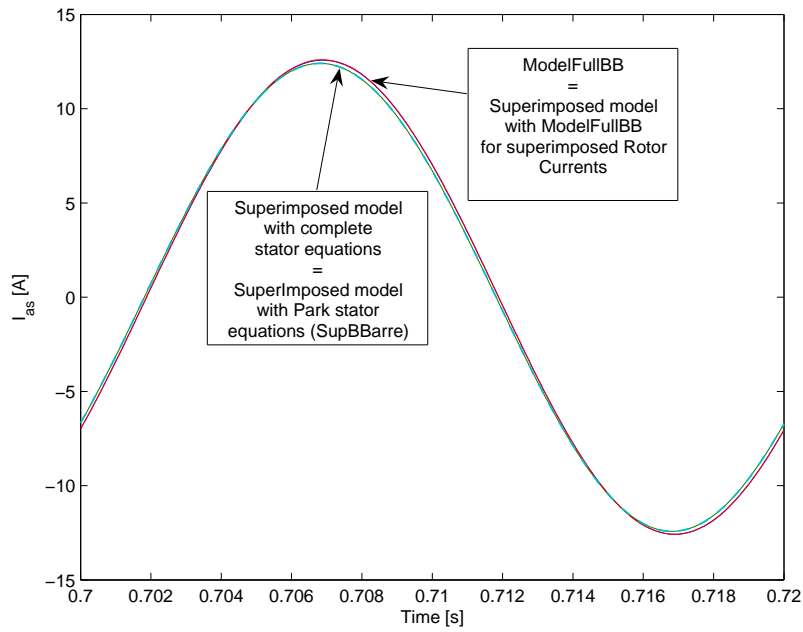


Figure 5.21: Stator Current I_{as} with 1 broken bar.

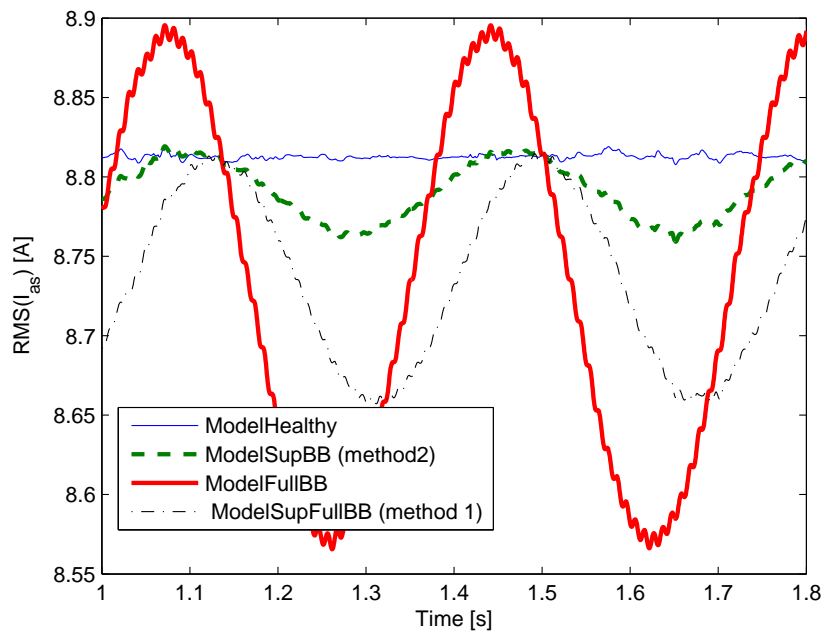


Figure 5.22: Comparison of the RMS values of the stator current at nominal load with 1 broken bar for the superimposed models.

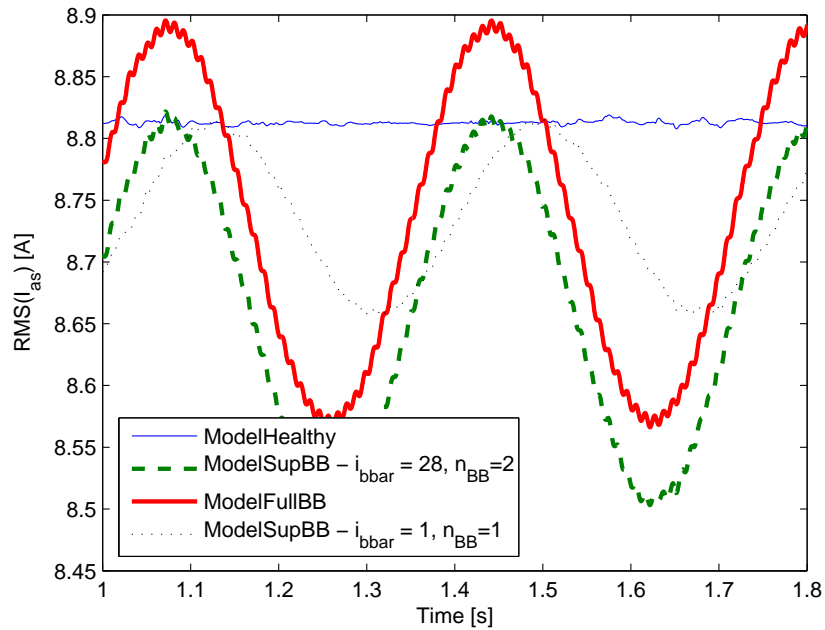


Figure 5.23: Effect of broken bar number and position on the RMS values of the stator current computed by *ModelSupBB*.

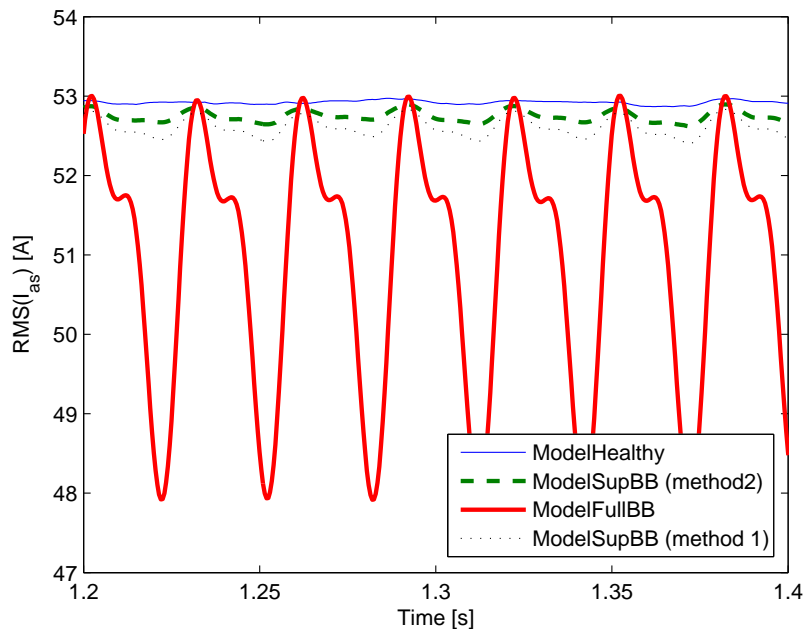


Figure 5.24: Comparison of the RMS values of the stator current at a speed of 1000rpm with 1 broken bar for the superimposed models.

Simulation	Computing time [s]				
	<i>ModelHealthy</i>	<i>ModelSupBB</i>		<i>ModelParkBB</i>	<i>ModelFullBB</i>
		Rotor Part	Stator Part		
Healthy	1	0	0	2.1	31
1 broken bar	1	0.9	1.5	2.1	57
2 broken bars	1	0.9	1.5	2.1	67
3 broken bars	1	0.9	1.5	2.1	73
4 broken bars	1	0.9	1.5	2.1	82
5 broken bars	1	0.9	1.5	2.1	85

Table 5.3: Computing time required by the different models to represent 2s of the machine behaviour.

ModelFullBB is the most precise as its only simplification on the equation of the mathematical model consists in the transformation of the three stator windings in equivalent $d-q$ windings. As long as the phase winding are sinusoidally distributed, this does not have any influence on the mathematical description of the machine. *ModelParkBB* represents fairly precisely the stator currents for low fault magnitudes but requires to realise the identification of its parameters by comparison with *ModelFullBB*. The main benefits of this model compared to *ModelFullBB* is the great reduction of computing time obtained by reducing the number of state variables from $n + 1$ to 4. If the utilisation of the model is limited to a small range of speeds around a certain working point, the representation of the stator currents can be even more accurate. The main drawback of this model is the incorrect representation of the rotor currents as it implies a sinusoidal distribution of the fault. *ModelSupBB* is the less precise for stator currents but offers a better representation of the rotor currents. Moreover, the superimposed approach requires low computing time as it is summarised in table *Please place \label after \caption*.

Therefore, *ModelFullBB* is well suited to realise a simulation platform of faulty machine. Implementation 1 of *ModelSupBB* gives identical accuracy with a much lower computing time as long as the speed variation due to the fault is neglected. Finally, simulation platform of the stator currents for low fault magnitude can be realised using *ModelParkBB*.

For fault diagnosis, *ModelParkBB* and implementation 2 of *ModelSupBB* can be used. The first one is more precise but requires more computing time if iterative calls for different fault magnitude are performed to detect and quantify the fault. More details will be given in section 7.3.

5.4 Conclusion on circuit modelling

In this chapter healthy and faulty induction machines are presented. These models are obtained from a common mathematical description of the machine. The use of this common description leads to an objective comparison of the accuracy and the computing time of the models. This information is quite valuable as one can draw conclusions on the proper use of the models.

Furthermore, it has been shown that the presence of faults greatly complicates the mathematical description as many symmetries present in healthy machines disappear. From a model representing the machine with all its asymmetries, a reduction of the complexity will require the use of approximations. Much work has been made in the comparison of the different approximation, balancing benefits and drawback of each.

The use of an appropriate $d-q$ reference frame allows to represent machine asymmetries. However this approach supposes a sinusoidal spatial repartition of the fault in this reference frame. The superposition

principle was also exploited to represent broken bars. Even though results are acceptable, limitations of the conditions of use of this model are numerous.

Another important achievement of this chapter is the formulation of the steady-state behaviour of a faulty machine at constant speed by a linear system of equations. The application of such method covers the initialisation of time domain faulty models as well as fault detection in steady-state.

In this chapter, thanks to the use of a common description, neither the identification of the parameters of the models nor the amount of data required to build the models has altered the comparison. This will be the subject of the next chapter.

Finally, through this study, it was possible to come up with two models of machines with broken bars suitable for on-line diagnosis. They will be used in such way in chapter 7.

Chapter 6

Parameter identification of circuit models

6.1 Introduction

In chapter 5, several models have been presented and compared. However, the practical use of a model greatly depends on the identifiability of its parameters, on the sensitivity of the outputs of the model to precision in identified parameters as well as on the ease one will have to identify the parameters. In literature, many procedures have been proposed and an important distinction can be made between "off-line" or "on-line" identification.

"Off-line" identification refers to methods for which the estimation of the parameters is performed using measurements obtained from different well-defined working points. Furthermore, the computing time does not matter since data analysis is made off-line.

"On-line" identification refers to estimations of the parameters using data from the current working point. Previous estimations are then often used as initial guess and the computing time of the method is of great importance.

In the field of model-based diagnosis of electrical machines, two main approaches are considered. Some authors propose to use a model of healthy machines where the values of some parameters are affected by the presence of the fault. For example, the variation of the rotor resistance in a 4-state-variables $d - q$ model of the machine is used in [Cho 92] as an indicator of the presence of a broken bar or broken end-ring. In these applications, the parameter estimation has to be performed on-line. The hypothesis on which is based this approach is that the model is the same if the machine is healthy or not. As it has been shown in section 3.3.1, for broken bars, the only change in the f component of the stator currents can be represented using a model primarily dedicated to healthy machines. However, this component is not the most sensitive to the presence of the fault. A similar conclusion has been drawn for other types of faults.

If a dedicated model is used for detection, its parameters are not dependant on the presence of the fault. Therefore, only the unknown inputs of this model, for example, the fault magnitude, will have to be determined on-line. In these cases, and depending on the model hypotheses, other frequency components than f can be represented and used as detection criterion. The drawback of these faulty-machine models is that they require, for the sake of accuracy, more computing time and hence less time is available for on-line identification of the parameters of the model.

Because this last approach is chosen for this work, off-line procedure for machine parameter estimation will be performed. A first section will be devoted to the parameter estimation of a healthy-machine model as most of the parameters of this model will be used to define the faulty-machine model. Afterwards, the rotor cage parameters required by models of faulty machines will be estimated.

6.2 Parameter estimation of healthy machine model (*ModelHealthy*)

When off-line measurements are available, many authors agree to use steady-state model equations (instead of dynamic model equations) obtained from a classical Park approach of the machine¹.

The interest of this approach is to use classical test results namely circle diagram and torque characteristic.

6.2.1 Model structure

In [Bellini 76, Cho 92, Corcoles 02, Araujo 02, Wang 05a, Wang 05b] the model structure presented in figure 6.1 is shown to be overparameterised. This has for consequence that several combinations of parameters lead to the same external characteristics.

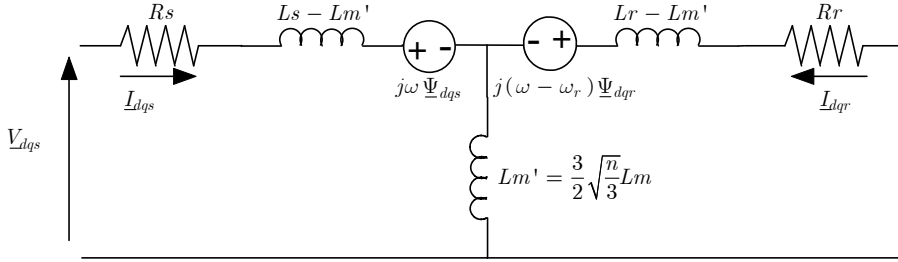


Figure 6.1: Classical Machine Model [Muñoz 99]

This is due to the unknown transformation ratio between the stator and the rotor windings. The ratio is unknown because no electrical measurements are taken on the rotor windings (especially in the case of squirrel cage machine) [Bellini 76].

Therefore, some authors propose to use construction details of the machine to univocally obtain the parameters [Bellini 76]. Another solution proposed in [Cho 92, Corcoles 02, Araujo 02, Abdelhadi 05] is to use a constraint by imposing the value of one of the rotor parameters L_r , L_m or R_r .

Finally, an electrical circuit based on a reduced number of parameters can also be used [Wildi 91, Araujo 02]. This can be seen as a constraint of the type: $L_{ls} = L_{lr}$, $L_{lr} = 0$ or $L_{ls} = 0$.

From the electrical circuit of figure 6.1, it can be written that

$$\begin{cases} V_{dqs} &= R_s I_{dqs} + p(L_s) I_{dqs} + p\left(\frac{3}{2}\sqrt{\frac{n}{3}} L_m\right) I_{dqr} \\ 0 &= R_r I_{dqr} + p s(L_r) I_{dqr} + p s\left(\frac{3}{2}\sqrt{\frac{n}{3}} L_m\right) I_{dqs} \end{cases} \quad (6.1)$$

where p is the Laplace operator. By eliminating I_{dqr} we obtain

¹This model is presented in detail in section 5.2

$$\begin{cases} \underline{I}_{dqr} &= \frac{-ps(\frac{3}{2}\sqrt{\frac{n}{3}}L_m)}{R_r+ps(L_r)} \\ \underline{Z}_s &= \frac{V_{dqs}}{\underline{I}_{dqs}} = \frac{R_s+p(L_s)+ps(\frac{L_r R_s}{R_r})+p^2s\left(\frac{L_s L_r - (\frac{3}{2}\sqrt{\frac{n}{3}}L_m)^2}{R_r}\right)}{1+ps(\frac{L_r}{R_r})} \end{cases} \quad (6.2)$$

In equation 6.2, we can see that only 4 parameters describe the behaviour of a machine with one rotor cage and no modelled core losses².

In [Corcoles 02], it is recommended to use the invariants (i.e. the 4 univocally identifiable parameters representing the behaviour of the machine)

$$\begin{aligned} A &= R_s \\ B &= L_s \\ C &= \frac{R_s L_r}{R_r} \\ D &= \frac{L_s L_r - (\frac{3}{2}\sqrt{\frac{n}{3}}L_m)^2}{R_r} \end{aligned} \quad (6.3)$$

$$\text{therefore } \underline{Z}_s = \frac{A+pB+psC+p^2sD}{1+ps\frac{C}{A}}.$$

In our approach, we will choose invariants commonly used in dynamic control:

$$\begin{aligned} A &= R_s \\ B &= L_s \\ C &= \frac{L_r}{R_r} \\ D &= 1 - \frac{(\frac{3}{2}\sqrt{\frac{n}{3}}L_m)^2}{L_s L_r} \end{aligned} \quad (6.4)$$

therefore $\underline{Z}_s = \frac{A+pB+psAC+p^2sBCD}{1+psC}$ where C is the well-known rotor time constant (T_r) and D is the total leakage factor (σ).

6.2.2 Identification procedure

The identification procedure is mainly formulated either as a curve fitting problem using a genetic algorithm [Abdelhadi 05] or a least square approach [Bellini 76, Abdelhadi 05, Cho 92]. This last possibility will be chosen. Best results are obtained using a numerical method based on the *fminsearch* function of the Matlab optimization toolbox. This function that realises a cost function minimisation using the simplex search method is called several time using previous results as new starting guess and so until change in the cost function becomes negligible.

Furthermore the different developed methods proposed in the literature mainly depend on the choice of

- the measurements used for the identification,
- the optimisation function,
- the working points used.

²Note that a similar approach is made in [Corcoles 02] for a machine with two rotor cages and iron losses. The conclusions are similar.

6.2.2.1 Choice of measurements used

In the literature we find identification procedures based on:

- Stator electrical quantities and speed or
- Stator electrical quantities, speed and torque.

Stator electrical quantities and speed In this category we can find algorithms that use either $(\underline{I}_s(s), \underline{V}_s(s))$ or $(|\underline{I}_s|(s), |\underline{V}_s|(s), P_s(s))$. Using these quantities, two equations can be written for each working point (i.e. for each value of the slip s); for example $\Re(\underline{Z}_s(s))$, $\Im(\underline{Z}_s(s))$ [Corcoles 02].

As the problem contains four invariants, at least two working points are needed to determine the set of parameters. Therefore, some authors define constant set of invariants for all speed for immunity of the identification to measurement noise [Lima 97] (i.e. in order to have more equations than unknowns). However, as the parameters of the machine change with load or voltage level (i.e. temperature, saturation and rotor frequency [Depenbrock 89]), a model with variable set of invariants, can be determined using a few working points in a small range of velocities [Cho 92] (i.e. more than two working points). The choice of the working points will be discussed in the section relative to the choice of the objective function. However, it can already be stressed that the equations used in the formulation should be "sufficiently" different to bring new information to the system of equations.

As example, we find in this category the determination of the 4 invariants using 2 working points for locked rotor and no-load situations. This leads to one set of invariants valid for the whole speed range. This set of invariants is often used as initial guess for a more elaborated estimation of parameters.

Stator electrical quantities, speed and torque In some cases, the torque characteristic is available. Therefore, the use of the torque equation for each working point gives us one more equation (i.e. three equations). Even though this number of equations is still lower than the number of parameters to determine, this information lowers the sensitivity of the identification process regarding to measurement noise.

However, this improvement of robustness is achieved at the cost of a torque sensor which is quite more expensive than classical current and voltage measurement devices, often already available in motor drives.

Conclusions In the considered application, only electrical stator quantities and speed will be used for the estimation of the parameters.

6.2.2.2 Choice of the cost function

In the previous paragraph, a discussion has been made about the number of equations that can be written for each working point. Regarding to which equations can be used, different systems can be found in the literature:

$$\left\{ \begin{array}{l} \Re(\underline{Z}_s(s)) \\ \Im(\underline{Z}_s(s)) \end{array} \right. \text{ [Corcoles 02]; } \left\{ \begin{array}{l} P_s(s) \\ |\underline{I}_s|(s) \\ T(s) \end{array} \right. \text{ [Lima 97]; ...}$$

Directly based on these equations, several cost functions can be built. The choice of the function has a significant influence on the results obtained when the model does not represent exactly the device from which the data are issued. Two different cost functions are used in the literature:

- A cost function based on $\begin{cases} \Re(\underline{Z}_s(s)) \\ \Im(\underline{Z}_s(s)) \end{cases}$;

$$F = \frac{1}{2} \sum_i \left(\begin{aligned} & \left(\Re(\underline{Z}_s(s_i)) - \Re(\hat{\underline{Z}}_s(s_i)) \right)^2 \\ & + \left(\Im(\underline{Z}_s(s_i)) - \Im(\hat{\underline{Z}}_s(s_i)) \right)^2 \end{aligned} \right) \quad (6.5)$$

- and a cost function based on $\begin{cases} \Re(\underline{I}_s(s)) \\ \Im(\underline{I}_s(s)) \end{cases}$;

$$F = \frac{1}{2} \sum_i \left(\left(I_{ds}(s_i) - \hat{I}_{ds}(s_i) \right)^2 + \left(I_{qs}(s_i) - \hat{I}_{qs}(s_i) \right)^2 \right) \quad (6.6)$$

where " ^ " represents the estimated value. The results obtained with these two cost functions will be compared in section 6.2.5 where the identification is done from data obtained by FE simulations.

6.2.2.3 Choice of working points

As it has been stated before, each equation used for the identification should bring new information to the system. As voltages are maintained throughout the whole speed range, a criterion will be built based on speed and current. The relative change in complex stator current and the change in speed between two consecutive working points should be higher than a certain threshold.

As example, if we state

- $\sqrt{\left(\frac{I_{ds}(i) - I_{ds}(i+1)}{I_{ds}(i)} \right)^2 + \left(\frac{I_{qs}(i) - I_{qs}(i+1)}{I_{qs}(i)} \right)^2} > 0.24$
- $|\Omega_i - \Omega_{i+1}| > 2 \text{ rpm}$

where i and $i + 1$ refer to two consecutive working points.

For a machine modelled using the electrical circuit of figure 6.1 and the invariants given in equation 6.7, the following set of working points (0, 739, 994, 1126, 1208, 1266, 1310, 1344, 1372, 1396, 1417, 1434, 1448, 1460, 1469, 1476, 1482, 1486, 1489, 1492, 1494, 1496, 1498, 1500)rpm can be found. The thresholds are chosen to have 24 working points throughout the speed range. A condition on the speed is present to avoid the presence of too many points in low slip condition with very small speed changes.

$$\begin{aligned} R_s &= 0.9032\Omega \\ L_s &= 0.1353H \\ T_r &= 0.2090s \\ \sigma &= 0.0525 \end{aligned} \quad (6.7)$$

This set of data, shown in figure 6.2a, will be used to test the identification algorithm before using it with data obtained for either measurements or FE computations.

6.2.3 Data used to study the convergence of the formulation

In order to study the convergence of the formulation, two sets of data will be used. In both sets, currents and speed are given at the same working points:

- **Analytical Model** : This first set of data is generated using the same model as the one used for the identification. This should lead to the correct identification of the parameters with a residual error of the objective function numerically null. The parameters are given by equation 6.7. The stator voltages have a magnitude of 190V and the currents are shown in figure 6.2a.
- **FE Model** : This second set of data is generated using magneto-dynamic FE simulations of machine *INDI*. The stator voltages have a magnitude of 190V and the currents are shown in figure 6.2b.

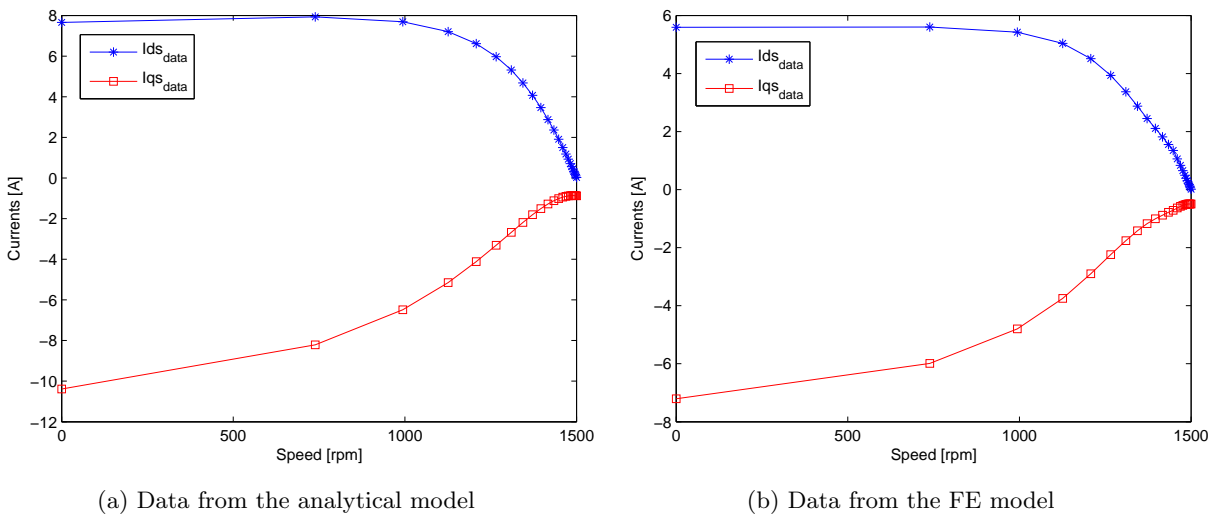


Figure 6.2: Data used for parameter identification.

6.2.4 Convergence of the identification

In the section on the model structure (6.2.1), two approaches have been compared:

- A model with 5 parameters and one constraint.
- A model with 4 invariants.

The convergence of the models listed above will be studied in order to obtain a formulation that allows to get, in the least amount of time, the best set of parameters. The cost function chosen will be the one in current (equation 6.6).

In the following sections, the convergence of the algorithms is studied on well-known issues:

- Presence of local minima;
- Sensitivity of the identification to noise on data;
- Sensitivity of the identification to error on invariants.

6.2.4.1 Does the identification presents problematic local minima?

By problematic local minima it is meant local minima in which the iterative least square algorithm can be stuck. In these situations, the algorithm will not find the set of parameters that produces the lower residual error (Global minimum).

In non-linear problems the choice of the initial guess may be important. The authors of [Lima 97, Minami 91] recommend for their formulation of the problem to use initial guesses as close as possible to the solution that produces the lower residue to avoid local minima.

As we have stated before, the constraint should be defined using for example the transformation ratio. However, the choice of this value has no impact on the ability of the model to represent the machine from the stator side but it has some influence on the convergence of the least-square algorithm.

To illustrate this statement and find the constraint that best conditions the problem we will run the identification process using the 8 constraints³ proposed in equation 6.8 and the formulation in invariants (9).

$$\begin{aligned}
 R_s &= cst & (1) \\
 R_r &= cst & (2) \\
 L_s &= cst & (3) \\
 L_r &= cst & (4) \\
 L_m &= cst & (5) \\
 L_{ls} &= L_s - L'_m = 0 & (6) \\
 L_{lr} &= L_r - L'_m = 0 & (7) \\
 L_{ls} &= L_{lr} & (8)
 \end{aligned} \tag{6.8}$$

However, as R_s and L_s are invariants, the overparametrisation of the model will not be reduced using constraints (1) and (3). Therefore the equation 6.8 leads to:

$$\begin{aligned}
 R_r &= cst & (2) \\
 L_r &= cst & (4) \\
 L_m &= cst & (5) \\
 L_s &= \frac{3}{2}\sqrt{\frac{n}{3}} L_m & (6) \\
 L_r &= \frac{3}{2}\sqrt{\frac{n}{3}} L_m & (7) \\
 L_s &= L_r & (8)
 \end{aligned} \tag{6.9}$$

In the literature, constraints (6) and (7) are recommended in [Corcoles 02] while constraint (8) is used in [Cho 92, Wang 05a].

Computation of the basin of attraction The basin of attraction of the global minimum will be defined as the set of initial values that will lead the algorithm to a solution which is the global minimum.

In a system of coordinates based on the invariants, this locus is a region in 4 dimensions. A visualisation is therefore complicated. We will compute and present for every formulation the projection of this locus in the planes:

³The numerical values of the constants have no influence on the convergence of the formulation. For information, these values are set to $R_r = 1.2917\Omega$, $L_m = 0.0406H$ and $L_r = 0.27H$.

$$\begin{aligned}
(R_s, L_s) &= (100\%, 100\%) \\
(R_s, T_r) &= (100\%, 100\%) \\
(R_s, \sigma) &= (100\%, 100\%) \\
(L_s, T_r) &= (100\%, 100\%) \\
(L_s, \sigma) &= (100\%, 100\%) \\
(T_r, \sigma) &= (100\%, 100\%)
\end{aligned} \tag{6.10}$$

where the units are chosen in percent of the optimum value. The locus is computed for each invariant at values $[\frac{1}{8}, \frac{1}{7}, \frac{1}{6}, \frac{1}{5}, \frac{1}{4}, \frac{1}{3}, \frac{1}{2}, 1, 2, 3, 4, 5, 6, 7, 8] * 100\%$.

Only the most interesting projections are shown in figure 6.3. The necessary conditions on initial guesses for the convergence of the algorithm are summarised in table 6.1.

Formulations	Invariants			
(2)	-	$L_s \leq 300\%$	$20\% \leq T_r$	$\sigma \leq 200\%$
(4)	$R_s \leq 600\%$	-	$20\% \leq T_r \leq 700\%$	-
(5)	-	-	$33\% \leq T_r$	$17\% \leq \sigma$
(6)	$33\% \leq R_s$	$L_s \leq 100\%$	-	$20\% \leq \sigma$
(7)	-	$L_s \leq 200\%$	-	-
(8)	$17\% \leq R_s$	$L_s \leq 200\%$	$25\% \leq T_r$	$20\% \leq \sigma$
(9)	-	-	-	-

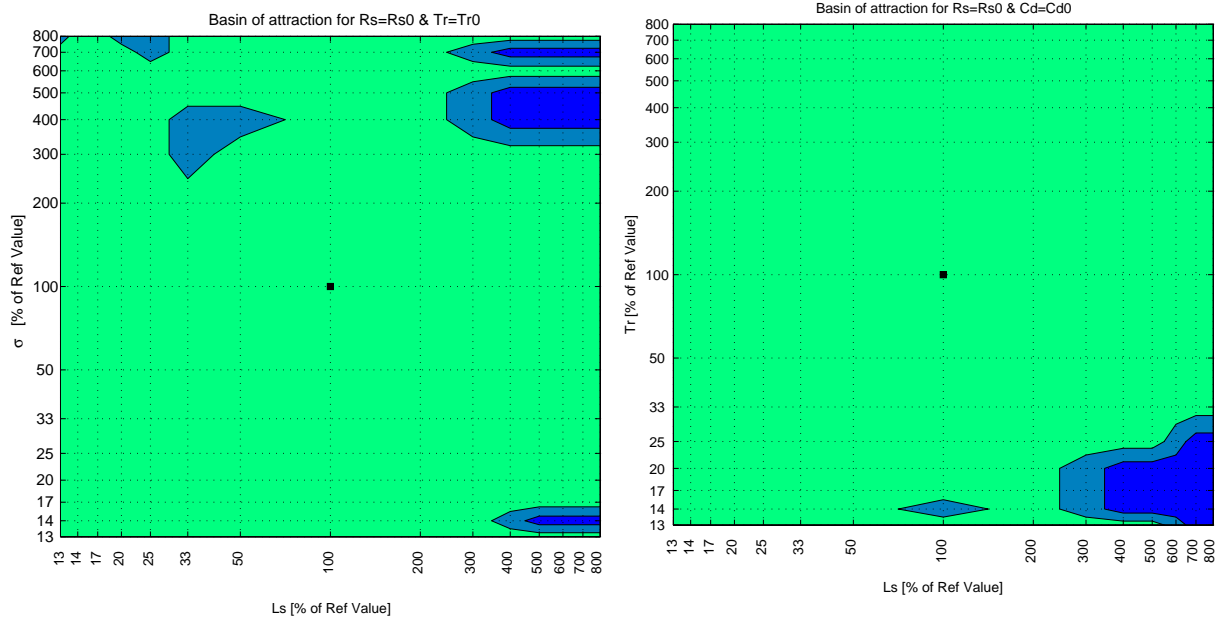
Table 6.1: Minimal necessary conditions on initial guesses for correct convergence.

Random initial condition in the entire region In order to give a cross validation of the previous test, for each formulation, the estimation using 1000 different initial guesses is performed. The sets are randomly chosen in a range between 25% and 400% of the set that gives the minimum residue. The deviation between the different solution sets is quantified using a distance (d) function defined by equation 6.11.

$$d = \frac{1}{5(N_{test} - 1)} \sqrt{\left(\frac{\sum_{i=2}^{N_{test}} |R_s(i) - R_s(1)|}{R_s(1)} \right)^2 + \left(\frac{\sum_{i=2}^{N_{test}} |R_r(i) - R_r(1)|}{R_r(1)} \right)^2 + \dots + \left(\frac{\sum_{i=2}^{N_{test}} |L_m(i) - L_m(1)|}{L_m(1)} \right)^2} \tag{6.11}$$

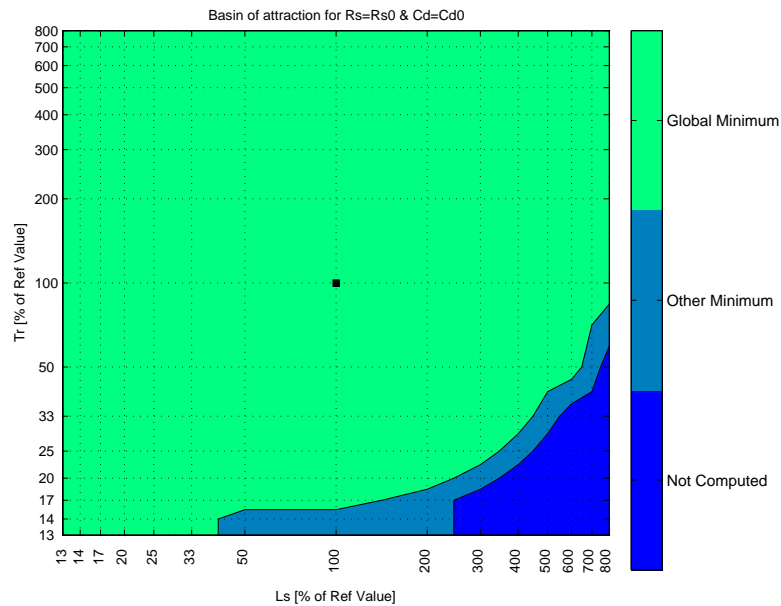
where N_{test} refers to the 1000 computations. Results are presented in figure 6.4.

From the analysis of the figure, it can be concluded that the use of constraints (4), (5) and (7) as well as a formulation in invariants lead to a good conditioning of the formulation with residues, for each initial guess, numerically null and a distance between the solution sets very small. Furthermore, the formulation in invariants requires a computing time smaller than the formulations with parameters. From now on, the focus will be set on a formulation based on the invariants.



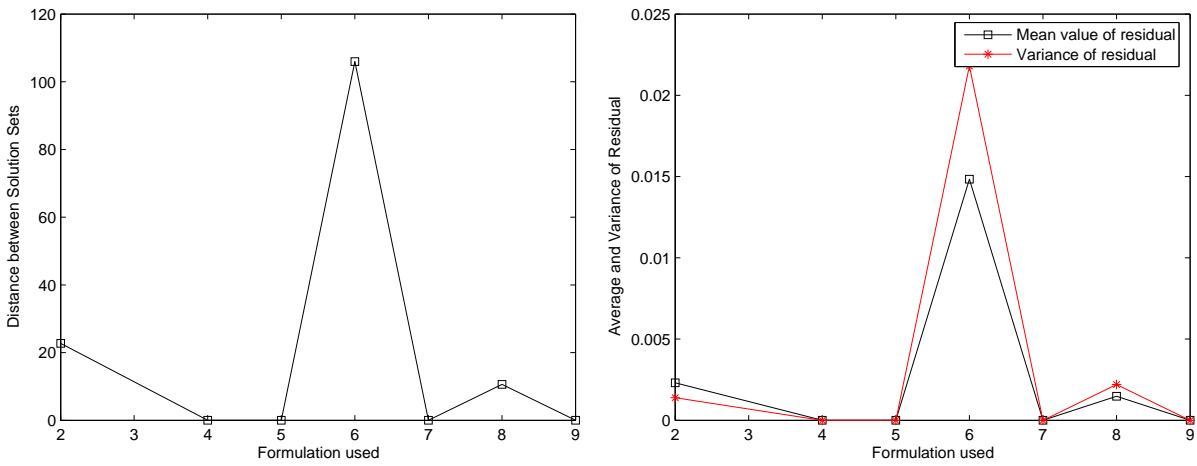
(a) Constraint (2) plane
 $(R_s, T_r) = (100\%, 100\%)$

(b) Constraint (5) plane
 $(R_s, \sigma) = (100\%, 100\%)$



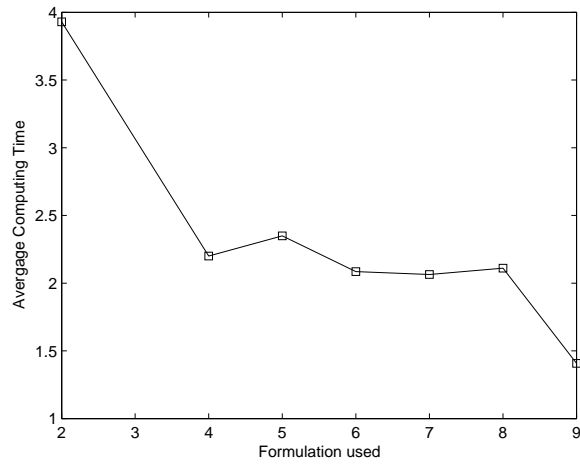
(c) Constraint (8) plane
 $(R_s, \sigma) = (100\%, 100\%)$

Figure 6.3: Projections of the basin of attraction.



(a) Distance between solution sets

(b) Average and variance values of residue



(c) Average Computing time

Figure 6.4: Comparison of the convergence based on the constraint

6.2.4.2 Sensitivity of the identification to noise on the measurement of the currents, voltages or speed

The sensitivity of parametric identification using invariants is tested using 1000 sets of data containing first a 1% uniform noise on the stator currents, then a 1% uniform noise on the stator voltages and finally a 1rpm uniform noise of the rotation speed. As before, the data contain 24 working points throughout the whole speed range of the motor. The results are shown in table 6.2.

Noise on Data	Mean error on Invariants [%]				Residue [A]	
	R_s	L_s	T_r	σ	Mean	Variance
(1% on I)	0.045%	0.005%	0.010%	0.004%	0.014A	$4.6 \cdot 10^{-6} A$
(1% on V)	0.007%	0.004%	0.012%	0.001%	0.014A	$8.5 \cdot 10^{-6} A$
(1 rpm on Ω)	0.012%	0.003%	0.014%	0.003%	0.01A	$1.5 \cdot 10^{-6} A$

Table 6.2: Error on Invariants due to noise in data.

It can be observed that the determination of the parameters is quite accurate even though noise is present in the data. This parametric identification algorithm can therefore be considered quite insensitive to noise on the data.

6.2.5 Identification using data from FE simulation

The identification will now be made on the data shown in figure 6.2b. These data are obtained from FE simulations. The computation is made using previously explained algorithms and a formulation with invariants (R_s , L_s , T_r and σ).

6.2.5.1 Constant parameters for all working points

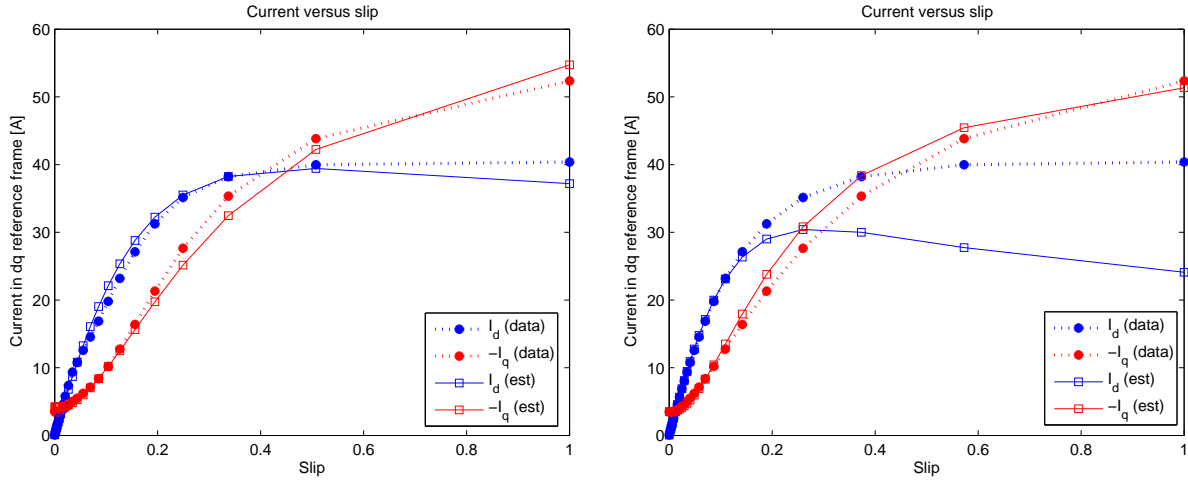
A first goal is to find one set of invariants that matches the behaviour of the machine for all speeds. The results presented in table 6.3 are compared using the two cost functions proposed in section 6.2.2.2.

Formulation in Impedance	Formulation in Current
$R_s = 0.7901 \Omega$	$R_s = 0.9072 \Omega$
$L_s = 0.1625 H$	$L_s = 0.1356 H$
$T_r = 0.2783 s$	$T_r = 0.2093 s$
$\sigma = 0.0559$	$\sigma = 0.0523$
Residue using Equation 6.5 = 0.0431 Ω /working point	Residue using Equation 6.5 = 0.4402 Ω /working point
Residue using Equation 6.6 = 0.4856 A/working point	Residue using Equation 6.6 = 0.1656 A/working point

Table 6.3: Residue versus formulation

Table 6.3 shows that both algorithms stopped for a small value of the cost function. However, a minimum value of the residue (F) based on the impedance does not coincide with a minimum value of the residue (F) based on the stator currents.

The d and q axis currents computed by the model using the obtained sets of invariants are compared to the data values of the currents. Currents obtained using both formulations are shown in figure 6.5a and figure 6.5b



(a) Cost function based on the currents.

(b) Cost function based on the impedance.

Figure 6.5: Comparison of stator currents from the FE data or computed by the model.

It appears clearly that the formulation using the impedance will not optimise the representation of the stator currents. Therefore, the formulation of the identification procedure will greatly depend on the objective of the model. In the present case, the model will feed a fault detection algorithm based on the currents. The formulation in current will therefore be used.

6.2.5.2 Sensitivity of the solution for each invariant

In order to test the sensitivity of the solution to variation of the invariants, each of them will be modified in a range from 85% to 115% of the value given by the optimisation algorithm. While an invariant is changed, the others are retained at their value given by the algorithm.

In order to quantify this sensitivity, a "parametric error index" which is the amount by which each invariant could vary without causing more that a 50% increase of the residue is used [Stephan 94].

The residues are then computed while changing the value of one of the invariants at the time. The results are shown in figure 6.6.

The "parametric error index" for each of the invariants are shown in table 6.4.

Parametric error index of			
R_s	L_s	T_r	σ
24.9%	7.4%	12.1%	11.4%

Table 6.4: Parametric error index for each invariant.

It can be seen that the value of R_s has the smallest influence on the residue. This has two consequences:

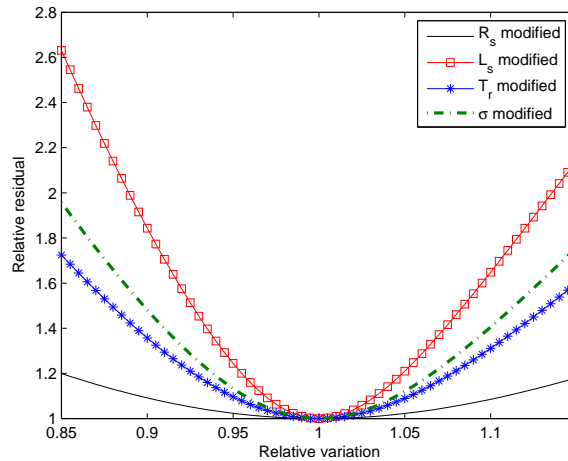


Figure 6.6: Residue versus solution set around optimal solution

- First, it means that the accuracy of the model will not depend much on the determination of R_s ;
- Secondly, if one wants to precisely determine R_s , another technique should be used. For example, R_s can be estimated prior the other parameters by injecting DC current into the stator coils [Lee 01].

This is in agreement with results of previous section where noise on data was primarily affecting R_s .

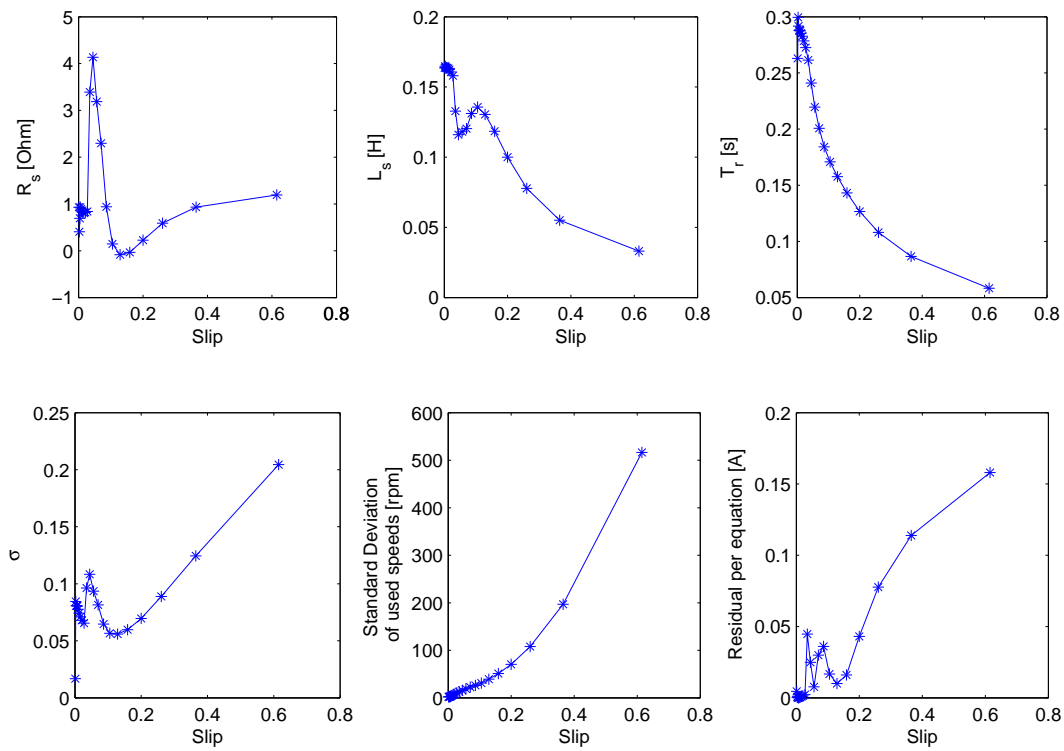
6.2.5.3 Parameters function of the working point

Our second goal is to identify parameters of the machine that depend on the working point. Three working points in a small range of speeds will be used to compute a set of parameters valid in the neighbourhood of these working points. Results of the computations are shown in figure 6.7a. For the presentation of the results, the parameters are computed from the solution set in invariants using the constraint $L_m = 4.06 \cdot 10^{-2} H$. These are shown in figure 6.7b. The d and q axis currents computed by the model are compared to the data values of the current in figure 6.8.

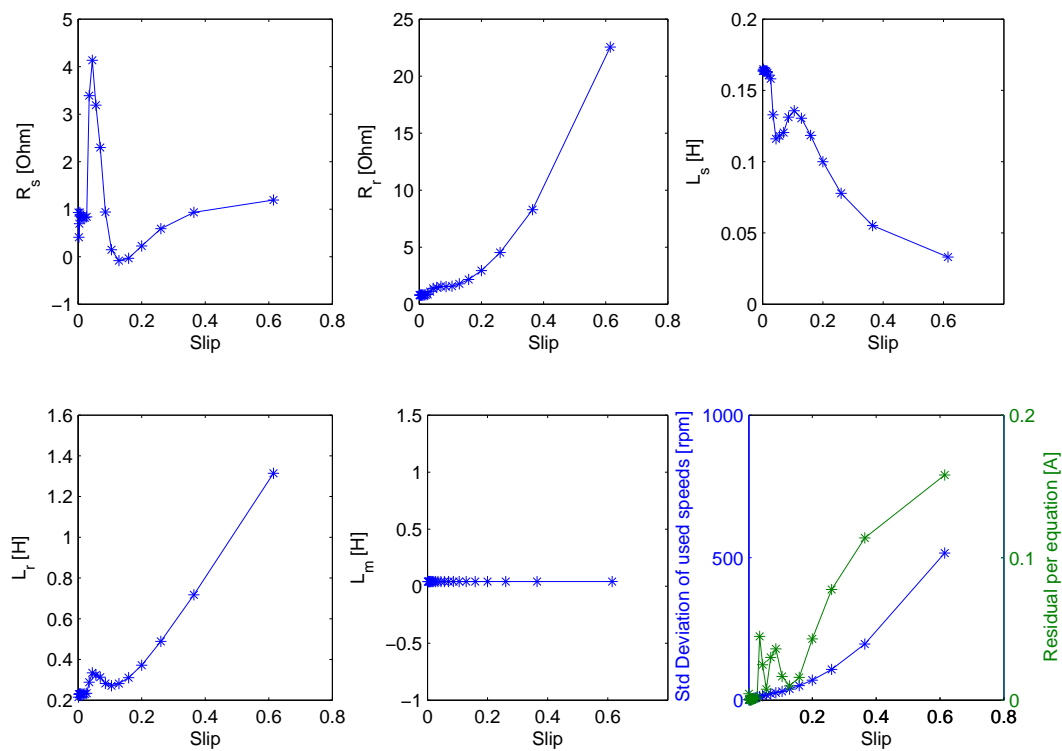
From the analysis of the figures, it appears that the residue per equation is much lower than in the case of an identification with constant parameters for the whole speed range. However, the variation of the invariants (or the parameters) with speed can be difficultly explained. Some doubts can arise on the accuracy of the data used to represent the induction machine in high slip conditions. Indeed, the use of magneto-dynamic simulations is not recommended in such conditions as it has been shown in section 3.2.3.3.

Furthermore, the computation of the "Parametric error index" for each invariant and each identification based on three working points is shown in figure 6.9. The sensitivity of the residue to a variation of R_s is low. This is in agreement with the conclusions that have been drawn for an identification based on the whole speed range. It can also be observed that the sensitivity of the residue to change in T_r rises with the slip.

Finally, the correspondence between the data and the output of the model is better using variable parameters. However the practical use of such model is less easy. Therefore, for now on, a model with constant parameters for the whole speed range will be used.



(a) Invariants



(b) Reconstructed parameters from the invariants

Figure 6.7: Solution of the identification using groups of three adjacent working points.

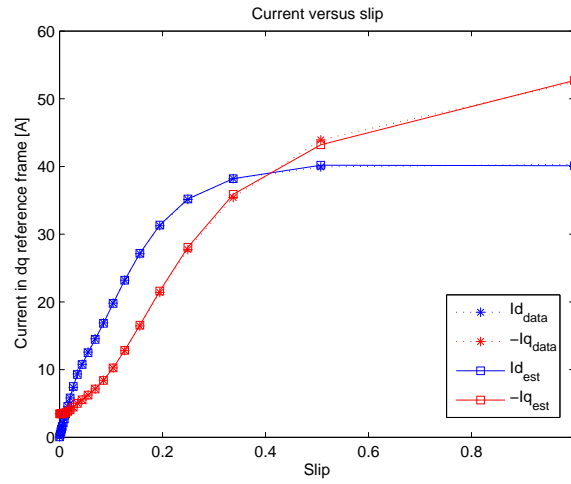


Figure 6.8: Comparison of stator currents from the FE data or computed by the model.

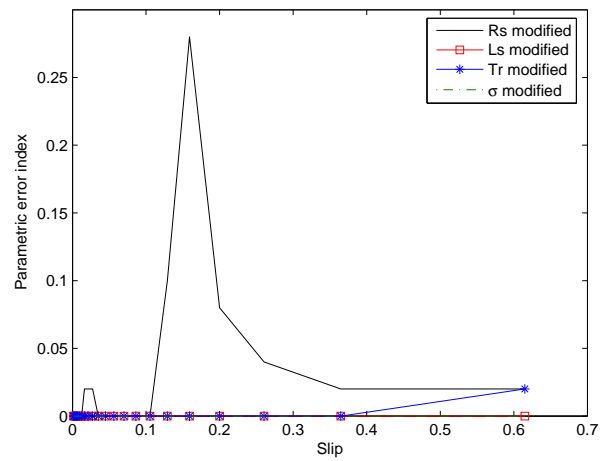


Figure 6.9: Parametric error index for each invariant and each identification.

6.2.6 Simulation results

The above identification has been made using steady-state implementation of *ModelHealthy* and magneto-dynamic FE computation. Results show good agreement specially when working points used for the parameter identification process are limited to a small range of speeds around the comparison working point.

The current can be plotted versus time at nominal speed and compared to FE results obtained under the same conditions. This is done in figure 6.10. The FE results are filtered at 120Hz to remove slot and saturation harmonics. In the figure is also plotted the difference between the two outputs.

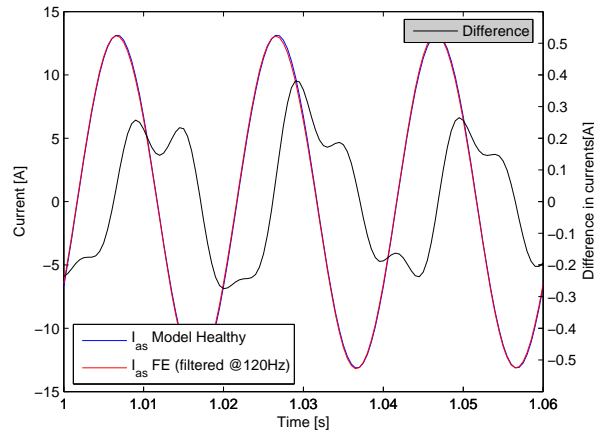


Figure 6.10: Comparison between I_a from healthy model and FE simulation at nominal speed.

The fundamental amplitude is correctly represented but a time shift is present between the results. This can clearly be seen on the error ripple. If this time shift is fictively removed, the error stays below 0.24A which is lower than 2.6% of the RMS value of the current.

This time shift has several origins:

- the time shift between magneto-dynamic and transient simulation (see section 3.2.3). Indeed, magneto-dynamic results were used for the parametric identification while time-domain results are compared to the model outputs.
- and the necessity for the parameter identification process to use data from several working points.

When using a constant set of parameters for all speed, error with time-shift compensation stays below 4.4% of the RMS value of the current.

6.2.7 Conclusions

The previous section has presented a non-linear least square algorithm used to determine the parameters of a classical model of healthy machines. The use of the physical parameters leads to an overparametrisation of the problem and best identification is obtained through the use of four invariants R_s , L_s , T_r and σ .

Only stator voltages, currents and rotor speed have to be measured in steady state operation and at least two working points are necessary to determine the solution.

When an error of modelling is present, it is important to choose an objective function in regard of the goal of the model. As an example, if the stator currents have to be reconstructed accurately by the model, the objective function should be based on d and q components of the currents.

However, the proposed approach does not assure a precise identification of the parameters but the precise reconstruction of the objective function using the model. As example, R_s will not be precisely identified while the stator currents are precisely represented by the model.

6.3 Estimation of the rotor cage parameters

As it was shown in the previous section, in the representation of healthy machines using Park transformations, the only necessary knowledge of the rotor circuit are R_r and L_r . However, some models built to represent a machine with broken bars or end-rings, require knowing the resistances and inductances of the elements constituting the rotor cage (R_b , R_e , L_b , L_e , L_{kk} and L_{ki}) as shown in figure 6.11⁴.

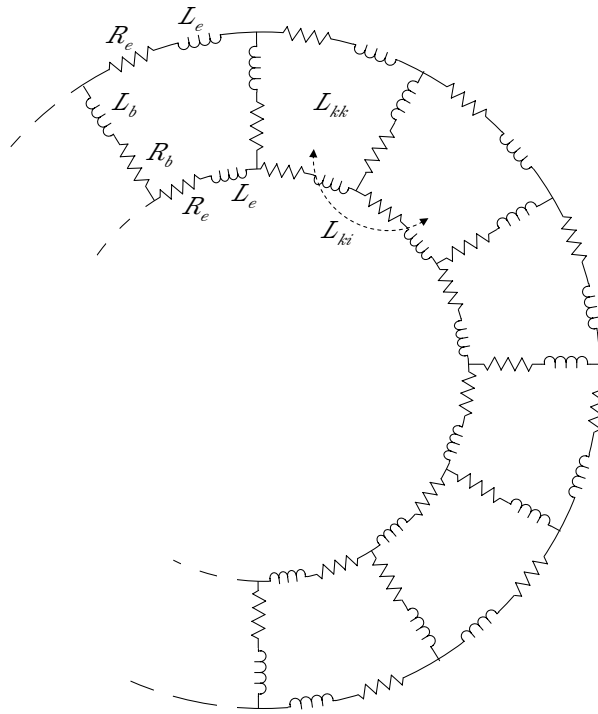


Figure 6.11: Rotor Electrical Circuit.

As before, from the stator point of view an infinite number of rotor cages have the same behaviour. From the demonstration of the analytical Park model for healthy motors (*ModelHealthy*), it has been shown that

$$R_r = 2R_e + 2R_b (1 - \cos(P \alpha_r)) \quad (6.12a)$$

$$L_r = 2L_e + 2L_b (1 - \cos(P \alpha_r)) + \frac{\mu_0 l r}{g} \alpha_r \quad (6.12b)$$

⁴Note that these elements are also required for the modelling of a healthy machine without Park transformation.

where R_e and L_e are the end-ring segment resistance and inductance, R_b and L_b are the bar resistance and inductance, l is the rotor stack length, r is the radius in the middle of the airgap, g is the airgap width and $\alpha_r = \frac{2\pi}{n}$.

In appendix A, L_{kk} and L_{ki} are expressed as $L_{kk} = \frac{\mu_0 l r}{g} \alpha_r (1 - \frac{\alpha_r}{2\pi})$ and $L_{ki} = \frac{\mu_0 l r}{g} \left(-\frac{\alpha_r^2}{2\pi}\right)$ and therefore, equation 6.12b becomes

$$L_r = L_{kk} + L_0 - 2L_b \cos P \alpha_r - L_{ki} \quad (6.12c)$$

The parameters of the rotor cage can not be determined without rotor measurements in the healthy machine. Some authors are using construction details of the rotor and empiric formulae. Some of these formulae have been used in section 3.2.2.2.

In this work, we propose to perform FE simulations of induction machines that bring forward the effect of most of the cage elements. An interesting situation is the phenomenon linked to the presence of a broken bar.

- Approach 1: A first FE simulation consists in the modelling of *IND1* with opened stator windings and a current source placed in series with one of the bars. The rotor speed is imposed and the iron permeability of each mesh element is fixed at its value given by the situation of the healthy and normally fed motor. The parameters of the rotor circuit of figure 6.12 are computed using non-linear minimisation algorithm. The residue is built by comparing the rotor bar currents given by the FE simulation to the ones obtained from the resolution of the rotor circuit.

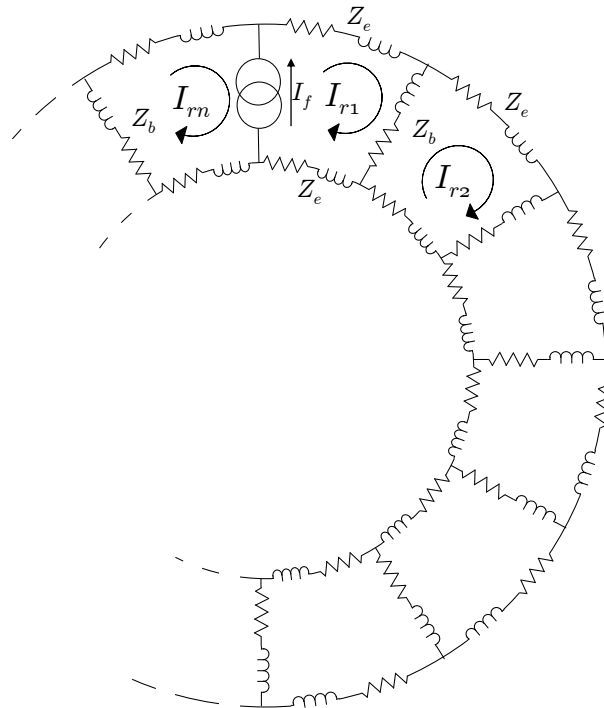


Figure 6.12: Rotor electrical circuit for FE simulation.

- Approach 2: Another possibility consists in getting similar data by subtracting the currents computed by a FE simulation of a healthy machine and of a machine with one broken bar. The advantage of

this approach is that it easily represents the superimposed effect of a rotor bar without the need to freeze rotor permeability. However, as the effects of the stator winding and the changes of local saturation are not modelled with the circuit of figure 6.12, it will lead to less accurate estimation of rotor parameters.

As it has been detailed in chapter 3, a 2D FE simulation requires the knowledge of end-ring resistance and inductance. The estimation of their values was presented in section 3.2.2.2.

6.3.1 Data of FE simulations

- Approach 1: A time-domain FE simulation of the machine with frozen permeability (see section 3.3.3) is performed to represent 1s of simulated time with a time step of $5 \cdot 10^{-5}$ s. The speed is chosen to be nominal (i.e. 1459rpm). From the results, the last fundamental period of the rotor currents ($f_{rot} = sf$) is extracted and used to determine the rotor phasors presented by the curve with square-markers in figure 6.13.

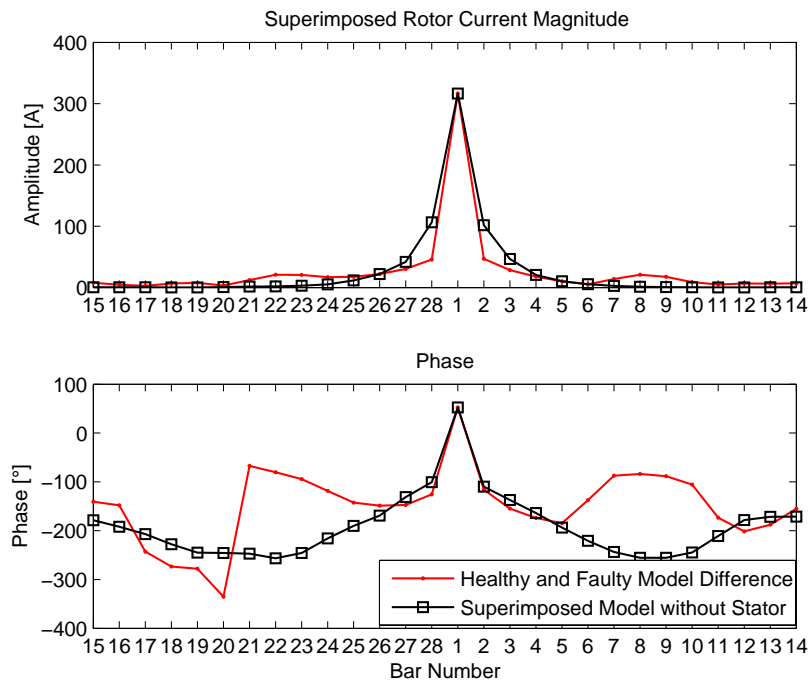


Figure 6.13: Rotor phasors extracted from the two presented FE approaches

- Approach 2: The rotor phasors are obtained by difference between healthy (*SimNoBB*) and faulty simulations (*SimBB*) results. They are presented in the same picture by the curve with dot-markers. In this figure, differences between the two approaches are clear. They are mainly due to the presence of the stator windings. Indeed, the magnetic field created by the "fault current" mainly induces currents in the stator conductor of the slot situated in front of the broken bar. However, in the case of a 2-pole machine, the stator windings are distributed in several slots. Some of them are adjacent to the first one (slots of the same phase and same pole) while others are located approximately 180 electrical degrees away from the first one (slots of the same phase and the other pole). The current

flowing in these conductors will create a field that will induce, in its turn, EMF and therefore currents in the bars situated in front of them.

In the case of the two pole-pairs parallel-connected machine with 28 bars (i.e. *IND1*), the situation is slightly different. The bar situated at 180° from the broken bar must be located under the same pole pair as the broken bar to see induced current in its material. This is alternatively the case of the bar at $+180^\circ$ (Bar8) and at -180° (Bar22) from the broken bar (Bar1). Differences between the currents of these bars from healthy and faulty simulations are shown in figure 6.14. In order to bring forward the studied effects, the currents have been filtered at 150Hz to remove the influence of slot harmonics. The figure shows that the current of Bar8 and 22 are oscillating between two values. The current having the smallest absolute value is flowing in the bar when it is situated under the other pole pair than Bar1. The current having the highest absolute value is flowing in the bar when this bar and Bar1 are situated under the same pole pair. Therefore, the current phasor of this approach (shown in figure 6.13) correspond to an average between these two situations.

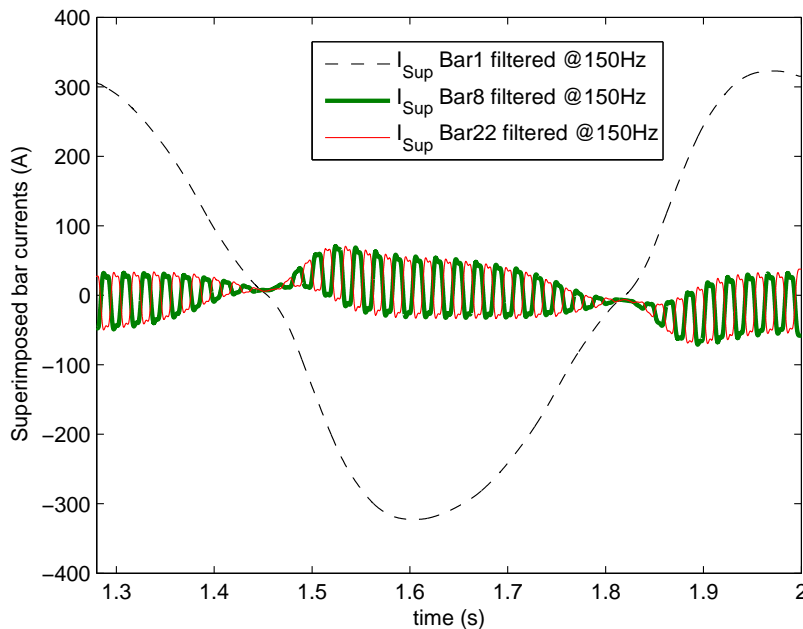


Figure 6.14: Superimposed rotor bar currents filtered at 150 Hz to remove the influence of the slots

6.3.2 Parameter estimation

As it can be observed on figure 6.13, the situation is symmetrical with regard to the current source/broken bar. Therefore, the identification of the rotor parameters can be made using half of the rotor currents and half of the rotor circuit of figure 6.12. This half circuit is shown in figure 6.15a and further reduction can be realised using Thevenin-Norton transformation as shown in figure 6.15b for an even number of bars. The situation is quite similar when the number of bars is uneven.

In steady-state, the electrical circuit can be described using

$$\underline{E} = R\underline{I} + j s \omega \underline{I} \quad (6.13)$$

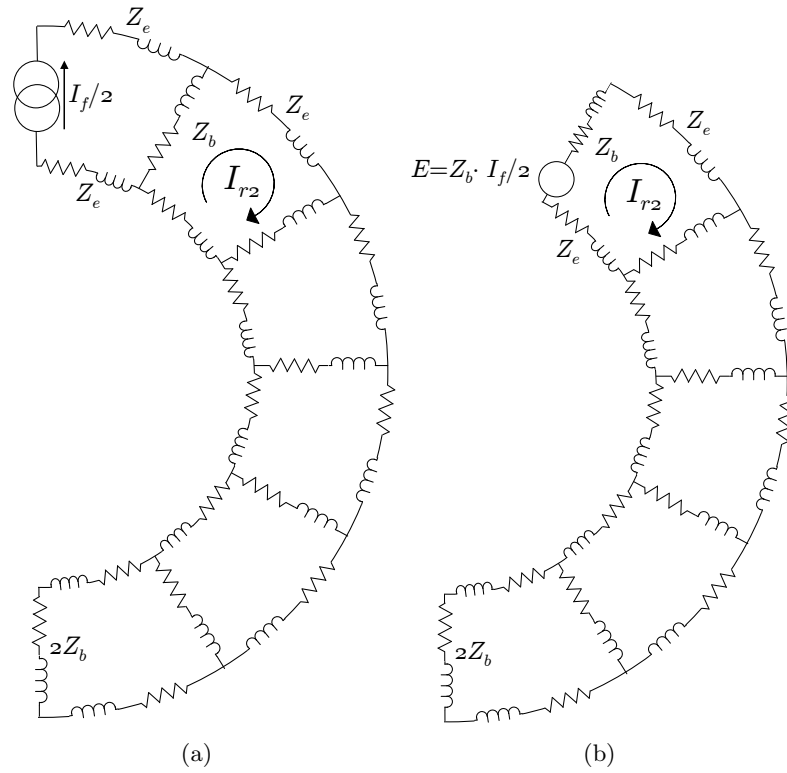


Figure 6.15: Simplification of the rotor circuit.

$$\text{with } \underline{E} = \begin{bmatrix} R_b + j s \omega L_b \frac{I_f}{2} \\ 0 \\ \vdots \\ 0 \end{bmatrix}, R = \begin{bmatrix} R_0 & -R_b & 0 & 0 \\ -R_b & \ddots & \ddots & 0 \\ 0 & \ddots & R_0 & -R_b \\ 0 & 0 & -R_b & R_0 - 2R_b \end{bmatrix}$$

$$L = \begin{bmatrix} L_0 + L_{kk} - L_{ki} & -L_b & 0 & 0 \\ -L_b & \ddots & \ddots & 0 \\ 0 & \ddots & L_0 + L_{kk} - L_{ki} & -L_b \\ 0 & 0 & -L_b & L_0 + L_{kk} - L_{ki} - 2L_b \end{bmatrix}$$

and

$$I = \begin{bmatrix} I_{r2} \\ I_{r3} \\ \vdots \\ I_{r \frac{n}{2}} \end{bmatrix}$$

The length of vectors is $\frac{n}{2} - 1$ and the size of matrices is $(\frac{n}{2} - 1) \times (\frac{n}{2} - 1)$. It is important to understand that mutual-coupling between rotor loop j and the other rotor loops does not appear in the inductance matrix as the contribution of loops $n - i$ and i cancel each other except when $i = j$. The $\frac{n}{2}^{\text{th}}$ rotor loop is different from the other ones as a double bar impedances appear in this half circuit.

Furthermore, as equation 6.13 shows, the curve fitting algorithm without constraints will lead to null values of the parameters as it corresponds to the solution $0 = 0 \cdot I$ where I are the currents given by

the FE simulation. A constraint is realised by equations 6.12a and 6.12b. This also assures to have the same stator-rotor transformation ratio as the one fixed by the constraint defined in section 6.2.5.3.

Furthermore, inductances L_0 , L_{kk} and L_{ki} only appear in the group $L_0 + L_{kk} - L_{ki}$ in equation 6.13. It is therefore not possible to identify separately the three terms.

Based on previous considerations, the variables used for the identification are R_b and L_b . The other parameters can be obtained from these variables after the identification procedure using

$$\begin{aligned} R_b &= R_b \\ R_0 &= R_r + 2 R_b \cos P \alpha_r \\ L_b &= L_b \\ L_{kk} + L_0 - L_{ki} &= L_r + 2 L_b \cos P \alpha_r \end{aligned}$$

6.3.3 Results

Before starting the error minimisation algorithm data are treated to enhance precision. The treatment consists in the symmetrisation of the FE current distribution. This is realised by replacing $I_{bar}(i)$ and $I_{bar}(n - i + 2)$ by $\frac{I_{bar}(i) + I_{bar}(n - i + 2)}{2}$.

Using $R_r = 1.2870\Omega$ and $L_r = 0.2694H$, obtained in section 6.2.5 with constraint $L_m = 4.06 \cdot 10^{-2}H$, and using data from the FE simulation of approach 1, we find the following values:

$$\begin{aligned} R_b &= 2.225\Omega \\ R_0 &= 5.296\Omega \\ L_b &= 8.008 \cdot 10^{-2}H \\ L_{kk} + L_0 - L_{ki} &= 4.137 \cdot 10^{-1}H \end{aligned} \tag{6.14}$$

The residual error is given by $R = \frac{1}{n} \sqrt{\sum_{i=1}^n |I_{bar}(i)|_{reconstructed} - I_{bar}(i)|_{FE}|^2}$ and is equal to $R = 0.41981 A$.

In figure 6.16a, the reconstructed superimposed rotor currents using the circuit equation and the parameter values are compared to the symmetrised superimposed rotor currents given by the FE simulation. The imprecision in the phase estimation of the bar currents of bars 9 to 21 is not relevant as the magnitude of these currents is very small⁵.

If approach 2 is used, the identification of the rotor parameters is less precise as it leads to the parameters of equation 6.15 with a residue $R = 1.8011 A$. The reconstructed superimposed rotor currents are shown figure 6.16b. Note that, in opposition to figure 6.16a that represents amplitude and phase of the currents, this figure shows the real and imaginary parts to better understand that the identification method is based on an error minimisation process.

$$\begin{aligned} R_b &= 2.396\Omega \\ R_0 &= 5.604\Omega \\ L_b &= 8.409 \cdot 10^{-1}H \\ L_{kk} + L_0 - L_{ki} &= 1.785H \end{aligned} \tag{6.15}$$

⁵Note that the error is due to an imprecise FFT of a signal containing more energy in its harmonic than in the fundamental component.

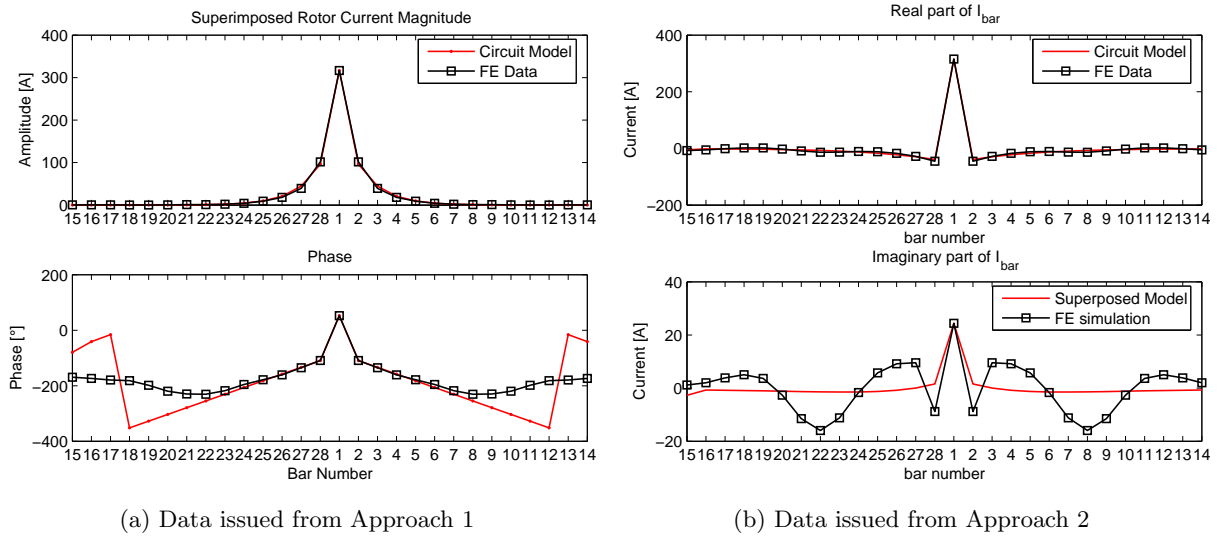


Figure 6.16: Comparison of superimposed rotor currents from circuit model and FE simulation.

Further tests are realised using a batch of 500 randomly chosen initial guesses taken between 0 and 50 times the optimal value. Each estimation leads exactly to the same solution. Therefore a precise pre-knowledge of the parameters is not required.

6.3.4 Conclusions

Two FE approaches are used to determine some of the rotor cage parameters. The approach for which the data match the most the circuit model gives the best results but simpler tests, close enough to the modelled phenomenon could also lead to a good approximation of the parameters.

The fact that all the parameters are not identified is not important in this work as the goal is not to have a precise identification of the parameters but rather to be able to correctly represent the stator currents of a healthy machine and of one with broken bars. In the first situation, only the group of rotor parameters $2R_e + 2R_b(1 - \cos(P\alpha_r)) (= R_r)$ and $L_{kk} + L_0 - 2L_b \cos P\alpha_r - L_{ki} (= L_r)$ will influence the stator currents whereas in the second situation, the groups R_b , R_0 , L_b and $L_{kk} + L_0 - L_{ki}$ will influence the stator currents.

6.4 Conclusions

The modelling of induction machines requires parameters that the user needs to determine. It is very important to have a clear idea of the goal of the parameter identification. Indeed, a precise knowledge of the parameters is not always required when the user is only interested by the outputs of the model built upon these parameters. However, in other applications, such as fault detection, the knowledge of the parameters representing the fault magnitude or its position is more important. This will lead to different methodologies.

Furthermore, the problem should always be formulated in order to have a unique solution. The analysis of the classical equivalent circuit of an induction motor has been made and four unique parameters

have been determined using steady-state measurements at different working points. A conclusion regarding this topic has been already developed in section 6.2.7.

A method based on FE simulation has been proposed to determine the rotor cage parameters as the determination of these parameters using only stator measurement on a healthy machine is not possible. The conclusion of this part was presented in section 6.3.4.

Chapter 7

Implementation of fault detection

7.1 Introduction

In this chapter, different methods for detection and quantification of faults are proposed. Most of the effort will be based on the quantification of broken bars by means of model-based approach.

The algorithms are tested using results from FE simulations developed in chapter 3. The main features of each of these scenario is presented in table 7.1. Each scenario represents about 2s of machine run. The quantification by means of models will be compared to the quantification based on the forementioned frequency technique MCSA (see section 4.5.3).

7.2 Detection and quantification using MCSA

In order to perform a precise FFT, the discrete time vector $I_{as}(i)$ should be such that $I_{as}(i) = I_{as}(i + kN)$ where N is the length of the vector and k is any integer.

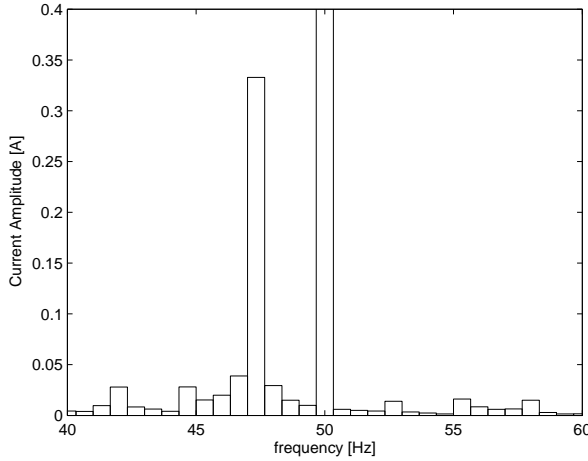
In the case of stator currents of a machine with rotor faults, some of the frequency components are not multiple of the supply frequency (f). If the above-mentioned criterion is not satisfied, frequency leakage can be observed for the frequency components whose period can not fit an integer number of times in the time window considered [DeFatta 88, p. 259]. The resulting discontinuities of the signal create additional spectral contributions in the neighbourhood of the frequency considered. These effects can be attenuated using weighting function. As example, the stator currents of a machine with one broken bar at nominal load and under constant speed contains frequency components at f and $(1 - 2s)f$. If the time vector is analysed, the amplitude of the f component is oscillating at $2sf$ with $s = 0.02733\dots$. The obtained signal is not rigorously periodic and spectral leakage will always be present in a frequency spectrum based on a time window of finite length. In normal load conditions, the oscillation of the fundamental amplitude is present at very low frequency (2.73Hz for nominal load). The leakage of the f component must be avoided because the high amplitude of this component is situated very close to the component of the fault signature $((1 - 2s)f)$. Therefore, best results for the frequency spectra are obtained using a sampling frequency multiple of the fundamental frequency and a time length containing an integer number of period of f and as close as possible to an integer number of the period of the oscillation at $2sf$. To illustrate these conclusions, figure 7.1 shows results for different time-windows for a machine at nominal load and with one broken bar. This figure proposes a zoom of the FFT results for low amplitudes of the frequency

Name	Mechanical Characteristics	Broken bar	Stator short-circuit	Eccentricity
<i>Sim1</i> (<i>Sim-NoBB</i>)	Full load (1459 rpm), Infinite inertia	-	-	-
<i>Sim2</i> (<i>SimBB</i>)	Full load (1459 rpm), Infinite inertia	1 BB	-	-
<i>Sim3</i>	Full load (1459 rpm), Finite inertia	1 BB	-	-
<i>Sim4</i>	Full load (1459 rpm)	0.5 BB	-	-
<i>Sim5</i>	Full load (1459 rpm)	2 BB	-	-
<i>Sim6</i>	Full load (1459 rpm), Oscillating torque	-	-	-
<i>Sim7</i>	Full load (1459 rpm), Oscillating torque	1 BB	-	-
<i>Sim8</i>	Low load (1480 rpm)	-	-	-
<i>Sim9</i>	Low load (1480 rpm)	1 BB	-	-
<i>Sim10</i>	Full load (1459 rpm)	-	10% short circuit	-
<i>Sim11</i>	Full load (1459 rpm)	-	-	40% static ecc.
<i>Sim12</i>	Full load (1459 rpm)	-	-	40% Dynamic ecc.
<i>Sim13</i>	Full load (1459 rpm)	-	-	20% static ecc. and 20% dynamic ecc.
<i>Sim14</i>	Transient situation from 1000rpm to 1500 rpm	-	-	-
<i>Sim15</i>	Transient situation from 1000rpm to 1500 rpm	1 BB	-	-
<i>Sim16</i>	Transient situation from 1500rpm to 1459 rpm	-	-	-
<i>Sim17</i>	Transient situation from 1500rpm to 1459 rpm	1 BB	-	-

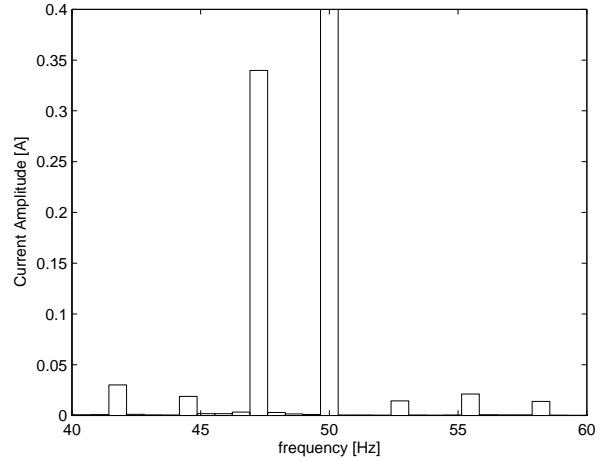
Table 7.1: Reference scenarios

around 50Hz. This zoom allows to focus on the amplitude of the faulty component. The best results are shown in figure 7.1b.

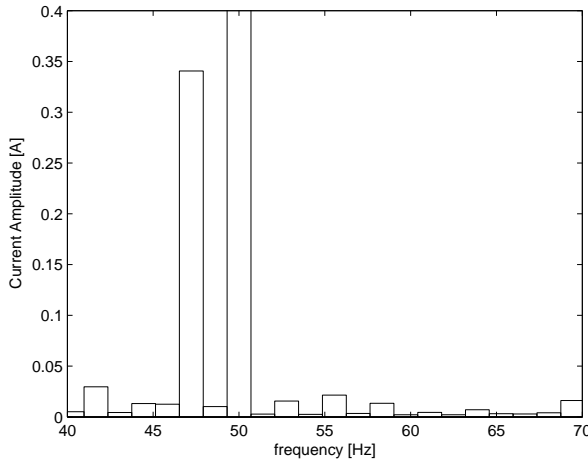
Furthermore, in the case of a rectangular window, the frequency resolution is directly linked to the inverse of the duration of the time window. Therefore, in low slip condition, the window must be long in order to separate f and $(1 - 2s)f$ components. However, as the period of the oscillation increases when the slip decreases, about one period of this oscillation is a sufficient criterion to distinguish the different frequency components. This is illustrated in figure 7.1c.



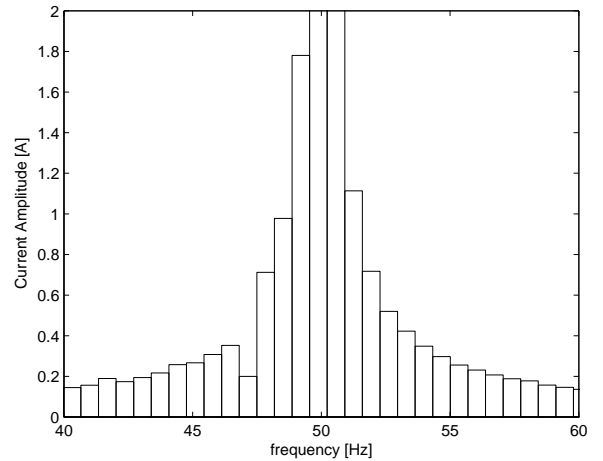
(a) Time vector of 1.5s - Important leakage of $(1 - 2s)f$



(b) Time vector of 1.46s (Approximately 2 periods of the oscillation) - Low leakage of $(1 - 2s)f$



(c) Time vector of 0.73s (Approximately 1 period of the oscillation) - Low leakage of $(1 - 2s)f$ and low frequency resolution



(d) Time vector of 1.4634s (Exactly 2 periods of the oscillation) - Important leakage of f

Figure 7.1: Spectra of stator currents using windows of different lengths.

It is to be recalled that, in the FE simulations, the supply frequency is precisely known and remains constant at 50Hz. However, this is not always the case in practice. A sampling frequency chosen to be a multiple of the line frequency is valuable. Furthermore, perfect steady-state conditions are rarely

encountered during a time frame as long as couple of seconds. Therefore, practical frequency spectra are expected to be of less good quality as the ones presented in this work.

The quantification using this method will be made using formula proposed in [Bellini 00] and already discussed in chapter 4. The estimated number of broken bars (\hat{n}_{BB}) is given by

$$\hat{n}_{BB} = n \frac{I_{(1-2s)f} + I_{(1+2s)f}}{I_f}$$

where I_x is the amplitude of the x Hz component of the stator current. This approach is mainly presented as comparison with other methods presented further down this chapter. The results are given in table 7.2.

FE Simulation	MCSA \hat{n}_{BB}
<i>Sim1</i> (Full load, NoBB)	$7.0 \cdot 10^{-4}$
<i>Sim2</i> (Full load, 1BB)	0.77
<i>Sim3</i> (Full load, 1BB, Finite J)	0.68
<i>Sim4</i> (Full load, 0.5BB)	0.36
<i>Sim5</i> (Full load, 2BB)	1.65
<i>Sim6</i> (Full load, NoBB, Osc. T_r)	0.79
<i>Sim7</i> (Full load, 1BB, Osc. T_r)	0.73
<i>Sim8</i> (Low load, NoBB)	$1.4 \cdot 10^{-3}$
<i>Sim9</i> (Low load, 1BB)	0.63
<i>Sim10</i> (Full load, 10% Short-circuit)	$1.7 \cdot 10^{-2}$
<i>Sim11</i> (Full load, 40% Stat. ecc.)	$6.6 \cdot 10^{-2}$
<i>Sim12</i> (Full load, 40% Dyn. ecc.)	$3.9 \cdot 10^{-3}$
<i>Sim13</i> (Full load, 20% Stat. ecc. & 20% Dyn. ecc.)	$1.4 \cdot 10^{-2}$
<i>Sim14</i> (Trans 1100-1459 rpm, NoBB)	—
<i>Sim15</i> (Trans 1100-1459 rpm, 1BB)	—
<i>Sim16</i> (Trans 1480-1459 rpm, NoBB)	—
<i>Sim17</i> (Trans 1480-1459 rpm, 1BB)	—

Table 7.2: Quantification by means of MCSA.

Except for healthy situations and torque oscillations, the method always tends to underestimate the number of broken bars. The healthy situation is correctly identified except when torque oscillations are present. In this last situation, the method finds 0.79 broken bars which is comparable to the 0.77 broken bar result in case of one broken bar at nominal speed.

7.3 Detection of broken bars using circuit models

In this section, we will propose a method to detect and quantify broken bars using the comparison of the measured stator currents with the stator currents computed by a model taking into account the presence of broken bars. In order to perform the diagnostic two quantities must be estimated. The first one is the number of broken bars (\hat{n}_{BB}) while the second one is the position of the broken bars. It has to be stressed that this unknown parameter is directly linked to the initial rotor position, part of the initial state of the model, which is unknown. Using any of the models presented in chapter 5, it is impossible to determine this initial rotor position using stator measurements as long as the machine is healthy. Indeed, for a sinusoidal

distribution of the stator windings, the rotor position has no influence on the stator currents when the machine is healthy. However, once a broken bar is present, a quantity regrouping the initial rotor position and the broken bar position can be estimated. In this work, we will always consider the breakage of bar number 1 and the estimation of the rotor position ($\hat{\theta}_0$) will be the sum of the actual initial rotor position and the angle between the real broken bar and bar number 1. The estimations are realised by comparing the 50Hz running RMS values of the measured stator currents to the running RMS values of the stator currents computed by the models. This is presented in figure 7.2. The reason for using the running RMS is to be insensitive to small phase shifts between measured and simulated currents. These phase-shifts can stem from the filtering stage or the imprecision of the model in the representation of the stator currents. This has been discussed in chapter 6.

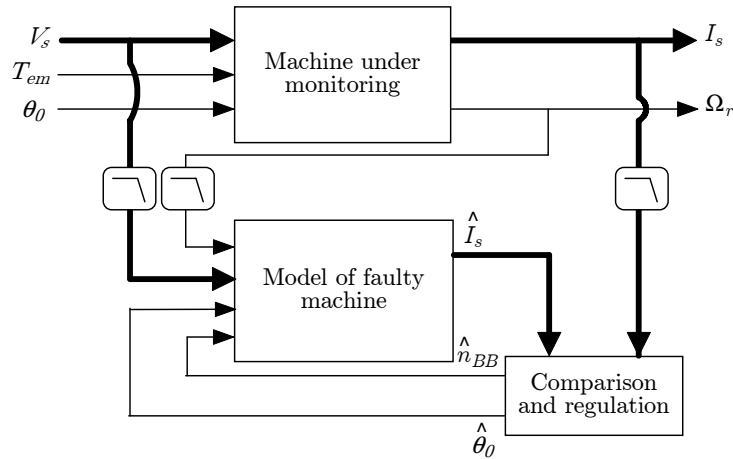


Figure 7.2: Monitoring set up.

Two different models of faulty machines are considered for diagnostic; *ModelSupBB* and *ModelParkBB*. More information on these models was provided in chapter 5.

In the following section, the fault detection is performed off-line which means that the computing time and the dynamic of the estimation of the two unknowns are not considered. Later, algorithms for on-line detection will be proposed.

7.3.1 Off-line implementation of the fault detection

7.3.1.1 Accuracy in the representation of the machine behaviour

In the first part of this section, we will build a quantity (R) that we have to minimise in order to determine the accuracy of the models to represent the measurements. The fault detection will be first based on data issued from *ModelFullBB* and only later from data provided by the FE simulations.

A first residue could be defined as the squared error between the RMS values of the models and the data. This is realised by

$$R = \frac{1}{\text{RMS}(I_{a_{Data}})} \sqrt{\frac{1}{N} \sum_1^N (\text{RMS}(I_{a_{Data}}) - \text{RMS}(I_{a_{Model}}))^2} \quad (7.1)$$

where N is the number of points in the time window. In this section, the time window considered represents about 0.5s of simulated time.

In the case of an estimation using *ModelParkBB* and data generated with *ModelFullBB* for one broken bar, at full load and with an initial rotor position of 160.9° , the values for \hat{n}_{BB} and $\hat{\theta}_0$ that minimise the residue are $\hat{n}_{BB} = 1.09$ and $\hat{\theta}_0 = 159.16^\circ \pm k90^\circ$ where k is any integer. The residue is $R = 1.8 \cdot 10^{-3}$. Figure 7.4 illustrates this first residue versus the two unknowns. The running RMS value of the stator currents for this solution is shown in figure 7.3. The running RMS value of *ModelParkBB* and *ModelFullBB* are close as the first model has been build by curve fitting with the latter.

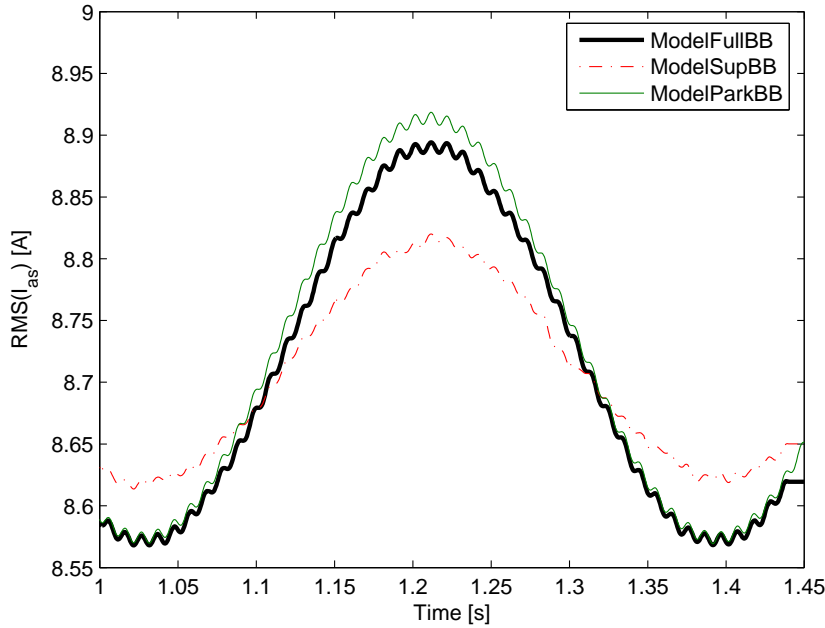


Figure 7.3: Running RMS value of the stator currents for estimated unknowns using the first residue.

As this is a two pole-pairs machine, one would expect to have the same effect on the stator currents for bars situated 180° apart. However, if the influence of the broken bar on the RMS value of the stator currents is considered, only the position of the bar regarding to the absolute value of the stator field matters. Therefore, the situation of bar 1 broken or of bar 8 broken (90° apart) will lead to the same stator currents but offset by a time depending of the rotating speed. This explains the set of estimated initial rotor positions spaced by 90° . Figure 7.4 shows that the influence of the initial rotor position becomes less important when the estimated number of broken bars becomes small. At the limit, when the estimated number of broken bars is null, the initial rotor position has no influence on the stator currents computed by the model as it has been stated before.

ModelSupBB leads to a less precise fit with $R = 4.7 \cdot 10^{-3}$ as shown in figure 7.3. Furthermore, the estimated values $\hat{n}_{BB} = 1.45$ and $\hat{\theta}_0 = 147.8^\circ$ are farther from simulated ones.

A new residue is defined by removing a constant offset from the RMS values of the stator currents of the model and from the data before applying formula 7.1. Using this new residue, another set of optimal values can be found. This is especially the case for *ModelSupBB* due to the fact that, on top of the error due to incorrect estimation of the unknowns, an error of modelling is present between *ModelSupBB* and *ModelFullBB*. The running RMS value of the stator currents for the new optimal solution using *ModelSupBB*

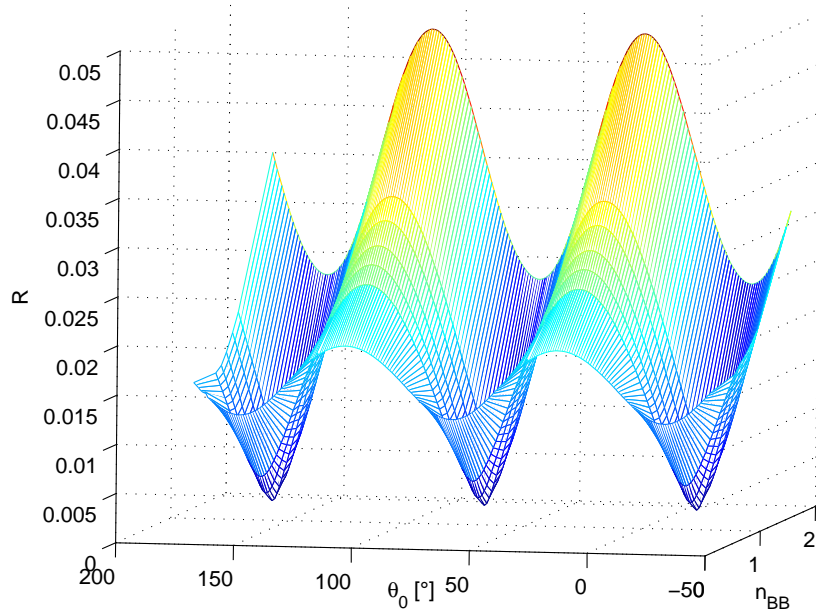


Figure 7.4: First residue versus estimation of unknowns using *ModelParkBB*.

($\hat{n}_{BB} = 2.1$ and $\hat{\theta}_0 = 147.81^\circ$) is shown in figure 7.5. The modification brought by this new residue is quite less pronounced for the estimation using *ModelParkBB* where the new optimal solution, $\hat{n}_{BB} = 1.05$ and $\hat{\theta}_0 = 159.80^\circ$ is similar to the previous one.

The use of the first residue will lead to estimated stator currents closer to the stator currents used as data. However, the second residue will best represent the oscillating component of the RMS value which is characteristic of the fault and will not take into account the fundamental component. This can be an advantage as a circuit model with constant parameters for the whole speed range will be imprecise in the representation of the 50Hz component of the stator currents obtained through measurements or generated by FE models.

In fault detection using models, the chosen residue should emphasize the sensitivity of the model to the quantities linked to the fault and lower its sensitivity to perturbing effects. In transient conditions, the offset may not be constant as the representation of the 50Hz currents can be more precise for certain speeds than for others. This effect being of lower magnitude will be neglected. In the section on on-line diagnosis, the chosen residue will be based on this second approach.

The values of \hat{n}_{BB} of each model that minimise the second residue (R) is shown in table 7.3. As it was suggested in chapter 5, *ModelParkBB* leads to a good estimation of the number of broken bars for the low fault magnitudes studied in this work. Furthermore, the error in the localisation of the fault is lower than 5° even in transient conditions. If the initial rotor position was precisely known this could allow the localisation of the fault. However, in practice, this quantity is of lower importance as the initial rotor position is rarely recorded.

ModelSupBB allows accurate fault detection but quantification is only acceptable for low fault magnitudes ($n_{BB} \leq 2$) and/or low slip conditions. Furthermore, the use of this model leads to a bad estimation of the number of broken bars in high slip conditions ($\hat{n}_{BB} = 5.8$ instead of 1 for *Sim15*). For all tested

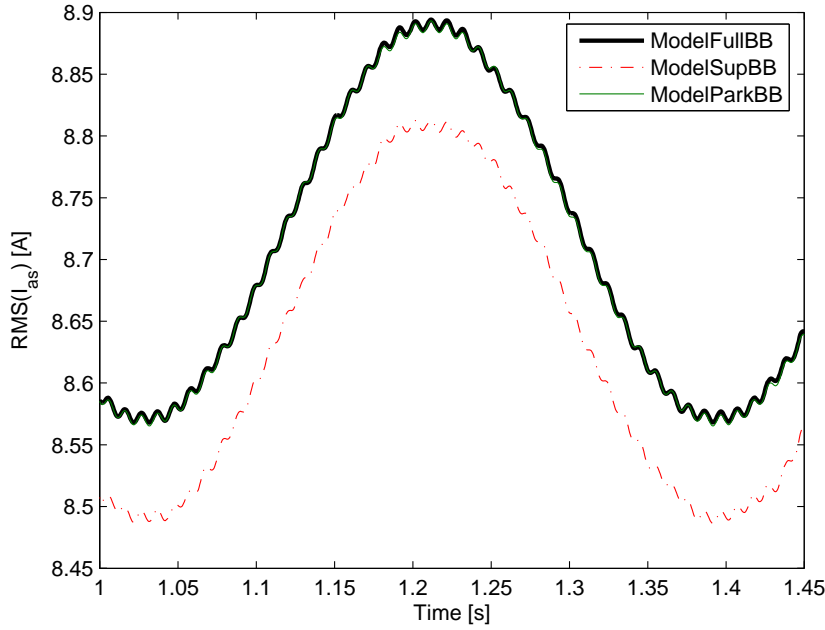


Figure 7.5: Running RMS value of the stator currents for estimated unknowns using the second residue.

conditions, it clearly tends to overestimate the number of broken bars as its estimation for one broken bar is 2.1 and for two broken bars is 5.4 at nominal load. The estimation of the initial rotor position is less accurate than *ModelParkBB* and is in the range of 7° to 13° . The results of *Sim 2* and *ModelSupBB* is very similar to the ones of chapter 5 where bar 28 was broken. Indeed the angle between two adjacent bars is 12.86° which is similar to the 13.09° error in the estimation of the initial rotor position.

It is important to emphasize that both models correctly identify healthy conditions and their performances are very similar in steady-state or transient situations.

<i>ModelFullBB</i>	<i>ModelSupBB</i>				<i>ModelParkBB</i>		
	n_{BB}	R	\hat{n}_{BB}	$\theta_0 - \hat{\theta}_0$	R	\hat{n}_{BB}	$\theta_0 - \hat{\theta}_0$
OK <i>Sim1</i> (Full load)	0	$2.0 \cdot 10^{-4}$	$6.2 \cdot 10^{-4}$	-	$2.2 \cdot 10^{-4}$	$6.2 \cdot 10^{-4}$	-
<i>Sim2</i> (Full load)	1	$3.1 \cdot 10^{-4}$	2.09	13.09°	$1.6 \cdot 10^{-4}$	1.05	1.1°
<i>Sim4</i> (Full load)	0.5	$4.4 \cdot 10^{-4}$	0.78	8.19°	$3.7 \cdot 10^{-4}$	0.57	-4.39°
<i>Sim5</i> (Full load)	2	$3.7 \cdot 10^{-4}$	5.42	7.32°	$9.8 \cdot 10^{-5}$	1.95	1.06°
<i>Sim8</i> (Low load)	0	$2.4 \cdot 10^{-4}$	$2.5 \cdot 10^{-4}$	-	$1.9 \cdot 10^{-4}$	$63 \cdot 10^{-7}$	-
<i>Sim9</i> (Low load)	1	$1.0 \cdot 10^{-4}$	1.34	9.28°	$2.8 \cdot 10^{-4}$	1.06	-0.02°
<i>Sim14</i> (Trans 1100-1459 rpm)	0	$3.9 \cdot 10^{-4}$	0.05	-	$6.7 \cdot 10^{-4}$	$1.2 \cdot 10^{-4}$	-
<i>Sim15</i> (Trans 1100-1459 rpm)	1	$1.9 \cdot 10^{-2}$	5.8	7.18°	$1.2 \cdot 10^{-3}$	1.11	3.98°
<i>Sim16</i> (Trans 1480-1459 rpm)	0	$2.4 \cdot 10^{-4}$	0.01	-	$3.5 \cdot 10^{-4}$	$9.4 \cdot 10^{-5}$	-
<i>Sim17</i> (Trans 1480-1459 rpm)	1	$8.1 \cdot 10^{-4}$	1.87	10.35°	$2.7 \cdot 10^{-4}$	1.06	0.98°

Table 7.3: Estimation of n_{BB} and θ_0 based on data generated by *ModelFullBB*.

If the estimation is performed using data issued from the FE models, both approaches present a more important error of modelling. As the circuit models do not account for the effects of rotor slots and saturation on the stator currents, low pass filters with cutoff frequency of 120Hz must be applied before

the comparison of the stator currents. In order to avoid any distortion and time-offset of the filtered stator currents, zero-phase filters will be used. The residues are given in table 7.4. One can see that these values are bigger than the one presented in table 7.3. This is due to the error of modelling. In the same table and in figure 7.7, a comparison with the estimation of the number of broken bars obtained using MCSA is given. As expected, for both models the estimation of the fault amplitude is less precise than the estimation using data generated by *ModelFullBB*. Furthermore, the models are clearly overestimating the fault magnitude while MCSA is underestimating it.

ModelSupBB is the less precise method specially for high fault magnitude and cannot be used in high slip conditions. Furthermore, as this model tends to overestimate the fault magnitude, in case of torque oscillations the error in the modelling of the speed influence on stator currents will be seen as a small fault. In this situation, the model estimates the fault to be 0.5 broken bars. This is however lower than the estimation of 0.5 broken bars and a threshold can be set.

Another observation is that the model is not affected by transient situations except when slip becomes important as it is shown in figure 7.6. This figure shows a zoom of the transient condition proposed by *Sim15*. In this time frame, the speed is increasing from 1100rpm ($t = 0.4$ s) to 1300rpm ($t = 1.3$ s). The accuracy in the reconstruction of the stator currents is decreasing while the slip is increasing.

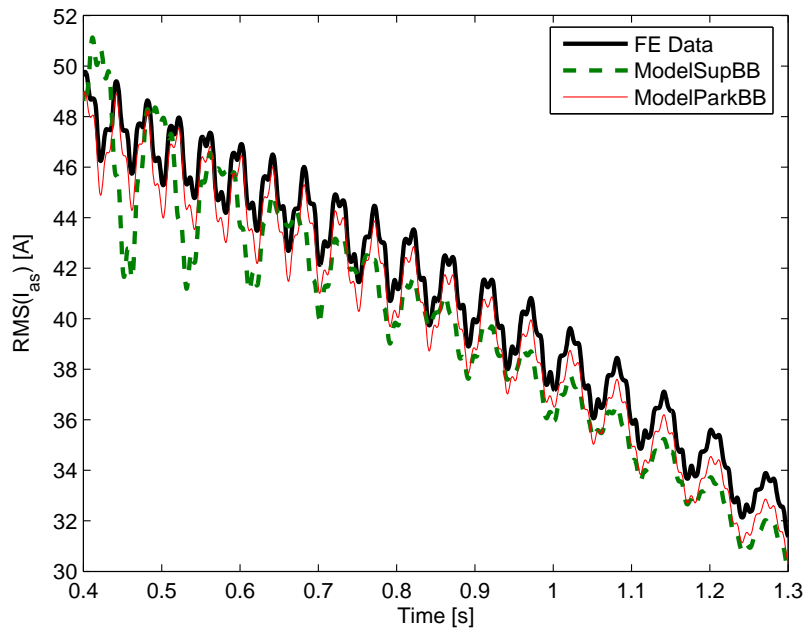
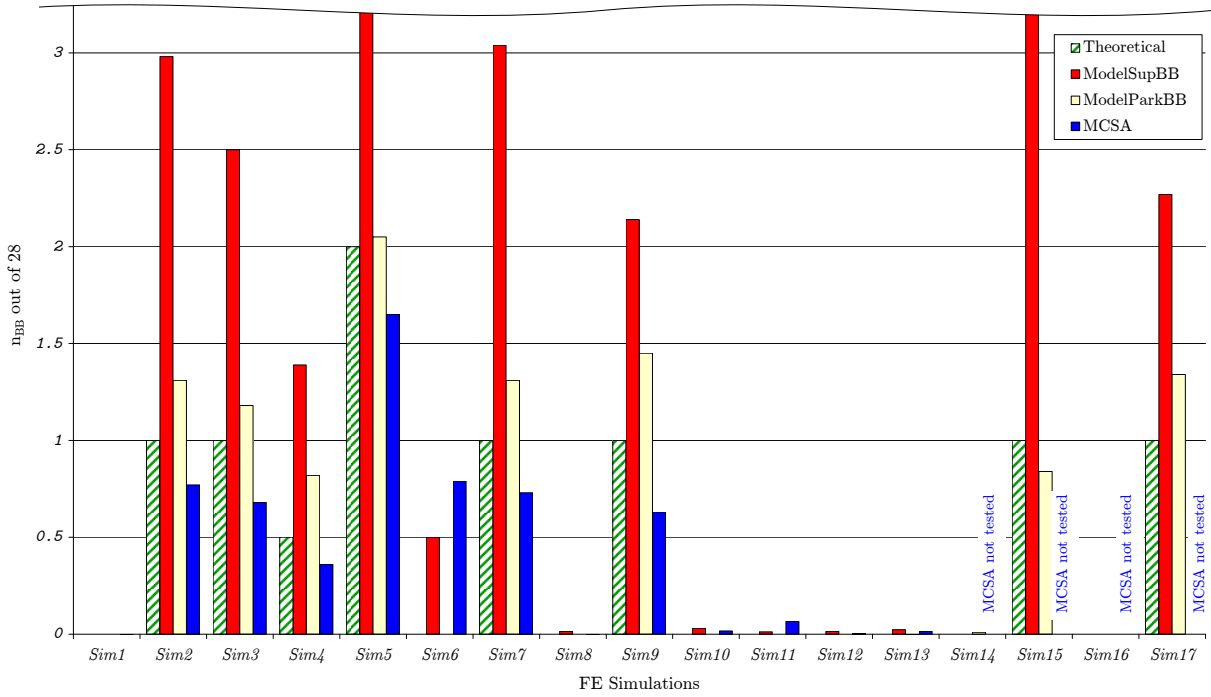


Figure 7.6: Running RMS value of the stator currents for situation of *Sim15*. Zoom between 1100 and 1300rpm.

ModelParkBB gives a good estimation of the number of broken bars in all tested conditions. The absolute error stays lower than 0.45 broken bars which is equivalent to MCSA. Furthermore, this method is not sensitive to torque oscillations and can be applied in transient conditions as shown in figure 7.6 (*Sim15*). This is an advantage compared to MCSA.

Figure 7.7: Comparison of the estimations of n_{BB} based on data generated by FE simulations.

FE Simulation	<i>ModelSupBB</i>		<i>ModelParkBB</i>		MCSA
	R	n_{BB}	R	n_{BB}	n_{BB}
<i>Sim1</i> (Full load, NoBB)	$1.4 \cdot 10^{-3}$	$6.25 \cdot 10^{-5}$	$1.5 \cdot 10^{-3}$	$3.7 \cdot 10^{-6}$	$7 \cdot 10^{-4}$
<i>Sim2</i> (Full load, 1BB)	$2.7 \cdot 10^{-3}$	2.98	$2.6 \cdot 10^{-3}$	1.31	0.77
<i>Sim3</i> (Full load, 1BB, Finite J)	$2.3 \cdot 10^{-3}$	2.50	$2.5 \cdot 10^{-3}$	1.18	0.68
<i>Sim4</i> (Full load, 0.5BB)	$1.7 \cdot 10^{-3}$	1.39	$1.7 \cdot 10^{-3}$	0.82	0.36
<i>Sim5</i> (Full load, 2BB)	$3.6 \cdot 10^{-3}$	5.77	$3.6 \cdot 10^{-3}$	2.05	1.65
<i>Sim6</i> (Full load, NoBB, Osc. T_r)	$1.5 \cdot 10^{-3}$	0.50	$2.8 \cdot 10^{-3}$	$3.7 \cdot 10^{-4}$	0.79
<i>Sim7</i> (Full load, 1BB, Osc. T_r)	$2.7 \cdot 10^{-3}$	3.04	$2.4 \cdot 10^{-3}$	1.31	0.73
<i>Sim8</i> (Low load, NoBB)	$3.3 \cdot 10^{-3}$	0.01	$3.2 \cdot 10^{-3}$	$2.5 \cdot 10^{-4}$	$1.4 \cdot 10^{-3}$
<i>Sim9</i> (Low load, 1BB)	$3.6 \cdot 10^{-3}$	2.14	$3.6 \cdot 10^{-3}$	1.45	0.63
<i>Sim10</i> (Full load, 10% Short-circuit)	$4.3 \cdot 10^{-4}$	0.03	$1.3 \cdot 10^{-3}$	$1.8 \cdot 10^{-6}$	$1.7 \cdot 10^{-2}$
<i>Sim11</i> (Full load, 40% Stat. ecc.)	$1.2 \cdot 10^{-3}$	0.01	$1.2 \cdot 10^{-3}$	$4.9 \cdot 10^{-7}$	$6.6 \cdot 10^{-2}$
<i>Sim12</i> (Full load, 40% Dyn. ecc.)	$1.2 \cdot 10^{-3}$	0.01	$1.2 \cdot 10^{-3}$	$4.9 \cdot 10^{-7}$	$3.9 \cdot 10^{-3}$
<i>Sim13</i> (Full load, 20% Stat. ecc. & 20% Dyn. ecc.)	$1.7 \cdot 10^{-3}$	0.02	$1.2 \cdot 10^{-3}$	$4.9 \cdot 10^{-7}$	$1.4 \cdot 10^{-2}$
<i>Sim14</i> (Trans 1100-1459 rpm, NoBB)	$3.1 \cdot 10^{-2}$	$3.8 \cdot 10^{-7}$	$3.1 \cdot 10^{-2}$	0.01	—
<i>Sim15</i> (Trans 1100-1459 rpm, 1BB)	$8.4 \cdot 10^{-3}$	5.22	$5.6 \cdot 10^{-3}$	0.84	—
<i>Sim16</i> (Trans 1480-1459 rpm, NoBB)	$1.7 \cdot 10^{-2}$	$2.1 \cdot 10^{-7}$	$1.7 \cdot 10^{-2}$	$3.1 \cdot 10^{-6}$	—
<i>Sim17</i> (Trans 1480-1459 rpm, 1BB)	$1.7 \cdot 10^{-2}$	2.27	$1.6 \cdot 10^{-2}$	1.34	—

Table 7.4: Estimation of n_{BB} based on data generated by FE simulations

7.3.1.2 Sensitivity of the parameters

From section 6.3, one has sense the difficulty to precisely determine the rotor cage parameters (R_b , L_b , R_e , L_e , ...). The current section will illustrate the estimation of the number of broken bars using data generated by *ModelFullBB* with original rotor parameters and using *ModelSupBB* and *ModelParkBB* whose rotor resistances are modified as follows:

- Case 1: $R_b = R_{b_{orig}} 0.5$ and $R_o = R_r + 2 R_b \cos(P \alpha_r)$
- Case 2: $R_b = R_{b_{orig}} 1.5$ and $R_o = R_r + 2 R_b \cos(P \alpha_r)$

This modification of the rotor bar resistance and end-ring resistance will not affect the representation of the healthy machine behaviour as the rotor resistance R_r is not modified.

In the case of *ModelParkBB*, new functions for the rotor parameters R_{rd} , R_{rq} , R_{rdq} , L_{rd} , L_{rq} , L_{rdq} are determined for each of the two cases.

Numerical Details:

The dependence of the parameters with the number of broken bars is approximated using functions of the type $A (n_{BB})^B + C$ where C is equal to the healthy value of the parameters. The coefficients and the sum of the squared errors (sse) for the identification based on the parameters for the first four broken bars are given in table 7.5 for Case 1 and in table 7.6 for Case 2.

Parameters	A	B	C	sse
R_{rd}	$1.949 10^{-3}$	2.02	R_r	$2.38 10^{-8}$
R_{rq}	$2.596 10^{-2}$	1.64	R_r	$6.27 10^{-6}$
R_{rdq}	$6.445 10^{-3}$	1.48	0	$4.513 10^{-7}$
L_{rd}	$1.074 10^{-4}$	2.74	L_r	$2.28 10^{-7}$
L_{rq}	$2.929 10^{-3}$	1.88	L_r	$6.74 10^{-8}$
L_{rdq}	$6.838 10^{-4}$	1.80	0	$9.74 10^{-9}$

Table 7.5: Coefficients of the dependence of the parameters with broken bars (Case 1).

Parameters	A	B	C	sse
R_{rd}	$4.428 10^{-3}$	1.95	R_r	$3.86 10^{-9}$
R_{rq}	$6.219 10^{-2}$	1.34	R_r	$1.79 10^{-6}$
R_{rdq}	$1.606 10^{-2}$	1.20	0	$9.69 10^{-7}$
L_{rd}	$1.094 10^{-4}$	2.69	L_r	$2.06 10^{-7}$
L_{rq}	$2.929 10^{-3}$	1.87	L_r	$6.64 10^{-8}$
L_{rdq}	$6.75 10^{-4}$	1.79	0	$8.87 10^{-9}$

Table 7.6: Coefficients of the dependence of the parameters with broken bars (Case 2).

The residue versus the estimated number of broken bars are given in figure 7.8 for *ModelSupBB* and *ModelParkBB*. An overestimation of 50% of the rotor bar resistance will lead to an underestimation of the number of broken bars which is acceptable for low fault magnitude. On the other hand, an underestimation of the rotor resistance of 50% will lead to an acceptable overestimation of the number of broken bars. Similar conclusions can be obtained for modification of the leakage inductance of the bars.

This conclusion is of great practical importance as a diagnosis based on such models would not lead to extensive commissioning of the installation. The order of magnitude of the rotor bars impedance is sufficient to detect and quantify early stage faults.

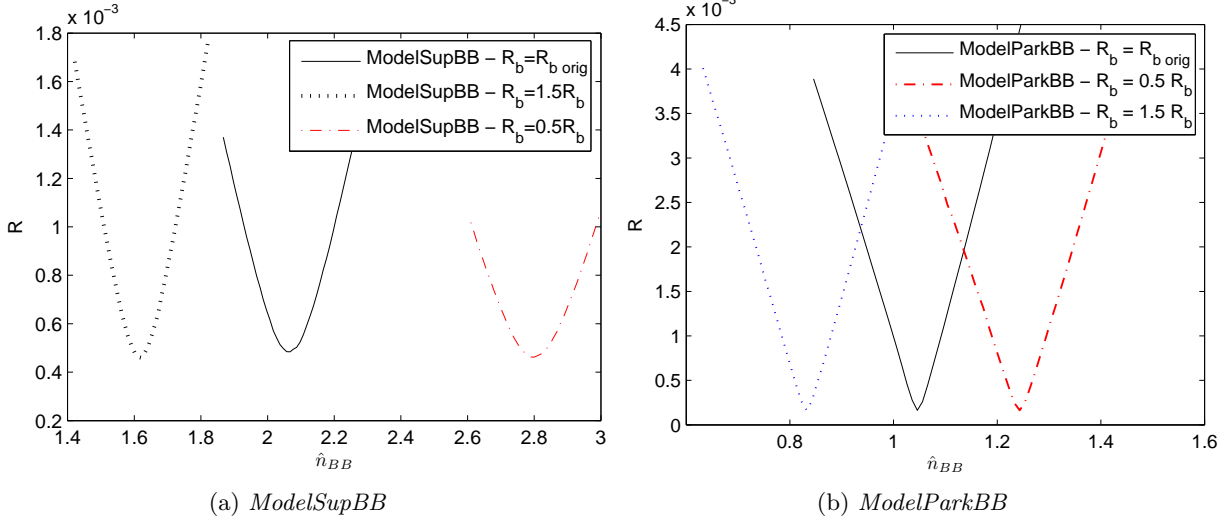


Figure 7.8: Influence of the rotor parameters on the estimation of the number of broken bars.

In the following section algorithms for practical fault detection using models will be presented. Even though *ModelParkBB* offers better performance than *ModelSupBB*, both models will be considered for on-line detection as the computing time will influence the algorithms.

7.3.2 On-line implementation of the fault detection

The setup used for on-line detection and quantification is similar to the one presented in figure 7.2. The measured quantities are the three stator voltages, one stator current as well as the rotor speed. In order to remove the effect of rotor slots and saturation on the stator currents low-pass filters with cutoff frequency of 120Hz are applied. In the proposed setup, these filters are analog and they should be as close as possible to linear phase filters. The same filters should be used on the voltages and speed in order to feed, to the model used for diagnosis, signals time-offset by a constant quantity from measurement. This constant time-offset will have no influence on the detection algorithm.

In this section, a numerical simulation of the algorithm is proposed. The data generated by the FE simulations and used as test-platform will be numerically filtered using the same zero-phase filters as the ones used in the previous section. White noise is added on the FE signals to represent realistic monitoring conditions;

$$\begin{aligned}
 \Omega_r &= \epsilon_{1(\sigma=7.5\text{rpm})} + \Omega_r \\
 I &= (1 + \epsilon_{2(\sigma=1\%)}) I \\
 V &= (1 + \epsilon_{2(\sigma=1\%)}) V
 \end{aligned} \tag{7.2}$$

where $\epsilon_{1(\sigma=7.5\text{rpm})}$ is a normally distributed random noise with a standard deviation of 7.5rpm, $\epsilon_{2(\sigma=1\%)}$ is the same type of noise with a standard deviation of 1% of the nominal value, I and V are the measured stator currents and voltages.

After the analog filtering stage, the signals are sampled at $f_e = 2\text{kHz}$ as proposed in chapter 5 and stored in a buffer. When about one period of the main oscillation of the running RMS has been acquired, the buffer is handed to the detection algorithm. While the algorithm determines the fault magnitude, new data are recorded in a second buffer. This buffer is treated after the previous one. Its length is therefore function of the computing time needed by the algorithm to perform the diagnosis on the previous buffer. As the diagnosis based on previous data is used as initial guess for the analysis of the new buffer, the computing time taken by the algorithm decreases unless a modification of the health of the system occurs. This method allows to perform on-line monitoring of the machine. However, the estimation of θ_0 on a short time window is more difficult. For this reason, the minimum buffer length is limited to one half of the period of the rotor current. This value is still twice smaller than the maximum length necessary to perform an accurate FFT. Moreover, the stationarity of the signal is not required during this window which is different than FFT analysis. For the numerical simulation, the computing time under Matlab is divided by an arbitrary factor of 3 to represent the computing time of the procedure implemented on a digital signal processor (DSP).

The detection algorithm calls the model several times for different estimations of the fault magnitude and the initial rotor position. At each iteration, two regulators, one for the initial rotor position and one for the number of broken bars propose the estimation of the unknowns to be used for the next iteration. These regulators are based on different residues.

Two versions of this algorithm are proposed depending on the use of *ModelSupBB* or *ModelParkBB*. For both approaches the regulators as well as the residues are identical. The described approach is summarised in figure 7.9. The description of the blocks "Model Computation" and "Comparison and regulation" will be detailed in the following lines.

7.3.2.1 Algorithm based on *ModelSupBB*

The model is composed of three parts, the healthy model, the computation of the superimposed rotor currents and the computation of the stator currents. The last two parts form the superimposed model. It is important to realise that, for each buffer, the healthy model only has to be computed when (θ_0) is not yet identified. In parallel with the estimation of θ_0 , an iterative process is realised by calling the computationally cheap superimposed model for the different estimated fault magnitudes (\hat{n}_{BB}) until a stopping criteria is reached. Furthermore, for each estimated initial rotor position, the superimposed rotor currents only need to be computed for one fault magnitude as their amplitude is linear in fault magnitude. This is summarised in figure 7.10.

The main difficulties consist in the determination of the residues. Their construction will be illustrated for the situation where $\hat{n}_{BB} = 0.5$, $n_{BB} = 1$, speed is nominal and $\hat{\theta}_0 \neq \theta_0$.

For the estimation of the initial rotor position, a time shift between two non stationary oscillating signals will be determined;

- First, the running RMS values of the three stator currents of phase a (I_{as}) respectively obtained from measurement, healthy and faulty simulations are computed. These quantities are shown in

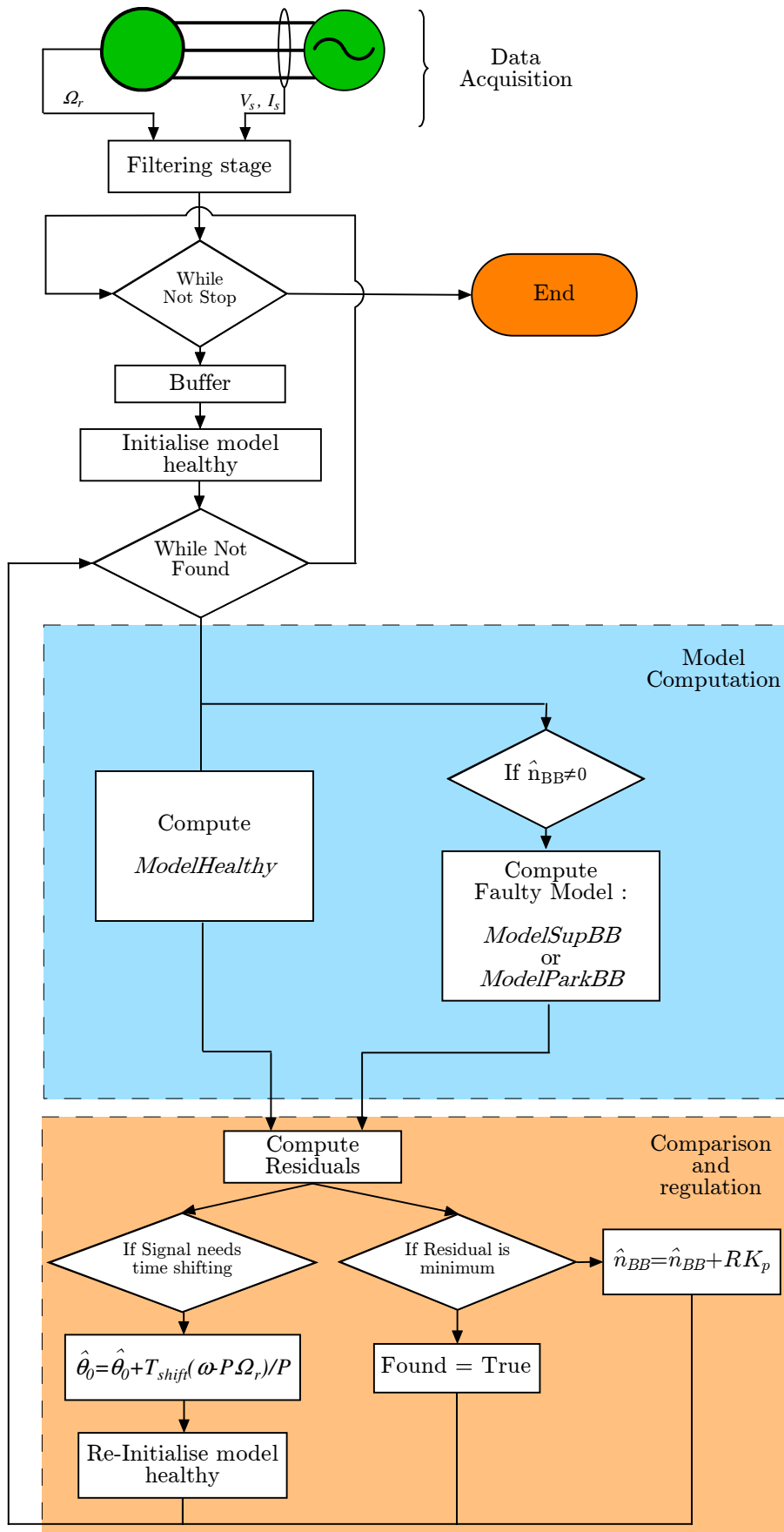


Figure 7.9: Algorithm for detection and quantification of broken bars.

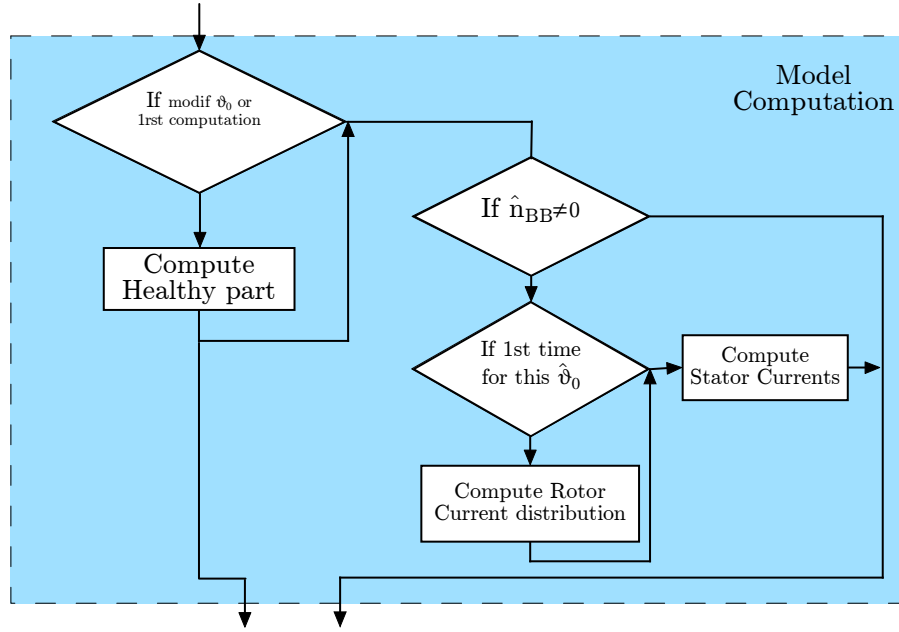


Figure 7.10: Model of the algorithm for detection using *ModelSupBB*.

figure 7.11a. A transient in the value obtained from *ModelSupBB* can be observed due to the improper initialisation of this system of equations (see chapter 5).

- Then the difference between healthy values and values for both faulty model and measurements are computed and filtered using a low-pass filter with cutoff frequency of twice the maximum fundamental rotor frequency. This maximum fundamental rotor frequency can be determined using the stator frequency (f), the minimum value of the speed on the time-window and the number of pole-pairs:

$$\max(f_r) = f - \frac{P \min(\Omega_r)}{2\pi}$$

This leads to the two curves $C_{SupModel}$ and $C_{SupData}$ of figure 7.11b. These represent respectively the faulty behaviour and the faulty behaviour plus an error of modelling.

- Then the local extrema of the two curves are computed. The closest pair of extrema of the same type is taken as reference and one of the curves is time-shifted by the difference between the time instants of these two extrema. The chosen extrema are marked in figure 7.11b by the vertical dash lines and the shifted curves are shown in figure 7.11c. As the curves have been filtered several times (low-pass filter on the stator current, running RMS and low-pass filter on the difference of running RMS values), this method is quite robust. The residue linked to the error in the estimation of the initial rotor position ($\hat{\theta}_0$) is equal to the time shift mentioned above (T_{shift}). Note that, if $\hat{n}_{BB} = 0$, the curve which is the difference between healthy and faulty models is null and no time shift can be estimated. Indeed, θ_0 has no influence of the stator currents.
- The regulation of $\hat{\theta}_0$ is realised by

$$\hat{\theta}_0(i) = \hat{\theta}_0(i-1) + T_{shift} \frac{(\omega - P \text{avg}(\Omega_r))}{P}$$

where i is the iteration number and $\text{avg}(\Omega_r)$ is mean value of the rotor speed over the buffer. If the time-shift is perfectly identified and speed is constant, the correction of $\hat{\theta}_0$ can be made in one iteration.

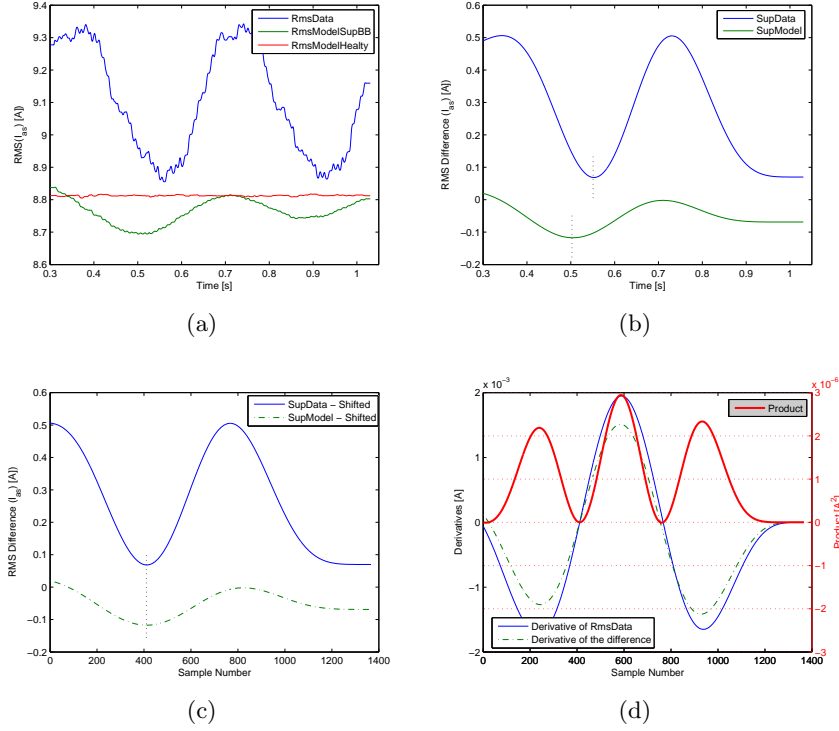


Figure 7.11: Steps of the determination of the error in $\hat{\theta}_0$ and \hat{n}_{BB} in the case of *Sim2*.

The residue linked to the error in amplitude is computed by the following steps:

- First, a constant offset is removed on the difference between the shifted curves obtained through previously described operations.

$$C_{Diff} = \text{detrend}(C_{SupData} - C_{SupModel})$$

- If the detrended difference (C_{Diff}) is in phase with one of the curves $C_{SupData}$ or $C_{SupModel}$, then \hat{n}_{BB} should be increased and if the difference is in phase opposition, the estimation is too high and \hat{n}_{BB} should be decreased. To evaluate this property without having to suppose that the signals are periodical and that the windows contains one period of the frequency of the main oscillation, this difference is derived and multiplied by the derivative of one of the curves $C_{SupData}$ or $C_{SupModel}$. In practice, the curve having the highest oscillation is chosen for better accuracy. If the obtained signal ($C_{Product}$) contains more positive values than negative values, the difference and the curve ($C_{SupData}$ or $C_{SupModel}$) are in phase. Otherwise, they are in phase opposition. This information will determine the sign of the residue. The derivative of the difference (C_{Diff}), the derivative of $C_{SupData}$ as well as their product ($C_{Product}$) is shown in figure 7.11d.
- The residue is then computed using

$$R = \pm \frac{1}{\text{avg}(\text{RMS}(I_{as \text{ Healthy}}))} \sqrt{\frac{1}{N} \sum_1^N C_{Diff}^2}$$

where N is the number of points of the buffer and the sign is determined by the analysis of $C_{Product}$.

- The regulation of the amplitude is realised by

$$\hat{n}_{BB}(i+1) = \hat{n}_{BB}(i) + R(i) K_p$$

where K_p is a proportional gain.

Using this method, the error in the estimation of the broken bar can be reduced even though the estimation of θ_0 has not yet converged. The algorithm stops iterating when one or several of the following conditions are reached:

- Condition 1: The time shift (T_{shift}) is smaller than a user-defined tolerance level. It means that the estimation of the initial rotor position has converged. This is a necessary condition.
- Condition 2: The residue becomes smaller than a certain tolerance. It means that the estimation of number of broken bars has converged.
- Condition 3: The sign of the residue is different from the one of the previous iteration. It means that the estimation is close to the optimal value.
- Condition 4: The amplitude of the residue is increasing while its sign remains the same. If this condition is encountered 4 times in a row, the problem is diverging. The value of the estimations before the problem started diverging is output.
- Condition 5: The difference in the amplitude of the residues between the current iteration and the previous one is smaller than a user-defined tolerance. It means that the problem does not evolve anymore.

Condition 1 is necessary and at least one of the four other ones must be satisfied to stop the algorithm. The information about which condition was achieved is stored and is valuable for the user. The philosophy that lies behind this approach is that the algorithm must be quick and that an improvement of the precision of the estimation will be obtained through the analysis of the following buffers. The utilisation of the residue for the regulation of the estimation is illustrated in the part "Comparison and regulation" of figure 7.9.

As example of this method, the results in the case of a machine with one broken bar and in low load steady-state conditions are illustrated in figure 7.12a. Due to the short length of the data generated by the FE model, only two buffers are shown on the figure. The iterations of the first buffer are represented by the plain (red) curves while the iterations of the second are shown in dashed (blue). The ordinate of each mark corresponds to the estimation of the quantity at the current iteration and its abscissa represents the accumulated fictive computing time from the start of the process (real computing time divided by 3). In the case of the first buffer, one can see from the amount of time taken by the first iteration that only *ModelHealthy* is computed. On the second iteration, both healthy and superimposed parts are computed. This allows the estimation of the rotor position. The third buffer is the last one that requires a long computing time as the healthy and superimposed parts of the model are still computed. Afterwards, the computation time of each iteration is smaller and the model is run several times to obtain the best

estimation. The model converges to a little more than 1.99 broken bars. On the second buffer, the determination of θ_0 is modified as well as the estimation of the fault magnitude ($\hat{n}_{BB} = 2.23$). This is mainly due to the difficulties to determine the time shift and due to the sensitivity of the residue for n_{BB} in presence of noise. Finally, the fictive computing time required for the treatment of the first buffer was 1.85s and the computing time of the second buffer was 1.15s. The analysis of the second buffer is shorter due to the reduced buffer length¹ and the use of previous estimations as initial guess. For both buffers the stopping criteria had consisted in a change in the sign of the residue.

In the case of oscillating torque without fault, similar results are shown in figure 7.12b. As in off-line implementations, the model is unable to avoid the false alarm. However the estimated fault magnitude is small and a threshold could be easily set.

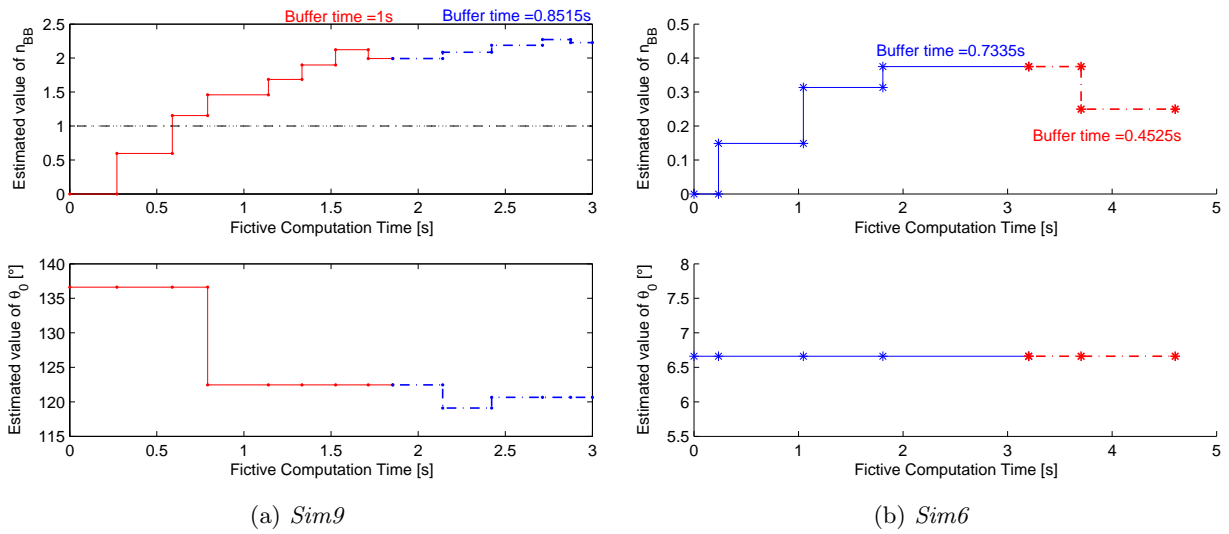


Figure 7.12: Estimation of n_{BB} and θ_0 in the case of *Sim9* and *Sim6* using *ModelSupBB*.

The results in the other steady-state situations are similar to the ones of the off-line implementation. However, the case of transient situation from no-load to full load with one broken bar (*Sim17*) is illustrated in figure 7.13a. It can be observed that the proposed method is unable to determine the fault magnitude and position. This can be understood through the analysis figure 7.13b. This figure shows the RMS value of the stator current from measurement, *ModelHealthy* and *ModelSupBB* at the last iteration of the buffer. It can be clearly seen that, as the working point is changing, the error in the representation of the healthy machine behaviour is also changing. The period of the variation of this error is similar to the oscillation created by the broken bar and its magnitude is greater than the oscillation created by one broken bar. In these conditions, the algorithm can not reach an adequate diagnosis. In transient situations, a more precise healthy model can therefore make the difference. Another possibility could be to avoid diagnosis in transient conditions for very low slip conditions.

7.3.2.2 Algorithm based on *ModelParkBB*

This approach is similar to the one using *ModelSupBB*. However, for each iteration, *ModelParkBB* has to be computed which is more time consuming. *ModelHealthy* is needed for the determination of the residues

¹Note that, from the description of the algorithm presented earlier in this text, the second buffer should have a length equal to the fictive computing time of the first buffer. This is not the case due to the limited amount of data generated by the FE simulations.

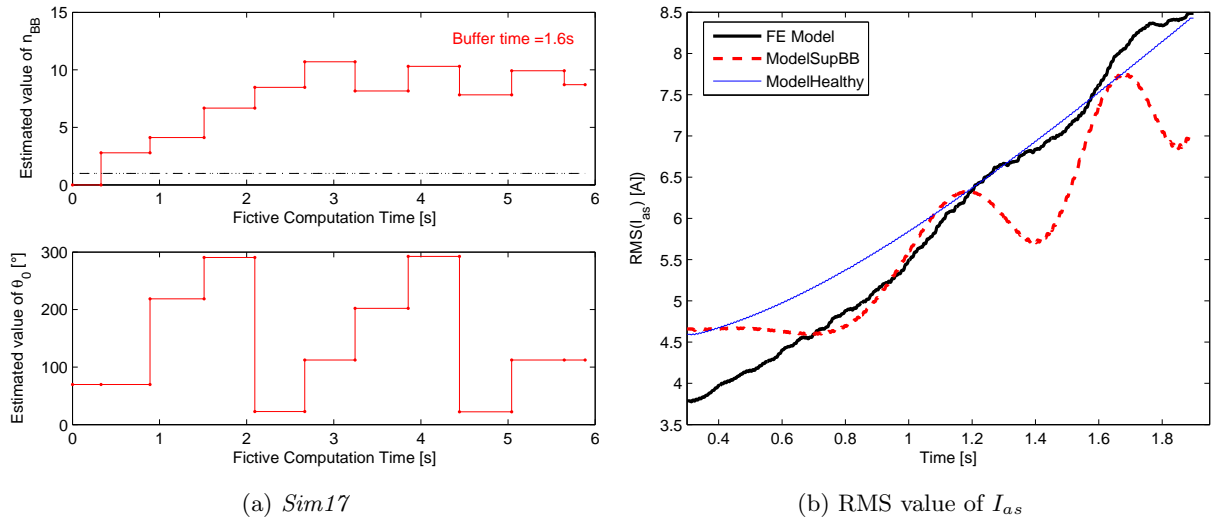
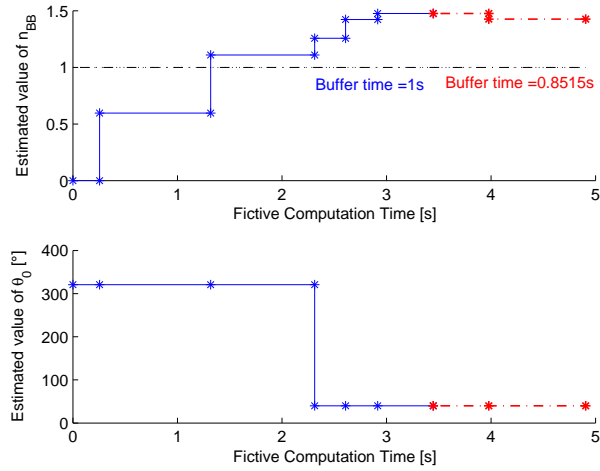


Figure 7.13: Estimation of n_{BB} and θ_0 in the case of *Sim17* using *ModelSupBB*

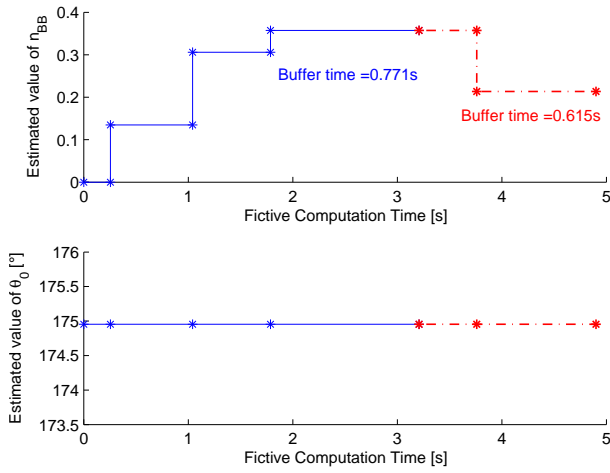
but its computation only has to be made once per buffer as the stator currents are neither depending on the initial rotor position nor on the number of broken bars. The algorithm is shown in the part "Model Computation" of figure 7.9. Furthermore, it is to be recalled that depending on the fault magnitude, the position of the Park reference frame is modified through the variable θ_d (see section 5.3.2). As the initial rotor position is an unknown of the problem, the coupling between \hat{n}_{BB} and $\hat{\theta}_0$ brought by θ_d would perturb the convergence of the algorithm. Therefore, in this section, θ_d is retained at 0.

Results in the case of a machine with one broken bar and in low load steady-state conditions are illustrated in figure 7.14a. It can be observed that the estimated value of \hat{n}_{BB} is very similar to the one of the off-line estimation. The comparison of figure 7.14a and figure 7.12a shows that the computing time required by this model is longer than the one of *ModelSupBB*. In the case of torque oscillations, the quantification is slightly perturbed by the phenomenon as shown for a healthy machine in figure 7.14b. A threshold could be set as for *ModelSupBB*. Finally, the algorithm has been tested in the higher slip transient situations of *Sim14* and *Sim15*. The quantification is good using this model. Note that, in these higher slip conditions, the diagnostic can be performed quicker as the period of the oscillation due to the broken bar is smaller.

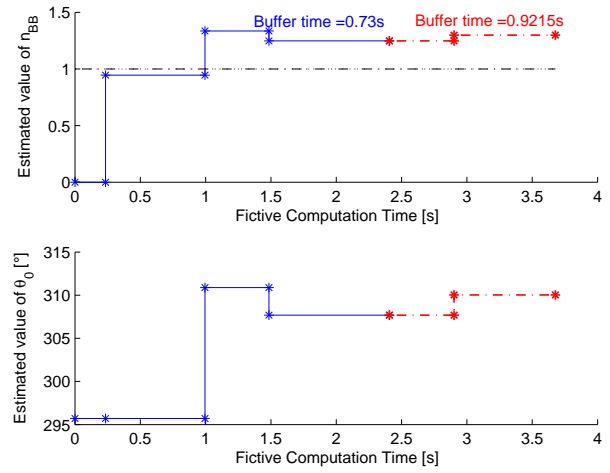
The simulation of on-line model-based diagnosis has allowed to propose two algorithms each based on a different model. The quantification using *ModelParkBB* is promising but the method should be tested on long term situations. This would require another test bench than FE simulations.



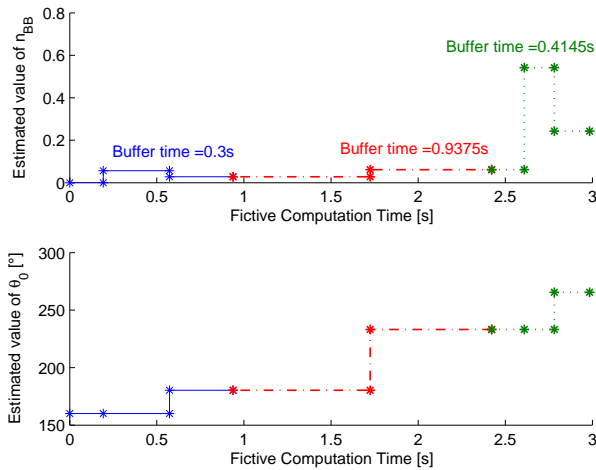
(a) Sim9



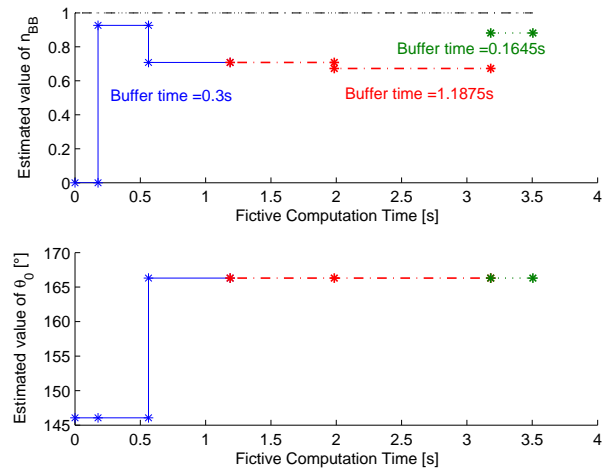
(b) Sim6



(c) Sim7



(d) Sim14



(e) Sim15

Figure 7.14: Estimation of n_{BB} and θ_0 using *ModelParkBB*

7.4 Conclusions

This chapter has presented two alternatives to perform on-line detection and quantification of broken bars.

The first is frequency-based. It proposes the monitoring of specific frequency components of the stator current. Its efficiency was proved in steady-state situations. However the application field of the method does not covers transient or oscillating torque situations.

The other studied approach is model-based detection and quantification. The approach requires the determination of unknown quantities of the models. These quantities are linked to the fault magnitude and the fault position. An objective function to minimise is used to perform the estimation. This function should be sensitive to changes of the unknown quantities but not specially to the representation of the measurement by the model. For this reason, this parameter estimation is much different than the one presented in chapter 6.

A sensitivity analysis of the quantification to imprecision of the rotor parameters used by the models has been made. It has been shown that rotor bar impedances do not need to be precisely determined to perform fault detection and quantification using the proposed method. This makes possible the practical use of this method for motor condition monitoring.

For the on-line approach, two residues have been built. Each is designed to be sensitive to only one of the unknowns and less sensitive to the variation of the working point. The main advantage of this technique is the realisation of two independent regulation loops for the estimation the unknowns. The reduced sensitivity to the working point is achieved through the use of the difference between healthy and faulty stator currents instead of the use of the faulty currents. However, the accuracy of the healthy model to represent the healthy working conditions was a limitation for the fault detection in steep transient situations.

Precision of *ModelSupBB* is low for the quantification of the fault while *ModelParkBB* offers efficient quantification of the fault in various situations.

The finite element test-bench showed its limits as the simulated time, limited to a couple of seconds, did not allowed to test long term monitoring.

Much work need to be done to implement fault detection using the proposed model-based method but the scope of this chapter was to show its feasibility and draw main orientations.

Chapter 8

General conclusions and future work

In the introduction, maintenance, motor monitoring techniques and physical influence of the faults have been shown to be strongly connected. Therefore, this work has proposed to start the study of faulty induction machines from a detailed and clear physical understanding of the phenomena linked to the faults. This knowledge has then been used for the development of monitoring techniques. It should be noted that main conclusions of each chapter was already provided at their respective end.

First, origins and evolutions of main faults have been analysed. It has been shown that the effect of each fault in electrical machines brings into play interactions between machine geometry, material property, electrical circuits and magnetic fields. Therefore, the choice of finite element models has been adequate for understanding faulty machines.

Finite element models have led to the followings:

- The main effect of a broken bar has been illustrated. The airgap flux distribution has been explained using Faraday and Ampère's law and the effect of machine saturation on the signature of the fault has been deeply studied.
- In the case of stator short-circuits, even though the shorted turns do not influence much the line currents, it strongly stresses the machine health.
- The pole connection have been shown to greatly affect the stator currents and flux distribution modification due to the presence of eccentricities. The important influence of the number of pole pairs has been suggested.

More details on these three points have been summarised in the conclusions of chapter 3. It is however interesting to observe that in healthy or faulty machines, saturation of materials as well as Lenz's law, both contribute to uniformly distribute the flux repartition in the machine. Therefore, when saturation level is smaller, machine asymmetries affect more the stator currents.

Moreover, an important inference of the detailed fault analysis study is that currents from individual stator coils are more sensitive to the presence of the fault than line currents. When available, these currents should be used to perform the diagnosis.

Time-domain finite element models have also proved their use for the realisation of virtual test-benches where all conditions (external and fault magnitude) are under precise control. The main drawback of this approach is the extensive computing time required which has restricted the simulation of induction machines to a couple of seconds.

This work has also analysed present trends in motor condition monitoring. The availability of current, voltage and speed sensors brings new possibility to electrical diagnosis either using frequency-based techniques or model-based techniques. The latter allows more external conditions, such as voltage and speed variations, to be taken into account to avoid false alarms and to reach precise diagnosis. Extended conclusions on this review are presented at the end of chapter 4.

Model-based techniques have been given an important focus in this work. The approach of developing models on a same mathematical description of the machine has allowed to objectively measure the influence of mathematical simplifications on the model accuracy and computing time. The presence of faults greatly complicates the mathematical description as many symmetries present in healthy machines disappear. A Park approach with a reference frame fixed with regard to the fault has proved efficiency in the representation of the stator currents of a machine with broken bars. The superposition principle offers important reduction of the computing time but at the cost of imprecision in the quantification of the fault magnitude and location of the fault.

An important achievement of the model development is the formulation of the steady-state behaviour of a machine with broken bars at constant speed using a linear system of equation. The applications of such method go from model initialisation to fault diagnosis in steady-state.

Finally, off-line parameter identification methods have been proposed for circuit models. Least-square algorithms have been used. When errors of modelling are present between the process and the model, the choice of the function to be minimised by the least-square algorithm is crucial and depends on the objective of the parameter identification. Two different approaches have been used in this work.

- For the identification of the parameters of a model used to represent the motor, the objective function has been built upon the model output. The accuracy in the estimation of the parameters is not guaranteed and is, as a matter of fact, not of great importance. Furthermore, it has been shown that, in both healthy and faulty situations, only groups of parameters and not each parameter individually affect the stator currents of a machine. More detailed conclusions on this field was provided in sections 6.2.7 and 6.3.4.
- For the model-based fault detection, some parameters linked to the fault magnitude and location need to be precisely determined. The objective function should be chosen such as to emphasise the sensitivity of the model output to the parameter estimation. In the case of broken bars, the oscillation of the RMS value of the stator current has been used as objective function. This is detailed in chapter 7.

Finally, model-based fault detection has been implemented and compared to frequency-based methods. The first approach has proved to be efficient not only in steady-state as the latter but also in slow transient conditions. However, room for improvements is available. Model-based diagnosis is therefore very promising.

This work has covered most of the aspects of faulty induction motor. Main contributions reside in the physical comprehension of faulty motors, faulty machines modelling and parameter identification and fault detection. However, much more work still need to be done to achieve practical on-line diagnosis of induction motor.

Further work In the field of faulty machine modelling, the determination of an analytical relation between rotor parameters of the *ModelParkBB* and the cage parameters in presence of fault would offer easier commissioning and better quantification of the fault.

Moreover, asymmetrical Park models could be used to represent eccentricities. This would require the use of winding functions for the representation of the inductances. Likewise, the implementation of short-circuit models would require to use a third group of windings (after the stator and rotor windings) to represent the short-circuit loop in a reference frame fixed with regard to the stator.

Furthermore, the field of experimental parameter identification of the rotor cage elements should benefit from new methods.

For healthy machine modelling, improvements could be made by taking into account the presence of main-field saturation as well as skin effect.

In the case of model-based fault detection and quantification, a DSP implementation in the drive control or in protection relays should be realised. This implementation should divide the diagnosis in two steps;

- first, the identification of the presence and nature of the fault using fast methods such as MCSA or steady-state faulty models;
- then a detailed quantification by means of an appropriate model.

Furthermore, interaction of the fault with the drive control loop, initially designed for healthy machines, should be studied. A more elaborate implementation could use the flexibility of the drive control to generate a command that ease the stress of the machine in presence of an identified fault. This could allow to continue to run the motor at reduced efficiency until maintenance is provided. As an example among others, this could be interesting in electric cars in presence of the fast expanding stator short-circuits.

Finally, synchronous generator with field currents or doubly-fed induction machines offers access to rotor measurements. This could be exploited to ease stator fault diagnosis as rotor windings are good sensors to detect such faults.

Bibliography

- [Abdelhadi 05] B. Abdelhadi, A. Benoudjit & N. Nait-Said. *Application of genetic algorithm with a novel adaptive scheme for the identification of induction machine parameters*. IEEE Transactions on Energy Conversion, vol. 20, no. 2, pages 284 – 291, June 2005.
- [Al-Nuaim 98] N. A. Al-Nuaim & H. A. Toliyat. *A novel method for modeling dynamic air-gap eccentricity in synchronous machines based on modified winding function theory*. IEEE Transactions on Energy Conversion, vol. 13, no. 2, June 1998.
- [Araujo 02] R. E. Araujo, A. V. Leite & D. S. Freitas. *Estimation of physical parameters of an induction motor using an indirect method*. In IEEE International Symposium on Industrial Electronics, volume 2, pages 535 – 540, 2002.
- [Bachir 01] S. Bachir, S. Tnani, G. Champenois & J. Saint-Michel. *Modélisation et diagnostic des ruptures de barres rotoriques par identification paramétrique*. In Colloque Electrotechnique du futur, Nov. 2001.
- [Bangura 00a] J. F. Bangura & N. A. Demerdash. *Comparison between characterization and diagnosis of broken bars/end-ring connectors and airgap eccentricities of induction motors in ASD's using a coupled finite element-state space method*. IEEE Transactions on Energy Conversion, vol. 15, no. 1, Mar. 2000.
- [Bangura 00b] J. F. Bangura & N. A. Demerdash. *Effects of broken bars/end-ring connectors and airgap eccentricities on ohmic and core losses of induction motors in ASD's using a coupled finite element-state space method*. IEEE Transactions on Energy Conversion, vol. 15, no. 1, pages 40 – 47, Mar. 2000.
- [Bellini 76] A. Bellini, A. De Carli & M. La Cava. *Parameter identification for induction motor simulation*. Automatica, vol. 12, no. 4, pages 383 – 386, July 1976.
- [Bellini 00] A. Bellini, F. Filippetti, G. Franceschini, C. Tassoni & G. B. Kliman. *Quantitative evaluation of induction motor broken bars by means of electrical signature analysis*. In IEEE Industry Applications Conference, volume 1, pages 484 – 491, Oct. 2000.
- [Benbouzid 03] M. E. H. Benbouzid & G. B. Kliman. *What stator current processing-based technique to use for induction motor rotor faults diagnosis?* IEEE Transactions on Energy Conversion, vol. 18, no. 2, pages 238 – 244, June 2003.
- [Boiarski 95] A. A. Boiarski, G. Pilate, T. Fink & N. Nilsson. *Temperature measurements in power plant equipment using distributed fiber optic sensing*. IEEE Transactions on Power Delivery, vol. 10, no. 4, pages 1771 – 1778, Oct. 1995.

- [Bonnett 92] A. H. Bonnett & G. C. Soukup. *Cause and analysis of stator and rotor failures in three-phase squirrel-cage induction motors*. IEEE Transactions on Industry Applications, vol. 28, no. 4, pages 921 – 937, July - Aug. 1992.
- [Bossio 05] G. Bossio, C. De Angelo, J. Solsona, G. O. García & M. I. Valla. *A model for induction motors with non-uniform air-gap*. Latin American Applied Research, vol. 35, no. 2, pages 77 – 82, 2005.
- [Burnett 94] R. Burnett, J. F. Watson & S. Elder. *The detection and localisation of rotor faults within three phase induction motors*. In International Conference on Electrical Machines (ICEM), volume 2, Sept. 1994.
- [Burnett 96] R. Burnett, J. F. Watson & S. Elder. *The application of modern signal processing techniques for use in rotor fault detection and localisation within three-phase induction motors*. Elsevier, Signal processing, vol. 49, pages 57 – 70, 1996.
- [Cabanas 05] M. F. Cabanas, F. Pedrayes, M. R. González, M. G. Melero, C. H. Rojas, G. A. Orcajo, J. M. Cano & F. Nuño. *A new electronic instrument for the early detection of broken rotor bars in asynchronous motors working under arbitrary load conditions*. In IEEE International Symposium on Diagnostics for Electric Machines, Power Electronics and Drives (SDEMPED), pages 29 – 34, Sept. 2005.
- [Cardoso 99] A. J. Marques Cardoso, S. M. A. Cruz & D. S. B. Fonseca. *Inter-turn stator winding fault diagnosis in three-phase induction motors, by Park's vector approach*. IEEE Transactions on Energy Conversion, vol. 14, no. 3, Sept. 1999.
- [Casimir 03] R. Casimir, E. Bouteleux, H. Yahoui, G. Clerc, H. Henao, C. Delmotte, G.-A. Capolino, G. Rostaing, J.-P. Rognon, E. Foulon, L. Loron, G. Didier, H. Razik, G. Barakat, B. Dakyo & S. Bachir. *Comparaison de plusieurs méthodes de modélisation et de diagnostic de la machine asynchrone en présence de défauts*. In Électrotechnique du futur, Dec. 2003.
- [Cedrat 99] Cedrat. Flux 2d version 7.4 - induction machine tutorial. Cedrat and Cedrat Technologies, Nov. 1999.
- [Cedrat 05] Cedrat. Flux. induction machine with skewed rotor: Technical paper. Cedrat and Cedrat Technologies, Oct. 2005.
- [Cho 92] K. R. Cho, J. H. Lang & S. D. Umans. *Detection of broken bars in induction motors using state and parameter estimation*. IEEE Transactions on Industry Applications, vol. 28, pages 702 – 709, 1992.
- [Contin 00] A. Contin, G. C. Montanari, A. Cavallini, G. Pasini & F. Puletti. *Stochastic analysis of partial discharges signals for diagnosis of insulation systems of AC rotating machine stator windings*. In IEEE Industry Applications Conference, volume 1, pages 359 – 366, Oct. 2000.
- [Corcoles 02] F. Corcoles, J. Pedra, M. Salichs & L. Sainz. *Analysis of the induction machine parameter identification*. IEEE Transactions on Energy Conversion, vol. 17, no. 2, pages 183 – 190, June 2002.
- [Couneson 97] P. Couneson. Câbles souterrains haute tension. Cours de l'Université Libre de Bruxelles - Tractebel Energy Engineering, Dec. 1997.

- [Cruz 00] S. M. A. Cruz & A. J. Marques Cardoso. *Stator winding fault diagnosis in three-phase synchronous and asynchronous motors, by the extended Park's vector approach*. In IEEE Industry Applications Conference, volume 1, pages 395 – 401, Oct. 2000.
- [Cunha 05] C.C.M. Cunha, R.O.C. Lyra & B.C. Filho. *Simulation and analysis of induction machines with rotor asymmetries*. IEEE Transactions on Industry Applications, vol. 41, no. 1, pages 18 – 24, Jan. - Feb. 2005.
- [DeFatta 88] D. J. DeFatta, J. G. Lucas & W. S. Hodgkiss. *Digital signal processing: A system design approach*. John Wiley & Sons, Inc., 1988.
- [Deleroi 82] W. Deleroi. *Squirrel Cage Motor with broken bar in the rotor - physical phenomena and their experimental assessment*. In International Conference on Electrical Machines (ICEM), pages 767 – 770, 1982.
- [Depenbrock 89] M. Depenbrock & N. R. Klaes. *Determination of the induction machine parameters and their dependencies on saturation*. In Industry Applications Society Annual Meeting, volume 1, pages 17 – 22, Oct. 1989.
- [Dorrell 97] D. G. Dorrell, W. T. Thomson & S. Roach. *Analysis of airgap flux, current, and vibration signals as a function of the combination of static and dynamic airgap eccentricity in 3-phase induction motors*. IEEE Transactions on Industry Applications, vol. 33, no. 1, pages 24 – 34, Jan. - Feb. 1997.
- [Elkasabgy 92] N. Elkasabgy, A. R. Eastham & G. E. Dawson. *Detection of broken bars in the cage rotor on an induction machine*. IEEE Transactions on Industry Applications, vol. 28, no. 1, pages 165 – 171, Jan. - Feb. 1992.
- [EPRI 82] EPRI. *Improved motors for utility applications industry assessment study*, volume 1. EPRI EL-2678, Oct. 1982.
- [Filippetti 92] F. Filippetti, M. Martelli, G. Franceschini & C. Tassoni. *Development of expert system knowledge base to on-line diagnosis of rotor electrical faults of induction motors*. In Industry Applications Society Annual Meeting, volume 1, pages 92 – 99, Oct. 1992.
- [Fink 94] W. T. Fink, H. G. Sedding & J. Penman. *Detection and localisation of interturn short circuits in the stator windings of operating motors*. IEEE Transactions on Energy Conversion, vol. 9, no. 4, Dec. 1994.
- [Fiser 97] R. Fiser & S. Ferkolj. *Simulation of steady-state and dynamic performance of induction motor for diagnostic purpose*. In IEEE International Electric Machines and Drives Conference, pages WB3/10.1 – WB3/10.3, May 1997.
- [Gyselinck 00] J. Gyselinck. *Twee-dimensionale dynamische eindige-elementenmodellering van statische en roterende elektromagnetische energieomzetters*. PhD thesis, Universiteit Gent, 2000.
- [Gyselinck 05] J. Gyselinck, J. Sprooten, L. Vandeveldel & X. M. Lopez-Fernandez. *Multi-slice finite element modeling of induction motors considering broken bars and inter-bar currents*. In International Symposium on Electromagnetic Fields in Mechatronics, Electrical and Electronic Engineering (ISEF), pages MTT-SA.19, Sept. 2005.

- [Gyselinck 06] J. Gyselinck, J. Sprooten & X. M. López-Fernández. *Multi-slice FE and MEC modelling of induction motors having a broken bar - influence of inter-bar currents and bar breakage location*. In International Conference on Electrical Machines (ICEM), volume 1, Sept. 2006.
- [Hirvonen 94] R. Hirvonen. *On-line condition monitoring of defects in squirrel cage motors*. In International Conference on Electrical Machines (ICEM), volume 2, pages 267 – 272, Sept. 1994.
- [Hénao 01] H. Hénao, C. Delmotte, G. Ekwe & G.-A. Capolino. *Méthodes de simulation adaptées aux machines à induction avec défauts électriques*. In Colloque Electrotechnique du futur, Nov. 2001.
- [Houdouin 03] G. Houdouin, G. Barakat, B. Dakyo & E Destobbeleer. *A winding function theory based global method for the simulation of faulty induction machines*. In IEEE International Electric Machines and Drives Conference, volume 1, pages 297 – 303, 2003.
- [Hsu 95] J. S. Hsu. *Monitoring of defects in induction motors through air-gap torque observation*. IEEE Transactions on Industry Applications, vol. 31, no. 5, pages 1016 – 1021, Sept. - Oct. 1995.
- [IEEEComitee 85] IEEEComitee. *Report of large motor reliability survey of industrial and commercial installations, Part I and Part II*. IEEE Transactions on Industry Applications, vol. 21, no. 4, pages 853 – 872, July - Aug. 1985.
- [Innes 94] A. G. Innes & R. A. Langman. *The detection of broken rotor bars in variable speed induction motor drives*. In International Conference on Electrical Machines (ICEM), volume 2, Sept. 1994.
- [Jang 03] G. H. Jang & S. J. Park. *Simulation of the electromechanical faults in a single-phase squirrel cage induction motor*. IEEE Transactions on Magnetics, vol. 39, no. 5, pages 2618 – 2620, Sept. 2003.
- [Jianzhong 98] Z. Jianzhong, J. Xinghua & Y. Zeyuan. *Vibration measurement of the generator stator end windings and precautions against insulation wearing*. In International Conference on Power System Technology (PowerCon), volume 2, pages 1021 – 1024, Aug. 1998.
- [Kliman 88] G. B. Kliman, R. A. Koegl, J. Stein, R. D. Endicott & M. W. Madden. *Noninvasive detection of broken rotor bars in operating induction motors*. IEEE Transactions on Energy Conversion, vol. 3, no. 4, pages 873 – 879, Dec. 1988.
- [Kogan 97] V. Kogan & B. Nindra. *Investigation of high voltage stator winding vibrations in full-scale slot model*. In Electrical Insulation Conference, pages 155 – 166, Sept. 1997.
- [Kostic-Perovic 00] D. Kostic-Perovic, M. Arkan & P. Unsworth. *Induction motor fault detection by space vector angular fluctuation*. In IEEE Industry Applications Magazine, volume 1, pages 388 – 394, Oct. 2000.
- [Kral 00a] C. Kral, F. Pirker & G. Pascoli. *Detection of rotor faults in squirrel cage induction machines at standstill for batch tests by means of the Vienna monitoring method*. In IEEE Industry Applications Conference, volume 1, pages 499 – 504, Oct. 2000.

- [Kral 00b] C. Kral, R. S. Wieser, F. Pirker & M. Schagginger. *Sequences of field-oriented control for the detection of faulty rotor bars in induction machines-the Vienna Monitoring Method*. IEEE Transactions on Industrial Electronics, vol. 47, no. 5, pages 1042 – 1050, Oct. 2000.
- [Krause 02] P. C. Krause, O. Wasynczuk & S. D. Sudhoff. Analysis of electric machinery and drive systems, 2nd edition. Wiley Inter-Science, 2002.
- [Lee 01] S.-B. Lee & T. G. Habetler. *An on-line stator winding resistance estimation technique for temperature monitoring of line-connected induction machines*. In IEEE Industry Applications Conference, volume 3, pages 1564 – 1571, Oct. 2001.
- [Lee 05] H.-H. Lee, N. N. Tu & K. J. Min. *A study on decision tree for induction motor diagnostic system*. In International Symposium on Electrical and Electronics Engineering (ISEE), volume 1, pages xii – xvi, Oct. 2005.
- [Legowski 96] S. F. Legowski, A. H. M. Sadrul Ula & A. M. Trzynadlowski. *Instantaneous power as a medium for the signature analysis of induction motors*. IEEE Transactions on Industry Applications, vol. 32, no. 4, pages 904 – 909, July - Aug. 1996.
- [Liao 94] Y. Liao & T. A. Lipo. *Effect of saturation third harmonic on the performance of squirrel-cage induction machines*. Electric Machines and Power Systems, vol. 22, no. 2, pages 155 – 171, 1994.
- [Lima 97] A. M. N. Lima, C. B. Jacobina & E. B. de Souza Filho. *Nonlinear parameter estimation of steady-state induction machine models*. IEEE Transactions on Industrial Electronics, vol. 44, no. 3, pages 390 – 397, June 1997.
- [Liwschitz-Garik 55] M. Liwschitz-Garik. *Computation of skin effect in bars of squirrel cage rotors*. Transactions of the American Institute of Electrical Engineers (AIEE) Transactions of the American Institute of Electrical Engineers (AIEE), vol. 74, pages 768 – 771, Aug. 1955.
- [Liwschitz 67] M. Liwschitz & L. Maret. Calcul des machines électriques, volume 1. Bibliothèque de l'ingénieur, 1967.
- [Lombard 92] P. Lombard & G. Meunier. *A general method for electric and magnetic coupled problem in 2D and magnetodynamic domain*. IEEE Transactions on Magnetics, vol. 28, no. 2, pages 1291 – 1294, Mar. 1992.
- [Lopez-Fernandez 03] X. M. Lopez-Fernandez & M. Piper. *MagnetoDynamic performance in cage induction motors with a broken bar*. In International Symposium on Electromagnetic Fields in Electrical Engineering, pages 261 – 266, Sept. 2003.
- [Meshgin-Kelk 02] H. Meshgin-Kelk, J. Milimonfared & H. A. Toliyat. *Interbar currents and axial fluxes in healthy and faulty induction motors*. In IEEE Industry Applications Conference, volume 1, pages 194 – 198, 2002.
- [Minami 91] K. Minami, M. Velez-Reyes, D. Elten, G. C. Verghese & D. Filbert. *Multi-stage speed and parameter estimation for induction machines*. In Power Electronics Specialists Conference, pages 596 – 604, June 1991.
- [Mohammed 05] O. A. Mohammed, S. Ganu, N. Abed & S. Liu. *Harmonic analysis of induction motor flux density waveform using wavelets in speed control application*. In IEEE SoutheastCon, volume 1, pages 60 – 64, Apr. 2005.

- [Muñoz 99] A. R. Muñoz & T. A. Lipo. *Complex vector model of the squirrel-cage induction machine including instantaneous rotor bar currents*. IEEE Transactions on Industry Applications, vol. 35, no. 6, pages 1332 – 1340, Nov. - Dec. 1999.
- [Nandi 00] S. Nandi & H. A. Toliyat. *Novel frequency domain based technique to detect incipient stator inter-turn faults in induction machines*. In IEEE Industry Applications Conference, volume 1, pages 367 – 37, Oct. 2000.
- [Neacsu 02] C. Neacsu, P. Bidan, T. Lebey & M. Valentin. *Presentation of a new off line test procedure for low voltage rotating machines fed by adjustable speed drives (ASD)*. In IEEE International Power Electronics Congress, pages 9 – 14, Oct. 2002.
- [Önel 05] I. Y. Önel, K. B. Dalci & I. Senol. *Detection of outer raceway bearing defects in small induction motors using stator current analysis*. Sadhana, vol. 30, no. 6, pages 713 – 722, Dec. 2005.
- [Ong 00] R. Ong, J. H. Dymond, R. D. Findlay & B. Szabados. *Shaft current in AC induction machine: an on line monitoring system and prediction rules*. In IEEE Industry Applications Conference, volume 1, pages 2822 – 2829, Oct. 2000.
- [Paoletti 89] G. J. Paoletti & A. Rose. *Improving existing motor protection for medium voltage motors*. IEEE Transactions on Industry Applications, vol. 25, no. 3, pages 456 – 464, May - June 1989.
- [Paoletti 01] G. J. Paoletti & A. Golubev. *Partial discharge theory and technologies related to medium-voltage electrical equipment*. IEEE Transactions on Industry Applications, vol. 37, no. 1, pages 90 – 103, Jan. - Feb. 2001.
- [Penman 86] J. Penman, M. N. Dey, A. J. Tait & W. E. Bryan. *Condition monitoring of electrical drives*. IEE Proceedings, vol. 133, no. 3, May 1986.
- [Penman 96] J. Penman & A. Stavrou. *Broken rotor bars: their effect on the transient performance of induction machines*. IEE Proceedings on Electric Power Applications, vol. 143, no. 6, Nov. 1996.
- [Pham 99] T.H. Pham, P.F. Wendling, S.J. Salon & H. Acikgoz. *Transient finite element analysis for an induction motor with external circuit connections and electromechanical coupling*. In IEEE Transactions on Energy Conversion, volume 14, pages 1407 – 1412, Dec. 1999.
- [Poncelet 99] R. Poncelet. Cours elec 269: Machines électrique. Université Libre de Bruxelles, 1999.
- [Raison 00] B. Raison & J.-P. Rognon. *Détection et localisation de défaillances sur un entraine-ment électrique*. PhD thesis, Institut National Polytechnique de Grenoble, 2000.
- [Ramirez-Niño 98] J. Ramirez-Niño, S. Rivera-Castañeda, V. R. Garcia-Colon & V. M. Castaño. *Analysis of partial electrical discharges in insulating materials through the wavelet transform*. Computational Materials Science, vol. 9, no. 3, pages 379 – 388, Jan 1998.
- [Razik 03] H. Razik, A. Abed & A. Rezzoug. *Un modèle du moteur asynchrone à cage dédié à la simulation et au diagnostic*. Revue Internationale de Génie Electrique, vol. 6, no. 3, pages 325 – 350, 2003.

- [Roger-Folch 04] J. Roger-Folch, J. A. Antonino, M. Riera & M. P. Molina. *A new method for the diagnosis of rotor bar failures in induction machines via wavelet decomposition*. In International Conference on Electrical Machines (ICEM), Sept. 2004.
- [Said 00] M. S. N. Said, M. E. H. Benbouzid & A. Benchaib. *Detection of broken bars in induction motors using an extended Kalman filter for rotor resistance sensorless estimation*. IEEE Transactions on Energy Conversion, vol. 15, no. 1, pages 66 – 70, Mar. 2000.
- [Salon 90] S. J. Salon. Finite element analysis of electrical machines. Kluwer Academic Publishers, 1990.
- [Schaeffer 98] E. Schaeffer, E. Le Carpentier & M. E. Zaïm. *Failure detection in induction machine by means of parametric identification*. In IEEE Conference on Computational Engineering in Systems Applications, Apr. 1998.
- [Schaeffer 99] E. Schaeffer, E. Le Carpentier, Z. El Hadi & L. Loron. *Diagnostic des entraînements électriques: Détection de courts-circuits statoriques dans la machine asynchrone par identification paramétrique*. In Colloque GRETSI sur le Traitement du Signal et des Images, volume 4, pages 1037 – 1040, Sept. 1999.
- [Schmitz 65] N. L. Schmitz & D. W. Novotny. Introductory electromechanics. Ronald Press Co., 1965.
- [Schoen 95a] R. R. Schoen & T. G. Habetler. *Effects of time-varying loads on rotor fault detection in induction machines*. IEEE Transactions on Industry Applications, vol. 31, no. 4, pages 900 – 906, July - Aug. 1995.
- [Schoen 95b] R. R. Schoen, T. G. Habetler, F. Kamran & R. G. Bartfield. *Motor bearing damage detection using stator current monitoring*. IEEE Transactions on Industry Applications, vol. 31, no. 6, pages 1274 – 1279, Nov. - Dec. 1995.
- [Schoen 97] R. R. Schoen & T. G. Habetler. *Evaluation and implementation of a system to eliminate arbitrary load effects in current-based monitoring of induction machines*. IEEE Transactions on Industry Applications, vol. 33, no. 6, pages 1571 – 1577, Nov. - Dec. 1997.
- [Sottile 93] Jr. Sottile J. & J. L. Kohler. *An on-line method to detect incipient failure of turn insulation in random-wound motors*. IEEE Transactions on Energy Conversion, vol. 8, no. 4, pages 762 – 768, Dec. 1993.
- [Sottile 00] J. Sottile, F. C. Trutt & J. L. Kohler. *Experimental investigation of on-line methods for incipient fault detection [in induction motors]*. In IEEE Industry Applications Conference, volume 4, pages 2682 – 2687, Oct. 2000.
- [Souto 00] O. C. N. Souto, J. C. de Oliveira & L. M. Neto. *Induction motors thermal behaviour and life expectancy under non-ideal supply conditions*. In International Conference on Harmonics and Quality of Power, volume 3, pages 899 – 904, 2000.
- [Sprooten 03] J. Sprooten. Diagnostic and condition monitoring of induction machines by means of the finite elements method. Master's thesis, Université Libre de Bruxelles, 2003.
- [Stavrou 94] A. Stavrou & J. Penman. *The on-line quantification of air-gap eccentricity in induction machines*. In International Conference on Electrical Machines (ICEM), volume 2, Sept. 1994.

- [Stavrou 01] A. Stavrou, H. G. Sedding & J. Penman. *Current monitoring for detecting Inter-turn short circuits in induction motors*. IEEE Transactions on Energy Conversion, vol. 16, no. 1, Mar. 2001.
- [Stephan 94] J. Stephan, M. Bodson & J. Chiasson. *Real-time estimation of the parameters and fluxes of induction motors*. IEEE Transactions on Industry Applications, vol. 30, no. 3, pages 746 – 759, May - June 1994.
- [Tallam 00] R. M. Tallam, T. G. Habetler & R. G. Harley. *Transient model for induction machines with stator winding turn faults*. In IEEE Industry Applications Magazine, volume 1, pages 304 – 309, Oct. 2000.
- [Tenhunen 01] A. Tenhunen. *Finite-element calculation of unbalanced magnetic pull and circulating current between parallel windings in induction motor with non-uniform eccentric rotor*. In Electromotion, pages 19 – 20, June 2001.
- [Thomas 03] V. V. Thomas, K. Vasudevan & V. J. Kumar. *Online cage rotor fault detection using air-gap torque spectra*. IEEE Transactions on Energy Conversion, vol. 18, no. 2, pages 265 – 270, June 2003.
- [Thorsen 95] O. V. Thorsen & M Dalva. *A survey of faults on induction motors in offshore oil industry, petrochemical industry, gas terminals, and oil refineries*. IEEE Transactions on Industry Applications, vol. 31, no. 5, pages 1186 – 1196, Sept. - Oct. 1995.
- [Thorsen 99] O. V. Thorsen & M. Dalva. *Failure identification and analysis for high-voltage induction motors in the petrochemical industry*. IEEE Transactions on Industry Applications, vol. 35, no. 4, pages 810 – 818, July - Aug. 1999.
- [Tnani 02] S. Tnani, G. Champenois & S. Bachir. *Squirrel cage rotor modeling for broken bars detection. Diagnosis by parameter estimation*. In International Conference on Electrical Machines (ICEM), Aug. 2002.
- [Toliyat 95] H. A. Toliyat & T. A. Lipo. *Transient analysis of cage induction machines under stator, rotor bar and end ring faults*. IEEE Transactions on Energy Conversion, vol. 10, no. 2, pages 241 – 247, June 1995.
- [Trickey 36] P. H. Trickey. *Induction motor resistance ring width*. Transactions of the American Institute of Electrical Engineers (AIEE), vol. 55, pages 144 – 150, Feb. 1936.
- [Vas 94] P. Vas, F. Filippetti, G. Fransceschini & C. Tassoni. *Transient modelling oriented to diagnostics of induction machines with rotor asymmetries*. In International Conference on Electrical Machines (ICEM), volume 2, Sept. 1994.
- [Vassent 89] E. Vassent, G. Meunier & J.-C. Sabonnadière. *Simulation of induction machine operation using complex magnetodynamic finite elements*. IEEE Transactions on Magnetics, vol. 25, no. 4, pages 3064 – 3066, July 1989.
- [Vassent 91] E. Vassent, G. Meunier & A. Foggia. *Simulation of induction machines using complex magnetodynamic finite element method coupled with the circuit equations*. IEEE Transactions on Magnetics, vol. 27, no. 5, pages 4246 – 4249, Sept. 1991.
- [Walliser 94] R. F. Walliser & C. F. Landy. *Determination of interbar current effects in the detection of broken rotor bars in squirrel cage induction motors*. IEEE Transactions on Energy Conversion, vol. 9, no. 1, pages 152 – 158, Mar. 1994.

- [Wang 05a] K. Wang, J. Chiasson, M. Bodson & L. M. Tolbert. *A nonlinear least-squares approach for identification of the induction motor parameters*. IEEE Transactions on Automatic Control, vol. 50, no. 10, pages 1622 – 1628, Oct. 2005.
- [Wang 05b] K. Wang, J. Chiasson, M. Bodson & L. M. Tolbert. *An on-line method for tracking the rotor time constant of an induction machine*. In American Control Conference, June 2005.
- [Watson 99] J. F. Watson & D. G. Dorrell. *The use of finite element methods to improve techniques for the early detection of faults in 3-phase induction motors*. IEEE Transactions on Energy Conversion, vol. 14, no. 3, pages 655 – 660, Sept. 1999.
- [White 59] D. C. White & H. H. Woodson. *Electromechanical energy conversion*. New York: J. Wiley & Sons, 1959.
- [Wildi 91] Th. Wildi. *Electrotechnique*. Les presses de l'université de Laval, 1991.
- [Xiangheng 00] W. Xiangheng, C. Songlin, W. Weijian, S. Yuguang & L. Xu. *A study of armature winding internal faults and protection schemes for turbogenerators*. In IEEE Industry Applications Conference, volume 1, pages 402 – 408, Oct. 2000.
- [Yahoui 96] H. Yahoui & G. Grellet. *Detection of an end-ring fault in asynchronous machines by spectrum analysis of the observed electromagnetic torque*. Journal de Physique III, vol. 6, no. 4, pages 443 – 448, Apr. 1996.

Appendix A

Demonstration of models

A.1 Torque expression

The first step of the process that will lead to the torque expression is to compute magnetic energy.

- This energy can be detailed in the case of a single inductance:

If one wants to inject a current i in an inductance, the rise of i creates the apparition of an electro-motive force given by:

$$\epsilon = -L \frac{di}{dt} = -\frac{d\phi}{dt} = -\frac{\Delta i}{\Delta t}$$

Because this force has to be beaten to inject the current, a work is necessary to modify the current in the inductance:

$$\Delta W = - \underbrace{\epsilon i}_{\text{Power}} \underbrace{\Delta t}_{\text{Time}} = L \frac{\Delta i}{\Delta t} i \Delta t = L i \Delta i$$

Work

The energy required to rise the current in the inductance from 0 to I is given by

$$W = \int_0^I L i di = \frac{L I^2}{2} = \frac{\psi I}{2}$$

where $\psi = L I$

- In the case of an electrical machine, $W = \frac{1}{2} \left(\sum_{i=1}^n \psi_i I_i \right)$ where $\psi_i = \sum_{j=1}^n M_{ij} I_j$

Using matrices, we have

$$W = \frac{1}{2} \begin{bmatrix} \bar{I}_s^t & \bar{I}_r^t \end{bmatrix} \begin{bmatrix} L_{ss} & L_{sr} \\ L_{sr}^t & L_{rr} \end{bmatrix} \begin{bmatrix} \bar{I}_s \\ \bar{I}_r \end{bmatrix} = \frac{1}{2} \bar{I}_s^t L_{ss} \bar{I}_s + \frac{1}{2} \bar{I}_s^t L_{sr} \bar{I}_r + \frac{1}{2} \bar{I}_r^t L_{sr}^t \bar{I}_s + \frac{1}{2} \bar{I}_r^t L_{rr} \bar{I}_r$$

If we apply the principle of virtual works, stated as $\Delta W = F \Delta x$, to the case of rotating machine, we obtain

$$\begin{aligned} T_{em} &= \frac{dW}{d\theta} \\ &= \frac{1}{2} \frac{d(\psi I)}{d\theta} \end{aligned}$$

Because L_{ss} and L_{rr} do not depend of the angular position of the rotor, the torque can be expressed as:

$$T_{em} = \frac{1}{2} \frac{dL_{sr}}{d\theta_r} \overline{I_r} + \frac{1}{2} \overline{I_r}^t \frac{dL_{sr}^t}{d\theta_r} \overline{I_s}$$

The torque being a scalar, it is equal to its transpose, then $\overline{I_r}^t \frac{dL_{sr}^t}{d\theta_r} \overline{I_s} = \left(\overline{I_r}^t \frac{dL_{sr}^t}{d\theta_r} \overline{I_s} \right)^t$

More, as $(A^t B^t C)^t = C^t B A$

Then the torque become $T_{em} = \overline{I_s}^t \frac{dL_{sr}}{d\theta_r} \overline{I_r}$

A.2 Space vector transformation of healthy machine model

A.2.1 Stator

A.2.1.1 $\Psi_{ass} =$ Stator flux due to stator currents:

$$\begin{bmatrix} \Psi_{ass} \\ \Psi_{bss} \\ \Psi_{css} \end{bmatrix} = \begin{bmatrix} L_{ls} + L_{ms} & -\frac{L_{ms}}{2} & -\frac{L_{ms}}{2} \\ -\frac{L_{ms}}{2} & L_{ls} + L_{ms} & -\frac{L_{ms}}{2} \\ -\frac{L_{ms}}{2} & -\frac{L_{ms}}{2} & L_{ls} + L_{ms} \end{bmatrix} \begin{bmatrix} I_{as} \\ I_{bs} \\ I_{cs} \end{bmatrix}$$

The spatial vector of the stator flux due to stator currents and the spatial vector of the stator currents can be defined as

$$\begin{aligned} \underline{\Psi}_{ss} &= \frac{2}{3} (\Psi_{ass} + \underline{\alpha} \Psi_{bss} + \underline{\alpha}^2 \Psi_{css}) \\ \underline{I}_s &= \frac{2}{3} (I_{as} + \underline{\alpha} I_{bs} + \underline{\alpha}^2 I_{cs}) \end{aligned}$$

Substituting the flux by its expression in terms of currents and inductances we obtain

$$\underline{\Psi}_{ss} = \frac{2}{3} \begin{bmatrix} 1 & \underline{\alpha} & \underline{\alpha}^2 \end{bmatrix} \begin{bmatrix} L_{aa} & L_{ab} & L_{ab} \\ L_{ab} & L_{aa} & L_{ab} \\ L_{ab} & L_{ab} & L_{aa} \end{bmatrix} \begin{bmatrix} I_{as} \\ I_{bs} \\ I_{cs} \end{bmatrix}$$

then, we find

$$\begin{aligned} \underline{\Psi}_{ss} &= \frac{2}{3} \begin{bmatrix} L_{aa} + \underline{\alpha} L_{ab} + \underline{\alpha}^2 L_{ab} & L_{ab} + \underline{\alpha} L_{aa} + \underline{\alpha}^2 L_{ab} & L_{ab} + \underline{\alpha} L_{ab} + \underline{\alpha}^2 L_{aa} \end{bmatrix} \begin{bmatrix} I_{as} \\ I_{bs} \\ I_{cs} \end{bmatrix} \\ &= \frac{2}{3} \left((L_{aa} + \underline{\alpha} L_{ab} + \underline{\alpha}^2 L_{ab}) I_{as} + (L_{ab} + \underline{\alpha} L_{aa} + \underline{\alpha}^2 L_{ab}) I_{bs} + (L_{ab} + \underline{\alpha} L_{ab} + \underline{\alpha}^2 L_{aa}) I_{cs} \right) \\ &= \frac{2}{3} \left(L_{aa} (I_{as} + \underline{\alpha} I_{bs} + \underline{\alpha}^2 I_{cs}) + \underline{\alpha} L_{ab} (I_{as} + \underline{\alpha} I_{bs} + \underline{\alpha} I_{cs}) + \underline{\alpha}^2 L_{ab} \left(I_{as} + \frac{1}{\underline{\alpha}^2} I_{bs} + \frac{1}{\underline{\alpha}} I_{cs} \right) \right) \end{aligned}$$

By considering that $\underline{\alpha} = e^{j\frac{2\pi}{3}}$, $\frac{1}{\underline{\alpha}} = e^{-j\frac{2\pi}{3}} = \underline{\alpha}^2$, $\frac{1}{\underline{\alpha}^2} = \underline{\alpha}$; we find

$$\underline{\Psi}_{ss} = (L_{aa} + \underline{\alpha} L_{ab} + \underline{\alpha}^2 L_{ab}) \underline{I}_s$$

Using $\begin{cases} L_{aa} = L_{ls} + L_{ms} \\ L_{ab} = -\frac{1}{2}L_{ms} \end{cases}$ and the fact that $\left(1 - \frac{\alpha}{2} - \frac{\alpha^2}{2}\right) = 1 - \frac{1}{2}\cos\left(\frac{2\pi}{3}\right) - \frac{1}{2}j\sin\left(\frac{2\pi}{3}\right) - \frac{1}{2}\cos\left(\frac{2\pi}{3}\right) + \frac{1}{2}j\sin\left(\frac{2\pi}{3}\right) = 1 - \frac{1}{2}\left(-\frac{1}{2}\right) - \frac{1}{2}\left(-\frac{1}{2}\right) = \frac{3}{2}$, we find

$$\underline{\Psi}_{ss} = \left(L_{ls} + L_{ms} \left(1 - \frac{\alpha}{2} - \frac{\alpha^2}{2} \right) \right) \underline{I}_s = \left(L_{ls} + \frac{3}{2}L_{ms} \right) \underline{I}_s$$

By defining $L_s = L_{ls} + \frac{3}{2}L_{ms}$ we find $\underline{\Psi}_{ss} = L_s \underline{I}_s$

A.2.1.2 $\Psi_{asr} =$ Stator flux due to rotor currents

$$\begin{bmatrix} \psi_{asr} \\ \psi_{bsr} \\ \psi_{csr} \end{bmatrix} = \begin{bmatrix} L_{a1} & \cdots & L_{an} \\ L_{b1} & \cdots & L_{bn} \\ L_{c1} & \cdots & L_{cn} \end{bmatrix} \begin{bmatrix} I_{r1} \\ \cdots \\ I_{rn} \end{bmatrix} \text{ where } I_{ri} \text{ are rotor loop currents.}$$

using $\cos(\theta) = \frac{e^{j\theta} + e^{-j\theta}}{2}$ and $\underline{\beta} = e^{jP\alpha_r}$ becomes

$$\begin{aligned} & \begin{bmatrix} \psi_{asr} \\ \psi_{bsr} \\ \psi_{csr} \end{bmatrix} \\ &= \frac{L_m}{2} \begin{bmatrix} e^{jP(\theta_r+\delta)} + e^{-jP(\theta_r+\delta)} & \cdots & e^{jP\left(\frac{\theta_r+\delta}{+(n-1)\alpha_r}\right)} + e^{-jP\left(\frac{\theta_r+\delta}{+(n-1)\alpha_r}\right)} \\ e^{j(P(\theta_r+\delta)-120^\circ)} + e^{-j(P(\theta_r+\delta)-120^\circ)} & \cdots & \vdots \\ \vdots & \cdots & \vdots \\ e^{jP(\theta_r+\delta)} & \begin{bmatrix} 1 & \underline{\beta} & \cdots & \underline{\beta}^{n-1} \\ \underline{\alpha}^2 & \underline{\alpha}^2\underline{\beta} & \vdots & \underline{\alpha}^2\underline{\beta}^{n-1} \\ \underline{\alpha} & \underline{\alpha}\underline{\beta} & \vdots & \underline{\alpha}\underline{\beta}^{n-1} \end{bmatrix} & \cdots \\ +e^{-jP(\theta_r+\delta)} & \begin{bmatrix} 1 & \underline{\beta}^{-1} & \cdots & \underline{\beta}^{1-n} \\ \underline{\alpha} & \underline{\alpha}\underline{\beta}^{-1} & \vdots & \underline{\alpha}\underline{\beta}^{1-n} \\ \underline{\alpha}^2 & \underline{\alpha}^2\underline{\beta}^{-1} & \vdots & \underline{\alpha}^2\underline{\beta}^{1-n} \end{bmatrix} & \cdots \end{bmatrix} \begin{bmatrix} I_{r1} \\ \cdots \\ I_{rn} \end{bmatrix} \\ &= \frac{L_m}{2} \left(\begin{bmatrix} e^{jP(\theta_r+\delta)} & \begin{bmatrix} 1 & \underline{\beta} & \cdots & \underline{\beta}^{n-1} \\ \underline{\alpha}^2 & \underline{\alpha}^2\underline{\beta} & \vdots & \underline{\alpha}^2\underline{\beta}^{n-1} \\ \underline{\alpha} & \underline{\alpha}\underline{\beta} & \vdots & \underline{\alpha}\underline{\beta}^{n-1} \end{bmatrix} \\ +e^{-jP(\theta_r+\delta)} & \begin{bmatrix} 1 & \underline{\beta}^{-1} & \cdots & \underline{\beta}^{1-n} \\ \underline{\alpha} & \underline{\alpha}\underline{\beta}^{-1} & \vdots & \underline{\alpha}\underline{\beta}^{1-n} \\ \underline{\alpha}^2 & \underline{\alpha}^2\underline{\beta}^{-1} & \vdots & \underline{\alpha}^2\underline{\beta}^{1-n} \end{bmatrix} \end{bmatrix} \right) \begin{bmatrix} I_{r1} \\ \cdots \\ I_{rn} \end{bmatrix} \end{aligned}$$

If we multiply the second row by $\underline{\alpha}$ and the third by $\underline{\alpha}^2$ we get

$$\begin{bmatrix} \psi_{asr} \\ \underline{\alpha}\psi_{bsr} \\ \underline{\alpha}^2\psi_{csr} \end{bmatrix} = \frac{L_m}{2} \left(\begin{bmatrix} e^{jP(\theta_r+\delta)} & \begin{bmatrix} 1 & \underline{\beta} & \cdots & \underline{\beta}^{n-1} \\ 1 & \underline{\beta} & \vdots & \underline{\beta}^{n-1} \\ 1 & \underline{\beta} & \vdots & \underline{\beta}^{n-1} \end{bmatrix} \\ +e^{-jP(\theta_r+\delta)} & \begin{bmatrix} 1 & \underline{\beta}^{-1} & \cdots & \underline{\beta}^{1-n} \\ \underline{\alpha}^2 & \underline{\alpha}^2\underline{\beta}^{-1} & \vdots & \underline{\alpha}^2\underline{\beta}^{1-n} \\ \underline{\alpha} & \underline{\alpha}\underline{\beta}^{-1} & \vdots & \underline{\alpha}\underline{\beta}^{1-n} \end{bmatrix} \end{bmatrix} \right) \begin{bmatrix} I_{r1} \\ \cdots \\ I_{rn} \end{bmatrix}$$

We now have to add the 3 rows and multiply by 2/3 to obtain

$$\begin{aligned}
\underline{\Psi}_{sr} &= \frac{2}{3} \left(\psi_{asr} + \underline{\alpha} \psi_{bsr} + \underline{\alpha}^2 \psi_{csr} \right) \\
&= \frac{L_m}{3} \left(e^{jP(\theta_r+\delta)} 3 \begin{bmatrix} 1 & \underline{\beta} & \dots & \underline{\beta}^{n-1} \end{bmatrix} \begin{bmatrix} I_{r1} \\ \dots \\ I_{rn} \end{bmatrix} \right. \\
&\quad \left. + e^{-jP(\theta_r+\delta)} \underbrace{(1 + \underline{\alpha}^2 + \underline{\alpha})}_{=0} \begin{bmatrix} 1 & \underline{\beta}^{-1} & \dots & \underline{\beta}^{1-n} \end{bmatrix} \begin{bmatrix} I_{r1} \\ \dots \\ I_{rn} \end{bmatrix} \right) \\
&= L_m e^{jP(\theta_r+\delta)} \begin{bmatrix} 1 & \underline{\beta} & \dots & \underline{\beta}^{n-1} \end{bmatrix} \begin{bmatrix} I_{r1} \\ \dots \\ I_{rn} \end{bmatrix}
\end{aligned}$$

$$\text{if we define } \underline{I}_r \text{ as } \underline{I}_r = \frac{2}{n} \begin{bmatrix} 1 & \underline{\beta} & \dots & \underline{\beta}^{n-1} \end{bmatrix} \begin{bmatrix} I_{r1} \\ \dots \\ I_{rn} \end{bmatrix}$$

Then the expression of stator flux due to rotor current becomes

$$\underline{\Psi}_{sr} = \frac{n}{2} L_m e^{jP(\theta_r+\delta)} \underline{I}_r$$

A.2.1.3 Finally the stator flux is given by

$$\underline{\Psi}_s = \underline{\Psi}_{ss} + \underline{\Psi}_{sr} = L_s \underline{I}_s + \frac{n}{2} L_m e^{jP(\theta_r+\delta)} \underline{I}_r \tag{A.1}$$

A.2.2 Rotor

We can write this equation for the n rotor loops

$$\begin{bmatrix} 0 \\ \dots \\ \dots \\ 0 \end{bmatrix} = \begin{bmatrix} R_0 & -R_b & 0 & \dots & 0 & -R_b \\ -R_b & R_0 & -R_b & 0 & \dots & 0 \\ \dots & \dots & \dots & \dots & \dots & \dots \\ -R_b & 0 & \dots & 0 & -R_b & R_0 \end{bmatrix} \begin{bmatrix} i_{r1} \\ \dots \\ i_{rn} \end{bmatrix} + p \begin{bmatrix} \psi_{r1} \\ \dots \\ \psi_{rn} \end{bmatrix}$$

with $R_0 = 2(R_b + R_e)$

$$\Leftrightarrow \underline{0} = R_r \underline{I}_r + p \underline{\psi}_r$$

A.2.2.1 The rotor flux due to stator current is given by

$$\begin{bmatrix} \Psi_{r1s} \\ \dots \\ \Psi_{rns} \end{bmatrix} = \begin{bmatrix} L_{1a} & L_{1b} & L_{1c} \\ \dots & \dots & \dots \\ L_{na} & L_{nb} & L_{nc} \end{bmatrix} \begin{bmatrix} i_{as} \\ i_{bs} \\ i_{cs} \end{bmatrix}$$

The principle of conservation of the energy leads to $L_{xi} = L_{ix} \begin{cases} \forall i = 1, \dots, n \\ \forall x = a, b, c \end{cases}$

As before, we have

$$\begin{bmatrix} L_{1a} & L_{1b} & L_{1c} \\ \dots & \dots & \dots \\ L_{na} & L_{nb} & L_{nc} \end{bmatrix} = \frac{L_m}{2} \left(\begin{array}{c} e^{jP(\theta_r+\delta)} \begin{bmatrix} 1 & \underline{\beta} & \dots & \underline{\beta}^{n-1} \\ \underline{\alpha}^2 & \underline{\alpha}^2 \underline{\beta} & \vdots & \underline{\alpha}^2 \underline{\beta}^{n-1} \\ \underline{\alpha} & \underline{\alpha} \underline{\beta} & \vdots & \underline{\alpha} \underline{\beta}^{n-1} \end{bmatrix} \\ + e^{-jP(\theta_r+\delta)} \begin{bmatrix} 1 & \underline{\beta}^{-1} & \dots & \underline{\beta}^{1-n} \\ \underline{\alpha} & \underline{\alpha} \underline{\beta}^{-1} & \vdots & \underline{\alpha} \underline{\beta}^{1-n} \\ \underline{\alpha}^2 & \underline{\alpha}^2 \underline{\beta}^{-1} & \vdots & \underline{\alpha}^2 \underline{\beta}^{1-n} \end{bmatrix} \end{array} \right)$$

if we transpose the matrix and multiply each line by $1, \underline{\beta}, \dots, \underline{\beta}^{n-1}$ we obtain

$$\begin{bmatrix} \Psi_{r1s} \\ \underline{\beta} \Psi_{r2s} \\ \dots \\ \underline{\beta}^{n-1} \Psi_{rns} \end{bmatrix} = \frac{L_m}{2} \left(\begin{array}{c} e^{jP(\theta_r+\delta)} \begin{bmatrix} 1 & \underline{\alpha}^2 & \underline{\alpha} \\ \underline{\beta}^2 & \underline{\alpha}^2 \underline{\beta}^2 & \underline{\alpha} \underline{\beta}^2 \\ \vdots & \vdots & \vdots \\ \underline{\beta}^{2(n-1)} & \underline{\alpha}^2 \underline{\beta}^{2(n-1)} & \underline{\alpha} \underline{\beta}^{2(n-1)} \end{bmatrix} \\ + e^{-jP(\theta_r+\delta)} \begin{bmatrix} 1 & \underline{\alpha} & \underline{\alpha}^2 \\ \vdots & \vdots & \vdots \\ 1 & \underline{\alpha} & \underline{\alpha}^2 \end{bmatrix} \end{array} \right) \begin{bmatrix} i_{as} \\ i_{bs} \\ i_{cs} \end{bmatrix}$$

The complex vector $\underline{\Psi}_{rs}$ is obtained by adding all the rows and multiplying by $\frac{2}{n}$

$$\underline{\Psi}_{rs} = \frac{L_m}{n} \left(\begin{array}{c} e^{jP(\theta_r+\delta)} \left(1 + \dots + \underline{\beta}^{2(n-1)} \right) \begin{bmatrix} 1 & \underline{\alpha}^2 & \underline{\alpha} \end{bmatrix} \\ + n e^{-jP(\theta_r+\delta)} \begin{bmatrix} 1 & \underline{\alpha} & \underline{\alpha}^2 \end{bmatrix} \end{array} \right) \begin{bmatrix} i_{as} \\ i_{bs} \\ i_{cs} \end{bmatrix}$$

More, because $\left(1 + \underline{\beta}^2 + \dots + \underline{\beta}^{2(n-1)} \right) = 0$ we obtain

$$\underline{\Psi}_{rs} = L_m e^{-jP(\theta_r+\delta)} \begin{bmatrix} i_{as} \\ i_{bs} \\ i_{cs} \end{bmatrix} \begin{bmatrix} 1 & \underline{\alpha} & \underline{\alpha}^2 \end{bmatrix}$$

and because $\underline{I}_s = \frac{2}{3} (I_{as} + \underline{\alpha} I_{bs} + \underline{\alpha}^2 I_{cs})$

we have

$$\underline{\Psi}_{rs} = \frac{3}{2} L_m e^{-jP(\theta_r+\delta)} \underline{I}_s$$

Remarks: Demonstration that $\left(1 + \underline{\beta}^2 + \dots + \underline{\beta}^{2(n-1)} \right) = 0$

$\underline{\beta} = e^{jP\alpha_r}$ and $n\alpha_r = 2\pi$

For a geometric progression we have:

$$\sum_{k=0}^{n-1} \underline{\beta}^{2k} = \frac{1 - \underline{\beta}^{2n}}{1 - \underline{\beta}^2} = \frac{1 - e^{j2nP\alpha_r}}{1 - e^{jP\alpha_r}} = \frac{1 - 1}{1 - e^{jP\alpha_r}} = 0$$

A.2.2.2 Ψ_{rr} = Rotor flux due to rotor currents

The flux cut by the loop k and created by the rotor currents is give by

$$\Psi_{rkr} = L_{k1} I_{r1} + \dots + L_{kn} I_{rn} + 2(L_e + L_b) I_{rk} - L_b (I_{r(k-1)} + I_{r(k+1)})$$

This equation is valid for every rotor loops, and this leads to

$$\begin{bmatrix} \Psi_{r1r} \\ \dots \\ \Psi_{rnr} \end{bmatrix} = \begin{bmatrix} L_{11} + L_0 & L_{12} - L_b & L_{13} & \dots & L_{1n} - L_b \\ \vdots & \vdots & \vdots & \vdots & \vdots \\ L_{n1} - L_b & L_{n2} & \dots & \dots & L_{nn} + L_0 \end{bmatrix} \begin{bmatrix} i_{r1} \\ \dots \\ i_{rn} \end{bmatrix}$$

where $L_0 = 2(L_b + L_e)$

As we can see, L_{kk} and L_{ki} are constant, only dependant on the rotor dimensions and not dependant of their relative position.

Then the previous equation becomes

$$\begin{bmatrix} \Psi_{r1r} \\ \dots \\ \Psi_{rnr} \end{bmatrix} = \begin{bmatrix} L_{kk} + L_0 & L_{ki} - L_b & L_{ki} & \dots & L_{ki} - L_b \\ \vdots & \vdots & \vdots & \vdots & \vdots \\ L_{ki} - L_b & L_{ki} & \dots & \dots & L_{kk} + L_0 \end{bmatrix} \begin{bmatrix} i_{r1} \\ \dots \\ i_{rn} \end{bmatrix}$$

if we multiply each line of the equation by $1, \underline{\beta}, \dots, \underline{\beta}^{n-1}$, we obtain

$$\begin{bmatrix} \Psi_{r1r} \\ \underline{\beta} \Psi_{r2r} \\ \dots \\ \underline{\beta}^{n-1} \Psi_{rnr} \end{bmatrix} = \begin{bmatrix} L_{kk} + L_0 & L_{ki} - L_b & L_{ki} & \dots & L_{ki} - L_b \\ \vdots & \vdots & \vdots & \vdots & \vdots \\ \underline{\beta}^{n-1} (L_{ki} - L_b) & \underline{\beta}^{n-1} (L_{ki}) & \dots & \dots & \underline{\beta}^{n-1} (L_{kk} + L_0) \end{bmatrix} \begin{bmatrix} i_{r1} \\ \dots \\ i_{rn} \end{bmatrix}$$

Then if we multiply the line of the rotor currents vector by $1, \underline{\beta}, \dots, \underline{\beta}^{n-1}$ and the column of the inductances matrix by $1, \underline{\beta}^{-1}, \dots, \underline{\beta}^{1-n}$ to compensate, we get

$$\begin{bmatrix} \Psi_{r1r} \\ \underline{\beta} \Psi_{r2r} \\ \dots \\ \underline{\beta}^{n-1} \Psi_{rnr} \end{bmatrix} = \begin{bmatrix} (L_{kk} + L_0) & \underline{\beta}^{-1} (L_{ki} - L_b) & \underline{\beta}^{-2} (L_{ki}) & \dots & \underline{\beta}^{1-n} (L_{ki} - L_b) \\ \vdots & \vdots & \vdots & \vdots & \vdots \\ \underline{\beta}^{n-1} (L_{ki} - L_b) & \underline{\beta}^{-1} \underline{\beta}^{n-1} (L_{ki}) & \dots & \dots & \underline{\beta}^{1-n} \underline{\beta}^{n-1} (L_{kk} + L_0) \end{bmatrix} \begin{bmatrix} i_{r1} \\ \underline{\beta} i_{r2} \\ \dots \\ \underline{\beta}^{n-1} i_{rn} \end{bmatrix}$$

Then taking into account that $\underline{\beta}^{n+m} = \underline{\beta}^m$, we find

$$\begin{pmatrix} \Psi_{r1r} \\ \underline{\beta} \Psi_{r2r} \\ \dots \\ \underline{\beta}^{n-1} \Psi_{rnr} \end{pmatrix} = \begin{bmatrix} (L_{kk} + L_0) & \underline{\beta}^{-1} (L_{ki} - L_b) & \underline{\beta}^{-2} (L_{ki}) & \dots & \underline{\beta} (L_{ki} - L_b) \\ \vdots & \vdots & \vdots & \vdots & \vdots \\ \underline{\beta}^{n-1} (L_{ki} - L_b) & \underline{\beta}^{n-2} (L_{ki}) & \dots & \dots & (L_{kk} + L_0) \end{bmatrix} \begin{pmatrix} i_{r1} \\ \underline{\beta} i_{r2} \\ \dots \\ \underline{\beta}^{n-1} i_{rn} \end{pmatrix}$$

We can now sum the lines to have

$$\begin{aligned}
\underline{\Psi}_{rr} &= \begin{matrix} (L_{kk} + L_0) i_{r1} & + \underline{\beta}^{n-1} (L_{ki} - L_b) \underline{\beta} i_{r2} & + \dots & + \underline{\beta} (L_{ki} - L_b) \underline{\beta}^{n-1} i_{rn} \\ + \underline{\beta} (L_{ki} - L_b) i_{r1} & + \underline{\beta} (L_{kk} + L_0) i_{r2} & + \dots & + \underline{\beta}^2 (L_{ki}) \underline{\beta}^{n-1} i_{rn} \\ + \dots & + \dots & + \dots & + \dots \\ + \underline{\beta}^{n-1} (L_{ki} - L_b) i_{r1} & + \underline{\beta}^{n-2} (L_{ki}) \underline{\beta} i_{r2} & + \dots & + (L_{kk} + L_0) \underline{\beta}^{n-1} i_{rn} \end{matrix} \\
&= (L_{kk} + L_0 - \underline{\beta} L_b - \underline{\beta}^{n-1} L_b) \underline{I}_r + (\underline{\beta}^2 + \dots + \underline{\beta}^{2(n-1)}) L_{ki} \underline{I}_r
\end{aligned}$$

Note that $\underline{\beta}^{n-1} = \underline{\beta}^{-1}$, $\underline{\beta} + \underline{\beta}^{-1} = e^{jP} \alpha_r + e^{-jP} \alpha_r = 2 \cos(P \alpha_r)$ and $L_{kk} = \frac{\mu_0 l r}{g} \alpha_r + L_{ki}$, therefore

$$\underline{\Psi}_{rr} = (2 L_b (1 - \cos(P \alpha_r)) + 2 L_e + \frac{\mu_0 l r}{g} \alpha_r) \underline{I}_r = L_r \underline{I}_r$$

A.2.2.3 Then the rotor flux is given by

$$\underline{\Psi}_r = \underline{\Psi}_{rs} + \underline{\Psi}_{rr} = L_r \underline{I}_r + \frac{3}{2} L_m e^{-jP(\theta_r + \delta)} \underline{I}_s \tag{A.2}$$

A.2.2.4 Equivalent rotor resistance

Earlier we had

$$\begin{bmatrix} 0 \\ \dots \\ \dots \\ 0 \end{bmatrix} = \begin{bmatrix} R_0 & -R_b & 0 & \dots & 0 & -R_b \\ -R_b & R_0 & -R_b & 0 & \dots & 0 \\ \dots & \dots & \dots & \dots & \dots & \dots \\ -R_b & 0 & \dots & 0 & -R_b & R_0 \end{bmatrix} \begin{bmatrix} i_{r1} \\ \dots \\ i_{rn} \end{bmatrix} + p \begin{bmatrix} \psi_{r1} \\ \dots \\ \psi_{rn} \end{bmatrix}$$

which leads to $\underline{0} = R_r \underline{I}_r + p \underline{\Psi}_r$

Let us now determine the value of the rotor resistance R_r

then, using the same method than the one we used for the flux, we have

$$\begin{aligned}
&\begin{bmatrix} 0 \\ \dots \\ \dots \\ 0 \end{bmatrix} \\
&= \begin{bmatrix} R_0 & -R_b & 0 & \dots & 0 & -R_b \\ -\underline{\beta} R_b & \underline{\beta} R_0 & -\underline{\beta} R_b & 0 & \dots & 0 \\ \dots & \dots & \dots & \dots & \dots & \dots \\ -\underline{\beta}^{n-1} R_b & 0 & \dots & 0 & -\underline{\beta}^{n-1} R_b & \underline{\beta}^{n-1} R_0 \end{bmatrix} \begin{bmatrix} i_{r1} \\ \dots \\ i_{rn} \end{bmatrix} + p \begin{bmatrix} \psi_{r1} \\ \dots \\ \psi_{rn} \end{bmatrix} \\
&= \begin{bmatrix} R_0 & -\underline{\beta}^{-1} R_b & 0 & \dots & 0 & -\underline{\beta}^{1-n} R_b \\ -\underline{\beta} R_b & R_0 & -\underline{\beta}^{-1} R_b & 0 & \dots & 0 \\ \dots & \dots & \dots & \dots & \dots & \dots \\ -\underline{\beta}^{n-1} R_b & 0 & \dots & 0 & -\underline{\beta} R_b & R_0 \end{bmatrix} \begin{bmatrix} i_{r1} \\ \underline{\beta} i_{r2} \\ \dots \\ \underline{\beta}^{n-1} i_{rn} \end{bmatrix} + p \begin{bmatrix} \psi_{r1} \\ \underline{\beta} \psi_{r2} \\ \dots \\ \underline{\beta}^{n-1} \psi_{rn} \end{bmatrix}
\end{aligned}$$

Which leads to

$$\underline{0} = (R_0 - (\underline{\beta} + \underline{\beta}^{n-1}) R_b) \underline{I}_r + p \underline{\Psi}_r$$

And using $R_0 = 2(R_b + R_e)$, we have

$$\underline{Q} = (2R_e + 2R_b(1 - \cos(P\alpha_r))) \underline{I}_r + p \underline{\Psi}_r$$

The rotor resistance only depend off the resistances of the bars and the resistances of the end-rings. Then it is easy to take into account their variation with temperature or skin effect.

Finally, the circuit equation leads to

$$\begin{cases} \underline{V}_s = R_s \underline{I}_s + L_s p \underline{I}_s + \frac{n}{2} L_m e^{jP(\theta_r + \delta)} (p + jP\omega_r) \underline{I}_r \\ \underline{Q} = R_r \underline{I}_r + L_r p \underline{I}_r + \frac{3}{2} L_m e^{-jP(\theta_r + \delta)} (p - jP\omega_r) \underline{I}_s \end{cases}$$

A.2.3 Torque Expression

Previously we had

$$\begin{aligned} L_{sr} &= \frac{L_m}{2} \left(e^{jP(\theta_r + \delta)} \begin{bmatrix} 1 & \underline{\beta} & \dots & \underline{\beta}^{n-1} \\ \underline{\alpha}^2 & \underline{\alpha}^2 \underline{\beta} & \vdots & \underline{\alpha}^2 \underline{\beta}^{n-1} \\ \underline{\alpha} & \underline{\alpha} \underline{\beta} & \vdots & \underline{\alpha} \underline{\beta}^{n-1} \end{bmatrix} + e^{-jP(\theta_r + \delta)} \begin{bmatrix} 1 & \underline{\beta}^{-1} & \dots & \underline{\beta}^{1-n} \\ \underline{\alpha} & \underline{\alpha} \underline{\beta}^{-1} & \vdots & \underline{\alpha} \underline{\beta}^{1-n} \\ \underline{\alpha}^2 & \underline{\alpha}^2 \underline{\beta}^{-1} & \vdots & \underline{\alpha}^2 \underline{\beta}^{1-n} \end{bmatrix} \right) \\ &= \frac{L_m}{2} \left(e^{jP(\theta_r + \delta)} \begin{bmatrix} 1 \\ \underline{\alpha}^2 \\ \underline{\alpha} \end{bmatrix} \begin{bmatrix} 1 & \underline{\beta} & \underline{\beta}^{n-1} \end{bmatrix} + e^{-jP(\theta_r + \delta)} \begin{bmatrix} 1 \\ \underline{\alpha} \\ \underline{\alpha}^2 \end{bmatrix} \begin{bmatrix} 1 & \underline{\beta}^{-1} & \underline{\beta}^{1-n} \end{bmatrix} \right) \end{aligned}$$

Then

$$\frac{dL_{sr}}{d\theta_r} = \frac{L_m}{2} jP \left(e^{jP(\theta_r + \delta)} \begin{bmatrix} 1 \\ \underline{\alpha}^2 \\ \underline{\alpha} \end{bmatrix} \begin{bmatrix} 1 & \underline{\beta} & \underline{\beta}^{n-1} \end{bmatrix} - e^{-jP(\theta_r + \delta)} \begin{bmatrix} 1 \\ \underline{\alpha} \\ \underline{\alpha}^2 \end{bmatrix} \begin{bmatrix} 1 & \underline{\beta}^{-1} & \underline{\beta}^{1-n} \end{bmatrix} \right)$$

The electromechanical torque $Tem = I_s^t \frac{dL_{sr}}{d\theta_r} I_r$ becomes:

$$Tem = P \frac{L_m}{2} j \left(\underbrace{e^{jP(\theta_r + \delta)} \begin{bmatrix} I_{as} & I_{bs} & I_{cs} \end{bmatrix}}_{\frac{3}{2} I_s^*} \begin{bmatrix} 1 \\ \underline{\alpha}^2 \\ \underline{\alpha} \end{bmatrix} \begin{bmatrix} 1 & \underline{\beta} & \underline{\beta}^{n-1} \end{bmatrix} \begin{bmatrix} I_{r1} \\ \vdots \\ I_{rn} \end{bmatrix} + \underbrace{e^{-jP(\theta_r + \delta)} \begin{bmatrix} I_{as} & I_{bs} & I_{cs} \end{bmatrix}}_{\frac{3}{2} I_s} \begin{bmatrix} 1 \\ \underline{\alpha} \\ \underline{\alpha}^2 \end{bmatrix} \begin{bmatrix} 1 & \underline{\beta}^{-1} & \underline{\beta}^{1-n} \end{bmatrix} \begin{bmatrix} I_{r1} \\ \vdots \\ I_{rn} \end{bmatrix} \right)$$

Indeed, $\begin{bmatrix} I_{as} & I_{bs} & I_{cs} \end{bmatrix}^* = \begin{bmatrix} I_{as} & I_{bs} & I_{cs} \end{bmatrix}$ because I_{as}, I_{bs} and I_{cs} are real values and $\begin{bmatrix} 1 \\ \underline{\alpha}^2 \\ \underline{\alpha} \end{bmatrix}^* = \begin{bmatrix} 1 \\ \underline{\alpha} \\ \underline{\alpha}^2 \end{bmatrix}$

$$Tem = P \frac{L_m}{2} j \frac{n}{2} \frac{3}{2} \left(\underline{I}_s^* \underline{I}_r e^{jP(\theta_r + \delta)} - \underline{I}_s \underline{I}_r^* e^{-jP(\theta_r + \delta)} \right)$$

Using the complex algebra property $\frac{1}{2} j (a - a^*) = -\Im(a)$, we have

$$Tem = -\frac{n}{2} \frac{3}{2} P L_m \Im \left(\underline{I}_s^* \underline{I}_r e^{jP(\theta_r + \delta)} \right)$$

A.3 Complete circuit model of a machine

A.3.1 Stator

The stator winding equations can be written as

$$\underline{V}_s = R_{ss} \underline{I}_s + L_{ss} \frac{d}{dt} \underline{I}_s + \frac{d}{dt} (L_{sr} \underline{I}_r)$$

where

$$\begin{cases} \underline{I}_s = \begin{bmatrix} I_{as} & I_{bs} & I_{cs} \end{bmatrix} \\ \underline{I}_r = \begin{bmatrix} I_{r1} & I_{r2} & \cdots & I_{rn} & I_{re} \end{bmatrix} \end{cases}$$

$$R_{ss} = \begin{bmatrix} R_s & 0 & 0 \\ 0 & R_s & 0 \\ 0 & 0 & R_s \end{bmatrix}$$

$$L_{ss} = \begin{bmatrix} L_{ls} + L_{ms} & \frac{-L_{ms}}{2} & \frac{-L_{ms}}{2} \\ \frac{-L_{ms}}{2} & L_{ls} + L_{ms} & \frac{-L_{ms}}{2} \\ \frac{-L_{ms}}{2} & \frac{-L_{ms}}{2} & L_{ls} + L_{ms} \end{bmatrix}$$

and

$$L_{sr} = \begin{bmatrix} L_{a1} & \cdots & L_{an} & L_{ae} \\ L_{b1} & \cdots & L_{bn} & L_{be} \\ L_{c1} & \cdots & L_{cn} & L_{ce} \end{bmatrix}$$

If we recall from *ModelHealthy*, we have $L_m = \frac{4P \sin(P\delta)}{\pi N_s} L_{ms}$ and $L_s = L_{ls} + \frac{3}{2} L_{ms}$ and

$$L_{ai} = L_m \cos(P(\theta_r + (i-1)\alpha_r + \delta))$$

with $\theta_r = \theta_0 + \Omega_r t$ therefore

$$\frac{d}{dt}L_{ai} = -P\Omega_r L_m \cos(P(\theta_r + (i-1)\alpha_r + \delta))$$

A.3.2 Rotor

The rotor winding equations can be written as

$$\underline{0} = R_{rr} \underline{I}_r + L_{rr} \frac{d}{dt} \underline{I}_r + \frac{d}{dt} (L_{sr}^t \underline{I}_s)$$

Appendix B

Data of FE models

The name plate of the motor as well as main information is shown in table 3.1.

B.1 Geometrical Data of *IND1*

The schematics of the motor is given in figure 3.1. The dimensions of the elements of this plan are given in table B.1.

General	
airgap width (g)	0.25mm
stack length (l)	139.5mm
Stator	
stator outer diameter (sod)	170mm
stator inner diameter (sid)	117mm
stator slot height (h_{ss})	13mm
stator slot opening	3.8mm
stator slot bottom radius	3.6mm
Rotor	
rotor outer diameter (rod)	116.5mm
rotor inner diameter (rid)	38mm
rotor bar height (h_b)	18mm
rotor bar bottom radius	1.15mm
rotor bar top radius	2.75mm
bar external diameter (D_{eb})	115.76mm

Table B.1: Geometrical dimensions.

B.2 Electrical data of *IND1*

In the case of the healthy machine as well as a machine with broken bars of eccentricity, the electrical characteristics of the windings and cage elements are given in table B.2.

Stator	
Stator slots filling factor (F)	0.4171
Number of turns per slot per phase (N_{tsp})	44 <i>turns</i>
Number of slots per pole per phase (N_{spp})	3 <i>slots</i>
Diameter of wires (d_w)	0.932mm
Copper resistivity ($\rho_{cu} = 1.724e - 8\Omega m$)	0.932mm
End winding Axial length (l_{zew})	32.5mm
Section of end winding bundle (S_{ew})	191mm ²
Rotor	
ring height (h)	27.3mm
ring thickness (e)	5.7mm
ring internal Diameter (D_i)	81.9mm

Table B.2: Winding description

B.3 Electrical data of *IND1* with 10-turns stator short-circuit

In the case of a machine with a 10-turn stator short-circuit in phase a , the winding electrical characteristics of this phase are given in table B.3.

Component	Values
<i>PA1</i> and <i>MA1</i>	$N = 132 - 44$; $R = 0.31038\Omega$
<i>PA1NoCC</i> and <i>MA1NoCC</i>	$N = 44 - 10$; $R = 0.11992\Omega$
End-Impedances of healthy parts	$R = 1.03053\Omega$; $L = 0.003882H$
<i>PA1CC</i> and <i>MA1CC</i>	$N = 10$; $R = 0.03527\Omega$
End-Impedances of fault part	$R = 0.08447\Omega$; $L = 0.000318H$
R_{fault}	$R = 0.01\Omega$

Table B.3: Winding description of phase a in case of 10-turn short-circuit.

The generalisation to any phase and any number of short-circuit turns is straightforward.